POLITECNICO
MILANO 1863

Mathematical Models and
Methods in Engineering

Mathematical and numerical modeling of the heart function: integrating electrophysiology, mechanics and fluid dynamics

Doctoral dissertation of **Michele Bucelli**

Advisor: Prof. Alfio Quarteroni
Co-advisor: Prof. Luca Dede'
Chair of the doctoral program: Prof. Michele Correggi

XXXV cycle, February 2023

Abstract

The scope of this thesis is the development of a comprehensive and fully coupled heart model, which can serve as a basis for the construction of highly accurate digital twins of the cardiac function. I incorporate in a novel computational framework cardiac electrophysiology (through the monodomain equation and suitable ionic models), contractile force generation, muscular mechanics, hemodynamics and the circulatory system. The model accounts for electro-mechanical and mechano-electrical feedback, the coupling between muscular deformation and contractile force generation, and fluid-structure interaction (FSI) between the blood and the myocardium. Due to the complexity of the problem, suitable numerical methods must be employed for its solution. Focusing on the solution of the FSI subproblem, I identify a geometrically explicit monolithic method as the scheme offering the best trade-off among solver robustness, efficiency and accuracy. The coupling of electrophysiology, force generation, and FSI is treated in a segregated-staggered way, so as to leverage the multiphysics nature of the problem for computational efficiency and flexibility. Numerical methods are implemented in a high-performance computing framework. I simulate a realistic human left heart in physiological conditions and compare the numerical results against normal ranges for several biomarkers for ventricular volumes and pressures, flow rates through cardiac valves and the duration of heartbeat phases. The results show that the proposed model is capable of reproducing the heart function in healthy conditions. Finally, a proof-of-concept simulation indicates that previous results can be extended to simulations involving all four cardiac chambers, thus providing an extremely comprehensive representation of the heart. I believe that the proposed computational model stands as a milestone towards the development of cardiac digital twins.

Contents

Contents **v**

1 Introduction **1**
1.1 Cardiac anatomy and physiology 3
1.2 An overview of mathematical models of the heart 11
1.3 Thesis objectives and main contributions 13

2 Mathematical models of the heart function **17**
2.1 Modeling the cardiac fiber architecture 19
2.2 Electrophysiology 20
2.3 Force generation 24
2.4 Cardiac mechanics 26
2.5 Fluid dynamics 32
2.6 Fluid-structure coupling conditions 38
2.7 Modeling the circulatory system 39

3 Numerical methods for cardiac electro-mechanics-fluid dynamics interaction **45**
3.1 A segregated-staggered scheme for EMF interaction 46
3.2 Numerical methods for cardiac FSI 49
3.3 Space discretization and solvers 61
3.4 A comparison of strongly coupled schemes for cardiac FSI . 66
3.5 A comparison between strongly and loosely coupled algorithms for cardiac FSI 76

4 An integrated model of the left heart **93**
4.1 Setup of the test case 93

4.2 Simulation results 97

5 An integrated model of the whole heart **117**
5.1 Setup of the test case 117
5.2 Simulation results 122

6 Conclusions and future perspectives **139**
6.1 Discussion, limitations and future developments 141

A Relaxation and convergence acceleration **143**

B Model parameters **145**

C List of acronyms **159**

Bibliography **161**

Acknowledgements

This project has received funding from the European Research Council (ERC) under the European Union's Horizon 2020 research and innovation programme (grant agreement No 740132, iHEART - An Integrated Heart Model for the simulation of the cardiac function, P.I. Prof. A. Quarteroni).

I acknowledge the CINECA award under the ISCRA B and ISCRA C initiatives, for the availability of high performance computing resources and support (ISCRA grants IsB22_CoreMaS, P.I. Alfio Quarteroni, 2020-2022; IsC92_HeartEMF, P.I. Michele Bucelli, 2021; IsC96_EMFH, P.I. Michele Bucelli, 2022).

Chapter 1

Introduction

In the western countries, cardiac and cardiovascular diseases are responsible for the majority of deaths in the adult population [33, 330, 351]. The construction of personalized digital twins of the human heart and cardiovascular system [230, 235, 250, 262, 263, 299] can foster progress in this respect, by allowing unprecedented high-resolution analysis of the physics behind the heart function. This allows to gain insight into the mechanisms driving the heartbeat, both in physiological and pathological scenarios, ultimately assisting the decision-making procedures and allowing to develop precision medicine techniques for personalized treatment [46, 179, 239].

Developing a mathematical model and numerical simulation of the heart function is a challenging endeavor. Indeed, the heart is characterized by multiple processes of different nature (schematically represented in Figure 1.1), interacting at multiple spatial and temporal scales [262], ranging from sub-cellular processes to organ-scale mechanisms. Understanding, modeling and reproducing this complex panorama of multiphysics and multiscale interactions, ubiquitous in biological systems, is of fundamental importance towards the construction of a faithful mathematical representation of the heart [313, 344].

In recent years, several cardiac models have been proposed and developed. Most of them focus on some specific feature of the heartbeat, while representing the remaining ones through surrogate models, simplifying assumptions or experimental data: electrophysiology [13, 52, 258, 285, 333,

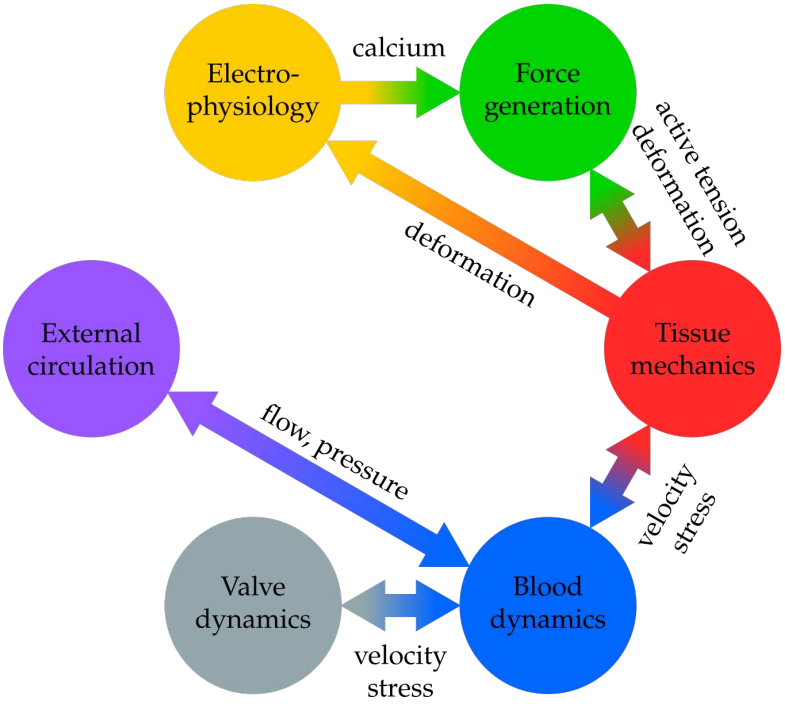

Figure 1.1: Schematic representation of the heart function. The circles represent the physical processes enabling the heart function, while arrows between them indicate their interactions.

341], electromechanics [17, 21, 108, 123, 145, 198, 255, 259, 310, 338], fluid dynamics of the blood [76, 178, 187, 249, 248, 282, 290, 302, 318, 322, 326, 336, 339, 363], fluid-structure interaction (FSI) [7, 47, 50, 66, 100, 111, 120, 152, 183, 234, 361]. All these standalone approaches provide meaningful insight into the heart physiology [133, 275, 364] and pathology [81, 89, 294].

However, full multiphysics coupling of the heart has the potential of shedding light on the complex interplay of several mechanisms that drives the heartbeat, highlighting how the macroscopic behavior of the organ emerges from the underlying microscopic processes. This comprehensive representation can allow to study pathologies and devices that affect many aspects of the cardiac function, such as the thrombogenesis associated to atrial fibrillation [77] or ventricular assist devices [22], and may support physically accurate in-silico clinical trials [347]. Due to the mathematical and computational complexity of such a holistic, bottom-up approach, few

models of this kind have been proposed in the literature [22, 297, 313, 347].

The objective of this thesis is to integrate in a single computational framework several state-of-the-art models of the cardiac function, providing a fully coupled representation of cardiac electrophysiology [74], muscular mechanics [272, 275] and hemodynamics [364], together with simplified models for cardiac valves [107] and the circulatory system [153, 275, 364]. Suitable numerical methods are put in place for the solution of the resulting coupled problem, investigating in detail different coupling schemes for the fluid and solid subproblems [50, 51]. Simulations under healthy conditions are performed and compared qualitatively and quantitatively with the heart physiology [53].

In the rest of this introductory chapter, I will describe cardiac anatomy and physiology (Section 1.1), review the existing approaches to cardiac modeling (Section 1.2) and describe the objectives, original contributions and the outline of this thesis (Section 1.3).

1.1 Cardiac anatomy and physiology

The human heart is a muscular organ with the purpose of pumping blood into the circulatory system, allowing the delivery of oxygen and nutrients to all the organs of the body [110, 168, 180, 184, 241, 303]. This is the result of the complex interplay of multiple physical processes, that act at multiple scales, ranging from sub-cellular to tissue- and organ-scale mechanisms. The following sections provide an overview of the different components of the heart function. The interested reader is referred to [168, 180, 184, 241, 303] for further details on the heart anatomy and physiology.

1.1.1 Anatomy of the heart

The heart is composed of four chambers, corresponding to muscular walls that surround cavities containing blood (Figure 1.2): the *left atrium* (LA), *left ventricle* (LV), *right atrium* (RA) and *right ventricle* (RV). The LA and LV form the *left heart* (LH), while the RA and RV form the *right heart* (RH).

Atria receive blood from the circulation and pump it towards the ventricles, which in turn pump it again into the circulatory system. Newly oxygenated

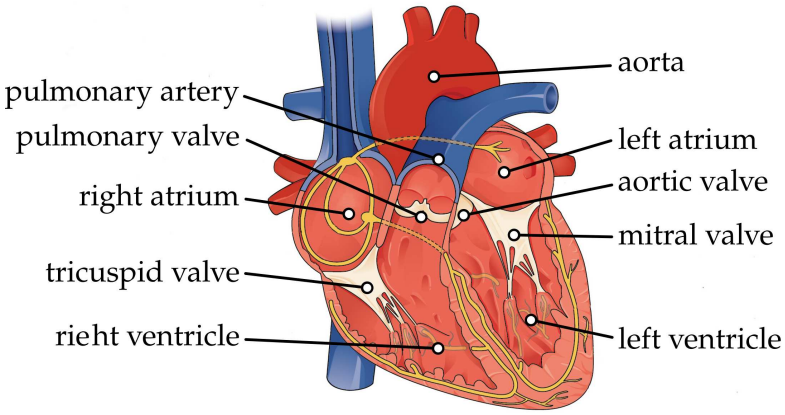

Figure 1.2: Schematic representation of the anatomy of the heart, highlighting chambers, valves and outflow tracts. Figure adapted from Wikimedia Commons (https://commons.wikimedia.org/wiki/File:2018_Conduction_System_of_Heart.jpg).

blood reaches the LA from the lungs through the pulmonary veins. From there, it is pumped into the LV, which contracts and pushes blood into the *ascending aorta* (AA) and towards the systemic circulation. In this way, oxygen is delivered to all organs of the body and consumed during metabolic processes. Eventually, de-oxygenated blood enters the RA, and is pumped into the RV, which ejects it into the *pulmonary trunk* (PT) and the pulmonary circulation. Blood reaches the lungs and is oxygenated, finally entering the LA once again.

Cardiac chambers are separated by valves that, in healthy conditions, make sure blood always flows in the right direction. LA and LV are separated by the *mitral valve* (MV), the LV is separated from the AA by the *aortic valve* (AV), the RA and the RV are separated by the *tricuspid valve* (TV), and the RV and the PA are separated by the *pulmonary valve* (PV). Mitral and tricuspid valves are supported by the fibrous *chordae tendinae*, attached to the *papillary muscles* that protrude from the cardiac walls. This prevents prolapse of the valve into the atrium, avoiding regurgitation.

Cardiac walls are organized in elongated fibers of muscular cells known

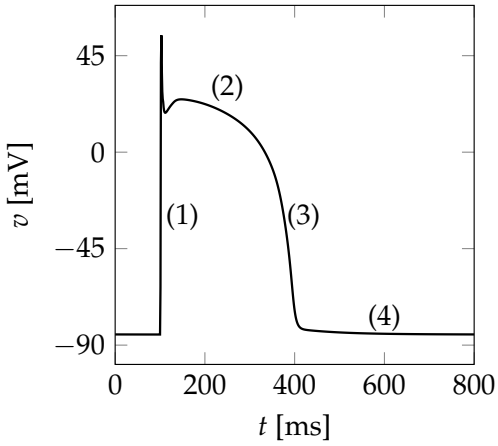

Figure 1.3: Evolution of transmembrane potential for a typical action potential: (1) depolarization; (2) plateau; (3) repolarization; (4) resting phase.

as *cardiomyocytes* [103, 132, 154, 180, 283]. Ventricular walls are thicker than atrial walls, and LV walls are approximately twice as thick as the RV ones. The bulk of the wall is referred to as *myocardium*, while the thin internal layer is known as *endocardium* and the outer layer is known as *epicardium*. The heart is contained within a fluid-filled cavity, known as *pericardium*, that provides mechanical support, lubrication and protection from infections [172, 298].

1.1.2 Cardiac electrophysiology

The heartbeat is driven by the contraction of cardiomyocytes, which in turn is initiated by bio-electric processes collectively known as *cardiac electrophysiology*.

The presence of several ionic species in the intra- and extracellular spaces determines a difference of potential across the cellular membrane, known as *transmembrane potential*, which is around $-90\,\mathrm{mV}$ at resting conditions [296]. In response to excitation, ionic channels across the cellular membrane open and close in a precise sequence, allowing the flow of ions and resulting in electrical ionic currents through the membrane. This leads first to a rapid depolarization, bringing the transmembrane potential to

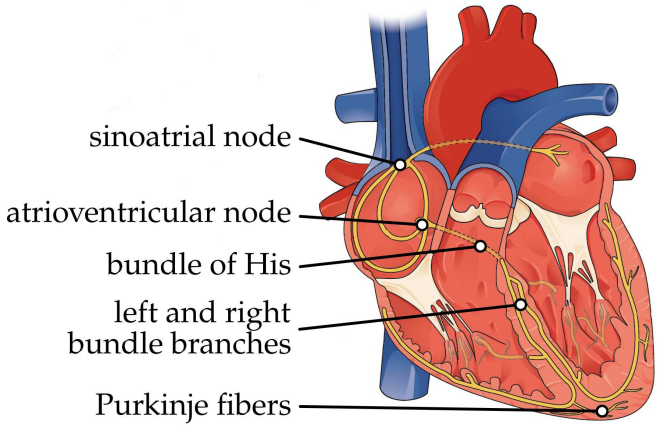

Figure 1.4: Schematic representation of the cardiac conduction system, with specialized conduction fibers represented in yellow. Figure adapted from Wikimedia Commons (https://commons.wikimedia.org/wiki/File:2018_Conduction_System_of_Heart.jpg).

about 50 mV, followed by a brief repolarization, a plateau, and a complete repolarization that brings back the potential to its resting value (see Figure 1.3). This sequence is referred to as *action potential*. The morphology of the action potential varies widely within the heart, depending on the location and on the type of cell considered.

The initial stimulus is spontaneously generated by a group of specialized cells forming the *sinoatrial node* (SAN), located on the RA. These cells serve as the natural pacemaker of the heart, and can trigger heartbeats at variable frequency in response to the autonomic nervous and endocrine systems [135]. In normal health and stress conditions, stimuli are generated at a rate of about 60 to 100 per minute.

From the SAN, the electric stimulus propagates to the whole heart through the *cardiac conduction system* (CCS), shown in Figure 1.4: the signal travels through the RA, and from the RA to the LA along specialized interatrial connections [292]. The atria become fully activated about 100 ms after the SAN stimulus [98], and are electrically insulated from the ventricles by

the fibrous tissue of the atrioventricular rings. When the electric signal reaches the *atrioventricular node* (AVN), located at the junction between the interatrial septum and the atrioventricular plane, it is delayed by about 90 ms, to ensure proper coordination between atria and ventricles. Then, the excitation is propagated to ventricles through the rapidly conducting fibers of the *bundle of His*, the *bundle branches* and finally the *Purkinje network* [180, 184].

The signal propagates to cardiomyocytes at the Purkinje-muscle junctions, and then between neighboring cardiomyocytes through *gap junctions*. Junctions are more frequent in the longitudinal direction of fibers, so that fibers determine a preferential direction for conduction [132, 283]. In practice, the propagation of the action potential is 3 to 4 times faster along fibers than in other directions [176]. Due to their interconnections, cardiac muscular cells are said to form a *functional syncytium*. The ventricles are completely activated within 100 ms from the onset of ventricular stimulation [98].

1.1.3 Generation of contractile force

Individual cardiomyocytes are composed of *myofibrils*, cylindrical structures formed of protein filaments organized in contractile units known as *sarcomeres*. Protein filaments are divided into two groups, the thin and thick filaments, composed of *actin* and *myosin* proteins respectively. Thin filaments include proteins known as *troponin* and *tropomyosin* that have the role of regulating the contraction process in response to calcium ions signals. Thick and thin filaments are able to slide along each other to produce the contraction of the sarcomere.

When a cardiomyocyte is excited, the intracellular concentration of calcium ions increases, triggering the release of calcium ions from the *sarcoplasmic reticulum*, a sub-cellular structure that stores calcium, into the intracellular space. This leads to a large increase in calcium concentration. Calcium ions bind to the troponin complexes of thin filaments, allowing the formation of *cross-bridges*, binds between myosin heads and actin that result in the shortening of the contractile unit [35, 62]. This interplay between electrical excitation and force generation is known as *excitation-contraction coupling*.

At the macroscopic scale, the coordinated shortening of multiple filaments within multiple sarcomeres results in the generation of a contractile force

in the muscular tissue, directed along the direction of fibers [103, 132].

The amount of contractile force generated by a sarcomere depends on its length [9, 306]. This force-length relationship forms the sub-cellular basis of the well known *Frank-Starling mechanism*, by which an increase in ventricular end-diastolic volume results in a stronger contraction and a larger stroke volume [169, 180, 184, 241]. Moreover, the contraction is characterized by the force-velocity relationship [35, 62, 151, 180]: as the shortening velocity increases, the amount of generated contractile force reduces, until a maximum velocity is reached for which the generated force is zero. Both effects are relevant in regulating the heart function in response to variations in the external conditions [169, 184].

1.1.4 The cardiac cycle

Figure 1.5 reports the typical evolution of volume and pressure for the LV collected in a *Wiggers diagram* [220] together with a typical electrocardiogram, while Figure 1.6 reports a left-ventricular *pressure-volume loop*, typically used in cardiology to represent and assess the cardiac function [180]. Several phases can be distinguished during the heartbeat cycle, based on the contraction of the chambers and the state of the valves [180, 184].

At the beginning of the heartbeat cycle, the MV and the TV are open, while the AV and the PV are closed. The activation of the atrial muscle leads to the *atrial systole*, during which the two atria contract pushing blood towards the ventricles. This is referred to as *atrial kick*, and contributes 20 % to 30 % of the blood volume for ventricular filling [219, 227], providing an additional preload to ventricles.

Subsequently, ventricular contraction begins. The blood pressure within ventricles increases, while atria relax, leading to the closing of MV and TV. Ventricles are at their *end-diastolic volume* (EDV). This marks the beginning of the *isovolumetric contraction* (IVC) phase: all valves are closed, and ventricular pressure rises quickly while ventricular volume is constant.

As soon as ventricular pressure overcomes the arterial one, aortic and pulmonary valves open, allowing the blood to be ejected from the ventricles into the circulation. The ejection is characterized by a flow acceleration phase and a deceleration phase, and the ventricles reach their *peak systolic*

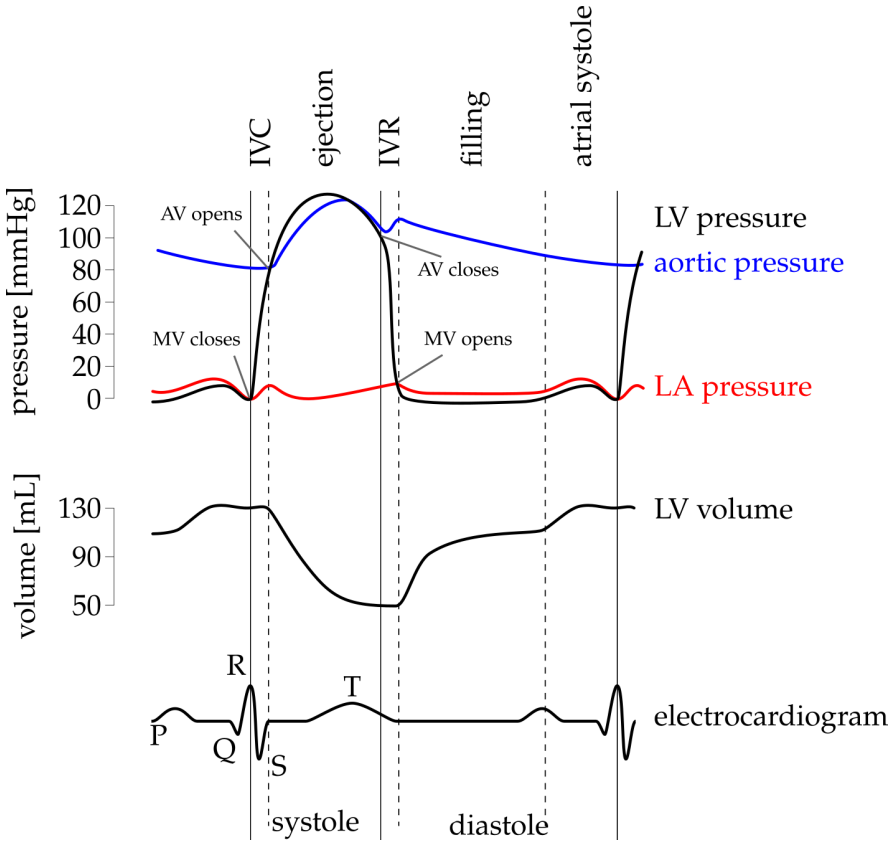

Figure 1.5: Wiggers diagram showing pressures for the LH and left ventricular volume. Heartbeat phases are indicated on the top. Figure adapted from Wikimedia Commons (https://commons.wikimedia.org/wiki/File:Wiggers_Diagram_2.svg).

pressure. During the ejection, blood flow can reach a peak Reynolds number of 5700 to 10 000 in ventricular outflow tracts [305], corresponding to a regime of transition to turbulence [40, 343, 363, 364]. The ejection and IVC phases form the *ventricular systole*. The ventricles begin relaxing at the end of the systolic phase. This leads to ventricular pressure becoming smaller than arterial pressure, causing flow deceleration and ultimately resulting in the closure of AV and PV. At the end of the systole, the ventricles reach their *end-systolic volume* (ESV). The difference between EDV and ESV is referred to as *stroke volume* (SV), and it quantifies the amount of blood ejected by the heart in a heartbeat (Figure 1.6). The ratio of SV and EDV is

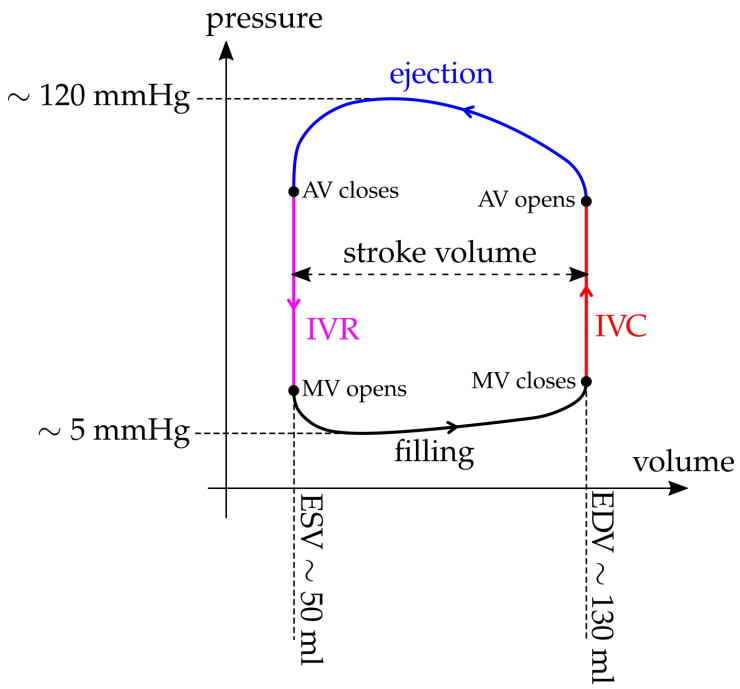

Figure 1.6: Typical pressure-volume loop for a LV.

known as *ejection fraction* (EF):

$$\mathrm{SV} = \mathrm{EDV} - \mathrm{ESV}\ , \qquad \mathrm{EF} = \frac{\mathrm{SV}}{\mathrm{EDV}}\ .$$

Both indicators are routinely used by cardiologists to quantify the cardiac function in terms of blood output.

Once ejection ends, with all valves closed, the *isovolumetric relaxation* (IVR) phase starts. The ventricular muscle relaxes, and the ventricular pressure drops while the ventricular volume remains constant. As soon as the ventricular pressure becomes smaller than the atrial one, MV and TV open.

This leads to the *passive diastolic filling* phase: blood flows from the atria into the ventricles due to the pressure gradient, in absence of any active contraction. This contributes 70 % to 80 % of the blood volume for ventricular filling [227]. The flow is characterized by a jet through the mitral and tricuspid valves, forming a vortex ring [95, 249]. IVR, passive filling and atrial systole form the *ventricular diastole*.

1.2 An overview of mathematical models of the heart

A large amount of mathematical models of the heart have been developed over the years [137, 230, 235, 250, 262, 299], with the aim of improving the understanding of the physics behind the heart function, as well as providing useful diagnostic and clinical personalization tools.

Several computational models focus on the representation of cardiac electrophysiology [52, 258, 285, 333, 341], neglecting mechanics and hemodynamics. Indeed, electrophysiology is the driver of several pathologies, such as atrial fibrillation [115, 148, 242], ventricular tachycardia [334] or bundle branch blocks [342]. Standalone models of this kind can help in understanding the pathophysiology of arrhythmia [129, 215, 315], allow for risk stratification [13] and assist in the clinical decison making [46, 61, 196, 286, 311]. Electrophysiology can be endowed with models for the propagation of the electric potential in the torso, resulting in the generation of synthetic electrocardiograms [119, 133, 254], which can be used in the estimation of electrical properties through data assimilation techniques [253]. Special effort has been put in developing fast solvers for cardiac electrophysiology, so as to allow for a rapid response to clinical questions, e.g. through matrix-free techniques [3] or by exploiting modern computational architectures [89].

Coupled electromechanical models are employed whenever muscular mechanics, both active and passive, is of interest. This requires the development of suitable models that bridge the electrical processes and the generation of contractile force [190, 272, 277]. Several electromechanical models have been proposed, focusing on the left ventricle [17, 87, 128, 177, 198, 255, 275] or the two ventricles [145, 259]. More recently, whole heart electromechanical models have been developed [21, 108, 123, 257, 309, 310], allowing to capture with high detail the interplay between the different chambers of the heart. These models have been used to investigate the heart function in both physiological and pathological conditions [294, 295].

Electromechanical models usually include hemodynamics in a reduced way through zero-dimensional lumped-parameter models [39, 153, 182, 266, 275]. This approach is capable of capturing the pressure of cardiac chambers [47], and can provide insight into the hemodynamic con-

sequences of cardiac function and dysfunction [294]. However, it neglects the effect of pressure gradients and shear stresses, as well as ignoring the three-dimensional characteristics of hemodynamics. Complementary to this, several works model the blood in a computational fluid dynamics (CFD) framework [71, 267, 320, 324]. The wall displacement is prescribed as a datum [67, 68, 236, 249, 302, 339], obtained from medical images [69, 117, 118, 136, 178, 195, 229], from independent electromechanical simulations [326, 364] or from idealized analytical laws [77, 88, 363]. CFD modeling can be used to provide accurate descriptions of blood dynamics in healthy conditions [67, 178, 339, 364] and in pathological scenarios [77, 117, 194, 211, 212, 327], allowing for risk stratification.

However, CFD models neglect the dynamic interaction between the blood and the cardiac wall. A more comprehensive approach is provided by FSI modeling, in which the solid mechanics and blood dynamics are solved in a bidirectionally coupled way [7, 50, 66, 234, 252, 300, 361]. In this respect, a large amount of studies focus on the FSI between the blood and the valves [48, 100, 111, 116, 120, 207, 218, 301, 323], due to its clinical significance [81, 161, 206, 218]. Other works include the interaction between the blood and cardiac muscular walls [7, 66, 84, 183, 234, 278, 355, 361]. FSI modeling can overcome some limitations of the standalone CFD approach, e.g. allowing to represent isovolumetric phases of the heartbeat [50, 326, 362], and generally provide more physically accurate results. However, this comes at the price of an increased computational complexity, requiring the use of suitable numerical methods [18, 63, 80, 149, 173].

Finally, in recent years, models featuring full coupling of electrophysiology, cardiac mechanics and hemodynamics have been developed [53]. The UT-Heart simulator is one of the first models in this direction [158, 313], featuring a comprehensive representation of the various components of the heart. The model has been applied to the simulation of pathological scenarios [179, 239]. In [345], cable and immersed boundary methods are proposed for the construction of a coupled model of electrophysiology, mechanics and fluid dynamics for the investigation of bundle branch block. Another fully coupled model was proposed in [297], focusing on ventricular systole, neglecting the presence of valves and providing a simplified description of the atria. The authors provide important details on the computational strategies that allow to exploit high-performance computing facilities for cardiac simulations. In [22], a biventricular model is pro-

posed, based on a phenomenological description of electrophysiology and force generation and considering an idealized geometry. The complexity of the model is leveraged to analyze the effect of different working regimes of a left ventricular assist device, highlighting both the hemodynamic and mechanical effects. In [348, 349] a coupled left heart model is presented, relying on the immersed boundary method in a finite volumes/finite differences combined framework for the numerical discretization. The model yields a good agreement with physiology, in terms of both mechanical and hemodynamic indicators. However, it relies on a simplified description of the contractile force generation [228] and of the circulation-heart coupling. Recently, a GPU-accelerated version of the same model has been developed for computational speedup [350], and extended to the whole heart [347], while at the same time presenting a proof-of-concept virtual clinical trial that highlights how integrated models of this type can have a significant impact on the clinical practice.

Comprehensive and fully coupled models, while still in their infancy, appear to be very promising towards the development of highly accurate digital twins of the human heart. In particular, they can be exploited to investigate to a great extent the effect of specific therapies and implanted devices [22, 179], allowing to understand and possibly predict their impact on all the aspects of the cardiac function. This comprehensive modeling approach may enable large scale clinical trials based on generating virtual patients [347], allowing the systematic investigation of pathological scenarios without limitations due to the availability of patients, limited sample size and experimental uncertainty. Thus, simulation-based studies can become a valuable tool to complement and support more traditional approaches based on statistical sampling.

1.3 Thesis objectives and main contributions

The main original contribution of this thesis is the development of a fully coupled *electro-mechanics-fluid dynamics* (EMF) model of the heart function [53], leveraging state-of-the-art mathematical models for the construction of a physiologically accurate heart simulator. The proposed model combines an accurate description of cardiac electrophysiology, a biophysically detailed model for contractile force generation, solid mechanics of the

heart walls and three-dimensional modeling of the blood hemodynamics. Moreover, it includes a closed-loop lumped-parameter representation of the circulatory system, as well as a simplified model to account for the presence of valves. The model accounts for the feedback between all of these subsystems, resulting in a fully coupled representation of the heart function.

While each of the previously mentioned processes has been already investigated on its own [108, 118, 272, 364], by means of standalone models, comprehensive and fully coupled models are rare in the cardiac modeling literature. In particular, three-dimensional FSI coupling is seldom included in heart models [234, 297, 347, 361], and constitutes a significant novelty of the proposed EMF model. On top of that, cardiac FSI is often treated with an immersed approach [138, 252, 345, 347], while the model introduced in this thesis relies on the *Arbitrary Lagrangian Eulerian* (ALE) method [96, 166] to deal with the geometric coupling of fluid and solid. This yields accurate results in terms of the conservation of blood volume throughout the heartbeat, allowing the accurate simulation of isovolumetric phases [50, 53] (whereas alternative approaches such as the immersed boundary method, while geometrically more flexible, may suffer from spurious permeability the fluid-solid interface [27, 162, 223, 347, 348]). To allow for the large deformations associated to the heart cycle, I introduce non-linear mesh movement operators [53] and an adaptive method for the solution of the associated differential problem. Moreover, previous models of this kind usually feature a simplified representation of the muscular force generation [348], whereas the proposed model includes a highly detailed description of muscular contraction, previously introduced in [272], that allows to capture significant regulatory mechanisms such as the force-strain and force-velocity relationships.

In terms of numerical methods, I introduce a segregated-staggered time advancing scheme for the solution of the coupled EMF problem [53]. The scheme is based on discretization methods tailored at each of the sub-problems, combining them in a modular framework that leverages the multiphysics and multiscale nature of the coupled problem. All numerical methods are designed for high-performance computing (HPC), allowing to exploit large-scale parallel computing architectures.

The FSI coupling of muscular mechanics and hemodynamics is the com-

putational bottleneck of the EMF model, and special care is needed in selecting a discretization method that is stable, accurate and efficient. To this end, I compare different approaches in the family of strongly coupled FSI methods [50]. Numerical experiments in an idealized ventricular setting show that a monolithic approach is the most efficient, in the regime typical of cardiac simulations, when enforcing strong coupling between fluid and solid.

Then, I compare the strongly coupled monolithic scheme to a loosely coupled (segregated) scheme based on Robin-Neumann interface conditions [51]. Through numerical experiments, the latter is shown to be stable in the cardiac setting, and is significantly more computationally efficient than the monolithic method. However, it introduces a numerically consistent splitting error that hinders the accuracy of the solution. For this reason, in this thesis I choose the strongly coupled monolithic method as the one offering the best compromise among efficiency, robustness and accuracy.

Having selected the appropriate numerical methods, I carry out the simulation of a realistic human left heart in physiological conditions [53]. The numerical results are compared against physiological behavior, in terms of macroscopic indicators and three-dimensional quantities, with the aim of assessing whether the computational model is capable of representing the heart function. In particular, I highlight how the model can effectively reproduce all phases of the cardiac cycle, including the isovolumetric ones. This is a distinctive feature of the proposed model, made possible by the inclusion of FSI coupling in the ALE framework.

Finally, I present a proof-of-concept EMF simulation of a four-chamber fully integrated heart model, indicating how the proposed computational framework can be exploited for comprehensive computer simulations of the heart.

The remainder of the thesis is structured as follows:

- Chapter 2 is devoted to the mathematical description of the EMF model, with a detailed description of each process (electrophysiology, force generation, cardiac mechanics, fluid dynamics, FSI and circulation), also called *core models*, together with their interactions;
- in Chapter 3 the numerical methods used for the solution of the EMF model are discussed; after introducing a segregated-staggered EMF

coupling scheme, the choice of the numerical method for the FSI problem is discussed in detail. Idealized FSI benchmarks are used to assess the effectiveness and efficiency of several methods in the cardiac context;

- Chapter 4 describes the EMF simulation of a realistic human left heart in healthy conditions. The simulation setup is presented, and the numerical results are compared with physiological data, showing how the proposed model is capable of reproducing the behavior of a healthy heart over the whole heart cycle;
- in Chapter 5, a proof-of-concept extension of the EMF model to the whole heart is presented;
- finally, Chapter 6 contains a discussion, conclusions and further developments of this thesis.

Chapter 2

Mathematical models of the heart function

In this chapter, I review the models used in the mathematical description of the cardiac function [137, 230, 235, 262, 263, 299, 333] and introduce the coupled EMF model. Such model was originally presented in [53], and it is schematically represented in Figure 2.1. The models for electrophysiology, force generation, muscular mechanics, hemodynamics and the circulatory system are presented separately. Each of them is referred to as a *core model*. I highlight the way the core models interact with and influence each other in the EMF model, capturing the feedback mechanisms that determine the heart function.

Let $t \in (0, T)$ be the independent variable representing time, and let $\Omega_t \subset \mathbb{R}^3$ be a domain representing the volume occupied by the heart and the blood it contains, at every time instant during the heartbeat. Ω_t is partitioned into the fluid subdomain $\Omega_{\mathrm{f},t}$ and the solid subdomain $\Omega_{\mathrm{s},t}$. The two subdomains share a common interface $\Sigma_t = \partial\Omega_{\mathrm{f},t} \cap \partial\Omega_{\mathrm{s},t}$. On $\partial\Omega_t$, $\mathbf{n}$ denotes the normal unit vector directed outward from Ω_t. On Σ_t, $\mathbf{n}$ denotes the normal unit vector directed outward from $\Omega_{\mathrm{f},t}$. Notice that the valves are not included in $\Omega_{\mathrm{s},t}$, but they are represented as moving surfaces immersed in $\Omega_{\mathrm{f},t}$ (see Section 2.5.3).

The set $\Omega_{\mathrm{s},t}^{\mathrm{active}} \subset \Omega_{\mathrm{s},t}$ denotes the portion of the solid domain that corresponds to muscular (atrial or ventricular) tissue, while $\Omega_{\mathrm{s},t}^{\mathrm{passive}} \subset \Omega_{\mathrm{s},t}$

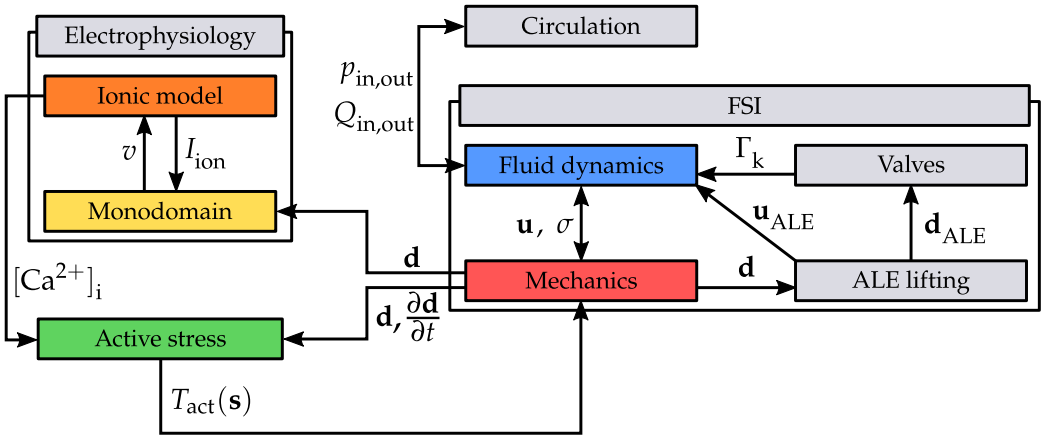

Figure 2.1: Schematic representation of the EMF model.

denotes the remaining part (arteries and atrioventricular rings). In the EMF model, the former is characterized by being electrically excitable and capable of generating contractile force, whereas the latter does not respond to electrical stimuli and is mechanically passive.

The domain Ω_t and its subdomains move in time as the heart beats. To keep the notation light, the subscript t is dropped from here on. Let us introduce a fixed *reference configuration* $\widehat{\Omega}$ (see Figure 2.2), and denote with a hat the counterpart in reference configuration of any of the sets defined above. The moving domain is referred to as *current configuration*. The motion of the current configuration is expressed by the following maps:

$$\mathcal{L}_{\text{f}} : \widehat{\Omega}_{\text{f}} \times (0, T) \to \Omega_{\text{f}} ,$$
$$\mathcal{L}_{\text{s}} : \widehat{\Omega}_{\text{s}} \times (0, T) \to \Omega_{\text{s}} .$$

The precise definition of the two maps depends on the models defined in Ω_{f} and Ω_{s}, and will be given later on.

The core models are expressed in terms of a system of partial and ordinary differential equations [261], whose unknowns are:

$$v : \widehat{\Omega}_{\text{s}}^{\text{active}} \times (0, T) \to \mathbb{R} \qquad \text{transmembrane potential,}$$
$$\mathbf{w} : \widehat{\Omega}_{\text{s}}^{\text{active}} \times (0, T) \to \mathbb{R}^{N_{\text{ion}}^{\mathbf{w}}} \qquad \text{ionic gating variables,}$$
$$\mathbf{z} : \widehat{\Omega}_{\text{s}}^{\text{active}} \times (0, T) \to \mathbb{R}^{N_{\text{ion}}^{\mathbf{z}}} \qquad \text{ionic concentrations,}$$

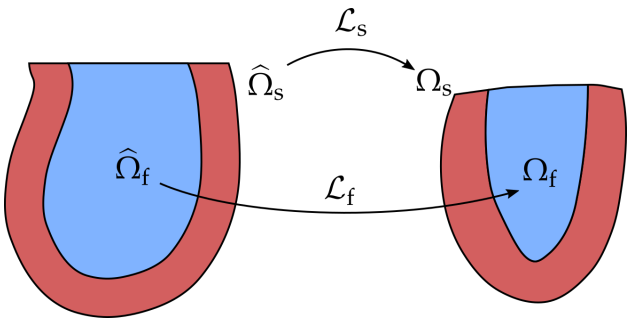

Figure 2.2: Schematic representation of the reference configuration $\widehat{\Omega}$ (left) and of the current configuration Ω (right).

$$
\begin{aligned}
\mathbf{s} &: \widehat{\Omega}_s^{\text{active}} \times (0,T) \to \mathbb{R}^{N_{\text{act}}} && \text{contraction state variables,}\\
\widehat{\mathbf{d}} &: \widehat{\Omega}_s \times (0,T) \to \mathbb{R}^3 && \text{solid displacement,}\\
\mathbf{d}_{\text{ALE}} &: \widehat{\Omega}_f \times (0,T) \to \mathbb{R}^3 && \text{fluid domain displacement,}\\
\mathbf{u} &: \Omega_f \times (0,T) \to \mathbb{R}^3 && \text{fluid velocity,}\\
p &: \Omega_f \times (0,T) \to \mathbb{R} && \text{fluid pressure,}\\
\mathbf{c} &: (0,T) \to \mathbb{R}^{N_{\text{circ}}} && \text{circulation state variables.}
\end{aligned}
$$

The solid displacement pushed forward to the current configuration is denoted by $\mathbf{d} : \Omega_s \times (0,T) \to \mathbb{R}^3$:

$$\mathbf{d}(\mathbf{x},t) = \widehat{\mathbf{d}}\left(\mathcal{L}_s^{-1}(\mathbf{x},t),t\right) .$$

Each core model is described in the following sections.

2.1 Modeling the cardiac fiber architecture

As anticipated in Section 1.1, cardiac fibers play a major role in both the electrical and mechanical properties of cardiac tissue. Therefore, a heart model must include a description of fiber architecture, in order to provide physiologicaly meaningful results.

Fibers can be measured both in vivo and ex vivo by means of *diffusion-tensor imaging* (DTI) acquisitions [12, 308, 160, 245]. Unfortunately, such acquisitions are time consuming and yield noisy data [6, 225], possibly with

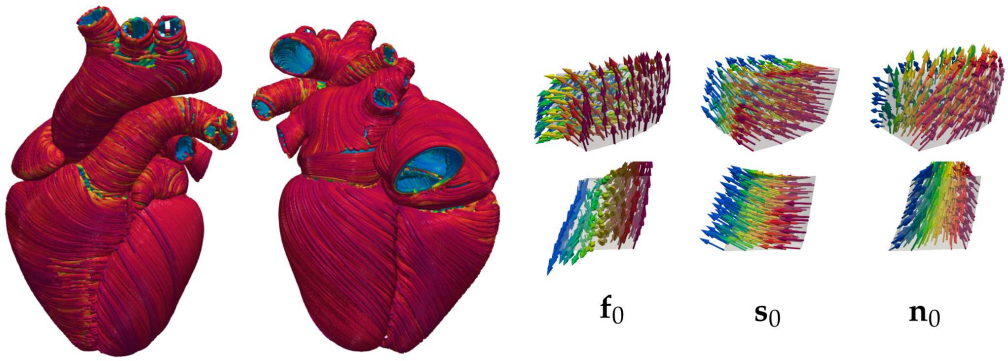

(a) (b)

Figure 2.3: (a) Streamline representation of the fiber field $\mathbf{f}_0$ on the whole heart, obtained through an LDRBM as in [108]. (b) Representation, on a ventricular slab, of the fiber reference system $\{\mathbf{f}_0, \mathbf{s}_0, \mathbf{n}_0\}$ with its transmural variation.

insufficient resolution to capture the structures of interest. An alternative approach to direct acquisition is the use of an atlas-based method [287], requiring the registration of a previously defined fiber architecture onto a new heart model.

A different strategy is based on using *Laplace-Dirichlet rule-based method*s (LDRBMs) [28, 97, 288, 258]: these methods solve a set of Laplace problems with suitable Dirichlet boundary conditions and post-process their solutions to define an orthonormal triplet $\{\mathbf{f}_0, \mathbf{s}_0, \mathbf{n}_0\}$ representing, at every point of $\widehat{\Omega}_s$, the direction of fibers, sheets of fibers and normal to sheets, respectively (Figure 2.3). LDRBMs are computationally cheap, yet allow to obtain a physiologically accurate description of the cardiac fiber architecture [258]. A detailed description of several existing LDRBMs for both atria and ventricles can be found in [257, 258].

2.2 Electrophysiology

As discussed in Section 1.1.2, cardiac electrophysiology is a multiscale process, in the sense that it features a macroscopic behavior emerging from cellular and sub-celluar processes. This is reflected into its mathematical

description through two coupled models [74]: the *monodomain model*, that represents the propagation of the action potential through the tissue, and one or more *ionic models*, that describe the ionic processes for an individual cell.

Both models are defined in $\widehat{\Omega}_s^{\text{active}}$, while no electrophysiology model is defined in $\widehat{\Omega}_s^{\text{passive}}$, corresponding to the arteries outgoing from the heart and to the atrioventricular rings.

2.2.1 The monodomain model

The state-of-the-art model for the description of cardiac electrophysiology is given by the *bidomain equations* [74, 314], which are derived through a homogeneization procedure, assuming that their domain of definition is the superimposition of two interpenetrating domains representing the intra- and extracellular spaces. While very accurate from the physical viewpoint, the bidomain model is expressed by a degenerate system of partial differential equations (PDEs), posing significant challenges from the mathematical and numerical viewpoints [45, 64, 75, 125].

An alternative model is provided by the monodomain equation, which is derived from the bidomain assuming that electrical conductivity tensors in the intra- and extracellular spaces are proportional [74, 314]. While simpler, the monodomain model has been found to yield results equivalent to the bidomain in physiological cases [73, 256], and to provide accurate results in many pathological settings [13, 46, 294, 295]. Since the focus of this thesis is on the simulation of the heart function in healthy conditions, electrophysiology is modeled using the monodomain equation, that reads:

$$\begin{cases} J\chi C_m \dfrac{\partial v}{\partial t} - \boldsymbol{\nabla} \cdot \left(J F^{-1} D_m F^{-T} \boldsymbol{\nabla} v \right) & \\ \qquad + J\chi I_{\text{ion}}(v, \mathbf{w}, \mathbf{z}) = J\chi I_{\text{app}}(\widehat{\mathbf{x}}, t) & \text{in } \widehat{\Omega}_s^{\text{active}} \times (0, T) \,, \\ J F^{-1} D_m F^{-T} \boldsymbol{\nabla} v \cdot \mathbf{n} = 0 & \text{on } \partial\widehat{\Omega}_s^{\text{active}} \times (0, T) \,, \\ v = v_0 & \text{in } \widehat{\Omega}_s^{\text{active}} \times \{0\} \,. \end{cases} \tag{2.1}$$

In the above equations, $F = I + \boldsymbol{\nabla}\widehat{\mathbf{d}}$ and $J = \det F$ account for the geometry-mediated *mechano-electric feedback*s (MEFs), that model the way

the deformation of the muscle affects the propagation of the electric signal [72, 203, 294, 295, 333]; χ is the cellular membrane surface-to-volume ratio, and C_m is the membrane capacitance. $I_{ion}(v, \mathbf{w}, \mathbf{z})$ is the ionic current, representing the net flow of charge through the cellular membrane due to the flow of ions (see Section 2.2.2), and D_m is the conductivity tensor, encoding the electrical properties of the tissue. It is defined as

$$D_m = \sigma_m^l \frac{F\mathbf{f}_0 \otimes F\mathbf{f}_0}{\|F\mathbf{f}_0\|^2} + \sigma_m^t \frac{F\mathbf{s}_0 \otimes F\mathbf{s}_0}{\|F\mathbf{s}_0\|^2} + \sigma_m^n \frac{F\mathbf{n}_0 \otimes F\mathbf{n}_0}{\|F\mathbf{n}_0\|^2}\,, \tag{2.2}$$

where σ_m^l, σ_m^t and σ_m^n are conductivities in the direction of fibers, fiber sheets and normal to fiber sheets, respectively.

The approach followed to model geometry-mediated MEFs is not the only possible one for what concerns both the monodomain equation (2.1) and the definition of the conductivity tensor (2.2). Multiple strategies are compared in [295], finding that the different approaches only yield mild differences in the numerical results. Moreover, (2.1) does not include other sources of mechano-electrical feedback such as nonselective stretch-activated currents or mechanically induced calcium release [329], which may become relevant in pathological conditions [295].

In (2.1), I_{app} is an external applied current that provides the initial stimulus. Indeed, the proposed model does not feature an explicit description of the CCS, which instead is surrogated by applying localized stimuli at specific points within the heart muscle, repeating them with period T_{hb} to obtain multiple heartbeats. This simplification is acceptable in physiological conditions, and allows to reconstruct effectively the activation pattern of the heart [258, 275]. Nonetheless, several computational models for the generation and inclusion of the CCS have been proposed [78, 89, 191, 285, 341], and they may become especially relevant if considering pathological conditions such as bundle branch blocks [347].

Problem (2.1) is endowed with zero-flux boundary conditions on $\partial\widehat{\Omega}_s^{active}$, representing the electrical insulation of the domain. This applies in particular to the interface of $\widehat{\Omega}_s^{active}$ and $\widehat{\Omega}_s^{passive}$. As a consequence, passive portions of the domain (such as atrioventricular rings) can electrically insulate disconnected regions of the active portion [108].

2.2.2 Ionic models

While the monodomain model deals with the propagation of the stimulus through the tissue, ionic models represent the bio-electrical activity of individual cells. They describe the evolution in time of ionic concentrations $\mathbf{z}$ in the intra- and extracellular spaces and of *gating variables* $\mathbf{w}$, namely fractions of ionic channels open through the cellular membrane.

Starting from the seminal work of Hodgkin and Huxley [155], several ionic models have been proposed [74, 314]. They can be broadly categorized into phenomenological models [8, 54, 284] and biophysically detailed models [26, 79, 205, 321, 238, 332]. The latter feature explicit representations of sub-cellular mechanisms, including in particular intracellular calcium dynamics, which is of fundamental importance when modeling the excitation-contraction coupling (see Section 1.1.3). Moreover, different ionic models are typically used for different parts of the heart, reflecting the spatial variability of the action potential.

Ionic models are typically expressed as a system of ordinary differential equations (ODEs) defined at every point in the computational domain, with the following general expression [74]:

$$\begin{cases} \dfrac{\partial \mathbf{w}}{\partial t} = \mathbf{F}_{\text{ion}}^{\mathbf{w}}(v, \mathbf{w}) & \text{in } \widehat{\Omega}_{\text{s}}^{\text{active}} \times (0, T) \ , \\ \dfrac{\partial \mathbf{z}}{\partial t} = \mathbf{F}_{\text{ion}}^{\mathbf{z}}(v, \mathbf{w}, \mathbf{z}) & \text{in } \widehat{\Omega}_{\text{s}}^{\text{active}} \times (0, T) \ , \\ \mathbf{w} = \mathbf{w}_0 & \text{in } \widehat{\Omega}_{\text{s}}^{\text{active}} \times \{0\} \ , \\ \mathbf{z} = \mathbf{z}_0 & \text{in } \widehat{\Omega}_{\text{s}}^{\text{active}} \times \{0\} \ , \end{cases} \tag{2.3}$$

where $\mathbf{F}_{\text{ion}}^{\mathbf{w}}$ and $\mathbf{F}_{\text{ion}}^{\mathbf{z}}$ depend on the choice of the ionic model. The vector $\mathbf{z}$ of ionic concentrations includes, in particular, the intracellular calcium concentration $[\text{Ca}^{2+}]_{\text{i}}$.

In the construction of the EMF heart model, the ionic model by Ten Tusscher and Panfilov (TTP06) [321] is used for ventricular tissue, while the one by Courtemanche, Ramirez and Nattel (CRN) [79] is used for atrial tissue (see Figure 2.4). The precise definitions of $\mathbf{F}_{\text{ion}}^{\mathbf{w}}$, $\mathbf{F}_{\text{ion}}^{\mathbf{z}}$ and I_{ion} associated to those models can be found in the original papers [79, 321].

For both the transmembrane potential and ionic variables, initial conditions are obtained by solving a zero-dimensional version of the monodomain

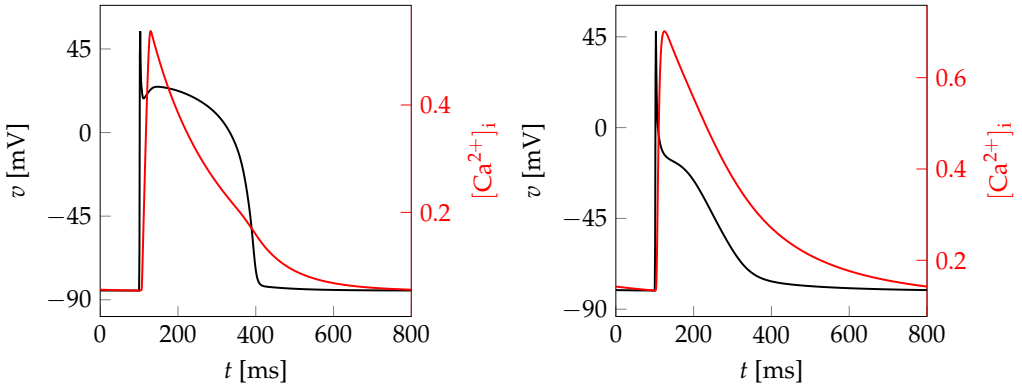

Figure 2.4: Action potential (black) and calcium transient (red) as predicted by (a) the TTP06 model and (b) the CRN model.

equation [74] coupled to (2.3), with a periodic applied current, until a limit cycle is reached [275, 332]. This facilitates the convergence to a limit cycle of period T_{hb} for the whole EMF model.

2.3 Force generation

The presence of calcium in the intracellular space leads to the generation of contractile force (Section 1.1.3). In the cardiac modeling literature, this process is represented in two different ways: phenomenological models, based on fitting experimental data with simple analytical curves [167, 190, 228], or biophysically detailed models [270, 272, 273, 277, 354]. The latter provide a description of the processes happening within the sarcomere, typically at the price of a high computational cost. Nonetheless, they allow to naturally incorporate feedback effects between the force generation and the muscular deformation.

In this thesis, two biophysically detailed models are considered, named RDQ18 [270] and RDQ20-MF [272]. Both of them can be expressed in terms of a system of ordinary differential equations (ODEs) for the evolution of

the state of contraction $\mathbf{s}$ at every point of $\widehat{\Omega}_s^{\text{active}}$:

$$\begin{cases} \dfrac{\partial \mathbf{s}}{\partial t} = \mathbf{F}_{\text{act}}\left(\mathbf{s},\, [\text{Ca}^{2+}]_i,\, \text{SL},\, \dfrac{\partial \text{SL}}{\partial t}\right) & \text{in } \widehat{\Omega}_s^{\text{active}} \times (0,T)\ , \\ \mathbf{s} = \mathbf{s}_0 & \text{in } \widehat{\Omega}_s^{\text{active}} \times \{0\}\ . \end{cases} \tag{2.4}$$

In the above, SL represents the sarcomere length, defined as the solution of the following regularization problem [275]:

$$\begin{cases} -\delta_{\text{SL}}^2 \Delta \text{SL} + \text{SL} = \text{SL}_0 \sqrt{I_{4\text{f}}} & \text{in } \widehat{\Omega}_s \times (0,T)\ , \\ \delta_{\text{SL}}^2 \boldsymbol{\nabla} \text{SL} \cdot \mathbf{n} = 0 & \text{on } \partial\widehat{\Omega}_s \times (0,T)\ , \end{cases}$$

where δ_{SL} is a regularization parameter, SL_0 is the sarcomere length at rest, and $I_{4\text{f}} = F\mathbf{f}_0 \cdot F\mathbf{f}_0$ measures the stretch along fibers. The time derivative of SL represents the shortening velocity along fibers.

Both the RDQ18 and the RDQ20-MF models include the force-length relationship, expressed by the dependence of $\mathbf{F}_{\text{act}}$ on SL. The sarcomere length affects both the calcium sensitivity and the active tension [272]. In practical terms, the generated contractile force is maximum for a given sarcomere length, and decreases if the sarcomere length is reduced. This microscopic effect is behind the Frank-Starling mechanism [169, 180], by which an increase in ventricular EDV leads to an increase in SV, due to the contractile force being greater if sarcomeres are stretched.

Moreover, the RDQ20-MF includes the force-velocity relationship (whereas the RDQ18 model does not), expressed by the dependence of $\mathbf{F}_{\text{act}}$ on $\dfrac{\partial \text{SL}}{\partial t}$. The generated contractile force decreases as the sarcomere velocity increases, and there exists a shortening velocity at which the generated force is zero. At the macroscopic level, this results in a spatial homogeneization of the fiber shortening velocity, avoiding sharp variations [108]. This effect was found to be extremely important to capture biomarkers such as the flow rate through semilunar valves, which would otherwise be unphysically high [108].

Due to the large amount of state variables of the RDQ18 model, which prevent it from being used directly in organ scale simulations, it is replaced by its reduced-order version presented in [273], that relies on artificial

neural networks to build a surrogate model with only two state variables [271]. Conversely, the RDQ20-MF model, despite being highly detailed, only features 20 unknowns thanks to dimensionality reduction techniques. Therefore, it does not have a significant impact in terms of computational costs.

Both models define a *permissivity* $P = P(\mathbf{s}) \in [0,1]$, representing the fraction of regulatory units that are in a permissive state, i.e. allow for the formation of a cross-bridge and for the generation of force. Permissivity can be seen as representing the microscopic active tension [272], and it is upscaled to a macroscopic active tension by a constant parameter a_{XB}, representing the maximum generated tension:

$$T_{\mathrm{act}}(\mathbf{s}) = a_{\mathrm{XB}}\, P(\mathbf{s}) \ .$$

The precise definitions of $\mathbf{F}_{\mathrm{act}}$ and P can be found in [270, 272].

Finally, the active tension is used to define an *active stress tensor*

$$P_{\mathrm{act}}(\mathbf{d},\mathbf{s}) = T_{\mathrm{act}}(\mathbf{s}) \left(n_{\mathrm{f}} \frac{F\mathbf{f}_0 \otimes \mathbf{f}_0}{\sqrt{I_{4\mathrm{f}}}} + n_{\mathrm{s}} \frac{F\mathbf{s}_0 \otimes \mathbf{s}_0}{\sqrt{I_{4\mathrm{s}}}} + n_{\mathrm{n}} \frac{F\mathbf{n}_0 \otimes \mathbf{n}_0}{\sqrt{I_{4\mathrm{n}}}} \right) \ . \tag{2.5}$$

In the above, $I_{4\mathrm{s}} = F\mathbf{s}_0 \cdot F\mathbf{s}_0$ and $I_{4\mathrm{n}} = F\mathbf{n}_0 \cdot F\mathbf{n}_0$. The coefficients n_{f}, n_{s} and n_{n} are used to calibrate the active tension in the direction of fibers, sheets and sheet normals respectively. This allows to surrogate the effect of fiber dispersion on the contraction [4, 103, 124, 139, 140, 257, 307]. In this thesis, the contraction acts only in the direction of fibers, so that $n_{\mathrm{f}} = 1$ and $n_{\mathrm{s}} = n_{\mathrm{n}} = 0$.

The initial condition for (2.4) is obtained by solving the system with a prescribed SL and $[\mathrm{Ca}^{2+}]_{\mathrm{i}}$ for a single point until a steady state is reached [275].

2.4 Cardiac mechanics

The mechanics of the cardiac walls is modeled by means of the elastodynamics equation in Lagrangian reference [237], relying on the hyperelastic framework to incorporate the passive properties of the material, and using an active stress approach to account for the active contraction [10, 134, 145, 246, 262, 275, 299].

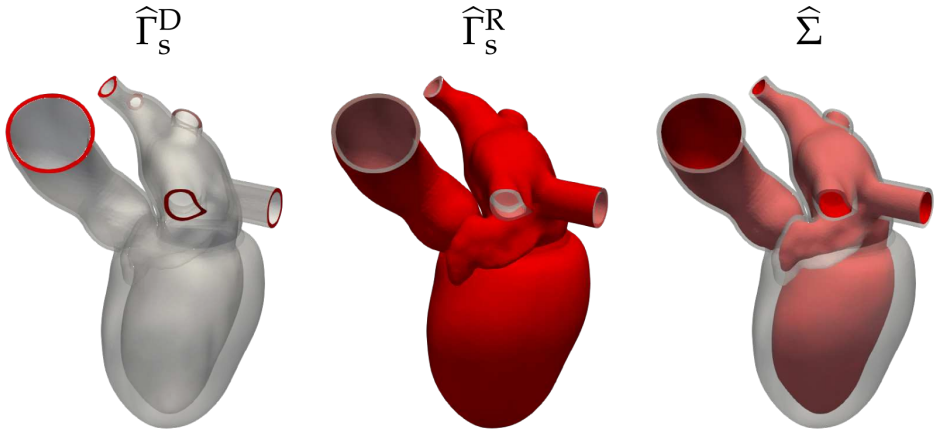

Figure 2.5: Dirichlet (left), Robin (middle) and fluid-solid interface (right) boundaries for the solid mechanics problem (2.6) for an LH model (see also Chapter 4).

The vector field $\widehat{\mathbf{d}}$ describes the displacement of the solid domain, so that the reference-to-current map is given by

$$\mathcal{L}_s(\widehat{\mathbf{x}}, t) = \widehat{\mathbf{x}} + \widehat{\mathbf{d}}(\widehat{\mathbf{x}}, t) \qquad \widehat{\mathbf{x}} \in \widehat{\Omega}_s \, , t \in (0, T) \, .$$

The evolution of the displacement is regulated by the following problem:

$$\begin{cases} \rho_s \dfrac{\partial^2 \widehat{\mathbf{d}}}{\partial t^2} - \boldsymbol{\nabla} \cdot P_s(\widehat{\mathbf{d}}, \mathbf{s}) = \mathbf{0} & \text{in } \widehat{\Omega}_s \times (0, T) \, , \\ \widehat{\mathbf{d}} = \mathbf{0} & \text{on } \widehat{\Gamma}_s^D \times (0, T) \, , \\ P_s(\widehat{\mathbf{d}}, \mathbf{s})\mathbf{n} = -(\mathbf{n} \otimes \mathbf{n}) \left(K_\perp^{epi} \widehat{\mathbf{d}} + C_\perp^{epi} \dfrac{\partial \widehat{\mathbf{d}}}{\partial t} \right) & \\ \qquad\qquad - (I - \mathbf{n} \otimes \mathbf{n}) \left(K_\parallel^{epi} \widehat{\mathbf{d}} + C_\parallel^{epi} \dfrac{\partial \widehat{\mathbf{d}}}{\partial t} \right) & \text{on } \widehat{\Gamma}_s^R \times (0, T) \, , \\ \widehat{\mathbf{d}} = \widehat{\mathbf{d}}_0 & \text{in } \widehat{\Omega}_s \times \{0\} \, , \\ \dfrac{\partial \widehat{\mathbf{d}}}{\partial t} = \mathbf{0} & \text{in } \widehat{\Omega}_s \times \{0\} \, . \end{cases} \tag{2.6}$$

$\widehat{\Gamma}_s^D$ and $\widehat{\Gamma}_s^R$ are subsets of $\partial\widehat{\Omega}_s \backslash \widehat{\Sigma}$ on which Dirichlet and Robin boundary conditions are applied, respectively (see Figure 2.5). The former are applied

on the inlet and outlet sections (corresponding to veins and arteries), while the latter are applied on the epicardial boundary to account for the presence of the pericardium [108, 255, 275, 310]. The coefficients $K_{\perp}^{\text{epi}}$ and $K_{\parallel}^{\text{epi}}$ are spring stiffness coefficients for the directions perpendicular and tangent to the boundary, respectively, while $C_{\perp}^{\text{epi}}$ and $C_{\parallel}^{\text{epi}}$ are viscosity coefficients. Although in the numerical experiments of this thesis the coefficients are assumed to be homogeneous, their values can in general depend on space, to account for anatomical features and organs surrounding the heart [108, 310]. No boundary conditions are defined on $\widehat{\Sigma}$, where instead FSI interface conditions are imposed (see Section 2.6).

In (2.6), ρ_s is the density of the muscle, and $P_s(\widehat{\mathbf{d}}, \mathbf{s})$ is the first Piola-Kirchhoff stress tensor. The latter is split into the sum of the active and passive contributions,

$$P_s(\widehat{\mathbf{d}}, \mathbf{s}) = P_{\text{pas}}(\widehat{\mathbf{d}}) + P_{\text{act}}(\widehat{\mathbf{d}}, \mathbf{s}) \, ,$$

with the active contribution P_{act} defined as in (2.5). The passive stress tensor P_{pas} is defined as the derivative of a strain energy function $\mathcal{W}$: $\text{Lin}^+ \to \mathbb{R} \cup \{+\infty\}$ (where Lin^+ is the set of linear transformation from $\mathbb{R}^3$ into itself, with positive determinant) that characterizes the mechanical properties of the material [157, 237]:

$$P_{\text{pas}}(\widehat{\mathbf{d}}) = \frac{\partial \mathcal{W}}{\partial F} \, .$$

Two different constitutive laws are considered in this thesis. For muscular tissue (atria and ventricles), the Guccione model is used [141, 337, 338]. The associated strain energy function is

$$\begin{aligned} \mathcal{W}_{\text{G}}(F) &= \frac{c}{2}\left(\exp(Q) - 1\right) + \frac{\kappa}{2}(J-1)\log(J) \, , \\ Q &= a_{\text{ff}}\left(E\mathbf{f}_0 \cdot \mathbf{f}_0\right) + a_{\text{ss}}\left(E\mathbf{s}_0 \cdot \mathbf{s}_0\right) + a_{\text{nn}}\left(E\mathbf{n}_0 \cdot \mathbf{n}_0\right) \\ &\quad + a_{\text{fs}}\left(E\mathbf{f}_0 \cdot \mathbf{s}_0\right) + a_{\text{fn}}\left(E\mathbf{f}_0 \cdot \mathbf{n}_0\right) + a_{\text{sn}}\left(E\mathbf{s}_0 \cdot \mathbf{n}_0\right) \, , \\ E &= \frac{1}{2}\left(F^T F - I\right) \, , \end{aligned} \tag{2.7}$$

with c, a_{ij} stiffness parameters, κ the bulk modulus, and $\mathbf{f}_0$, $\mathbf{s}_0$ and $\mathbf{n}_0$ the fiber orthonormal triplet defined as in Section 2.1. The constitutive law

accounts for the anisotropy induced by the arrangement of the myocardium in sheets of fibers by assuming the material to be orthotropic.

For arteries and atrioventricular rings, an isotropic neo-Hooke model is used [237], with strain energy function given by

$$\mathcal{W}_{\text{NH}}(F) = \frac{\mu}{2}\left(J^{-\frac{2}{3}}F : F - 3\right) + \frac{\kappa}{4}\left((J-1)^2 + \log^2(J)\right) , \qquad (2.8)$$

with μ a stiffness parameter and κ the bulk modulus.

Both constitutive laws treat the material as nearly incompressible by penalizing local variations in volume. An alternative approach is based on strictly enforcing incompressibility, leading to a saddle-point type problem [167, 234].

2.4.1 Regularization of material interfaces

The use of different constitutive laws results in sharp discontinuities across the interface between different materials. This does not constitute an issue from the point of view of the solid mechanics model, since the discontinuous constitutive law still satisfies the regularity requirements of the problem [23]. However, the discontinuity reflects in a reduced regularity of the displacement of the fluid-solid interface, which in practice entails the formation of corners on initially smooth surfaces. The fluid domain needs to deform to follow the interface displacement (see Section 2.5.1), and the reduced regularity of the boundary displacement leads to an irregular displacement of the interior of the fluid domain. This is problematic, since the fluid domain displacement must be regular enough to preserve the quality of mesh elements, avoiding their inversion.

To overcome this issue, I introduce the following novel interface regularization procedure as follows. Let $\widehat{\Omega}_0$ and $\widehat{\Omega}_1$ be two subsets of $\widehat{\Omega}_s$, with $\widehat{\Gamma}_{01} = \partial\widehat{\Omega}_0 \cap \partial\widehat{\Omega}_1 \neq \varnothing$ and $\widehat{\Omega}_{01} \subset \widehat{\Omega}_0$ such that it is adjacent to $\widehat{\Gamma}_{01}$ (Figure 2.6a). Let let P_0 and P_1 be the passive stress tensors in $\widehat{\Omega}_0$ and $\widehat{\Omega}_1$, respectively. As a preprocessing step, a Laplace problem is solved to obtain a function ψ that smoothly varies from 0 in $\widehat{\Omega}_0 \backslash \widehat{\Omega}_{01}$ to 1 in the interior of $\widehat{\Omega}_1$. Then, the following regularization coefficient is defined:

$$c_{\text{buf}}(\widehat{\mathbf{x}}) = \frac{1}{2}\left[1 - \cos\left(\frac{\pi \min\{\psi, \psi_{\text{th}}\}}{\psi_{\text{th}}}\right)\right] ,$$

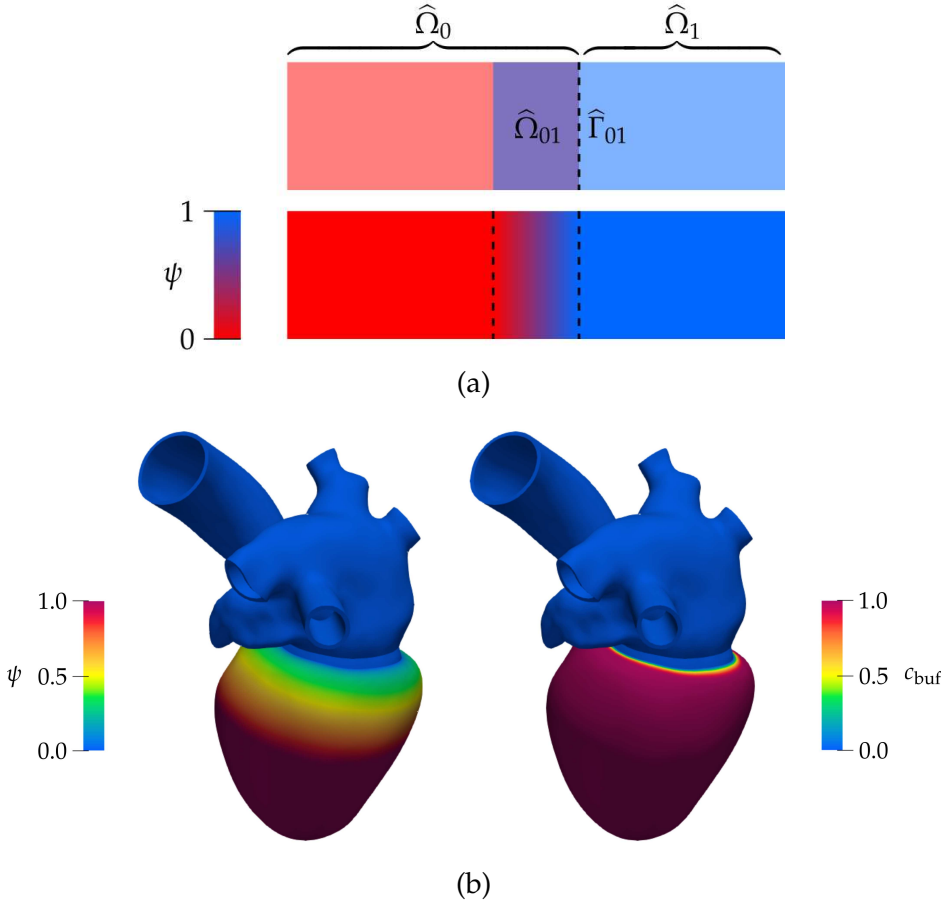

Figure 2.6: (a) Schematic representation of the material interface regularization domains $\widehat{\Omega}_0$, $\widehat{\Omega}_1$, $\widehat{\Gamma}_{01}$ and the associated regularization coefficient ψ. (b) Functions ψ (left) and c_{buf} used in the regularization of material interfaces in an LH model.

where $\psi_{\text{th}} \in (0,1)$ is a threshold value that controls the size of the regularization region. Both ψ and c_{buf} are shown in Figure 2.6. Finally, the stress tensor within $\widehat{\Omega}_{01}$ is redefined as a convex combination of P_0 and P_1, so that the transition between the two materials is smooth:

$$P_{\text{pas}}(\widehat{\mathbf{d}}) = c_{\text{buf}} P_1(\widehat{\mathbf{d}}) + (1 - c_{\text{buf}}) P_0(\widehat{\mathbf{d}}) \, .$$

2.4.2 Stress-free reference configuration recovery

Typically, models of the cardiac geometry are reconstructed starting from medical images such as MRI or CT, acquired in vivo. The images correspond to configurations in which the heart is subject to the load of the blood it contains, represented by a pressure $\widetilde{p}$. On the contrary, the domain $\widehat{\Omega}_s$ required by the formulation of (2.6) should represent a stress-free configuration.

Therefore, as a preprocessing step, the following inverse problem must be solved: given an input configuration $\widetilde{\Omega}_s$, subject to the known pressure load $\widetilde{p}$ on the endocardium, find the configuration $\widehat{\Omega}_s$ such that, when pressure $\widetilde{p}$ is applied on the endocardial surfaces, the input configuration $\widetilde{\Omega}_s$ is obtained. The inverse problem is solved by considering the quasi-static counterpart of (2.6), additionally imposing the condition

$$P_s(\widehat{\mathbf{d}}, \mathbf{s})\mathbf{n} = -\widetilde{p}JF^{-T}\mathbf{n} \qquad \text{on } \widehat{\Sigma}\,. \tag{2.9}$$

Let $\widehat{\mathbf{d}}_{eq}(\widehat{\mathbf{x}}, \widetilde{p})$ be the solution to the quasi-static mechanics problem, for the given pressure $\widetilde{p}$. Then, the inverse problem can be formalized as

$$\begin{aligned} \widetilde{\mathbf{x}} &= \widehat{\mathbf{x}} + \widehat{\mathbf{d}}_{eq}(\widehat{\mathbf{x}}, \widetilde{p})\,, \\ \widehat{\mathbf{x}} &= \widetilde{\mathbf{x}} - \widehat{\mathbf{d}}_{eq}(\widehat{\mathbf{x}}, \widetilde{p})\,, \end{aligned} \tag{2.10}$$

where $\widetilde{\mathbf{x}} \in \widetilde{\Omega}_s$ are the points in the input configuration and $\widehat{\mathbf{x}} \in \widehat{\Omega}_s$ those in the unknown reference configuration. Equation (2.10) is in the form of a fixed-point problem, whose unknown is the reference configuration, expressed in terms of its points $\widehat{\mathbf{x}}$. Therefore, the reference configuration is recovered through a fixed-point iteration algorithm, as presented in [275]. If multiple cardiac chambers are considered (such as in Chapters 4 and 5), the pressure $\widetilde{p}$ is spatially varying and has different values in each of the chambers [108].

2.4.3 Initial conditions

The initial condition corresponds to an instant during the heartbeat (typically at end-diastole) at which the heart wall is subject to the pressure p_0 of the blood within it. Therefore, to determine the initial displacement $\widehat{\mathbf{d}}_0$,

the stationary counterpart of (2.6) is solved, applying on the fluid-solid interface $\widehat{\Sigma}$ the pressure condition (2.9) [275]. To facilitate the solution of the stationary problem, which suffers from ill-conditioning, it is solved repeatedly, while gradually increasing the endocardial pressure from 0 to the desired value p_0. If multiple chambers are considered in the model, the pressure p_0 is spatially varying, with a different initial pressure for each of the chambers [108].

2.5 Fluid dynamics

Blood within the heart chambers can be regarded as incompressible and Newtonian. Indeed, while the presence of blood cells determines a complex rheology [5], its effects are mostly negligible for large vessels and heart chambers in healthy conditions [85], and the Newtonian assumption is typically made in models of heart hemodynamics [67, 178, 319, 364].

Navier-Stokes equations [261, 320] are used to model blood dynamics, accounting for the deformation of the chambers in the ALE framework [96, 166, 231], and incorporating valves by means of the *Resistive Immersed Implicit Surface* (RIIS) method [16, 107, 117, 118, 116]. The following sections provide details on each of these modeling approaches.

2.5.1 Fluid domain displacement

The displacement of the fluid domain is treated in the ALE framework [96, 166, 231]: the domain Ω_f moves in time with a velocity independent of that of the fluid, and fluid equations are formulated with respect to the moving frame of reference of the domain.

The deformation of the domain is described by the displacement field $\mathbf{d}_{\text{ALE}}$, through the reference-to-current map

$$\mathbf{x} = \mathcal{L}_f(\widehat{\mathbf{x}}, t) = \widehat{\mathbf{x}} + \mathbf{d}_{\text{ALE}}(\widehat{\mathbf{x}}, t) \ .$$

The displacement $\mathbf{d}_{\text{ALE}}$ is obtained by solving the following differential

problem (or *ALE lifting problem*):

$$\begin{cases} -\boldsymbol{\nabla} \cdot P_{\text{ALE}}(\mathbf{d}_{\text{ALE}}) = \mathbf{0} & \text{in } \widehat{\Omega}_{\text{f}} \times (0,T)\,, \qquad (2.11a) \\ \mathbf{d}_{\text{ALE}} = \widehat{\mathbf{d}} & \text{on } \widehat{\Sigma} \times (0,T)\,, \qquad (2.11b) \\ \mathbf{d}_{\text{ALE}} = \mathbf{0} & \text{on } \left(\partial\widehat{\Omega}_{\text{f}} \backslash \widehat{\Sigma}\right) \times (0,T)\,. \qquad (2.11c) \end{cases}$$

With this approach, the fluid domain is regarded as a fictitious solid in quasi-static regime, whose first Piola-Kirchhoff stress tensor is given by P_{ALE}. The velocity of the ALE reference frame is then computed as the time derivative of $\mathbf{d}_{\text{ALE}}$, pushed forward to the current configuration, namely:

$$\mathbf{u}_{\text{ALE}}(\mathbf{x},t) = \frac{\partial \mathbf{d}_{\text{ALE}}}{\partial t}\left(\mathcal{L}_{\text{f}}^{-1}(\mathbf{x},t),t\right)\,.$$

Different choices of P_{ALE} lead to different domain displacement strategies. In practice, the domain displacement should be such that, after spatial discretization, the quality of mesh elements is preserved and no inverted elements are generated [304], since they would lead to the breakdown of the numerical solver for Navier-Stokes equations.

This is a very challenging task: the simplest strategy is based on setting $P_{\text{ALE}}(\mathbf{d}_{\text{ALE}}) = \boldsymbol{\nabla}\mathbf{d}_{\text{ALE}}$, leading to the linear harmonic extension problem [304, 364]

$$\begin{cases} -\boldsymbol{\nabla} \cdot (\boldsymbol{\nabla}\mathbf{d}_{\text{ALE}}) = \mathbf{0} & \text{in } \widehat{\Omega}_{\text{f}} \times (0,T)\,, \\ \mathbf{d}_{\text{ALE}} = \widehat{\mathbf{d}} & \text{on } \widehat{\Sigma} \times (0,T)\,, \\ \mathbf{d}_{\text{ALE}} = \mathbf{0} & \text{on } \left(\partial\widehat{\Omega} \backslash \widehat{\Sigma}\right) \times (0,T)\,. \end{cases} \qquad (2.12)$$

A slightly more sophisticated approach uses quasi-static linear elasticity equations [304], setting

$$\begin{aligned} P_{\text{ALE}}(\mathbf{d}_{\text{ALE}}) = {} & \frac{E_{\text{ALE}}}{2(1+\nu_{\text{ALE}})}\left(\boldsymbol{\nabla}\mathbf{d}_{\text{ALE}} + \boldsymbol{\nabla}\mathbf{d}_{\text{ALE}}^T\right) \\ & + \frac{E_{\text{ALE}}\,\nu_{\text{ALE}}}{(1+\nu_{\text{ALE}})(1-2\nu_{\text{ALE}})}(\boldsymbol{\nabla}\cdot\mathbf{d}_{\text{ALE}})I\,, \end{aligned}$$

with E_{ALE} and ν_{ALE} the Young and Poisson moduli of the fictitious material. In my experience, both harmonic and linear elastic approaches are suitable

for geometrically idealized numerical experiments, but not reliable enough for realistic cardiac applications. Indeed, when realistic geometries are considered, the large deformations of cardiac chambers frequently lead to element inversion.

This can be improved by introducing local stiffening, i.e. by making the fictitious material stiffer in regions that are expected to undergo larger displacement or lead to element inversion. The stiffening can be based on the local mesh element volume, as done with the jacobian-based stiffening approach presented in [304], or on the distance from the moving boundary [171], where the largest deformation typically happens. However, even this approach often leads to element inversion for the realistic test cases discussed in this thesis.

More robust approaches can be obtained by assuming P_{ALE} to depend non-linearly on $\mathbf{d}_{\text{ALE}}$, effectively treating the fictitious material of the fluid domain as hyperelastic [7, 22]. The non-linearity induces slightly higher computational costs, with respect to previously described alternatives. However, this leads to significant improvements in the reliability of the mesh deformation method, by choosing a constitutive law for the fictitious material that penalizes highly distorted elements.

One possible non-linear strategy is based on choosing P_{ALE} according to the neo-Hooke constitutive law (2.8). Another option, introduced in [53] and inspired by [156, 300], comes from the following choice:

$$P_{\text{ALE}}(\mathbf{d}_{\text{ALE}}) = \frac{1}{q(\mathbf{d}_{\text{ALE}})}\left(I - \left(F_{\text{ALE}}F_{\text{ALE}}^T\right)^{-1}\right) , \tag{2.13}$$

$$F_{\text{ALE}} = I + \boldsymbol{\nabla}\mathbf{d}_{\text{ALE}} ,$$

where $q(\mathbf{d}_{\text{ALE}})$ is a scale-invariant mesh quality metric that has the purpose of stiffening the regions of the fluid domain with highly distorted elements, aiming at preventing solver breakdown. It is defined mesh-element-wise as

$$q(\widehat{\mathbf{x}}) = \frac{\|D_{\text{ALE}}\|_{\text{F}}^2}{3(\det D_{\text{ALE}})^{\frac{2}{3}}} ,$$

where $D_{\text{ALE}} = F_{\text{ALE}}\,\boldsymbol{\nabla}\mathcal{M}$ and $\mathcal{M}$ is the linear mapping from the unit simplex to the mesh element in current configuration, used in the finite element discretization.

For both the neo-Hooke law and (2.13), the resulting problem is non-linear, and as such requires special care in its numerical solution to ensure convergence and computational efficiency. I introduced an adaptive approach to this end, presented in detail in Section 3.3.4.

The most appropriate domain displacement strategy is largely dependent on the problem and on the mesh, and should be chosen according to the amount of deformation the domain undergoes, balancing the computational complexity and the robustness.

An alternative approach to the formulation (2.11) is provided by displacement interpolation methods, for example using radial basis functions [83], or mesh optimization techniques [185]. Moreover, all these approaches can be complemented by automatic remeshing methods, i.e. generating a new mesh whenever the existing one becomes too deformed [204]. The latter strategy, however, typically involves altering the mesh connectivity and projecting solutions between different meshes, and can become computationally expensive as well as complex to implement, whereas the formulation (2.11) provides a simpler framework for domain displacement.

2.5.2 Navier-Stokes equations

As is typical in the hemodynamics modeling literature [67, 80, 327, 364], the evolution of blood velocity $\mathbf{u}$ and pressure p is governed by the Navier-Stokes equations [261, 320] in ALE formulation:

$$\begin{cases} \rho_f \left[\dfrac{\partial \mathbf{u}}{\partial t} + \left((\mathbf{u} - \mathbf{u}_{\text{ALE}}) \cdot \boldsymbol{\nabla} \right) \mathbf{u} \right] & \\ \quad - \boldsymbol{\nabla} \cdot \sigma_f(\mathbf{u}, p) + \boldsymbol{\mathcal{R}}(\mathbf{u}, \mathbf{u}_{\text{ALE}}) = \mathbf{0} & \text{in } \Omega_f \times (0, T), \qquad (2.14a) \\ \boldsymbol{\nabla} \cdot \mathbf{u} = 0 & \text{in } \Omega_f \times (0, T), \qquad (2.14b) \\ \mathbf{u} = \mathbf{0} & \text{in } \Omega_f \times \{0\}. \qquad (2.14c) \end{cases}$$

In the above, ρ_f denotes the density of the blood, and $\sigma_f(\mathbf{u}, p)$ is the Cauchy stress tensor of a Newtonian fluid, defined as

$$\sigma_f(\mathbf{u}, p) = \mu_f \left(\boldsymbol{\nabla} \mathbf{u} + \boldsymbol{\nabla} \mathbf{u}^T \right) - pI \, ,$$

with μ_f denoting the dynamic viscosity. $\boldsymbol{\mathcal{R}}(\mathbf{u}, \mathbf{u}_{\text{ALE}})$ is a resistive term associated to the RIIS method (see Section 2.5.3).

System (2.14) is endowed with the FSI interface conditions on the fluid-solid interface Σ (see Section 2.6) and with coupling conditions with the circulatory system at inlet and outlet sections (see Section 2.7). Where Neumann conditions are imposed, instabilities due to backflow are prevented by means of the inertial backflow stabilization as described in [36, 221]: Neumann conditions in the form

$$\sigma_f(\mathbf{u}, p)\mathbf{n} = -p_N\mathbf{n} \qquad \text{on } \Gamma_f^N$$

are replaced by

$$\sigma_f(\mathbf{u}, p)\mathbf{n} = -p_N\mathbf{n} + \beta\frac{\rho_f}{2}|\mathbf{u}\cdot\mathbf{n}|_-\mathbf{u} \qquad \text{on } \Gamma_f^N\,,$$

where $|\mathbf{u}\cdot\mathbf{n}|_- = \min\{\mathbf{u}\cdot\mathbf{n}, 0\}$ and $\beta = 1$.

2.5.3 Resistive Immersed Implicit Surface modeling of cardiac valves

FSI modeling of cardiac valves is a very active area of research [100, 111, 120, 152, 187, 207, 301, 323], due to the important clinical implications of valve function [7, 81, 218], especially with reference to prosthetic valves [161, 197, 206, 359]. However, FSI simulations involving valves pose significant modeling and computational challenges: valves undergo large displacements, their opening and closing determines topological changes in the volume occupied by the blood, and contact plays a major role in their physiological function [7, 300, 322]. Moreover, the dynamics of atrioventricular valves is affected by the presence of chordae tendineae and papillary muscles [59, 217, 331], adding to the overall complexity of the problem.

On the other hand, the focus of the EMF model lies mainly in capturing the macroscopic effect that the valves have on the flow, rather than accurately describing their dynamic interaction with blood. In particular, the model should account for the role of valves in preventing reverse flow, as well as the way valve leaflets contribute to the formation of jets and vortices inside the heart chambers [95, 249]. Therefore, I choose a reduced approach in the modeling of valves, provided by the RIIS method [107, 117, 118, 364], in which valve FSI is neglected by prescribing valve kinematics.

The RIIS method is based on representing each valve through a surface Γ_k, with $k \in \mathcal{V} = \{MV, AV, TV, PV\}$, immersed in the fluid domain Ω_f. The RIIS term $\boldsymbol{\mathcal{R}}(\mathbf{u}, \mathbf{u}_{ALE})$ in (2.14a) penalizes the mismatch between the fluid velocity and the valve velocity, thus forcing the former to match the latter:

$$\boldsymbol{\mathcal{R}}(\mathbf{u}, \mathbf{u}_{ALE}) = \sum_{k \in \mathcal{V}} \frac{R_k}{\varepsilon_k} \delta_{\varepsilon_k}(\varphi_k^t(\mathbf{x}))(\mathbf{u} - \mathbf{u}_{ALE} - \mathbf{u}_{\Gamma_k}) \,. \tag{2.15}$$

In the above, R_k is a resistance coefficent that enforces the penalization; ε_k represents the valve half-thickness; φ_k^t is the signed distance function from the surface Γ_k, and δ_{ε_k} is a smoothed Dirac delta function that restricts the penalization to a layer of width $2\varepsilon_k$ near the surface:

$$\delta_{\varepsilon_k}(y) = \begin{cases} \dfrac{1}{2\varepsilon_k}\left(1 + \cos\left(\dfrac{\pi y}{\varepsilon_k}\right)\right) & \text{if } |y| \leq \varepsilon_k \,, \\ 0 & \text{if } |y| > \varepsilon_k \,. \end{cases}$$

Finally, $\mathbf{u}_{\Gamma_k} : \Omega_f \to \mathbb{R}^3$ is the valve velocity vector due to changes in its configuration (i.e. due to the opening and closing of the valve). Following [107], a quasi-static approximation is adopted, by setting $\mathbf{u}_{\Gamma_k} = \mathbf{0}$.

Implicitly representing the valve through the signed distance function φ_k avoids the need to have conforming discretizations between the valve and the fluid domain, which are instead required by ALE methods [7, 301], the Resistive Immersed Surface method [16, 326] or the planar modeling approach [82, 236]. This greatly facilitates the use of realistic geometries for valves.

Moreover, the RIIS method allows to easily move valves over time, to follow the displacement of the heart as well as to account for opening and closing. To do so, let $\Gamma_k^{closed} \subset \widehat{\Omega}_f$ denote a closed configuration for each valve $k \in \mathcal{V}$, and let $\mathbf{d}_k : \Gamma_k^{closed} \to \mathbb{R}^3$ be a displacement field that transforms the valve from the closed to the open configuration, obtained with a rule-based algorithm as a preprocessing step, as shown in [364] (see Figure 2.7 for an example). At any time $t \in (0, T)$, the current configuration of the surface is given by

$$\Gamma_k = \left\{ \mathbf{x} \in \Omega_f \,:\, \mathbf{x} = \widehat{\mathbf{x}} + \mathbf{d}_{ALE}(\widehat{\mathbf{x}}, t) + c_k(t)\mathbf{d}_k(\widehat{\mathbf{x}}),\ \widehat{\mathbf{x}} \in \Gamma_k^{closed} \right\} \,.$$

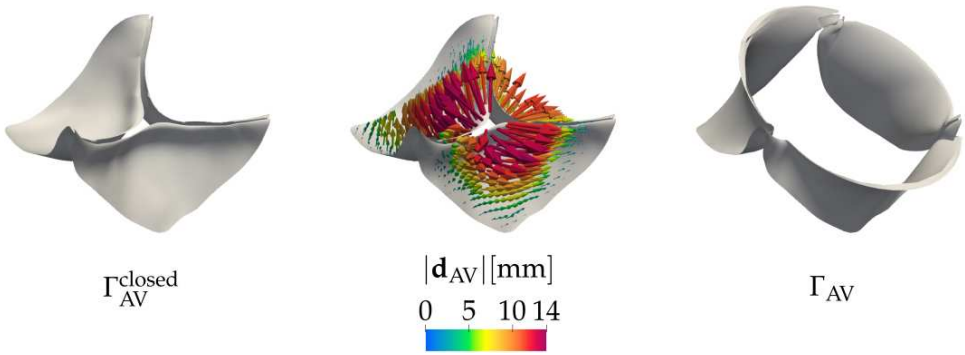

Figure 2.7: Immersed surface representing the aortic valve. From left to right: closed configuration Γ_{AV}^{closed}, opening displacement $\mathbf{d}_{AV}$, open configuratin Γ_{AV}.

The *opening coefficient* $c_k(t) \in [0,1]$ varies smoothly over time and is used to open and close the valve, effectively prescribing its kinematics. The time it takes for each valve to go from the open to the closed configuration and vice versa is prescribed. However, the times at which valves start opening and closing are chosen based on the difference between the pressure upstream and downstream of the valve, as in [53, 364]. Therefore, the duration of cardiac phases is determined by the solution of the model and not prescribed a priori.

2.6 Fluid-structure coupling conditions

On the interface Σ, fluid and solid are coupled through the following FSI interface conditions [31, 262]:

$$\begin{cases} \mathbf{u} = \dfrac{\partial \mathbf{d}}{\partial t} & \text{on } \Sigma \times (0,T)\,, \qquad (2.16a) \\ \sigma_f(\mathbf{u},p)\mathbf{n} = \sigma_s(\mathbf{d},\mathbf{s})\mathbf{n} & \text{on } \Sigma \times (0,T)\,, \qquad (2.16b) \end{cases}$$

where $\sigma_s(\mathbf{d},\mathbf{s})$ is the Cauchy stress tensor for the solid, related to the first Piola-Kirchhoff tensor by

$$\sigma_s(\mathbf{d},\mathbf{s}) = J^{-1} F P_s(\mathbf{d},\mathbf{s})^T\,.$$

Equation (2.16a) represents a no-slip condition on the fluid-solid interface, and is referred to as *kinematic coupling*, whereas (2.16b), known as *dynamic*

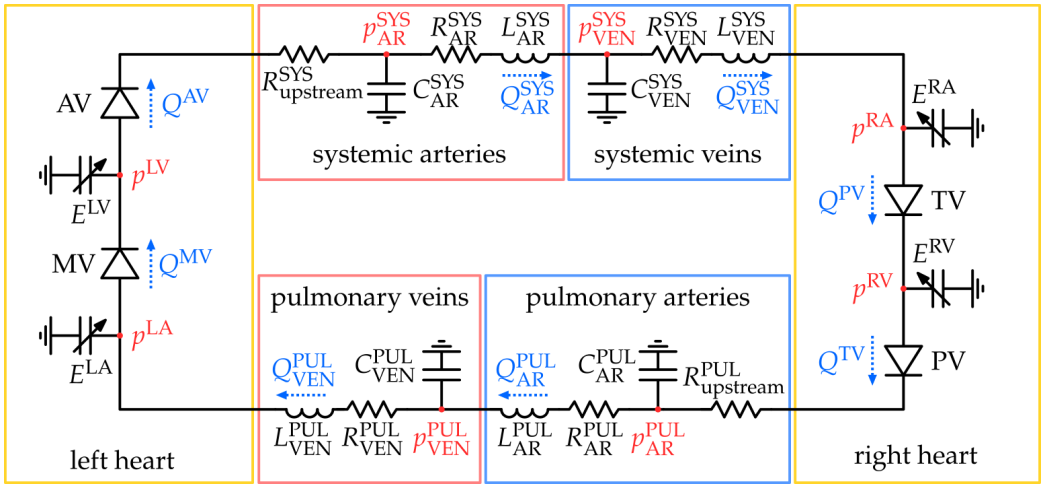

Figure 2.8: Representation through a circuital analogy of the 0D circulation model.

coupling, expresses Newton's third law. A third coupling condition, the *geometric coupling*, is given by (2.11b).

2.7 Modeling the circulatory system

The heart function is tightly related to the circulatory system. Indeed, the arterial pressure constitutes the afterload against which the heart pumps during systole, while venous return affects preload [180, 184]. This relation is also reflected in many pathological conditions such as hypertension.

Due to the geometrical complexity and the large variety in spatial scales of the vascular network, a three-dimensional simulation of both the heart and cardiovascular system is computationally unfeasible [266]. A valid alternative is the representation of the circulation through models of reduced dimensionality [60, 65]. This is often achieved through a surrogate lumped-parameter model, also referred to as 0D model to underline the lack of spatial resolution [39, 153, 259, 266, 275, 356, 364].

Models of this kind are obtained by averaging vascular fluid-structure interaction equations over their domain of definition, under suitable simplifying assumptions [251, 266]. The unknowns are spatially averaged

pressures and flow rates within compartments of the circulatory system. They can be conveniently represented through an analogy with electrical circuits (see Figure 2.8), with flow rate being the equivalent of electrical current and pressure that of voltage. In this analogy, viscous effects can be represented through resistance elements, vessel compliance is represented by capacitors and blood inertia by inductance elements [266].

In this thesis, I consider the closed loop model presented in [275], based on the ones of [39, 153] and previously applied to cardiac electromechanics simulations in [108, 259] and CFD simulations in [364]. The unknowns are average pressures and volumes of the cardiac chambers (p^{LA}, p^{LV}, p^{RA}, p^{RV}, V^{LA}, V^{LV}, V^{RA}, V^{RV}), flowrates through cardiac valves (Q^{MV}, Q^{AV}, Q^{TV}, Q^{PV}), and pressures and flowrates through the four circulation compartments: systemic arterial, ($p^{\mathrm{SYS}}_{\mathrm{AR}}$, $Q^{\mathrm{SYS}}_{\mathrm{AR}}$), systemic venous ($p^{\mathrm{SYS}}_{\mathrm{VEN}}$, $Q^{\mathrm{SYS}}_{\mathrm{VEN}}$), pulmonary arterial ($p^{\mathrm{PUL}}_{\mathrm{AR}}$, $Q^{\mathrm{PUL}}_{\mathrm{AR}}$) and pulmonary venous ($p^{\mathrm{PUL}}_{\mathrm{VEN}}$, $Q^{\mathrm{PUL}}_{\mathrm{VEN}}$).

The model represents the heart chambers through time-varying elastances:

$$
\begin{aligned}
p^{\mathrm{LA}}(t) &= p_{\mathrm{ex}}(t) + E^{\mathrm{LA}}(t)\left(V^{\mathrm{LA}}(t) - V_0^{\mathrm{LA}}\right) , \\
\frac{\mathrm{d}V^{\mathrm{LA}}}{\mathrm{d}t} &= Q^{\mathrm{PUL}}_{\mathrm{VEN}}(t) - Q^{\mathrm{MV}}(t) , \\
p^{\mathrm{LV}}(t) &= p_{\mathrm{ex}}(t) + E^{\mathrm{LV}}(t)\left(V^{\mathrm{LV}}(t) - V_0^{\mathrm{LV}}\right) , \\
\frac{\mathrm{d}V^{\mathrm{LV}}}{\mathrm{d}t} &= Q^{\mathrm{MV}}(t) - Q^{\mathrm{AV}}(t) , \\
p^{\mathrm{RA}}(t) &= p_{\mathrm{ex}}(t) + E^{\mathrm{RA}}(t)\left(V^{\mathrm{RA}}(t) - V_0^{\mathrm{RA}}\right) , \\
\frac{\mathrm{d}V^{\mathrm{RA}}}{\mathrm{d}t} &= Q^{\mathrm{SYS}}_{\mathrm{VEN}}(t) - Q^{\mathrm{TV}}(t) , \\
p^{\mathrm{RV}}(t) &= p_{\mathrm{ex}}(t) + E^{\mathrm{RV}}(t)\left(V^{\mathrm{RV}}(t) - V_0^{\mathrm{RV}}\right) , \\
\frac{\mathrm{d}V^{\mathrm{RV}}}{\mathrm{d}t} &= Q^{\mathrm{TV}}(t) - Q^{\mathrm{PV}}(t) ,
\end{aligned}
$$

where $p_{\mathrm{ex}}(t)$ is an external pressure that can be used to account for the effect of breathing (set to $p_{\mathrm{ex}}(t) = 0$ in this thesis). For each chamber $k \in \{\mathrm{LA}, \mathrm{LV}, \mathrm{RA}, \mathrm{RV}\}$, V_0^k is the resting volume, and $E^k(t)$ is a time-varying elastance function, analytically prescribed to represent contraction and

relaxation [275]. Cardiac valves are modeled by means of non-ideal diodes:

$$
\begin{aligned}
Q^{\mathrm{MV}}(t) &= \frac{p^{\mathrm{LA}}(t) - p^{\mathrm{LV}}(t)}{R^{\mathrm{MV}}(p^{\mathrm{LA}}(t), p^{\mathrm{LV}}(t))}\,, \\
Q^{\mathrm{AV}}(t) &= \frac{p^{\mathrm{LV}}(t) - p^{\mathrm{SYS}}_{\mathrm{AR}}(t)}{R^{\mathrm{AV}}(p^{\mathrm{LV}}(t), p^{\mathrm{SYS}}_{\mathrm{AR}}(t)) + R^{\mathrm{SYS}}_{\mathrm{upstream}}}\,, \\
Q^{\mathrm{TV}}(t) &= \frac{p^{\mathrm{RA}}(t) - p^{\mathrm{RV}}(t)}{R^{\mathrm{TV}}(p^{\mathrm{RA}}(t), p^{\mathrm{RV}}(t))}\,, \\
Q^{\mathrm{PV}}(t) &= \frac{p^{\mathrm{RV}}(t) - p^{\mathrm{PUL}}_{\mathrm{AR}}(t)}{R^{\mathrm{PV}}(p^{\mathrm{RV}}(t), p^{\mathrm{PUL}}_{\mathrm{AR}}(t)) + R^{\mathrm{PUL}}_{\mathrm{upstream}}}\,.
\end{aligned}
$$

Valvular resistances R^{MV}, R^{AV}, R^{TV} and R^{PV} are used to model the opening and closing of valves based on the difference between upstream and downstream pressures:

$$
R^{\mathrm{k}}(p^{\mathrm{up}}, p^{\mathrm{down}}) = \begin{cases} R^{\mathrm{k}}_{\mathrm{max}} & \text{if } p_{\mathrm{up}} < p_{\mathrm{down}}\,, \\ R^{\mathrm{k}}_{\mathrm{min}} & \text{if } p_{\mathrm{up}} \geq p_{\mathrm{down}}\,, \end{cases} \qquad \mathrm{k} \in \{\mathrm{MV}, \mathrm{AV}, \mathrm{TV}, \mathrm{PV}\}\,.
$$

With respect to previous applications of the model [275, 364], I added the two *upstream resistances* $R^{\mathrm{SYS}}_{\mathrm{upstream}}$ and $R^{\mathrm{PUL}}_{\mathrm{upstream}}$. When coupling with the Navier-Stokes equations (see Section 2.7.1), the two have the role of absorbing outgoing pressure waves, preventing spurious oscillations resulting from unphysical reflections [170].

Circulation compartments are modeled as RLC circuits: for $t \in (0, T)$,

$$
\begin{aligned}
C^{\mathrm{SYS}}_{\mathrm{AR}} \frac{\mathrm{d}p^{\mathrm{SYS}}_{\mathrm{AR}}(t)}{\mathrm{d}t} &= Q_{\mathrm{AV}}(t) - Q^{\mathrm{SYS}}_{\mathrm{AR}}(t)\,, \\
\frac{L^{\mathrm{SYS}}_{\mathrm{AR}}}{R^{\mathrm{SYS}}_{\mathrm{AR}}} \frac{\mathrm{d}Q^{\mathrm{SYS}}_{\mathrm{AR}}(t)}{\mathrm{d}t} &= -Q^{\mathrm{SYS}}_{\mathrm{AR}}(t) - \frac{p^{\mathrm{SYS}}_{\mathrm{VEN}}(t) - p^{\mathrm{SYS}}_{\mathrm{AR}}(t)}{R^{\mathrm{SYS}}_{\mathrm{AR}}}\,, \\
C^{\mathrm{SYS}}_{\mathrm{VEN}} \frac{\mathrm{d}p^{\mathrm{SYS}}_{\mathrm{VEN}}(t)}{\mathrm{d}t} &= Q^{\mathrm{SYS}}_{\mathrm{AR}}(t) - Q^{\mathrm{SYS}}_{\mathrm{VEN}}(t)\,, \\
\frac{L^{\mathrm{SYS}}_{\mathrm{VEN}}}{R^{\mathrm{SYS}}_{\mathrm{VEN}}} \frac{\mathrm{d}Q^{\mathrm{SYS}}_{\mathrm{VEN}}(t)}{\mathrm{d}t} &= -Q^{\mathrm{SYS}}_{\mathrm{VEN}}(t) - \frac{p_{\mathrm{RA}}(t) - p^{\mathrm{SYS}}_{\mathrm{VEN}}(t)}{R^{\mathrm{SYS}}_{\mathrm{AR}}}\,, \\
C^{\mathrm{PUL}}_{\mathrm{AR}} \frac{\mathrm{d}p^{\mathrm{PUL}}_{\mathrm{AR}}(t)}{\mathrm{d}t} &= Q_{\mathrm{PV}}(t) - Q^{\mathrm{PUL}}_{\mathrm{AR}}(t)\,,
\end{aligned}
$$

$$\frac{L_{\text{AR}}^{\text{PUL}}}{R_{\text{AR}}^{\text{PUL}}}\frac{\mathrm{d}Q_{\text{AR}}^{\text{PUL}}(t)}{\mathrm{d}t} = -Q_{\text{AR}}^{\text{PUL}}(t) - \frac{p_{\text{VEN}}^{\text{PUL}}(t) - p_{\text{AR}}^{\text{PUL}}(t)}{R_{\text{AR}}^{\text{PUL}}}\,,$$
$$C_{\text{VEN}}^{\text{PUL}}\frac{\mathrm{d}p_{\text{VEN}}^{\text{PUL}}(t)}{\mathrm{d}t} = Q_{\text{AR}}^{\text{PUL}}(t) - Q_{\text{VEN}}^{\text{PUL}}(t)\,,$$
$$\frac{L_{\text{VEN}}^{\text{PUL}}}{R_{\text{VEN}}^{\text{PUL}}}\frac{\mathrm{d}Q_{\text{VEN}}^{\text{PUL}}(t)}{\mathrm{d}t} = -Q_{\text{VEN}}^{\text{PUL}}(t) - \frac{p^{\text{LA}}(t) - p_{\text{VEN}}^{\text{PUL}}(t)}{R_{\text{VEN}}^{\text{PUL}}}\,.$$

Resistance, capacitance and inductance coefficients in the above equations surrogate the properties of the corresponding vascular network compartment [266]. The circulation problem is endowed with suitable initial conditions for its variables.

Collecting all circulation variables into the vector $\mathbf{c}(t) \in \mathbb{R}^{N_{\text{circ}}}$, the circulation model can be recast in compact form as an algebraic-differential equation:

$$\mathbf{F}_{\text{circ}}\left(\mathbf{c}, \frac{\mathrm{d}\mathbf{c}}{\mathrm{d}t}, t\right) = \mathbf{0} \qquad t \in (0, T)\,. \tag{2.17}$$

2.7.1 3D-OD coupling between circulation and heart hemodynamics

The circulation model described above provides a dimensionally reduced representation of the whole cardiovascular system. However, the EMF model aims at describing with high fidelity the cardiac function, with a 3D representation of cardiac chambers and a 0D representation of the circulatory system [38, 266, 364]. The 3D model of the heart and the 0D model of the circulation are therefore coupled in a *geometric multiscale* framework (see e.g. Figure 4.3). This has the twofold purpose of providing physiologically meaningful boundary conditions to Navier-Stokes equations (2.14) and of modeling the interaction between the heart and the systemic and pulmonary circulation.

In order to do that, the 0D compartments that have a 3D counterpart are removed from the circulation model [108, 275, 364], and replaced by interface conditions enforcing the continuity of flow rates and stresses (represented by pressure in the 0D model). The two conditions express mass and momentum conservation, respectively, at the 3D-0D interface.

More formally, let Γ_j^{inlet}, for $j \in \left\{1, 2, \ldots, N^{\text{inlet}}\right\}$ be the inlet sections of Ω_{f}, and Γ_j^{outlet}, for $j \in \left\{1, 2, \ldots, N^{\text{outlet}}\right\}$ the outlet sections. Let p_j^{inlet}, p_j^{outlet}, Q_j^{inlet} and Q_j^{outlet} be pressures and flow rates of the 0D model, corresponding to its terminal sections at inlets and outlets of Ω_{f}. Then, the 3D-0D coupling conditions are the following:

$$\begin{aligned} \sigma_{\text{f}}(\mathbf{u}, p)\mathbf{n} &= -p_j^{\text{inlet}}\mathbf{n} \qquad \text{on } \Gamma_j^{\text{inlet}} \\ Q_j^{\text{inlet}} &= -\int_{\Gamma_j^{\text{inlet}}} (\mathbf{u} - \mathbf{u}_{\text{ALE}}) \cdot \mathbf{n} d\gamma \qquad \text{for } j \in \left\{1, 2, \ldots, N^{\text{inlet}}\right\} \end{aligned}$$

$$\begin{aligned} \sigma_{\text{f}}(\mathbf{u}, p)\mathbf{n} &= -p_j^{\text{outlet}}\mathbf{n} \qquad \text{on } \Gamma_j^{\text{outlet}} \\ Q_j^{\text{outlet}} &= \int_{\Gamma_j^{\text{outlet}}} (\mathbf{u} - \mathbf{u}_{\text{ALE}}) \cdot \mathbf{n} d\gamma \qquad \text{for } j \in \left\{1, 2, \ldots, N^{\text{outlet}}\right\} \end{aligned}$$

Chapter 3

Numerical methods for cardiac electro-mechanics-fluid dynamics interaction

The numerical solution of the coupled problem introduced in Chapter 2 poses several challenges, due on the one hand to the inherent complexity of each of the core models, and on the other hand to their coupled multi-physics nature. Computational efficiency is crucial, due to the large scale of the problem, and the numerical solvers must be tailored towards HPC architectures.

In this chapter, I discuss the numerical discretization strategies employed in the solution of the EMF problem. To this end, I leverage previously developed numerical methods for the individual core models [275, 364], combining them in a novel coupled computational framework. The discretization methods discussed here have been published in [53].

A crucial part of the numerical discretization scheme is the method used for the solution of the FSI subproblem. I consider several different strategies, in both the strongly and loosely coupled families, and provide a numerical comparison to identify the scheme most suited to cardiac simulations. These latter results have been published in [50, 51].

3.1 A segregated-staggered scheme for EMF interaction

One possible approach towards the numerical solution of the EMF problem is a fully monolithic discretization [127], in which all the subproblems are discretized by means of standard techniques [165, 261] into a single algebraic non-linear system. This strategy leads to a very large problem, to be solved e.g. with Newton's method. In practice, it also requires the development of ad-hoc preconditioners, since the problems being coupled have significantly different spectral properties and conditioning, and the convergence of the numerical solvers employed (both non-linear and linear) can be a major issue. Moreover, it may lack in flexibility in the choice of discretization parameters for the different core models.

For these reasons, the fully monolithic approach for the EMF model is seldom used in the cardiac modeling literature, with [127] being the only exception, to the best of my knowledge. Instead, segregated or partitioned methods are typically preferred [297, 348]. These are based on solving independently each of the core models, either subiterating until convergence [183, 297] (thus realizing an implicit, or strong, coupling of all the core models, leading to a partitioned method) or performing a single step of each [348] (corresponding to an explicit, or loose, treatment of the coupling, and resulting in segregated methods).

I introduce a segregated method [53], in which the coupling between electrophysiology, force generation and mechanics is treated explicitly, as commonly done in the cardiac electromechanics literature [17, 108, 123, 259, 275]. The coupling of fluid and solid is more delicate, since an explicit treatment may lead to instability [63], and is discussed in more detail in Section 3.2. The scheme is derived from the one presented in [259, 275] for ventricular electromechanics simulations, adapted to include the three-dimensional description of blood hemodynamics and fluid-structure interaction.

Let us introduce an equally spaced partition of the time domain $(0, T)$ into the sub-intervals (t^i, t^{i+1}), for $i = 0, 1, \ldots, N_T$, with $t_0 = 0$ and $t_{N_T} = T$, and such that $t^{i+1} - t^i = \Delta t$. From here on, the numerical approximation of any of the solution variables at time t^n will be denote with a superscript

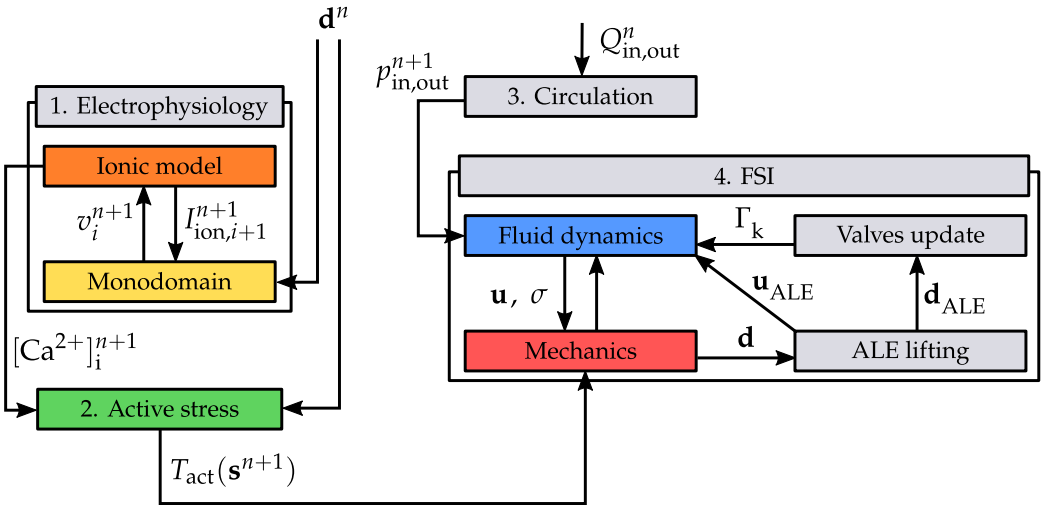

Figure 3.1: Schematic representation of the time discretization scheme. The numbers correspond to the steps decribed in Section 3.1, while the discretization of the FSI problem is discussed in Section 3.2.

n, e.g. $\mathbf{u}^n \approx \mathbf{u}(t^n)$.

Time derivatives appearing in the model are approximated by means of finite differences [261]. Since electrophysiology is characterized by a faster dynamics than the other models, it typically requires a finer time step for an accurate solution [275]. Therefore, it is discretized with a time step $\Delta t_{\text{EP}} = \dfrac{\Delta t}{N_{\text{EP}}}$, with $N_{\text{EP}} \in \mathbb{N}$, and N_{EP} electrophysiology time steps are solved for each time step of the EMF model, thus realizing a staggered coupling between electrophysiology and the other core models. This way, the discretization scheme leverages the multiphysics nature of the problem to deal with the multiple temporal scales it involves.

Given the solution variables and the domain Ω^n up to time step t^n, in order to compute the solution at time t^{n+1}, the following steps are performed:

1. electrophysiology: solve N_{EP} steps of the electrophysiology problem, that is: setting $v_0^{n+1} = v^n$ and $\mathbf{w}_0^{n+1} = \mathbf{w}^n$, for $i = 0, 1, \dots, N_{\text{EP}} - 1$:

(a) compute $\mathbf{w}_{i+1}^{n+1}$ and $\mathbf{z}_{i+1}^{n+1}$ by solving the ionic model

$$\begin{cases} \dfrac{\mathbf{w}_{i+1}^{n+1} - \mathbf{w}_{i}^{n+1}}{\Delta t_{\text{EP}}} = \mathbf{F}_{\text{ion}}^{\mathbf{w}}(v_i^{n+1}, \mathbf{w}_{i+1}^{n+1}) & \text{in } \widehat{\Omega}_{\text{s}}^{\text{LV}} \ , \\ \dfrac{\mathbf{z}_{i+1}^{n+1} - \mathbf{z}_{i}^{n+1}}{\Delta t_{\text{EP}}} = \mathbf{F}_{\text{ion}}^{\mathbf{z}}(v_i^{n+1}, \mathbf{w}_{i}^{n+1}, \mathbf{z}_{i}^{n+1}) & \text{in } \widehat{\Omega}_{\text{s}}^{\text{LV}} \ . \end{cases} \tag{3.1}$$

The previous is an *implicit-explicit* (IMEX) scheme, with an implicit discretization of gating variables and an explicit discretization of ionic concentrations [269, 275]. Indeed, gating variable equations are stiff but linear, while ionic concentration equations are non-linear yet not stiff, so that the explicit discretization poses no issues concerning numerical stability. This approach allows to solve the ionic model directly, i.e. without the need of an iterative non-linear solver;

(b) then, solve the monodomain equation to compute v_{i+1}^{n+1}:

$$\begin{cases} J^n \chi C_{\text{m}} \dfrac{v_{i+1}^{n+1} - v_{i}^{n+1}}{\Delta t_{\text{EP}}} \\ \quad - \boldsymbol{\nabla} \cdot \left(J^n (F^n)^{-1} D_{\text{m}} (F^n)^{-T} \boldsymbol{\nabla} v_{i+1}^{n+1} \right) \\ \qquad + J^n \chi I_{\text{ion}}(v_i^{n+1}, \mathbf{w}_{i+1}^{n+1}, \mathbf{z}_{i+1}^{n+1}) \\ \qquad\quad = J^n \chi I_{\text{app}}(\widehat{\mathbf{x}}, t^n + (i+1)\Delta t_{\text{EP}}) \end{cases} \quad \text{in } \widehat{\Omega}_{\text{s}}^{\text{LV}} \ , \\ \\ J^n (F^n)^{-1} D_{\text{m}} (F^n)^{-T} \boldsymbol{\nabla} v_{i+1}^{n+1} \cdot \mathbf{n} = 0 \qquad \text{on } \partial\widehat{\Omega}_{\text{s}}^{\text{LV}} \ . \end{cases} \tag{3.2}$$

System (3.2) relies on a semi-implicit discretization, since the ionic current term is computed using the tramsmembrane potential at previous electrophysiology subiteration, v_i^{n+1}. Therefore, the problem is linear.

Then, set $v^{n+1} = v_{N_{\text{EP}}}^{n+1}$, $\mathbf{w}^{n+1} = \mathbf{w}_{N_{\text{EP}}}^{n+1}$ and $\mathbf{z}^{n+1} = \mathbf{z}_{N_{\text{EP}}}^{n+1}$;

2. force generation model: compute the sarcomere length SL^n using the last available displacement $\widehat{\mathbf{d}}^n$, i.e.

$$\begin{cases} -\delta_{\text{SL}}^2 \nabla^2 \text{SL}^n + \text{SL}^n = \text{SL}_0 \sqrt{I_{4\text{f}}^n} & \text{in } \widehat{\Omega}_{\text{s}} \times (0,T) \ , \\ \delta_{\text{SL}}^2 \boldsymbol{\nabla} \text{SL}^n \cdot \mathbf{n} = 0 & \text{on } \partial\widehat{\Omega}_{\text{s}} \times (0,T) \ , \end{cases} \tag{3.3}$$

then solve the activation model to compute $\mathbf{s}^{n+1}$:

$$\frac{\mathbf{s}^{n+1}-\mathbf{s}^{n}}{\Delta t}=\mathbf{F}_{\text{act}}\left(\mathbf{s}^{n},[\text{Ca}^{2+}]_{\text{i}}^{n+1},\text{SL}^{n},\frac{\text{SL}^{n}-\text{SL}^{n-1}}{\Delta t}\right)\quad\text{in }\widehat{\Omega}_{\text{s}}^{\text{active}}\ ; \tag{3.4}$$

3. circulation: compute the flowrates at the 3D-0D interface by integrating over the corresponding boundary section of the 3D fluid domain, i.e.

$$Q_j^{\text{inlet}}=-\int_{\Gamma_j^{\text{inlet}}}(\mathbf{u}^{n}-\mathbf{u}_{\text{ALE}}^{n})\cdot\mathbf{n}d\gamma\qquad j\in\{1,2,\dots,N^{\text{inlet}}\}\ ,$$
$$Q_j^{\text{outlet}}=\int_{\Gamma_j^{\text{outlet}}}(\mathbf{u}^{n}-\mathbf{u}_{\text{ALE}}^{n})\cdot\mathbf{n}d\gamma\qquad j\in\{1,2,\dots,N^{\text{outlet}}\}\ .$$

Then, advance the circulation model (2.17) with an explicit Euler scheme [261] to compute $\mathbf{c}^{n+1}$;

4. fluid-structure interaction: solve the coupled FSI problem to compute $\mathbf{d}_{\text{ALE}}^{n+1}$, $\widehat{\mathbf{d}}^{n+1}$, $\mathbf{u}^{n+1}$ and p^{n+1}. The discretization of the FSI problem and the treatment of the fluid-solid coupling are discussed in detail in Section 3.2.

The segregated scheme allows to choose flexibly the discretization parameters for each of the problems. For instance, electrophysiology can be solved on a fine spatial or temporal grid [293] to satisfy its accuracy requirements, without propagating those requirements to the discretization of other problems.

3.2 Numerical methods for cardiac fluid-structure interaction

Among the core models composing the EMF model, the FSI one is, by far, the most computationally demanding [53]. This is due to the intrinsic cost of computational fluid dynamics simulations as well as to the non-linearity induced by the solid constitutive laws and FSI coupling. Therefore, it is of particular importance to investigate different discretization strategies for the FSI problem, to try and reduce the associated computational burden.

In the following, I provide a broad overview of methods for FSI, reviewing some of the classes of methods available in the literature, and then describe in more detail a few specific methods within the strongly coupled and loosely coupled classes. For the latter, I provide a comparison based on numerical experiments, with the aim of selecting the scheme that is most appropriate for cardiac simulations. The results presented in the next sections have been published in [50, 51].

3.2.1 A taxonomy of methods for fluid-structure interaction

Within the FSI literature, two broad families of FSI coupling methods can be distinguished: the *strongly coupled* ones, in which the interface conditions are imposed exactly at all time discretization steps [18, 50, 63, 127, 149, 173, 189, 192, 222, 232, 234, 280, 357, 361], and the *loosely coupled* ones, in which interface conditions are discretized in an explicit fashion so that fluid and solid problems can be solved once per time step [24, 55, 58, 113, 131, 130, 142]. The latter are seldom considered in the biological modeling literature, due to stability concerns related to the added mass effect [63]. Nonetheless, stable schemes in this family can provide relevant computational advantages with respect to their strongly coupled counterparts [51].

Strongly coupled schemes can be further classified into *partitioned schemes*, for which the solution algorithm is based on subiterating between the fluid and the solid problems [18, 63, 183, 189, 222, 232, 297], and *monolithic schemes*, that discretize fluid and solid into a single non-linear algebraic system to be solved with standard techniques [127, 149, 173, 202, 234, 361]. Upon convergence, the two methods provide the same solution. However, they differ significantly in their computational performance as well as in the implementation effort they require. While partitioned methods may suffer from convergence issues or require suitable acceleration methods to become effective [50, 63, 189], they are inherently modular and straightforward to implement. Monolithic schemes, on the other hand, require the development and implementation of dedicated solvers, often based on Newton's method or one of its variants, as well as suitable preconditioners for an efficient solution [50, 92, 193].

To facilitate the discussion, let us introduce the following shorthand nota-

tion for the differential problems related to FSI:

- $\mathcal{G}\left(\mathbf{d}_{\mathrm{ALE}}, \widehat{\mathbf{d}}\right) = \mathbf{0}$ expresses the fluid domain displacement problem (2.11) in compact form;
- $\mathcal{F}\left(\mathbf{u}^{n+1}, p^{n+1}, \mathbf{u}_{\mathrm{ALE}}^{n+1}\right) = \mathbf{0}$ expresses the Navier-Stokes equations in compact form, after time discretization, i.e.

$$\begin{cases} \rho_{\mathrm{f}}\left[\dfrac{\mathbf{u}^{n+1}-\mathbf{u}^{n}}{\Delta t} + \left(\left(\mathbf{u}^{n}-\mathbf{u}_{\mathrm{ALE}}^{n+1}\right)\cdot\boldsymbol{\nabla}\right)\mathbf{u}^{n+1}\right] & \\ \quad -\boldsymbol{\nabla}\cdot\sigma_{\mathrm{f}}\left(\mathbf{u}^{n+1}, p^{n+1}\right) + \boldsymbol{\mathcal{R}}\left(\mathbf{u}^{n+1}, \mathbf{u}_{\mathrm{ALE}}^{n+1}\right) = \mathbf{0} & \text{in } \Omega_{\mathrm{f}}^{n+1}\,, \\ \boldsymbol{\nabla}\cdot\mathbf{u}^{n+1} = 0 & \text{in } \Omega_{\mathrm{f}}^{n+1}\,, \end{cases} \tag{3.5}$$

  endowed with appropriate boundary conditions, but excluding interface conditions on Σ^{n+1};
- $\mathcal{M}\left(\widehat{\mathbf{d}}^{n+1}, \mathbf{s}^{n+1}\right) = \mathbf{0}$ expresses the time-discrete equations of mechanics in compact form, i.e.

$$\begin{cases} \rho_{\mathrm{s}}\dfrac{\widehat{\mathbf{d}}^{n+1}-2\widehat{\mathbf{d}}^{n}+\widehat{\mathbf{d}}^{n-1}}{\Delta t^2} - \boldsymbol{\nabla}\cdot P_{\mathrm{s}}(\widehat{\mathbf{d}}^{n+1}, \mathbf{s}^{n+1}) = \mathbf{0} & \text{in } \widehat{\Omega}_{\mathrm{s}}\,, \\ \widehat{\mathbf{d}}^{n+1} = \mathbf{0} & \text{on } \widehat{\Gamma}_{\mathrm{s}}^{\mathrm{D}}\,, \\ P(\widehat{\mathbf{d}}^{n+1}, \mathbf{s}^{n+1})\mathbf{n} = \mathbf{0} & \text{on } \widehat{\Gamma}_{\mathrm{s}}^{\mathrm{N}}\,, \\ P_{\mathrm{s}}(\widehat{\mathbf{d}}^{n+1}, \mathbf{s}^{n+1})\mathbf{n} & \\ \quad = -(\mathbf{n}\otimes\mathbf{n})\left(K_{\perp}^{\mathrm{epi}}\widehat{\mathbf{d}}^{n+1} + C_{\perp}^{\mathrm{epi}}\dfrac{\widehat{\mathbf{d}}^{n+1}-\widehat{\mathbf{d}}^{n}}{\Delta t}\right) & \text{on } \widehat{\Gamma}_{\mathrm{s}}^{\mathrm{R}}\,, \\ \quad -(I-\mathbf{n}\otimes\mathbf{n})\left(K_{\parallel}^{\mathrm{epi}}\widehat{\mathbf{d}}^{n+1} + C_{\parallel}^{\mathrm{epi}}\dfrac{\widehat{\mathbf{d}}^{n+1}-\widehat{\mathbf{d}}^{n}}{\Delta t}\right) & \end{cases} \tag{3.6}$$

  excluding interface conditions on $\widehat{\Sigma}$;
- $\mathcal{FSI}\left(\mathbf{u}^{n+1}, p^{n+1}, \mathbf{u}_{\mathrm{ALE}}^{n+1}, \mathbf{d}^{n+1}, \mathbf{s}^{n+1}\right) = \mathbf{0}$ expresses, in compact form, the coupled problem comprising (3.5), (3.6) and the interface conditions

$$\mathbf{u}^{n+1} = \left(\frac{\mathbf{d}^{n+1}-\mathbf{d}^{n}}{\Delta t}\right) \qquad \text{on } \Sigma^{n+1}\,,$$

Scheme	Section	Geometry	FSI coupling
GE-P	3.2.2	explicit	strong, partitioned
GE-P-RN2	3.2.2	explicit	two Robin-Neumann (RN) iterations
GI-P	3.2.3	implicit	strong, partitioned
GE-M	3.2.4	explicit	strong, monolithic
GI-M	3.2.5	implicit	strong, monolithic
GE-E	3.2.6	explicit	loose, segregated

Table 3.1: Summary of the numerical schemes considered for cardiac FSI.

$$\sigma_{\mathrm{f}}\left(\mathbf{u}^{n+1}, p^{n+1}\right)\mathbf{n} = \sigma_{\mathrm{s}}\left(\mathbf{d}^{n+1}, \mathbf{s}^{n+1}\right)\mathbf{n} \qquad \text{on } \Sigma^{n+1}\ .$$

In the following sections, I provide details on some discretization schemes for cardiac FSI in the strongly and loosely coupled classes, partitioned, monolithic and segregated. The schemes considered, as well as the abbreviations used, are summarized in Table 3.1. I carry out comparisons through numerical experiments in Sections 3.4 and 3.5.

3.2.2 Strongly coupled partitioned schemes with explicit geometric coupling (GE-P)

I describe below a partitioned scheme based on fixed-point iterations with explicit geometric coupling, represented schematically in Figure 3.2a and referred to as GE-P (geometrically explicit, partitioned). The scheme can be outlined as follows: given $\widehat{\mathbf{d}}^{n}$, $\widehat{\mathbf{d}}^{n-1}$ and $\mathbf{u}^{n}$, to compute the solution at time t^{n+1}:

1. compute $\mathbf{d}_{\mathrm{ALE}}^{n+1}$ by solving $\mathcal{G}\left(\mathbf{d}_{\mathrm{ALE}}^{n+1}, \widehat{\mathbf{d}}^{n}\right) = \mathbf{0}$, then update the domain $\Omega_{\mathrm{f}}^{n+1}$ and compute the ALE velocity as

$$\mathbf{u}_{\mathrm{ALE}}^{n+1} = \left(\frac{\mathbf{d}_{\mathrm{ALE}}^{n+1} - \mathbf{d}_{\mathrm{ALE}}^{n}}{\Delta t}\right) \circ \left(\mathcal{L}_{\mathrm{f}}^{n+1}\right)^{-1} ;$$

2. set $\widehat{\mathbf{d}}_{(0)}^{n+1} = \widehat{\mathbf{d}}^{n}$, and iterate for $k = 0, 1, 2, \ldots$ and until convergence:

(a) compute $\mathbf{u}_{(k+1)}^{n+1}$ and $p_{(k+1)}^{n+1}$ by solving the Navier-Stokes equations, using $\mathbf{d}_{(k)}^{n+1}$ to provide data on Σ^{n+1}:

$$\begin{cases} \mathcal{F}\left(\mathbf{u}_{(k+1)}^{n+1}, p_{(k+1)}^{n+1}, \mathbf{u}_{\text{ALE}}^{n+1}\right) = \mathbf{0}\,, \\ \mathbf{c}_{\text{f}}\left(\mathbf{u}_{(k+1)}^{n+1}, p_{(k+1)}^{n+1}, \mathbf{d}_{(k)}^{n+1}, \mathbf{s}^{n+1}\right) = \mathbf{0} \quad \text{on } \Sigma^{n+1}\,; \end{cases}$$

(b) compute an intermediate displacement $\widetilde{\mathbf{d}}_{(k+1)}^{n+1}$ by solving the elastodynamics equation, using the newly computed $\mathbf{u}_{(k+1)}^{n+1}$ and $p_{(k+1)}^{n+1}$ to provide data on $\widehat{\Sigma}$:

$$\begin{cases} \mathcal{M}\left(\widetilde{\mathbf{d}}_{(k+1)}^{n+1}, \mathbf{s}^{n+1}\right) = \mathbf{0}\,, \\ \mathbf{c}_{\text{s}}\left(\widetilde{\mathbf{d}}_{(k+1)}^{n+1}, \mathbf{u}_{(k+1)}^{n+1}, p_{(k+1)}^{n+1}, \mathbf{s}^{n+1}\right) = \mathbf{0} \quad \text{on } \widehat{\Sigma}\,. \end{cases}$$

(c) apply a suitable acceleration or relaxation method to the solid displacement:

$$\widehat{\mathbf{d}}_{(k+1)}^{n+1} = \mathbf{R}_{(k+1)}\left(\widetilde{\mathbf{d}}_{(k+1)}^{n+1}, \widehat{\mathbf{d}}_{(k)}^{n+1}, \widehat{\mathbf{d}}_{(k-1)}^{n+1}, \dots\right)\,.$$

After last iteration $\bar{k}$, set $\mathbf{u}^{n+1} = \mathbf{u}_{(\bar{k})}^{n+1}$, $p^{n+1} = p_{(\bar{k})}^{n+1}$ and $\widehat{\mathbf{d}}^{n+1} = \widehat{\mathbf{d}}_{(\bar{k})}^{n+1}$.

The iterations over k are stopped either when the norm of the residual associated to interface conditions (2.16) falls below a prescribed tolerance [18], or when the increment between subsequent iterations becomes small.

Operators $\mathbf{c}_{\text{f}}$ and $\mathbf{c}_{\text{s}}$ express suitable interface conditions used to realize the coupling between fluid and solid. Different methods are obtained by selecting different conditions, typically inspired by domain decomposition methods [265]. The simplest approach is given by Dirichlet-Neumann (DN) iterations [63], for which

$$\mathbf{c}_{\text{f}}\left(\mathbf{u}_{(k+1)}^{n+1}, \mathbf{p}_{(k+1)}^{n+1}, \mathbf{d}_{(k)}^{n+1}, \mathbf{s}^{n+1}\right) = \mathbf{u}_{(k+1)}^{n+1} - \frac{\mathbf{d}_{(k)}^{n+1} - \mathbf{d}^{n}}{\Delta t}\,,$$

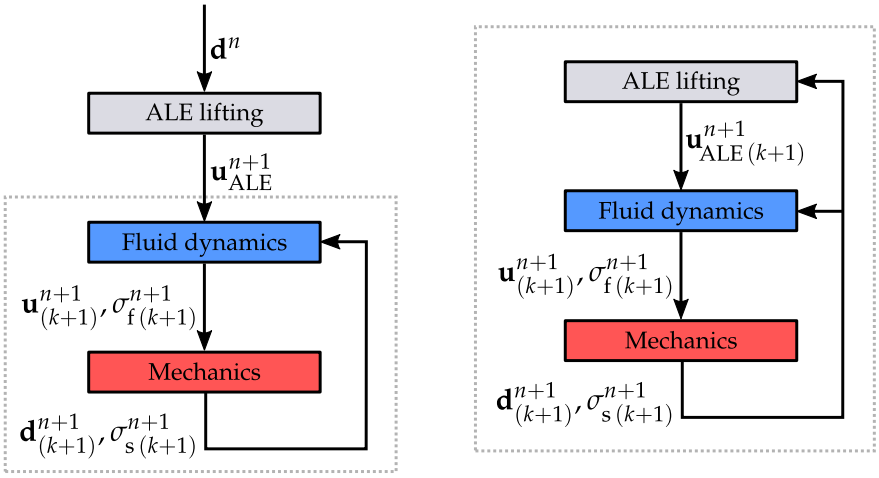

(a) GE-P (b) GI-P

Figure 3.2: (a) Schematic representation of the geometrically explicit strongly coupled partitioned scheme. (b) Schematic representation of the geometrically implicit strongly coupled partitioned scheme.

$$\begin{aligned}&\mathbf{c}_{\mathrm{s}}\left(\widetilde{\mathbf{d}}_{(k+1)}, \mathbf{u}^{n+1}_{(k+1)}, p^{n+1}_{(k+1)}, \mathbf{s}^{n+1}\right)\\&\quad = \sigma_{\mathrm{f}}\left(\mathbf{u}^{n+1}_{(k+1)}, p^{n+1}_{(k+1)}\right)\mathbf{n} - \sigma_{\mathrm{s}}\left(\widetilde{\mathbf{d}}_{(k+1)}, \mathbf{s}^{n+1}\right)\mathbf{n}\,.\end{aligned}$$

More general methods fall within the Robin-Robin (RR) class [18, 19, 58, 113, 265], in which interface conditions (2.16) are replaced by two independent linear combinations of kinematic and dynamic coupling. A particular method in this class is the Robin-Neumann (RN) method, for which

$$\begin{aligned}\mathbf{c}_{\mathrm{f}}\left(\mathbf{u}^{n+1}_{(k+1)}, \mathbf{p}^{n+1}_{(k+1)}, \mathbf{d}^{n+1}_{(k)}, \mathbf{s}^{n+1}\right) &= \alpha\left[\mathbf{u}^{n+1}_{(k+1)} - \frac{\mathbf{d}^{n+1}_{(k)} - \mathbf{d}^{n}}{\Delta t}\right]\\&\quad + \sigma_{\mathrm{f}}\left(\mathbf{u}^{n+1}_{(k+1)}, p^{n+1}_{(k+1)}\right)\mathbf{n} - \sigma_{\mathrm{s}}\left(\mathbf{d}^{n}_{(k)}, \mathbf{s}^{n+1}\right)\mathbf{n}\,,\end{aligned}$$

$$\begin{aligned}&\mathbf{c}_{\mathrm{s}}\left(\widetilde{\mathbf{d}}_{(k+1)}, \mathbf{u}^{n+1}_{(k+1)}, p^{n+1}_{(k+1)}, \mathbf{s}^{n+1}\right)\\&\quad = \sigma_{\mathrm{f}}\left(\mathbf{u}^{n+1}_{(k+1)}, p^{n+1}_{(k+1)}\right)\mathbf{n} - \sigma_{\mathrm{s}}\left(\widetilde{\mathbf{d}}_{(k+1)}, \mathbf{s}^{n+1}\right)\mathbf{n}\,,\end{aligned}$$

with $\alpha > 0$ a suitable Robin coefficient. The RN method was shown to have a better performance than other partitioned schemes, in particular DN [18, 19].

The partitioned method just described can be interpreted as a fixed-point iteration method over the interface displacement [18, 90]. The operator $\mathbf{R}_{(k+1)}$ in step 2c denotes a suitable relaxation or convergence acceleration procedure. Indeed, partitioned methods of this kind may require relaxation to ensure convergence [63]. Moreover, they might require a large number of iterations, so that the use of convergence acceleration methods such as *Aitken acceleration* (AitA) [189, 222] or *Anderson acceleration* (AndA) [43, 50, 106, 353] may significantly improve the computational performance. In this thesis, I considered static relaxation, AitA and AndA as possible acceleration methods. Their definitions are reported in Appendix A.

In the numerical benchmarks discussed in this thesis, I also consider a variation on this method, based on performing only 2 subiterations using RN interface conditions, without checking for convergence. This method is denoted by GE-P-RN2.

3.2.3 Strongly coupled partitioned schemes with implicit geometric coupling (GI-P)

A method in which the geometric coupling (2.11b) is treated implicitly can be derived by modifying the GE-P scheme by updating the fluid domain displacement within the fixed-point iterations. In the following, I refer to this scheme as GI-P (geometrically implicit, paritioned). The method is schematically represented in Figure 3.2b, and can be outlined as follows: given $\widehat{\mathbf{d}}^n$, $\widehat{\mathbf{d}}^{n-1}$ and $\mathbf{u}^n$, to compute the solution at time t^{n+1}, set $\widehat{\mathbf{d}}^{n+1}_{(0)} = \widehat{\mathbf{d}}^n$ and iterate for $k = 0, 1, 2, \dots$ and until convergence:

1. compute $\mathbf{d}^{n+1}_{\mathrm{ALE}\,(k+1)}$ by solving $\mathcal{G}\left(\mathbf{d}^{n+1}_{\mathrm{ALE}\,(k+1)}, \widehat{\mathbf{d}}^{n+1}_{(k)}\right) = \mathbf{0}$, then update the domain $\Omega^{n+1}_{\mathrm{f},(k+1)}$ and compute the ALE velocity as

$$\mathbf{u}^{n+1}_{\mathrm{ALE}\,(k+1)} = \left(\frac{\mathbf{d}^{n+1}_{\mathrm{ALE}\,(k+1)} - \mathbf{d}^{n}_{\mathrm{ALE}}}{\Delta t}\right) \circ \left(\mathcal{L}^{n+1}_{\mathrm{f},(k+1)}\right)^{-1};$$

2. compute $\mathbf{u}_{(k+1)}^{n+1}$ and $p_{(k+1)}^{n+1}$ by solving the Navier-Stokes equations, using $\mathbf{d}_{(k)}^{n+1}$ to provide data on Σ^{n+1}:

$$\begin{cases} \mathcal{F}\left(\mathbf{u}_{(k+1)}^{n+1}, p_{(k+1)}^{n+1}, \mathbf{u}_{\mathrm{ALE}\,(k+1)}^{n+1}\right) = \mathbf{0}\,, \\ \mathbf{c}_{\mathrm{f}}\left(\mathbf{u}_{(k+1)}^{n+1}, p_{(k+1)}^{n+1}, \mathbf{d}_{(k)}^{n+1}, \mathbf{s}^{n+1}\right) = \mathbf{0} \quad \text{on } \Sigma^{n+1}\,; \end{cases}$$

3. compute an intermediate displacement $\widetilde{\mathbf{d}}_{(k+1)}^{n+1}$ by solving the elasto-dynamics equation, using the newly computed $\mathbf{u}_{(k+1)}^{n+1}$ and $p_{(k+1)}^{n+1}$ to provide data on $\widehat{\Sigma}$:

$$\begin{cases} \mathcal{M}\left(\widetilde{\mathbf{d}}_{(k+1)}^{n+1}, \mathbf{s}^{n+1}\right) = \mathbf{0}\,, \\ \mathbf{c}_{\mathrm{s}}\left(\widetilde{\mathbf{d}}_{(k+1)}^{n+1}, \mathbf{u}_{(k+1)}^{n+1}, p_{(k+1)}^{n+1}, \mathbf{s}^{n+1}\right) = \mathbf{0} \quad \text{on } \widehat{\Sigma}\,. \end{cases}$$

4. apply a suitable acceleration or relaxation method to the solid displacement:

$$\widehat{\mathbf{d}}_{(k+1)}^{n+1} = \mathbf{R}_{(k+1)}\left(\widetilde{\mathbf{d}}_{(k+1)}^{n+1}, \widehat{\mathbf{d}}_{(k)}^{n+1}, \widehat{\mathbf{d}}_{(k-1)}^{n+1}, \dots\right)\,.$$

After last iteration $\bar{k}$, set $\mathbf{d}_{\mathrm{ALE}}^{n+1} = \mathbf{d}_{\mathrm{ALE}\,(\bar{k})}^{n+1}$, $\mathbf{u}^{n+1} = \mathbf{u}_{(\bar{k})}^{n+1}$, $p^{n+1} = p_{(\bar{k})}^{n+1}$ and $\widehat{\mathbf{d}}^{n+1} = \widehat{\mathbf{d}}_{(\bar{k})}^{n+1}$.

Stopping criteria, interface conditions $\mathbf{c}_{\mathrm{f}}$, $\mathbf{c}_{\mathrm{s}}$ and the relaxation operator $\mathbf{R}_{(k+1)}$ are defined as in the previous section. Other partitioned schemes with implicit geometric coupling can be obtained e.g. by performing two nested loops at each time step: in the outer loop, the fluid domain displacement problem is solved and the fluid domain updated, and in the inner loop the fluid and structure problems are solved for a fixed fluid domain [232].

3.2.4 Monolithic scheme with explicit geometric coupling (GE-M)

Let us now consider a geometrically explicit monolithic scheme: the geometric coupling is treated explicitly, while fluid and solid equations are

solved simultaneously, with strong imposition of kinematic and dynamic coupling. This scheme is referred to as GE-M (geometrically explicit, monolithic). The scheme is represented in Figure 3.3a, and can be outlined as follows: given $\widehat{\mathbf{d}}^n$, $\widehat{\mathbf{d}}^{n-1}$ and $\mathbf{u}^n$, to compute the solution at time t^{n+1}:

1. compute $\mathbf{d}_{\text{ALE}}^{n+1}$ by solving $\mathcal{G}\left(\mathbf{d}_{\text{ALE}}^{n+1}, \widehat{\mathbf{d}}^n\right) = \mathbf{0}$, then update the domain Ω_{f}^{n+1} and compute the ALE velocity as

$$\mathbf{u}_{\text{ALE}}^{n+1} = \left(\frac{\mathbf{d}_{\text{ALE}}^{n+1} - \mathbf{d}_{\text{ALE}}^{n}}{\Delta t}\right) \circ \left(\mathcal{L}_{\text{f}}^{n+1}\right)^{-1} ;$$

2. compute $\mathbf{u}^{n+1}$, p^{n+1} and $\widehat{\mathbf{d}}^{n+1}$ solving the coupled FSI problem

$$\mathcal{FSI}\left(\mathbf{u}^{n+1}, p^{n+1}, \mathbf{u}_{\text{ALE}}^{n+1}, \mathbf{d}^{n+1}, \mathbf{s}^{n+1}\right) = \mathbf{0} .$$

   The latter is a non-linear problem, due to the non-linear constitutive law of the structure. Therefore, it is solved by means of Newton iterations: setting $\mathbf{u}_{(0)}^{n+1} = \mathbf{u}^n$, $p_{(0)}^{n+1} = p^n$ and $\mathbf{d}_{(0)}^{n+1} = \mathbf{d}^n$, iterate for $k = 0, 1, 2, \ldots$ and until convergence:

   (a) solve the linearized problem

$$J_{(k)}^{\mathcal{FSI}}(\delta\mathbf{u}, \delta p, \delta\mathbf{d}) = \mathcal{FSI}\left(\mathbf{u}_{(k)}^{n+1}, p_{(k)}^{n+1}, \mathbf{u}_{\text{ALE}}^{n+1}, \mathbf{d}_{(k)}^{n+1}, \mathbf{s}^{n+1}\right) , \tag{3.7}$$

   where $J_{(k)}^{\mathcal{FSI}}$ is the Fréchet derivative of the function $\mathcal{FSI}$ with respect to $\mathbf{u}^{n+1}$, p^{n+1} and $\mathbf{d}^{n+1}$, evaluated at $\mathbf{u}_{(k)}^{n+1}$, $p_{(k)}^{n+1}$ and $\mathbf{d}_{(k)}^{n+1}$;

   (b) update the solution by setting

$$\begin{aligned}
\mathbf{u}_{(k+1)}^{n+1} &= \mathbf{u}_{(k)}^{n+1} - \delta\mathbf{u} , \\
p_{(k+1)}^{n+1} &= p_{(k)}^{n+1} - \delta p , \\
\mathbf{d}_{(k+1)}^{n+1} &= \mathbf{d}_{(k)}^{n+1} - \delta\mathbf{d} .
\end{aligned}$$

   After last iteration $\bar{k}$, set $\mathbf{u}^{n+1} = \mathbf{u}_{(\bar{k})}^{n+1}$, $p^{n+1} = p_{(\bar{k})}^{n+1}$ and $\mathbf{d}^{n+1} = \mathbf{d}_{(\bar{k})}^{n+1}$.

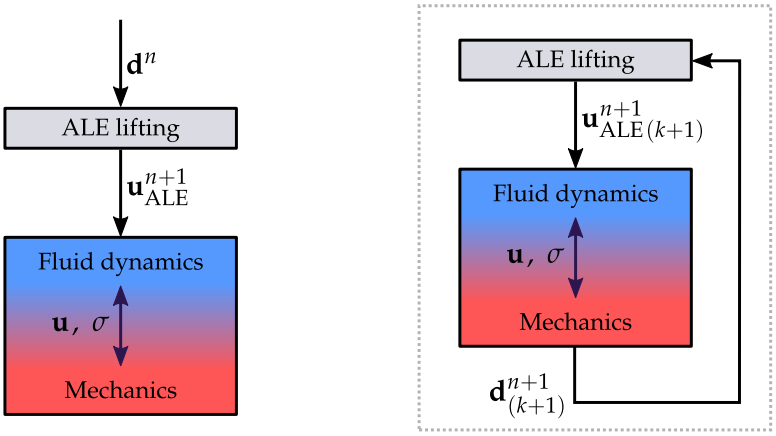

(a) GE-M (b) GI-M

Figure 3.3: (a) Schematic representation of the geometrically explicit strongly coupled monolithic scheme. (b) Schematic representation of the geometrically implicit strongly coupled monolithic scheme.

3.2.5 Monolithic scheme with implicit geometric coupling (GI-M)

A monolithic scheme with implicit geometric coupling, referred to as GI-M, can be obtained from the GE-M scheme by updating the fluid domain within the Newton loop. The resulting scheme is represented in Figure 3.3b, and can be outlined as follows: given $\widehat{\mathbf{d}}^n$, $\widehat{\mathbf{d}}^{n-1}$ and $\mathbf{u}^n$, to compute the solution at time t^{n+1}, set $\mathbf{u}^{n+1}_{(0)} = \mathbf{u}^n$, $p^{n+1}_{(0)} = p^n$ and $\mathbf{d}^{n+1}_{(0)} = \mathbf{d}^n$, and iterate for $k = 0, 1, 2, \ldots$ until convergence:

1. compute $\mathbf{d}^{n+1}_{\text{ALE}\,(k+1)}$ by solving $\mathcal{G}\left(\mathbf{d}^{n+1}_{\text{ALE}\,(k+1)}, \widehat{\mathbf{d}}^{n+1}_{(k)}\right) = \mathbf{0}$, then update the domain Ω^{n+1}_{f} and compute the ALE velocity as

$$\mathbf{u}^{n+1}_{\text{ALE}\,(k+1)} = \left(\frac{\mathbf{d}^{n+1}_{\text{ALE}\,(k+1)} - \mathbf{d}^{n}_{\text{ALE}}}{\Delta t}\right) \circ \left(\mathcal{L}^{n+1}_{\text{f},(k+1)}\right)^{-1} ;$$

2. solve the linearized FSI problem

$$J^{\mathcal{FSI}}_{(k)}(\delta\mathbf{u},\delta p,\delta\mathbf{d}) = \mathcal{FSI}\left(\mathbf{u}^{n+1}_{(k)}, p^{n+1}_{(k)}, \mathbf{u}^{n+1}_{\mathrm{ALE}\,(k+1)}, \mathbf{d}^{n+1}_{(k)}, \mathbf{s}^{n+1}\right) ;$$

3. update the solution by setting

$$\begin{aligned}
\mathbf{u}^{n+1}_{(k+1)} &= \mathbf{u}^{n+1}_{(k)} - \delta\mathbf{u} ,\\
p^{n+1}_{(k+1)} &= p^{n+1}_{(k)} - \delta p ,\\
\mathbf{d}^{n+1}_{(k+1)} &= \mathbf{d}^{n+1}_{(k)} - \delta\mathbf{d} .
\end{aligned}$$

After last iteration $\bar{k}$, set $\mathbf{d}^{n+1}_{\mathrm{ALE}} = \mathbf{d}^{n+1}_{\mathrm{ALE}\,(k)}$, $\mathbf{u}^{n+1} = \mathbf{u}^{n+1}_{(\bar{k})}$, $p^{n+1} = p^{n+1}_{(\bar{k})}$ and $\mathbf{d}^{n+1} = \mathbf{d}^{n+1}_{(\bar{k})}$.

This method corresponds to solving the fully coupled FSI problem composed of (2.11), (3.5), (3.6) and (2.16) by means of an inexact Newton method, in which Jacobian terms involving derivatives with respect to the fluid domain displacement (including shape derivatives [30, 112]) are neglected. Accounting for shape derivatives, either computed exactly [31, 94, 112, 173, 280, 281, 357] or approximated through finite differences [149, 159], is another viable option.

3.2.6 A stable, loosely coupled scheme (GE-E)

As seen in previous sections, schemes with strong coupling of fluid and solid involve iterative procedures to enforce the FSI coupling, either by means of fixed-point algorithms or through Newton's method. In practice, this means that, at every time step, the fluid and solid problems are assembled and solved multiple times. This entails a very significant computational cost.

Alternatively, loosely coupled (or explicit) discretization schemes can be considered, based on solving the fluid and solid problems only once per time step. Unfortunately, a naïve approach based e.g. on a DN loosely coupled scheme leads to an unstable solution [63]. Indeed, biological systems are characterized by the so-called added mass effect: when fluid and solid densities are comparable, explicit methods are prone to instability

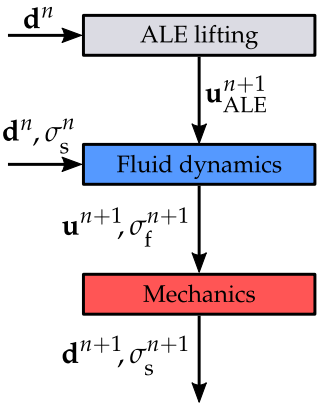

Figure 3.4: Schematic representation of the geometrically explicit loosely coupled FSI scheme (GE-E).

in time [63]. Therefore, while computationally attractive, loosely coupled methods must be designed carefully to ensure stability [58, 57, 113, 114, 130, 131]. In particular, the stability of loosely coupled schemes based on Robin interface conditions has been investigated in [130, 131] for vascular hemodynamics applications.

Here, I present a particular scheme in that class, using RN interface conditions. The scheme, represented in Figure 3.4, is referred to as GE-E (geometrically explicit with explicit FSI). Its steps are the following:

1. compute $\mathbf{d}^{n+1}_{\text{ALE}}$ by solving $\mathcal{G}\left(\mathbf{d}^{n+1}_{\text{ALE}}, \widehat{\mathbf{d}}^n\right) = \mathbf{0}$, then update the domain Ω^{n+1}_{f} and compute the ALE velocity as

$$\mathbf{u}^{n+1}_{\text{ALE}} = \left(\frac{\mathbf{d}^{n+1}_{\text{ALE}} - \mathbf{d}^{n}_{\text{ALE}}}{\Delta t}\right) \circ \left(\mathcal{L}^{n+1}_{\text{f}}\right)^{-1} ;$$

2. compute $\mathbf{u}^{n+1}$ and p^{n+1} by solving the Navier-Stokes equations, using

$\mathbf{d}^n$ to provide Robin data on Σ^{n+1}:

$$\begin{cases} \mathcal{F}\left(\mathbf{u}^{n+1}, p^{n+1}, \mathbf{u}_{\mathrm{ALE}}^{n+1}\right) = \mathbf{0}\,, \\ \mathbf{u}^{n+1} - \dfrac{\mathbf{d}^n - \mathbf{d}^{n-1}}{\Delta t} \\ \quad + \alpha\left[\sigma_{\mathrm{f}}\left(\mathbf{u}^{n+1}, p^{n+1}\right)\mathbf{n} - \sigma_{\mathrm{s}}\left(\mathbf{d}^n, \mathbf{s}^{n+1}\right)\mathbf{n}\right] = \mathbf{0} \end{cases} \quad \text{on } \Sigma^{n+1}\,;$$

3. compute $\widehat{\mathbf{d}}^{n+1}$ by solving the elastodynamics equation, using the newly computed $\mathbf{u}^{n+1}$ and p^{n+1} to provide Neumann data on $\widehat{\Sigma}$:

$$\begin{cases} \mathcal{M}\left(\widehat{\mathbf{d}}^{n+1}, \mathbf{s}^{n+1}\right) = \mathbf{0}\,, \\ \sigma_{\mathrm{f}}\left(\mathbf{u}_{(k+1)}^{n+1}, p_{(k+1)}^{n+1}\right)\mathbf{n} - \sigma_{\mathrm{s}}\left(\mathbf{d}^{n+1}, \mathbf{s}^{n+1}\right)\mathbf{n} = \mathbf{0} \quad \text{on } \widehat{\Sigma}\,. \end{cases}$$

3.3 Space discretization and solvers

Spatial discretization of PDEs is achieved by means of the finite element method (FEM) [165, 261]. Let us introduce a hexahedral or tetrahedral mesh in both domains $\widehat{\Omega}_{\mathrm{s}}$ and $\widehat{\Omega}_{\mathrm{f}}$. At their interface $\widehat{\Sigma}$, the fluid and solid meshes are conforming (i.e. surface elements on the interface on one of the two domain are coincident with surface elements on the other domain). This facilitates the communication of interface data between the two domains, avoiding the use of interpolation methods required by non-conforming meshes [91, 234]. The mesh in $\widehat{\Omega}_{\mathrm{f}}$ is updated over time follwing the displacement $\mathbf{d}_{\mathrm{ALE}}^{n+1}$, resulting in a mesh in $\Omega_{\mathrm{f}}^{n+1}$. Mesh resolution varies in space, and it is generally finer in the area around RIIS surfaces (when present), so as to better capture their presence and avoid spurious flow across them [107].

3.3.1 Electrophysiology

The ionic model (3.1) is solved independently for each degree of freedom (DoF) of the solid mesh, avoiding the computational costs associated to the storage, assembly and inversion of a matrix. The ionic current is evaluated at each DoF and then interpolated onto quadrature nodes in the interior

of mesh elements, in the approach known as *ionic current interpolation* (ICI) [186, 247].

The finite element discretization of the monodomain equation (3.2) yields a symmetric, positive definite linear system $A_{\text{EP}}\mathbf{V} = \mathbf{F}_{\text{EP}}$. It is solved using the conjugate gradient (CG) method, preconditioned using algebraic multigrid (AMG) [261, 289, 360].

3.3.2 Force generation

The discretization of the sarcomere length regularization problem (3.3) yields a symmetric positive definite linear system $A_{\text{SL}}\mathbf{S} = \mathbf{F}_{\text{SL}}$. It is solved using the CG method, preconditioned with AMG.

The force generation model (3.4) is solved at each DoF of the mesh, like done for the ionic model. The generated active force T_{act} is then computed at each DoF and interpolated onto quadrature nodes on element interiors.

3.3.3 Cardiac mechanics

After discretization, problem (3.6) results in a non-linear algebraic system, which is linearized with Newton's method. This yields a non-symmetric linear system $A_{\text{M}}\,\delta\mathbf{D} = \mathbf{F}_{\text{M}}$, which is solved using the GMRES method [261, 289] preconditioned with AMG.

When solving the quasi-static counterpart of (3.6), i.e. when recovering the reference configuration or computing the initial displacement (Section 2.4), an inexact Newton method is used instead, based on progressively reducing the linear solver tolerance during Newton iterations [25, 49, 101]. This prevents oversolving during the first Newton iterations, overall reducing the computational cost and facilitating the solver convergence.

3.3.4 Fluid domain displacement

The spatial discretization of the fluid domain displacement problem (2.11) yields an algebraic problem that may be linear or non linear according to the choice of P_{ALE}. For the linear cases (harmonic extension, linear elasticity) solve the resulting problem is solved using the CG method, preconditioned with AMG.

Non-linear cases (based either on the neo-Hooke law or on (2.13)) require more sophisticated methods. In principle, the problem (2.11) can be linearized by means of Newton's method, and the resulting linear system solved with GMRES, using an AMG preconditioner. However, Newton's method converges only if its initial guess is sufficiently close to the solution [261]. Since the initial guess is the solution at the previous time step, this may require Δt to be very small. The convergence of the solver is even more problematic when computing the initial fluid domain displacement $\mathbf{d}_{\text{ALE}}(t=0)$: since the initial solid displacement $\mathbf{d}_0$ is generally different from $\mathbf{0}$, it is hard to obtain an initial guess for the fluid domain displacement problem that guarantees convergence. In practice, this was a significant limitation of this approach for the numerical studies performed in this thesis.

To avoid this issue, I introduced an iterative method to solve (2.11) by means of an adaptive linear ramp in the boundary data: given $c_0 = 0$, $\Delta c_0 \in (0,1]$ and an initial guess $\mathbf{d}_{\text{ALE}}^{(0)}$, iterate for $k = 1, 2, \ldots$ and until $c_k < 1$:

1. set $c_k \leftarrow \min\{c_{k-1} + \Delta c_{k-1}, 1\}$;
2. try to solve $\mathcal{G}\left(\mathbf{d}_{\text{ALE}}^{(k)}, c_k \widehat{\mathbf{d}} + (1-c_k)\mathbf{d}_{\text{ALE}}^{(0)}|_{\widehat{\Sigma}}\right) = \mathbf{0}$, using Newton's method with $\mathbf{d}_{\text{ALE}}^{(k-1)}$ as initial guess:
   (a) if Newton's method succeeds, set $\Delta c_k \leftarrow \alpha_{\text{success}} \Delta c_{k-1}$ and $k \leftarrow k+1$, then advance to next iteration;
   (b) if Newton's method fails, set $\Delta c_{k-1} \leftarrow \alpha_{\text{failure}} \Delta c_{k-1}$ and repeat the current iteration.

Parameters Δc_0, $\alpha_{\text{success}} \in [1, \infty)$ and $\alpha_{\text{failure}} \in (0,1)$ can be selected by the user to tune the behavior of the adaptive ramp. The initial guess $\mathbf{d}_{\text{ALE}}^{(0)}$ is taken as the solution of the ALE lifting problem at previous time step. The results of this thesis were obtained by setting $\Delta c_0 = 1$, $\alpha_{\text{success}} = 1.1$, $\alpha_{\text{failure}} = 0.5$.

3.3.5 Fluid dynamics

The discretized Navier-Stokes equations are stabilized with either the SUPG-PSPG [325] or the VMS-LES [29, 71, 88, 164, 174, 363] stabilization method. This enables the use of equal-order polynomials for fluid velocity and pressure [261], and provides stabilization for the advection-dominated regime. On top of that, the VMS-LES stabilization provides fine scale modeling to represent the transition-to-turbulence regime of cardiac flow [40, 364]. Both stabilization methods are modified with respect to their original formulations, to account for the presence of the resistive method. The complete formulation can be found in [364].

After the finite element discretization, (3.5) results in a block linear system with the structure

$$A_{\text{NS}}\mathbf{X}_{\text{NS}} = \mathbf{F}_{\text{NS}}\,, \tag{3.8}$$
$$A_{\text{NS}} = \begin{bmatrix} F & B^T \\ -B & S \end{bmatrix} \qquad \mathbf{X}_{\text{NS}} = \begin{bmatrix} \mathbf{U} \\ \mathbf{P} \end{bmatrix}\,,$$

where F discretizes the inertial, viscous and resistive terms, B^T corresponds to the pressure gradient, B to the velocity divergence, and S is the algebraic counterpart of the pressure-pressure terms introduced by the stabilization.

The system (3.8) is solved with GMRES, using the SIMPLE preconditioner [93]:

$$P_{\text{SIMPLE}} = \begin{bmatrix} F & 0 \\ -B & -\widetilde{\Sigma} \end{bmatrix} \begin{bmatrix} I & D^{-1}B^T \\ 0 & I \end{bmatrix}\,, \tag{3.9}$$

where D is the matrix containing only the diagonal elements of F, and $\widetilde{\Sigma} = S + B\,D^{-1}\,B^T$ is an approximation of the Schur complement. In practice, the application of the preconditioner P_{SIMPLE} requires to compute the inverse of the matrices F and $\widetilde{\Sigma}$. To this end, they are approximated with AMG preconditioners, i.e. the inverse of P_{SIMPLE} is approximated by

$$P^{-1}_{\text{aSIMPLE}} = \begin{bmatrix} I & -D^{-1}B^T \\ 0 & I \end{bmatrix} \begin{bmatrix} P_{\text{AMG}}(F)^{-1} & 0 \\ P_{\text{AMG}}(\widetilde{\Sigma})^{-1}BP_{\text{AMG}}(F)^{-1} & P^{-1}_{\text{AMG}}(\widetilde{\Sigma}) \end{bmatrix}\,,$$

where $P_{\text{AMG}}(M)$ denotes an AMG preconditioner for the matrix M. Each application of the preconditioner requires one application of $P_{\text{AMG}}(F)^{-1}$ and one of $P_{\text{AMG}}(\widetilde{\Sigma})^{-1}$.

3.3.6 Fluid-structure interaction

The discretization of the linearized FSI problem (3.7) yields a block linear system in the form

$$\begin{bmatrix} A_{\mathrm{NS}} & C_{\mathrm{fs}} \\ C_{\mathrm{sf}} & A_{\mathrm{M}} \end{bmatrix} \begin{bmatrix} \delta \mathbf{X}_{\mathrm{NS}} \\ \delta \mathbf{D} \end{bmatrix} = \mathbf{F}_{\mathrm{FSI}} \,, \tag{3.10}$$

with the first block corresponding to fluid unknowns (velocity and pressure) and the second block to solid unknowns (displacement). Interface DoFs are condensed [50, 361]: interface fluid and solid control variables are represented by the same unknown in the linear system, resulting in the natural imposition of dynamic coupling conditions [31] and yielding the coupling terms C_{fs} and C_{sf}.

The linear system (3.10) is solved by means of GMRES, using the following block triangular preconditioner, introduced in [50]:

$$P_{\mathrm{FSI}} = \begin{bmatrix} A_{\mathrm{NS}} & 0 \\ C_{\mathrm{sf}} & A_{\mathrm{M}} \end{bmatrix} .$$

The application of the preconditioner requires the inversion of its diagonal blocks. A_{NS}^{-1} is approximated with $P_{\mathrm{aSIMPLE}}^{-1}$, and A_{M}^{-1} is approximated with an AMG preconditioner, so that the inverse of P_{FSI} becomes

$$P_{\mathrm{FSI}}^{-1} = \begin{bmatrix} P_{\mathrm{aSIMPLE}}^{-1} & 0 \\ -P_{\mathrm{AMG}}(A_{\mathrm{M}})^{-1} C_{\mathrm{sf}} P_{\mathrm{aSIMPLE}}^{-1} & P_{\mathrm{AMG}}(A_{\mathrm{M}})^{-1} \end{bmatrix} .$$

Multiplying P_{FSI}^{-1} by a vector requires one application of the SIMPLE preconditioner and one of the AMG preconditioner for the matrix A_{M}.

Similar preconditioners can be obtained e.g. by considering a block-diagonal or block-upper triangular structure, or a block-LU factorization [92, 149, 193]. Alternative approaches are based on deriving preconditioners from domain decomposition formulations, mimicking at the preconditioner level the behavior of partitioned schemes [19, 20].

3.3.7 Software implementation

As part of the PhD research work, I implemented the numerical methods previously discussed in `life`$^{\mathtt{x}}$ [1, 2, 199], a C++ library tailored at high-performance computing simulations of the cardiac function, supporting

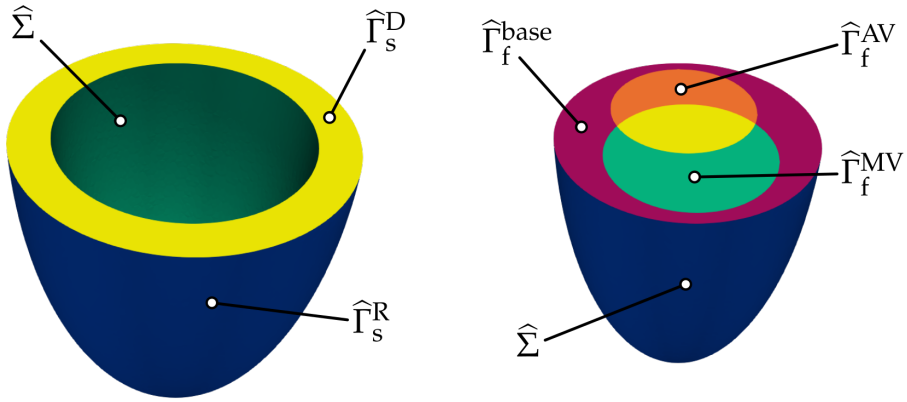

(a) (b)

Figure 3.5: Solid (a) and fluid (b) domains for the idealized left ventricular benchmarks.

multiphysics and multiscale simulations. The library is based on the finite element core `deal.II` [14, 15, 86], and relies on Trilinos [335] for its linear algebra backend, with reference in particular to AMG preconditioners [122]. The `life`^{x} library supports parallel execution with the MPI paradigm, and the implemented solvers are scalable up to thousands of cores [1].

3.4 A comparison of strongly coupled schemes for cardiac FSI

In this section, I provide a comparison of strongly coupled partitioned and monolithic schemes for cardiac applications, to assess which of the schemes is most suited in terms of overall computational efficiency. To this end, I introduce a cardiac benchmark in an idealized geometry, and compare the performance of the strongly coupled methods discussed in Section 3.2. The results presented in this section have been published in [50].

		Fluid			Structure		
Mesh	**Type**	**# elem.**	**# nodes**	h [mm]	**# elem.**	**# nodes**	h [mm]
$\mathcal{M}_A$	hex	20 980	25 103	4.0	24 712	31 495	4.0
$\mathcal{M}_B$	hex	57 080	66 173	2.5	61 296	75 673	2.5
$\mathcal{M}_1$	hex	4684	5927	6.1	6612	8789	5.2
$\mathcal{M}_1^{EP}$	hex	-	-	-	52 896	60 459	2.6
$\mathcal{M}_2$	hex	13 780	16 669	4.0	22 396	28 117	3.3
$\mathcal{M}_3$	hex	32 628	38 429	3.0	51 364	62 589	2.5
$\mathcal{M}_R$	tet	140 644	157 369	1.8	73 860	89 314	2.2

Table 3.2: Idealized ventricle benchmarks. Type of elements (hexahedra or tetrahedra), number of elements, number of nodes and average element diameter h for the meshes considered for the comparison among strongly coupled methods (Section 3.4; $\mathcal{M}_A$ and $\mathcal{M}_B$), for the comparison between strongly and loosely coupled methods (Section 3.5; $\mathcal{M}_1$, $\mathcal{M}_1^{EP}$, $\mathcal{M}_2$ and $\mathcal{M}_3$) and for the realistic ventricle mesh ($\mathcal{M}_R$), for both the fluid and the structure domain.

3.4.1 Benchmark problem description

Let us consider as domain the prolate ellipsoid depicted in Figure 3.5, representing an idealized left ventricle. Similarly to [316], I identify two intersecting circular regions, $\widehat{\Gamma}_f^{MV}$ and $\widehat{\Gamma}_f^{AV}$, on the base of the fluid domain, representing the mitral and aortic valve orifice, respectively. The remainder of the ventricular base is denoted by $\widehat{\Gamma}_f^{base}$.

The purpose of the benchmark is to assess the effectiveness of methods for FSI. Therefore, I do not consider the electrophysiology and force generation models, and instead define T_{act} through an analytical function of time [7, 50, 234], plotted in Figure 3.6, mimicking the contraction and relaxation of the ventricle:

$$T_{act}(t) = \begin{cases} 0 & \text{if } t < t_{act}^0, \\ T_{act}^{max} \left(\dfrac{t - t_{act}^0}{t_{act}^{peak}} \right)^{p_{act}} \exp\left\{ p_{act} \left(1 - \dfrac{t - t_{act}^0}{t_{act}^{peak}} \right) \right\} & \text{if } t \geq t_{act}^0 \end{cases}$$

I use the Guccione model for the structure, generating fibers with the rule-based algorithm presented in [288]. The whole solid domain is considered

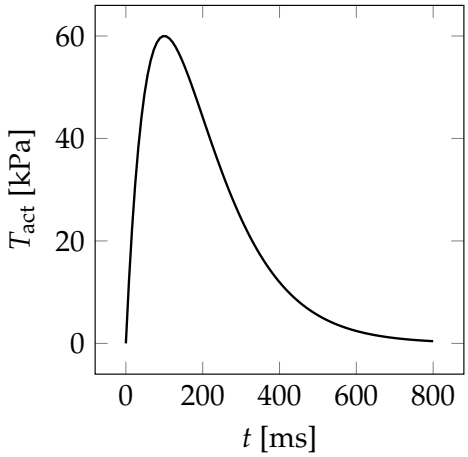

Figure 3.6: Graph of the analytical active force $T_{act}(t)$ for the idealized left ventricular benchmarks.

as mechanically active (i.e. $\widehat{\Omega}_s^{active} = \widehat{\Omega}_s$). The benchmark does not include RIIS or circulation. Fluid domain displacement is obtained using the harmonic extension (2.12). Navier-Stokes equations are stabilized with SUPG-PSPG. The base of the ventricle is kept fixed for simplicity, i.e.

$$\begin{aligned} \widehat{\mathbf{d}} &= \mathbf{0} \qquad \text{on } \widehat{\Gamma}_s^D \times (0,T)\,, \\ \mathbf{d}_{ALE} &= \mathbf{0} \qquad \text{on } \left(\widehat{\Gamma}_f^{base} \cup \widehat{\Gamma}_f^{AV} \cup \widehat{\Gamma}_f^{MV}\right) \times (0,T)\,. \end{aligned}$$

Different boundary conditions are imposed on $\widehat{\Gamma}_f^{MV}$ and $\widehat{\Gamma}_f^{AV}$ to model the opening and closing of valves [50, 316]. When both valves are closed, i.e. during isovolumetric phases, a no-slip condition is imposed:

$$\mathbf{u} = \mathbf{0} \qquad \text{on } \left(\Gamma_f^{MV} \cup \Gamma_f^{AV}\right) \times (0,T)\,.$$

During ejection, a no-slip condition is imposed on the MV orifice, and a resistance condition is imposed on the AV orifice, i.e.

$$\begin{aligned} &\mathbf{u} = \mathbf{0} && \text{on } \left(\Gamma_f^{MV} \backslash \Gamma_f^{AV}\right) \times (0,T)\,, \\ &\sigma_f(\mathbf{u},p) = -\left(p_{AV} + R_{AV}\int_{\Gamma_f^{AV}} \mathbf{u}\cdot\mathbf{n}\,d\Gamma\right)\mathbf{n} && \text{on } \Gamma_f^{AV} \times (0,T)\,, \end{aligned}$$

where p_{AV} and R_{AV} are prescribed. The resistance condition on the AV orifice, calibrated in qualitative accordance with [266], allows to account for the typical evolution in time of the aortic pressure [210], at the same time preventing spurious reflections of pressure waves [170, 266, 346], that would yield unphysical oscillations of ventricular pressure and volume. Finally, during filling, a no-slip condition is imposed on the AV, while a Neumann condition is prescribed on $\Gamma_{\mathrm{f}}^{\mathrm{MV}}$:

$$\begin{aligned} &\sigma_{\mathrm{f}}(\mathbf{u}, p) = -p_{\mathrm{MV}}\mathbf{n} && \text{on } \Gamma_{\mathrm{f}}^{\mathrm{MV}} \times (0, T) \,, \\ &\mathbf{u} = \mathbf{0} && \text{on } \left(\Gamma_{\mathrm{f}}^{\mathrm{AV}} \backslash \Gamma_{\mathrm{f}}^{\mathrm{MV}}\right) \times (0, T) \,. \end{aligned}$$

The values of the parameters used for this benchmark are reported in Appendix B.1. Unless otherwise specified, the simulations were run using 48 parallel processes on the GALILEO100 cluster[1] at the CINECA high-performance computing center (Italy).

3.4.2 Systolic test case

As a first benchmark, let us consider an idealized ventricular systole: the MV is closed and the AV is open, and the contraction of the ventricle results in an increase of pressure, the outflow of blood through the AV orifice and the consequent reduction in ventricular volume. For this test, I set a final time $T = 200\,\mathrm{ms}$ and a time step $\Delta t = 0.2\,\mathrm{ms}$, and consider the hexahedral mesh $\mathcal{M}_{\mathrm{A}}$ (see Table 3.2 for details).

The problem is solved using the GE-M, GE-P, GI-M and GI-P schemes. Concerning partitioned schemes, both the DN and the RN interface conditions are considered. One crucial issue when employing partitioned schemes is the choice of the parameters associated to convergence relaxation, acceleration or Robin interface conditions. Optimal values have been proposed in idealized settings for vascular hemodynamics, considering simplified linear elastic solids [63, 126, 130]. However, cardiac applications are characterized by non-linearity and anisotropy in the structure constitutive laws. Moreover, the flow regime is dominated by the contraction and relaxation of the cardiac muscle. The optimal values of partitioned schemes parameters depend heavily on the domain and problem setting [18]. Therefore,

[1] Refer to the website https://wiki.u-gov.it/confluence/display/SCAIUS/UG3.3%3A+GALILEO100+UserGuide for technical specifications (last accessed: 23 September 2022).

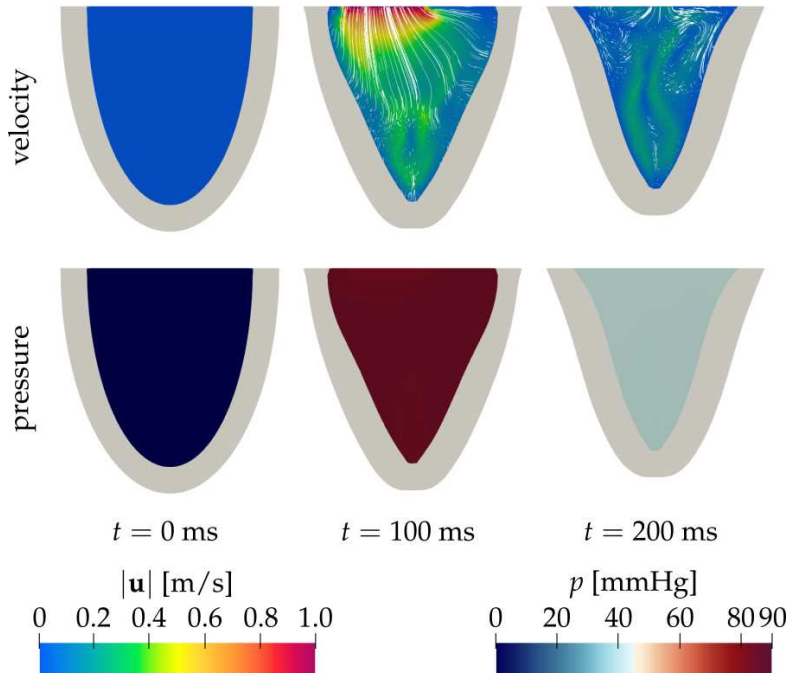

Figure 3.7: Idealized systolic test case (Section 3.4.2). Snapshots of fluid velocity magnitude (top) and pressure (bottom) at three different instants during the simulation, along an apicobasal slice of the prolate, as computed with the GE-M scheme. The domain is warped according to $\mathbf{d}$ and $\mathbf{d}_{\text{ALE}}$.

I manually calibrated those parameters to find settings that provided an effective and efficient solution of the FSI problem. I point out, however, that the need for calibration is in itself a potential drawback of partitioned schemes of this kind.

Figure 3.7 shows some snapshots of the solution variables, Table 3.3 reports the number of linear and non-linear iterations required by each scheme and Figure 3.8 the wall times required by the simulation with the different schemes, as well as the number of system assembly calls required by each. Partitioned schemes using static relaxation require more than 24 h of wall time to complete the simulation, while DN schemes using Aitken or Anderson acceleration fail to converge.

Scheme	Newton/partitioned iter. min.	avg.	max.	Average GMRES iter. monolithic	fluid	solid
GE-M	2	2.1	3	165.9	-	-
GE-P-DN-SR	wall time > 24 h					
GE-P-DN-AitA	convergence failure					
GE-P-DN-AndA	convergence failure					
GE-P-RN-SR	wall time > 24 h					
GE-P-RN-AitA	13	15.6	17	-	808.6	643.4
GE-P-RN-AndA	13	14.0	15	-	657.8	616.4
GI-M	4	6.4	7	396.2	-	-
GI-P-DN-SR	wall time > 24 h					
GI-P-DN-AitA	convergence failure					
GI-P-DN-AndA	convergence failure					
GI-P-RN-SR	wall time > 24 h					
GI-P-RN-AitA	14	15.9	18	-	827.8	654.9
GI-P-RN-AndA	13	14.2	15	-	751.6	582.7

Table 3.3: Performance of the different schemes for the idealized systolic test case (Section 3.4.2). The table reports: the minimum, average and maximum of the number of iterations per timestep required for convergence of the Newton or partitioned method; the average number of linear solver iterations per timestep (across all Newton or partitioned iterations). Refer to Table 3.1 for the explanation of the abbreviations used.

The results indicate that in this setting, with both an explicit and an implicit treatment of the geometric coupling, the monolithic schemes are significantly more efficient than the partitioned ones. Among the latter, the fastest is based on using RN interface conditions, with Anderson acceleration providing a significant improvement over static relaxation or Aitken acceleration. DN schemes suffer from slow convergence issues, and are prone to diverging if acceleration is applied, confirming the observations of [63].

Comparing the explicit and implicit treatment of geometric coupling, I found that the GI-M scheme is more costly than its explicit counterpart, whereas the implicit geometry has a relatively smaller impact on RN schemes, especially if Anderson acceleration is employed.

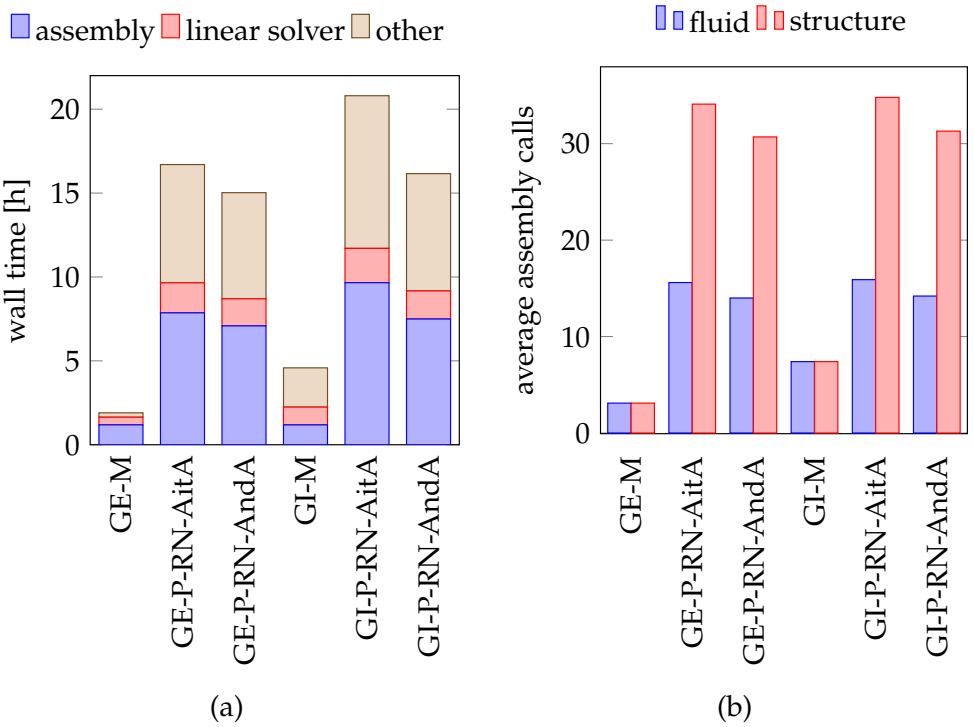

Figure 3.8: (a) Wall times required for the solution of the idealized systolic benchmark (Section 3.4.2) with the different schemes considered. (b) Number of fluid and structure system assembly calls required by each scheme, averaged over time steps. Only schemes that succeed in computing the solution within 24 h are reported.

3.4.3 Parallel performance

I compare the performance of the GE-M scheme and of the GE-P-RN-AndA (the best partitioned scheme from previous section) varying the number of cores used in the parallel computation, considering the same systolic benchmark as in previous section. For this test, I used a mesh $\mathcal{M}_B$ with a higher resolution (Table 3.2) and set the final time to $T = 100$ ms.

The wall times varying the number of cores are reported in Figure 3.9. The results suggest that, regardless of the number of processes used, the GE-M scheme is significantly faster. Indeed, for all tests performed, the GE-P-RN-AndA scheme completed the simulation in approximately 5.5

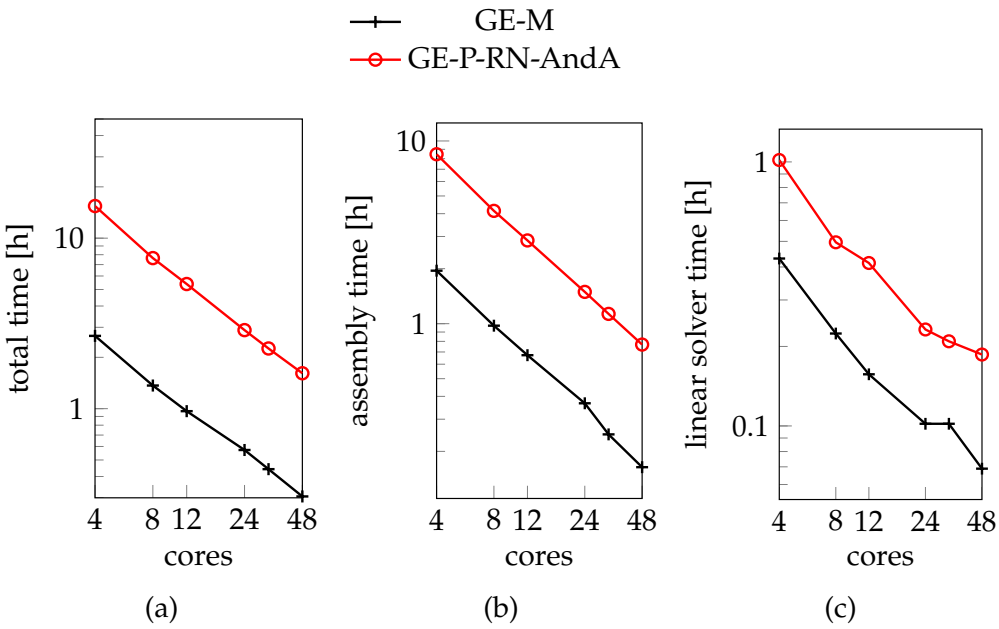

Figure 3.9: Total wall time (a), assembly time (b) and linear solver time (c) for the idealized systolic benchmark with varying number of cores.

times longer wall times.

3.4.4 Diastolic test case

Let us now consider a diastolic benchmark using the same domain and mesh as in Section 3.4.2. The MV is open and the AV is closed. To model the passive relaxation, I set $T_{act}(t) = 0$, and set $T = 200\,\text{ms}$, $\Delta t = 0.2\,\text{ms}$.

The initial conditions of this test are not consistent with the end-systolic conditions found in Section 3.4.2, since the aim of this test is to assess the performance of the FSI algorithms in the context of a slow inflow and in absence of the active contraction. A more comprehensive test case, featuring all phases in a single simulation, is described in Section 3.5.

Figure 3.10 shows some snapshots of the solution, Table 3.4 reports the number of linear and non-linear iterations with the different schemes, while Figure 3.11 reports the wall times and calls to system assembly rou-

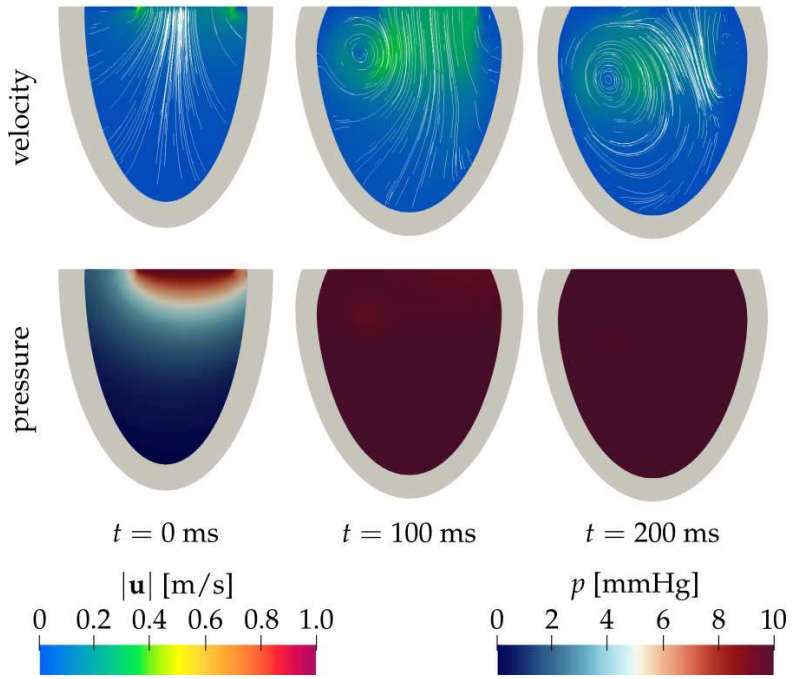

Figure 3.10: Idealized diastolic test case (Section 3.4.4). Snapshots of fluid velocity magnitude (top) and pressure (bottom) at three different instants during the simulation, along an apicobasal slice of the prolate, as computed with the GE-M scheme. The domain is warped according to $\mathbf{d}$ and $\mathbf{d}_{\text{ALE}}$.

tines. The results confirm the observations made for the systolic test case: even in the diastolic regime, partitioned schemes suffer from convergence issues, especially if DN interface conditions are considered, and are significantly slower than monolithic schemes.

3.4.5 Discussion

Both the systolic and diastolic benchmarks indicate that, among strongly coupled FSI schemes, the monolithic ones have better computational performances. Moreover, the latter do not require the calibration of convergence relaxation or acceleration methods, and in general have less parameters, making their use more robust with respect to changes in domain and problem setting. As a result, they appear more suited for strongly coupled

Scheme	Newton/partitioned iter. min.	avg.	max.	Average GMRES iter. monolithic	fluid	solid
GE-M	2	2.0	2	157.7	-	-
GE-P-DN-SR	wall time > 24 h					
GE-P-DN-AitA	convergence failure					
GE-P-DN-AndA	convergence failure					
GE-P-RN-SR	wall time > 24 h					
GE-P-RN-AitA	12	14.1	15	-	575.0	426.6
GE-P-RN-AndA	12	13.4	14	-	543.0	390.3
GI-M	3	4.0	4	262.7	-	-
GI-P-DN-SR	wall time > 24 h					
GI-P-DN-AitA	convergence failure					
GI-P-DN-AndA	convergence failure					
GI-P-RN-SR	wall time > 24 h					
GI-P-RN-AitA	12	14.0	15	-	583.6	432.6
GI-P-RN-AndA	12	13.7	14	-	562.1	405.9

Table 3.4: Performance of the different schemes for the idealized diastolic test case (Section 3.4.4). The table reports: the minimum, average and maximum of the number of iterations per timestep required for convergence of the Newton or partitioned method; the average number of linear solver iterations per timestep (across all Newton or partitioned iterations). Refer to Table 3.1 for the explanation of the abbreviations used.

FSI simulations of the heart.

This conclusion is corroborated by the fact that the strongly coupled partitioned schemes are essentially fixed point iterations, while the monolithic scheme relies on Newton's method, which is a particular fixed point iteration method with higher convergence order. Therefore, the latter needs less iterations to converge, thus requiring less calls to system assembly and linear solver routines (see Figures 3.8b and 3.11b). Although linear solver calls in the partitioned schemes are cheaper than those in the monolithic scheme, due to the reduced size of the system being solved, this does not compensate the larger cost due to the higher number of assembly calls.

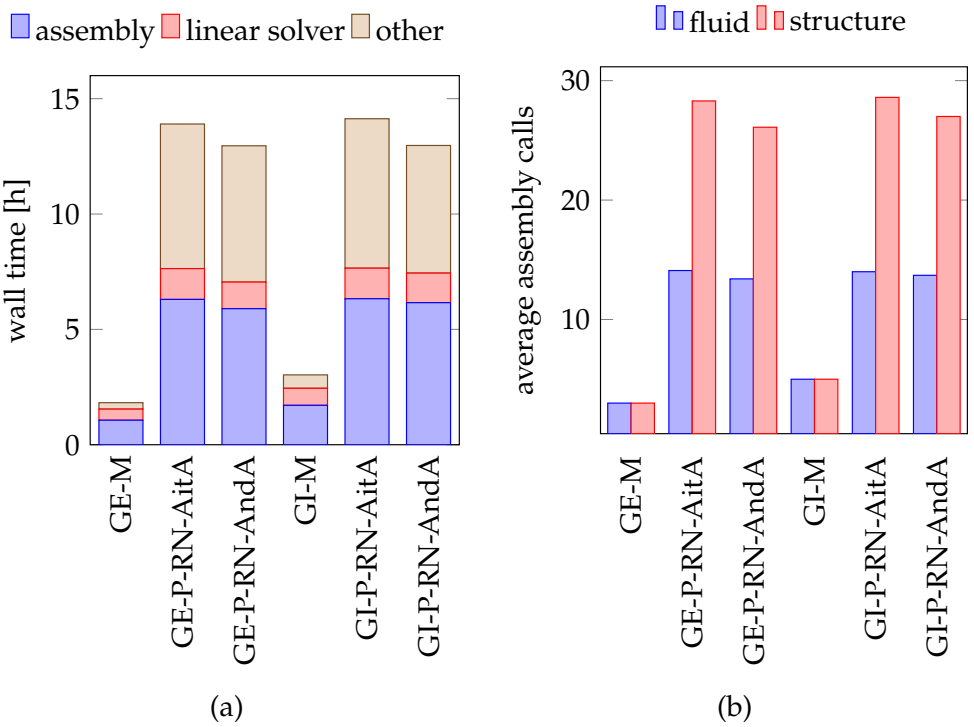

Figure 3.11: (a) Wall times required for the solution of the idealized diastolic benchmark (Section 3.4.4) with the different schemes considered. (b) Number of fluid and structure system assembly calls required by each scheme, averaged over time steps. Only schemes that succeed in computing the solution within 24 h are reported.

3.5 A comparison between strongly and loosely coupled algorithms for cardiac FSI

In this section, I compare the GE-M scheme against the fully loosely coupled GE-E scheme, to understand how the explicit discretization and the use of RN interface conditions affect stability, accuracy and efficiency. To do so, in I consider a slightly more sophisticated benchmark than in the previous section, by including electrophysiology and force generation, and by considering a full heartbeat. The results appearing in this section have been published in [51].

3.5.1 Benchmark problem description

Let us consider the same domain as in Section 3.4, represented in Figure 3.5, and consider the full EMF model (Figure 2.1), including electrophysiology and active contraction. For this test, I use the TTP06 ionic model and RDQ18 force generation model. All other modeling choices and boundary conditions are the same as in Section 3.4.

To represent a full heartbeat, the state of the MV and AV can change instantaneously from closed to open and vice versa, depending on the ventricular pressure and volume [316]:

- when the AV is closed, and the average ventricular pressure becomes larger than p_{AV}, the valve switches from closed to open;
- when the AV is open, and the volume of the ventricle starts increasing (i.e. there is reverse flow through the AV), the valve switches from open to closed;
- when the MV is closed, and the average ventricular pressure is smaller than p_{MV}, the valve switches from closed to open;
- when the MV is open, and the volume of the ventricle starts decreasing (i.e. there is reverse flow through the MV), the valve switches from closed to open.

This allows to reproduce all heartbeat phases, albeit in a simplified way, with the opening and closing times of valves being determined by the simulation rather than prescribed a priori.

The values of the parameters used for this benchmark are reported in Appendix B.2.

3.5.2 Stability of the loosely coupled scheme

The domain is discretized with the mesh $\mathcal{M}_1$ (Table 3.2). To account for the higher accuracy requirements of electrophysiology, it is solved on a finer mesh $\mathcal{M}_1^{\text{EP}}$, nested into the one used for mechanics and with half its mesh size. This allows to better capture the sharp propagating activation front [275, 293]. Displacement and calcium are interpolated between the fine and coarse meshes. I set $N_{\text{EP}} = 1$, i.e. solve electrophysiology, force generation

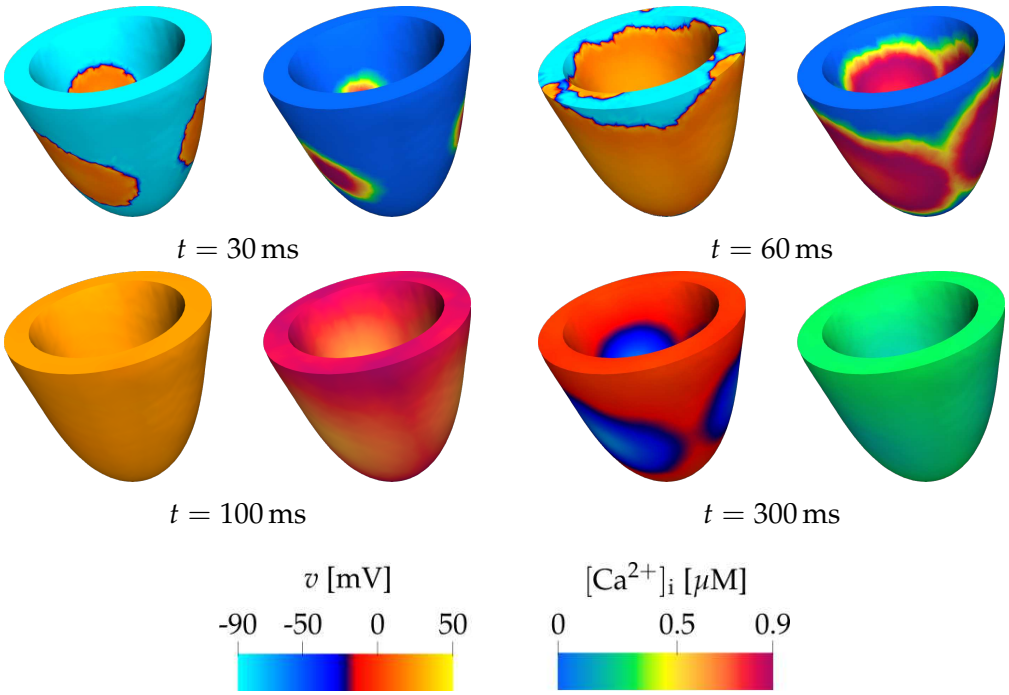

Figure 3.12: Strong and loose FSI coupling (Section 3.5). Snapshots of the electrophysiology solution, computed using the GE-E scheme.

and FSI with the same timestep $\Delta t = 0.2\,\mathrm{ms}$. The final simulation time is set to $T = 500\,\mathrm{ms}$.

For this test case, I simulate a whole heartbeat using the GE-M and GE-E schemes for FSI, to understand whether the loosely coupled discretization of the FSI subproblem yields stability issues for the physical regime and numerical settings typical of cardiac simulations. The GE-E scheme was shown to be conditionally stable in [130, 131], with the stability depending on h, Δt and on the Robin coefficient α. Indeed, as $\alpha \to \infty$, RN interface conditions tend to DN interface conditions, which are known to lead to unstable loosely coupled schemes in the hemodynamic regime [63]. As a consequence, the GE-E scheme can be expected to become unstable for α not small enough. My numerical experiments indicate that, for this test case, the GE-E method is stable provided $\alpha < 6750\,\mathrm{kg}/(\mathrm{m}^2 \cdot \mathrm{s})$, in qualitative accordance with [130], and using spatial and temporal discretizations

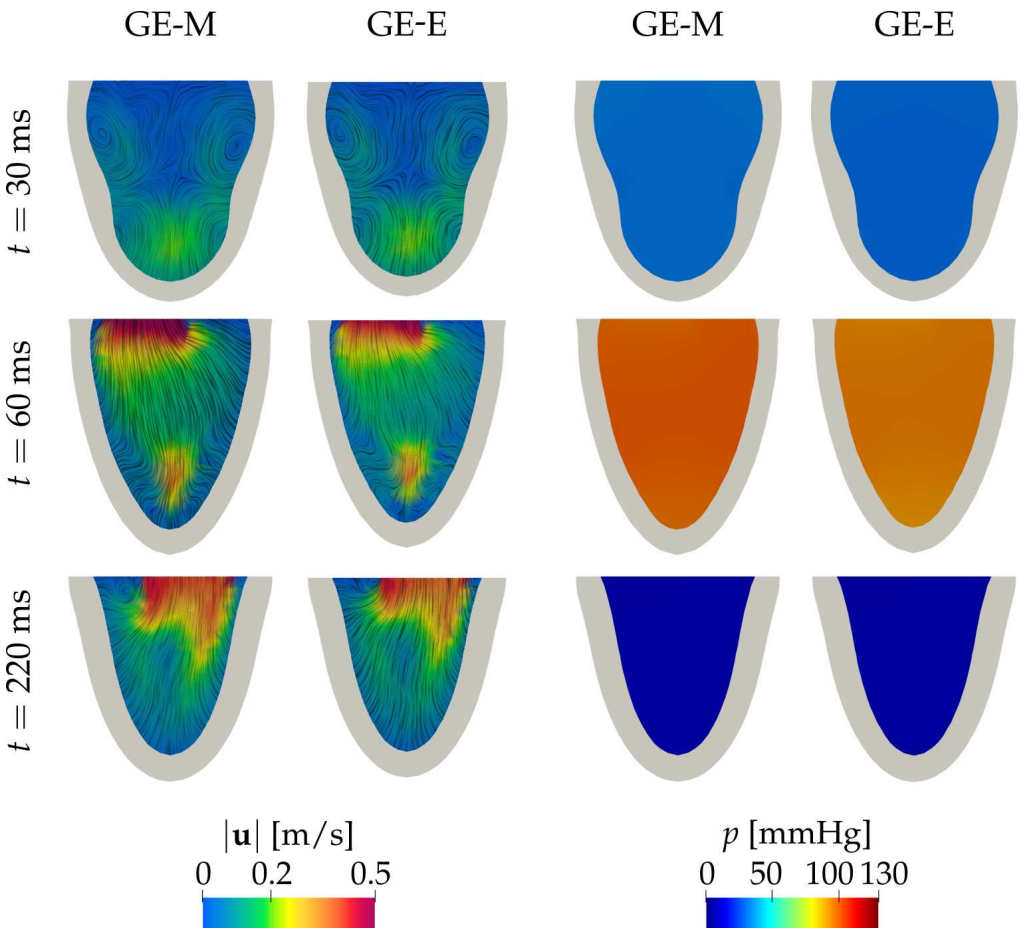

Figure 3.13: Strong and loose FSI coupling (Section 3.5). Fluid velocity magnitude $|\mathbf{u}|$ (left) and pressure p (right) at three time instants, computed with the GE-M and GE-E schemes. From top to bottom, the snapshots correspond to isovolumetric contraction, ejection and filling phases, respectively. The domain is warped according to $\mathbf{d}$ and $\mathbf{d}_{\text{ALE}}$.

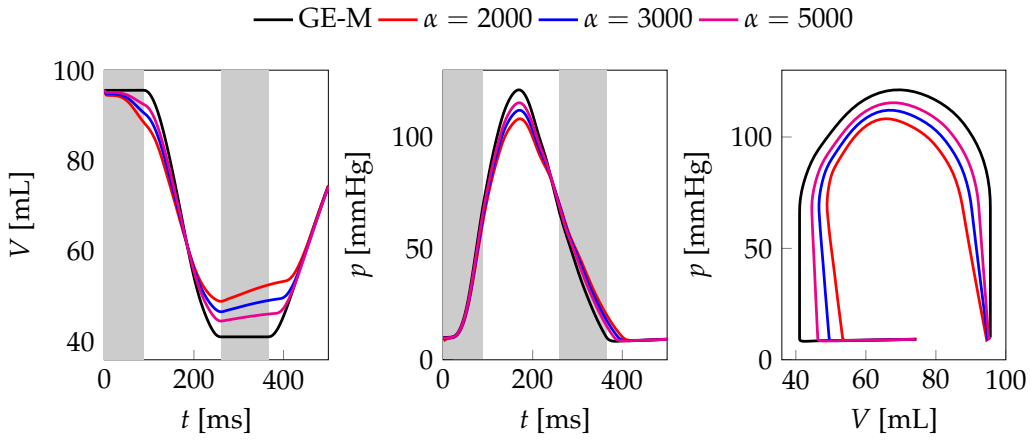

Figure 3.14: Strong and loose FSI coupling (Section 3.5). From left to right, ventricular volume, average pressure and pressure volume loop with the GE-M scheme and the GE-E scheme for different values of α. Gray bands indicate isovolumetric phases.

compatible with the cardiac regime.

I report in Figures 3.12 and 3.13 some snapshots of the solution computed at several time instants, using the GE-M and GE-E schemes, setting $\alpha = 5000\,\mathrm{kg}/(\mathrm{m}^2 \cdot \mathrm{s})$. The corresponding ventricular volume and pressure over time can be found in Figure 3.14. The results show how the GE-E scheme, despite being explicit, yields stable results in this setting, in qualitative agreement with the results obtained with the GE-M scheme.

3.5.3 Accuracy of the loosely coupled scheme

I aim now at comparing the GE-M and GE-E scheme in terms of accuracy of the solution, with reference in particular to the conservation of blood mass, especially during isovolumetric phases. To do so, I introduce two indices, the *isovolumetric loss indices* (ILIs), representing the relative variation of blood volume inside the ventricle during the isovolumetric phases:

$$\mathrm{ILI}_\mathrm{C} = \frac{|V_{\mathrm{C,i}} - V_{\mathrm{C,f}}|}{\max\{V_{\mathrm{C,i}}, V_{\mathrm{C,f}}\}} \qquad \mathrm{ILI}_\mathrm{R} = \frac{|V_{\mathrm{R,i}} - V_{\mathrm{R,f}}|}{\max\{V_{\mathrm{R,i}}, V_{\mathrm{R,f}}\}},$$

wherein $V_{\mathrm{C,i}}$ and $V_{\mathrm{C,f}}$ are the volumes at the beginning and end of the IVC phase, and $V_{\mathrm{R,i}}$ and $V_{\mathrm{R,f}}$ are the volumes at the beginning and end of the

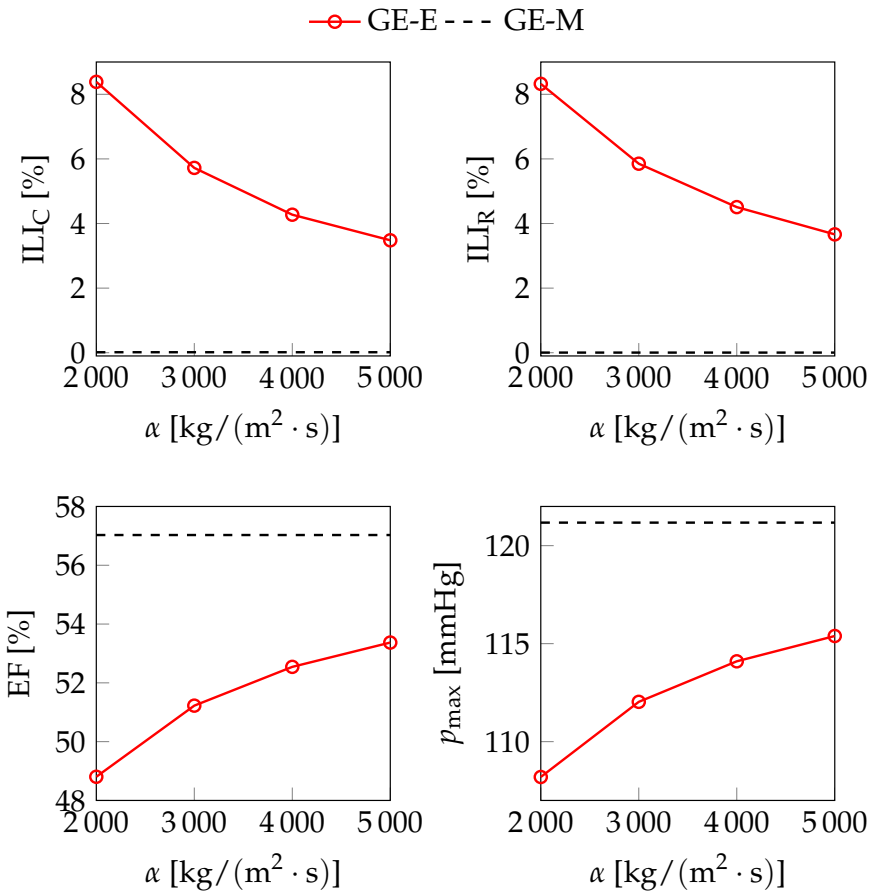

Figure 3.15: Strong and loose FSI coupling (Section 3.5). ILI_C, ILI_R, EF and p_{max} computed with the GE-E scheme for different values of α. Dashed lines indicate the corresponding value for the GE-M scheme.

IVR phase. Optimal values for these two indices are $\mathrm{ILI}_C = \mathrm{ILI}_R = 0$, while positive values indicate the introduction of a loss of mass associated to the isovolumetric phases. For the comparison, I also take into account the EF and the peak systolic pressure

$$p_{max} = \max_{t \in (0,T)} \bar{p}(t) \, ,$$

where $\bar{p}$ is the average ventricular pressure.

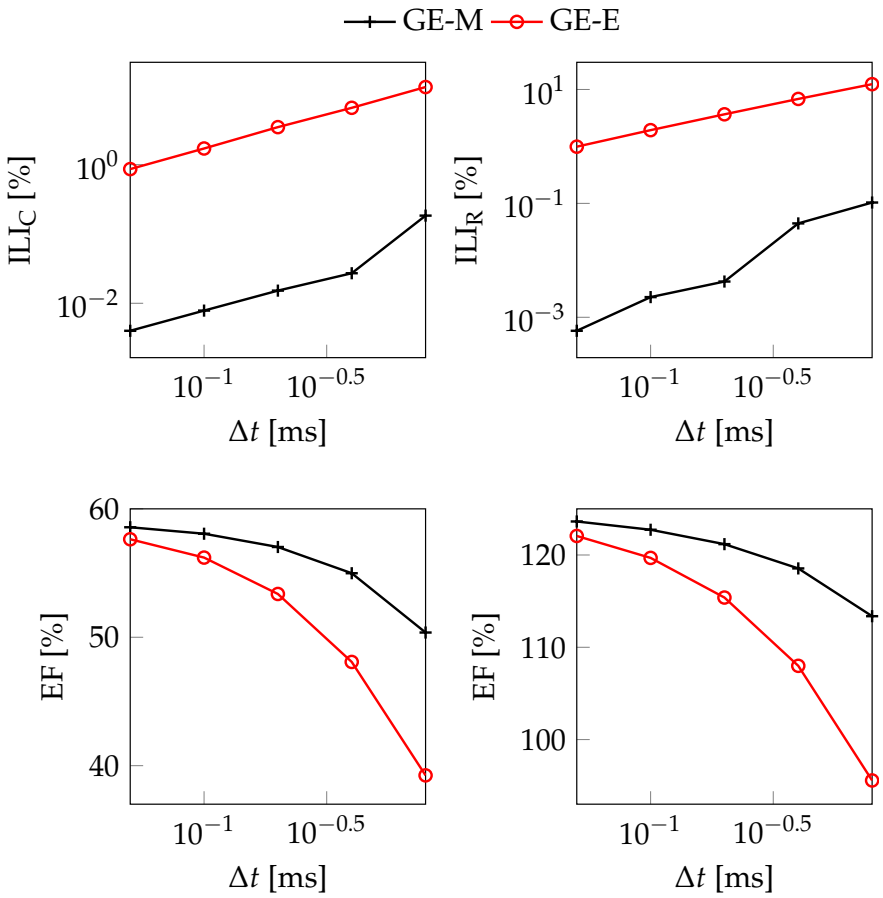

Figure 3.16: Strong and loose FSI coupling (Section 3.5). $\mathrm{ILI_C}$, $\mathrm{ILI_R}$, EF and $p_{\max}$ computed with the GE-M and GE-E scheme for different values of Δt.

Effect of α. In the same setting of Section 3.5.2, I compare the solutions computed with the GE-M and GE-E schemes, varying the Robin coefficient α in the range of stability ($\alpha < 6750\,\mathrm{kg}/(\mathrm{m}^2 \cdot \mathrm{s})$). The choice of α influences the accuracy of the method: indeed, as $\alpha \to 0$, RN interface conditions reduce to two Neumann-type conditions, and no kinematic coupling is present anymore.

Figure 3.14 reports the ventricular volume and pressure over time for different values of α. The solutions obtained with the GE-E scheme feature a sig-

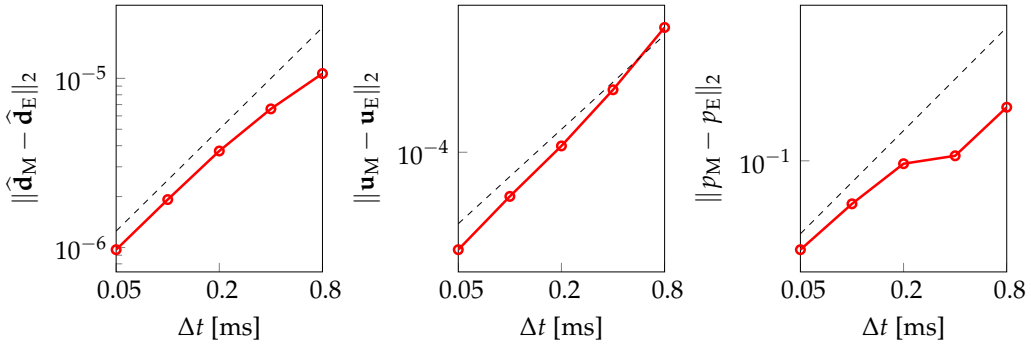

Figure 3.17: Strong and loose FSI coupling (Section 3.5). Mismatch between the solution variables computed with the GE-M and GE-E schemes at the final simulation time T. Dashed lines are parallel to the function $f(\Delta t) = \Delta t$, and are used as a reference for the convergence order.

nificant variation of the ventricular volume during isovolumetric phases. This leads to slower ejection and filling phases, if compared to the GE-M solutions, as well as lower peak systolic pressures. This behavior becomes more significant for decreasing values of α.

Similar conclusions can be drawn by looking at the plots in Figure 3.15, where the value of ILIs, EF and $p_{\max}$ are plotted against the Robin coefficient α. Although the mismatch between GE-E and GE-M reduces as α increases, even with the highest value of α the two results present differences of 6.3 % in EF and 4.7 % in peak systolic pressure.

Effect of Δt. The mismatch between the two schemes can be expected to reduce as Δt is reduced, with the explicit and implicit discretizations converging to the same solution. To verify this, setting $\alpha = 5000\,\mathrm{kg}/(\mathrm{m}^2 \cdot \mathrm{s})$, I run several simulations reducing the time step of both schemes. The resulting indicators are reported in Figure 3.16. As expected, I observe that as $\Delta t \to 0$ there is increasing agreement between the solutions computed by the two schemes in terms of EF and $p_{\max}$. For both schemes, ILI_C and ILI_R tend to zero as $\Delta t \to 0$, with similar rates. However, the ones obtained with the GE-M scheme are in all cases smaller than those of the GE-E one.

I also compute the mismatch between the GE-M and GE-E schemes at the

Scheme	$\mathrm{ILI_C}$ [%]	$\mathrm{ILI_R}$ [%]	EF [%]	$p_{\max}$ [mmHg]
GE-M	0.02	0.00	57.0	121.2
GE-E	3.48	3.66	53.4	115.4
GE-P-RN2	0.96	1.29	55.9	119.5

Table 3.5: Strong and loose FSI coupling (Section 3.5). Isovolumetric loss indices, ejection fraction and peak systolic pressure for three simulations, using the GE-M, GE-E and GE-P-RN2 schemes. For the last two schemes, the Robin coefficient was $\alpha = 5000\,\mathrm{kg}/(\mathrm{m}^2 \cdot \mathrm{s})$. Refer to Table 3.1 for the explanation of the abbreviations used.

final time T of the simulation, to quantify the order of convergence of the additional error introduced by the splitting of fluid and solid. Results are reported in Figure 3.17. The numerical results indicate that the mismatch of solution variables tends to zero as $\Delta t \to 0$, with asymptotic convergence order 1. Therefore, denoting by $\mathbf{x}_\mathrm{M}$ and $\mathbf{x}_\mathrm{E}$ a generic solution variable ($\widehat{\mathbf{d}}$, $\mathbf{u}$ or p) computed with the GE-M and GE-E scheme, respectively, there holds:

$$\|\mathbf{x}_\mathrm{M} - \mathbf{x}_\mathrm{E}\|_2 \leq C_\mathrm{split} \Delta t \,,$$

with C_split a constant independent of Δt. Denoting by $\mathbf{x}$ the exact solution, at any fixed time, there holds:

$$\|\mathbf{x}_\mathrm{E} - \mathbf{x}\|_2 \leq \|\mathbf{x}_\mathrm{E} - \mathbf{x}_\mathrm{M}\|_2 + \|\mathbf{x}_\mathrm{M} - \mathbf{x}\|_2 \leq \left(C_\mathrm{split} + C_\mathrm{M}\right) \Delta t \,,$$

where I have used the fact that the strongly coupled monolithic scheme is convergent of order 1 in time. Therefore, I conclude that the additional error introduced by the splitting is at most of order 1 with respect to Δt, so that the overall order of convergence is not hindered by the explicit discretization. However, if higher order discretizations are used for time derivatives, the splitting scheme should be modified to reflect that.

Effect of multiple RN subiterations. I compare the solution of the GE-M scheme with that of the GE-P-RN2 scheme. This scheme is not implicit, since the partitioned method is stopped at an arbitrary number of iterations, rather than checking for convergence. Nonetheless, increasing the number of RN iterations may lead to a better match with the implicit solution. Figure 3.18 reports the volume and pressure obtained in this way,

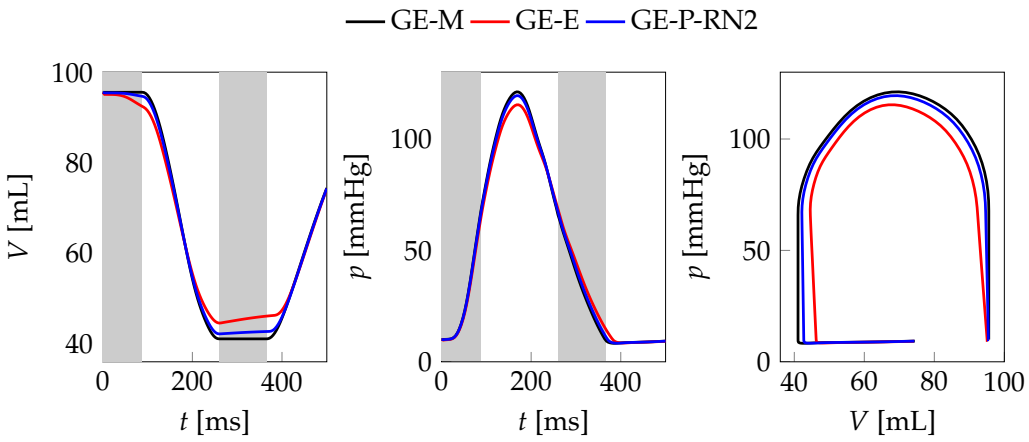

Figure 3.18: Strong and loose FSI coupling (Section 3.5). From left to right, ventricular volume, average pressure and pressure volume loop with the GE-M, GE-E and GE-P-RN2 schemes. Gray bands indicate isovolumetric phases.

while Table 3.5 collects the values of the computed indicators. Performing two RN iterations significantly improves the results, in terms of agreement with the GE-M scheme, in particular for what concerns the ILI indices.

Accuracy during ejection. Previous tests have shown how the explicit discretization introduces an error in the mass conservation that is most evident during isovolumetric phases, and this affects the solution during ejection and filling. To understand to what extent the mismatch between GE-M and GE-E is determined by isovolumetric phases, I simulate only the ejection phase with both schemes, by providing as initial condition the solution of the GE-M scheme at time $t_0 = 88\,\text{ms}$ (corresponding to the end of the IVC). Table 3.6 reports the resulting indicators, and Figure 3.19 shows the corresponding volume and pressure over time. The ejection-only simulation yields a better agreement between the GE-M and GE-E schemes. This suggests the possibility of exploring adaptive methods that adjust e.g. the number of RN subiterations depending on the simulated heartbeat phases.

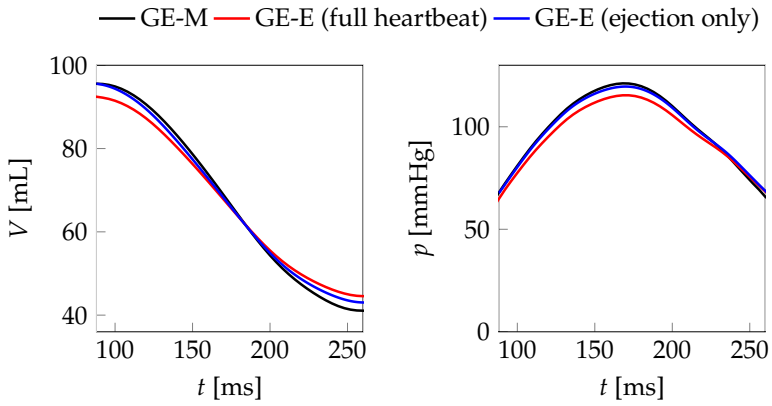

Figure 3.19: Strong and loose FSI coupling (Section 3.5). Ventricular volume and average pressure with the GE-M and GE-E schemes during the ejection phase.

3.5.4 Efficiency of the loosely coupled scheme

The chief advantage of a loosely coupled scheme is its computational efficiency if compared to a method where the FSI coupling is treated implicitly. To verify this, I perform numerical simulations of the GE-M, GE-E and GE-P-RN2 schemes with three differently refined meshes $\mathcal{M}_1$, $\mathcal{M}_2$ and $\mathcal{M}_3$, detailed in Table 3.2. Then, I compare the total wall time, the portion of wall time devoted to the assembly of fluid and structure systems, as well as the wall time spent in the solution of the fluid, structure or FSI systems. Computational times associated to electrophysiology, force generation and fluid domain displacement are not considered in the comparison, since the three schemes are identical in those steps. These simulations ran in parallel using 44 cores with Intel Xeon Platinum 8160@2.1GHz processors.

Results are reported in Figure 3.20. The GE-E scheme allows for a very significant reduction in computational time with respect to the GE-M one. This reduction becomes more significant as the mesh is refined: the total wall time for the simulation on the finest mesh $\mathcal{M}_3$ using the GE-E scheme is approximately 45 % less than the corresponding simulation using the GE-M scheme. In particular, the cost associated to both the assembly and the solution of the linear systems for the FSI problem is much smaller in the GE-E scheme than it is in the GE-M. Overall, the GE-E scheme allows for a significant saving in computational time with respect to the GE-M

Scheme	EF [%]	$p_{\max}$ [mmHg]
GE-M	57.0	121.2
GE-E	54.4	119.6
GE-E (full heartbeat)	53.4	115.4

Table 3.6: Strong and loose FSI coupling (Section 3.5). Ejection fraction and peak systolic pressure in the ejection phase test, for the GE-M and GE-E schemes. For comparison, the table reports the same quantities computed in the full heartbeat test with the GE-E scheme. In both cases, the Robin coefficient is set to $\alpha = 5000\,\mathrm{kg}/(\mathrm{m}^2 \cdot \mathrm{s})$.

one. Conversely, the GE-P-RN2 requires a computational time similar to that of the GE-M scheme.

3.5.5 A realistic test case for the left ventricle

Finally, I present in this section a test case in a more realistic setting to showcase the effectiveness of the proposed schemes. Let us consider the left ventricle from the heart model provided by Zygote Media Group [365], represented in Figure 3.21. The model includes ventricular inflow and outflow tracts, modeled as electrically and mechanically passive, using the neo-Hooke constitutive law. The domain is discretized with a tetrahedral mesh $\mathcal{M}_{\mathrm{R}}$ (see Table 3.2). To deal with the higher accuracy requirements of electrophysiology, quadratic finite elements are used for its discretization. This is an alternative approach to the one used in previous sections, based on nested mesh refinements. Indeed, quadratic elements can provide improved accuracy with a lower number of degrees of freedom, with respect to linear elements, for cardiac electrophysiology [3]. The time step is set to $\Delta t = 0.2\,\mathrm{ms}$.

The ventricular pressure and volume over time for this test case are reported in Figure 3.22, while the corresponding indicators are in Table 3.7. Figure 3.23 shows some snapshots of the electrophysiology solution, while Figure 3.24 reports a comparison of domain deformation and fluid dynamics variables using the GE-M and GE-E schemes. These results highlight once again that the GE-E scheme yields stable results, and in qualitative

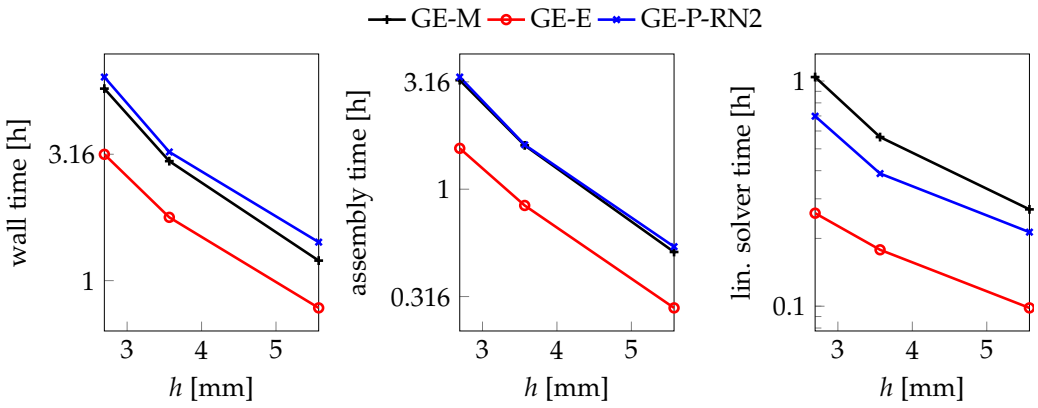

Figure 3.20: Strong and loose FSI coupling (Section 3.5). From left to right, total wall time, assembly time and linear solver time for the GE-M, GE-E and GE-P-RN2 schemes, against the average mesh size h.

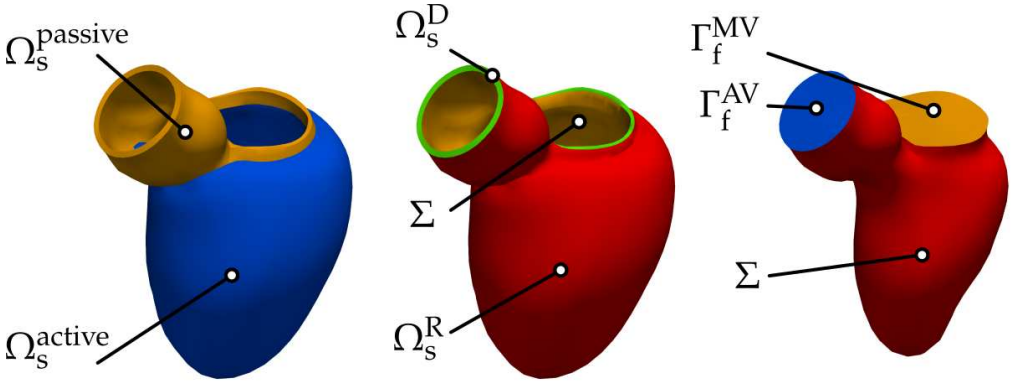

Figure 3.21: Strong and loose FSI coupling on a realistic ventricle (Section 3.5.5). Computational fluid and solid domains. Colors denote the different volumetric and boundary portions.

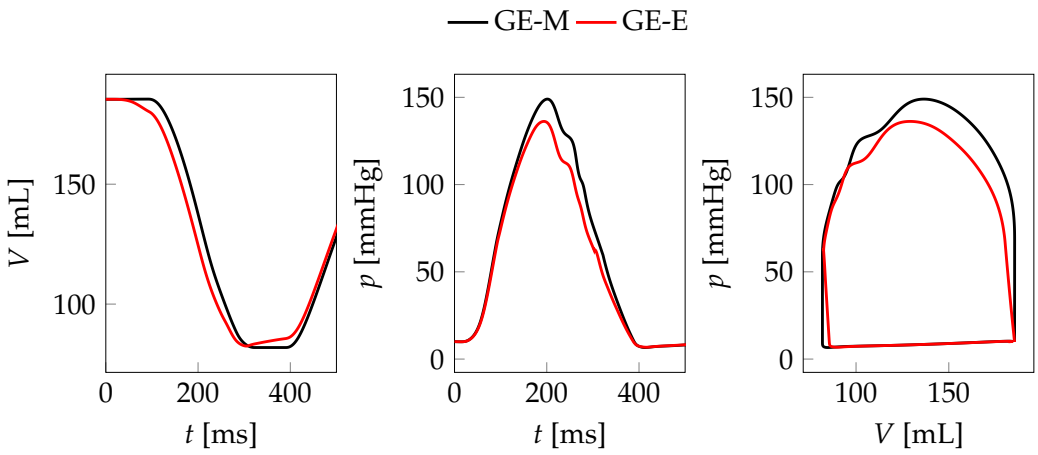

Figure 3.22: Strong and loose FSI coupling on a realistic ventricle (Section 3.5.5). From left to right, ventricular volume, average pressure and pressure volume loop with the GE-M scheme and the GE-E scheme.

agreement with those of the GE-M scheme, even if the GE-E scheme introduces an additional error that is mostly evident during isovolumetric phases: overall, the conclusions drawn in the idealized benchmark are confirmed in this geometrically realistic setting.

3.5.6 Discussion

The numerical tests of the previous sections indicate that the loosely coupled GE-E scheme is stable in the physiological regime, provided that the Robin coefficient α is small enough. However, the scheme generates an approximation error in the interface conditions, that leads to a loss of blood volume through the fluid-solid interface. This is particularly relevant during isovolumetric phases, that significantly influence the solution during other phases.

On the other hand, the GE-E scheme is significantly more computationally efficient than the GE-M. The computational saving becomes more evident as the mesh is refined, with savings up to 45 % in total wall time. Overall, the GE-E scheme is an effective algorithm for the simulation of cardiac FSI, allowing to strike a compromise between accuracy and efficiency.

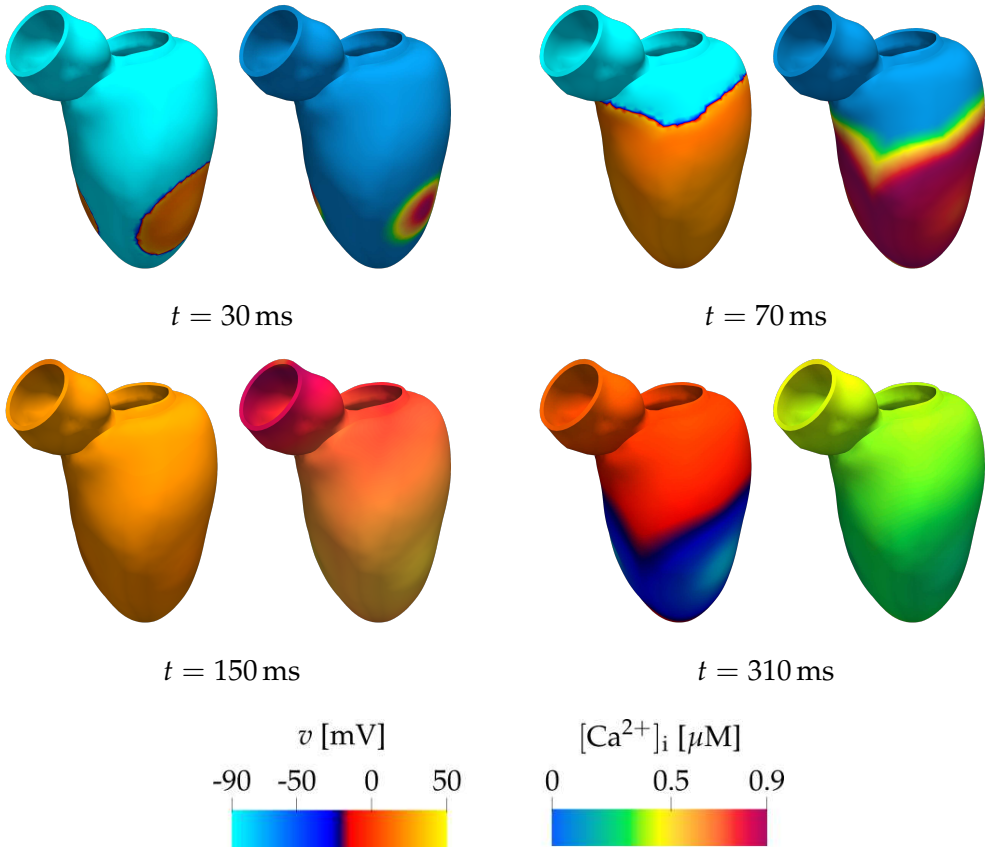

Figure 3.23: Strong and loose FSI coupling on a realistic ventricle (Section 3.5.5). Snapshots of the electrophysiology solution, computed using the GE-E scheme.

Scheme	$\mathrm{ILI_C}$ [%]	$\mathrm{ILI_R}$ [%]	EF [%]	$p_{\max}$ [mmHg]
GE-M	0.04	0.00	55.8	148.9
GE-E	2.76	3.60	55.5	136.2

Table 3.7: Strong and loose FSI coupling on a realistic ventricle (Section 3.5.5). Isovolumetric loss indicators, ejection fraction and peak systolic pressure for the realistic test case, using the GE-M and GE-E schemes, with $\alpha = 5000\,\mathrm{kg}/(\mathrm{m}^2 \cdot \mathrm{s})$.

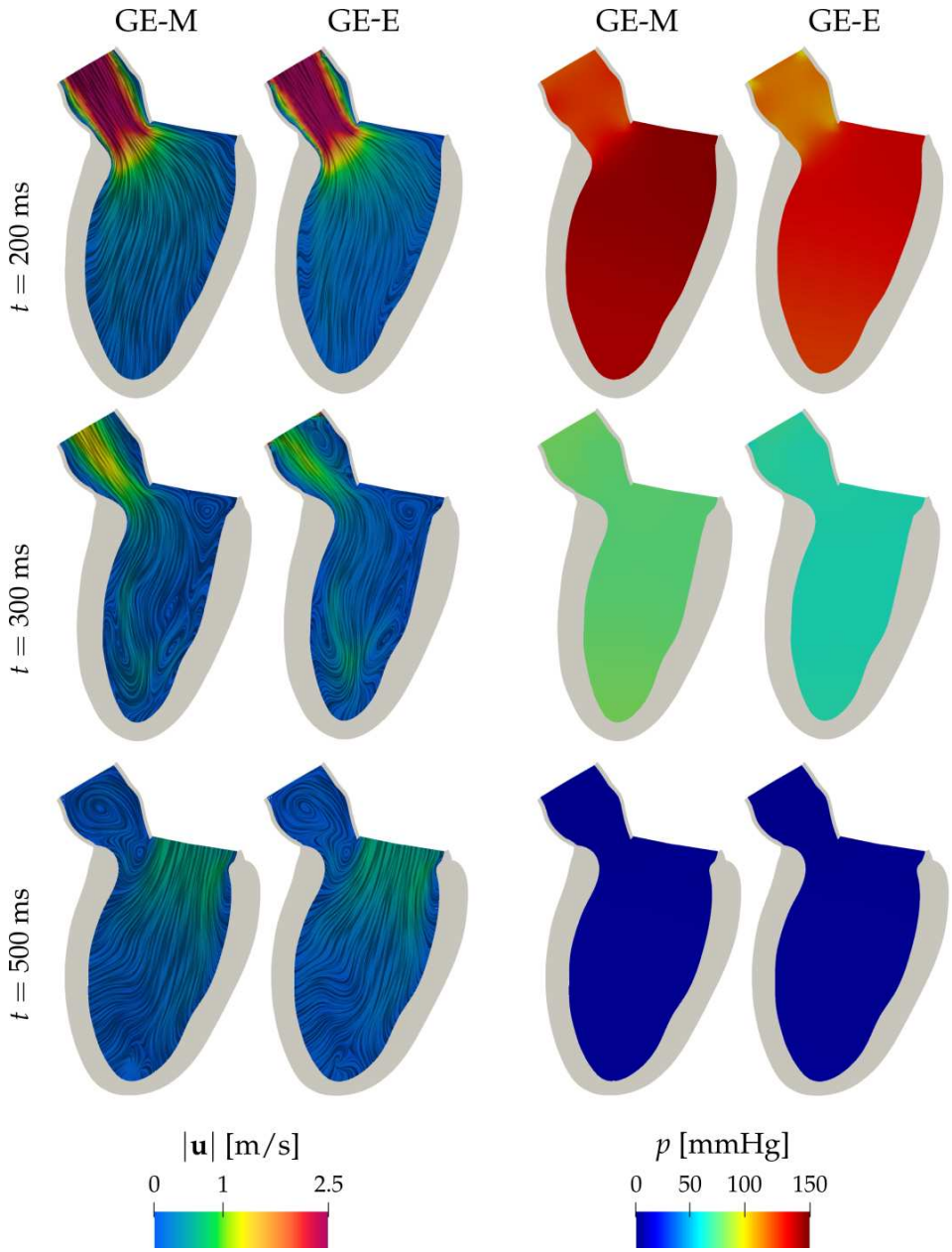

Figure 3.24: Strong and loose FSI coupling on a realistic ventricle (Section 3.5.5). Fluid velocity magnitude $|\mathbf{u}|$ (left) and pressure p (right) at three time instants, computed with the GE-M and GE-E schemes. The domain is warped according to $\mathbf{d}$ and $\mathbf{d}_{\text{ALE}}$.

Nonetheless, both these tests and those presented in Section 3.4 show how the GE-M approach balances the computational efficiency with robustness and accuracy. Therefore, it will be the scheme of choice in the following chapters.

Chapter 4

An integrated model of the left heart

In this chapter, I present the numerical results of the EMF simulation of a realistic, healthy human LH model, and I compare the simulation results against normal ranges for several physiological indicators of the cardiac function. The results show that our EMF model is capable of reproducing the behavior of a healthy heart.

The results presented in this chapter have been published in [53].

4.1 Setup of the test case

Let us consider the Zygote human heart model [365], representing the heart of an average 21-year-old male. Geometric preprocessing and mesh generation were done using the algorithms presented in [109] and implemented in the software library `VMTK` [352]. For this test case, the LA, LV, AA and mitral and aortic valves are considered. The resulting mesh is represented in Figure 4.1a, while details on mesh size and number of elements can be found in Table 4.1. The mesh resolution varies in space, and it is finer near the immersed surfaces, to better capture their presence [107].

The mesh used for the endocardial surface does not represent the complex structure of trabeculations and papillary muscles that characterize the interior of the left ventricle in human hearts [121]. This has only minor

	h_{min}[mm]	h_{avg}[mm]	h_{max}[mm]	**# elem.**	**# nodes**
fluid	0.51	1.6	4.7	790 533	137 504
solid	0.59	2.1	5.7	234 132	63 834

Table 4.1: Minimum, average and maximum mesh element diameter, number of elements and number of nodes used for the spatial discretization of the realistic left heart domain (Chapter 4).

implications in terms of overall ventricular pressure and volume. Therefore, it is a generally accepted approximation in CFD models of the heart [67, 178, 364], although these structures should be included if accurate evaluations of wall stresses or fine scale vortical structures are of interest [195, 290, 339].

Both the fluid and the solid domains are partitioned into subdomains corresponding to the LA, the atrioventricular ring (i.e. the region corresponding to MV and AV), the LV and the AA. They are denoted by $\widehat{\Omega}_i^{\text{LA}}$, $\widehat{\Omega}_i^{\text{ring}}$, $\widehat{\Omega}_i^{\text{LV}}$ and $\widehat{\Omega}_i^{\text{AA}}$, respectively, where $i \in \{f, s\}$ denotes the fluid and solid domains. The domain is clipped at the inlet sections representing pulmonary veins and at the outlet section on the AA. The partition and the boundary portions are shown in Figure 4.2.

There holds $\widehat{\Omega}_s^{\text{active}} = \widehat{\Omega}_s^{\text{LV}}$, while all other subdomains are regarded as passive, both electrically and mechanically. This is a simplification for what concerns the left atrium, and it prevents from capturing certain features related to atrial contraction, such as the after-wave, that have a significant impact on the cardiac function [108]. However, including the atrium, albeit as a passive medium, allows to account for its inertial and elastic effects, that are hardly surrogated by means of ad-hoc boundary conditions [297]. A test case in which atria are regarded as active is discussed in Chapter 5. Since only the ventricle is electrically active, the TTP06 ionic model is used.

Fibers are generated by combining the ventricular rule-based algorithm of [28] with the atrial one of [258]. The tissues of both atrium and ventricle are modeled with the Guccione constitutive law (2.7), while the atrioventricular ring and the AA are modeled using a stiff neo-Hooke constitutive law (2.8). Material interface regularization (as described in Section 2.4.1) is present between $\widehat{\Omega}^{\text{LA}}$ and $\widehat{\Omega}^{\text{ring}}$ and between $\widehat{\Omega}^{\text{LV}}$ and $\widehat{\Omega}^{\text{ring}}$, to smooth out

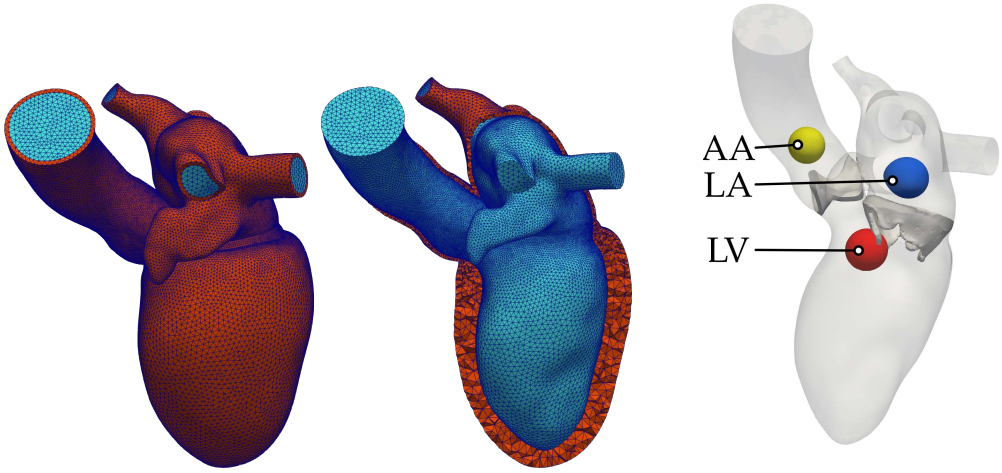

Figure 4.1: Realistic LH test case. (a) Computational mesh used for the solid (red) and the fluid (blue) domains. (b) Spherical control volumes used in estimating the average pressures within each chamber. Average pressure within control volumes is also used to trigger the opening and closing of valves.

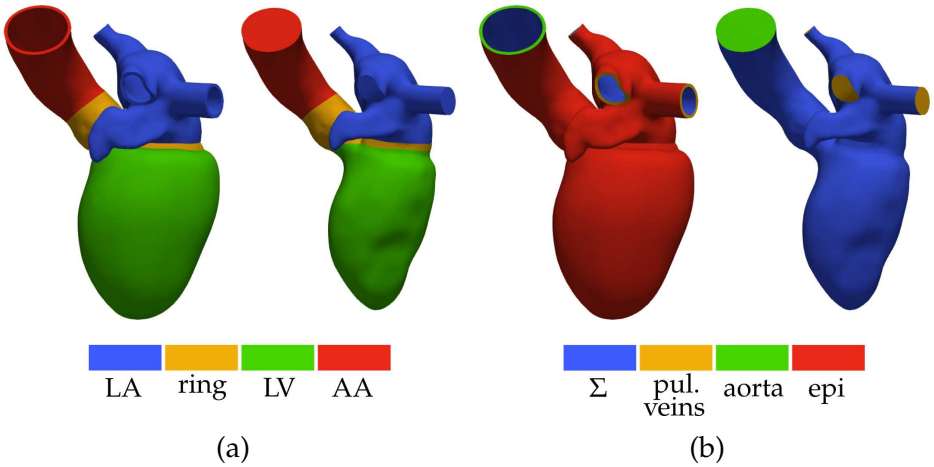

Figure 4.2: Realistic LH test case. (a) Partition of the solid and fluid domain into the subdomains for LA, atrioventricular ring, LV and AA. (b) Partition of the boundary of the fluid and solid domains.

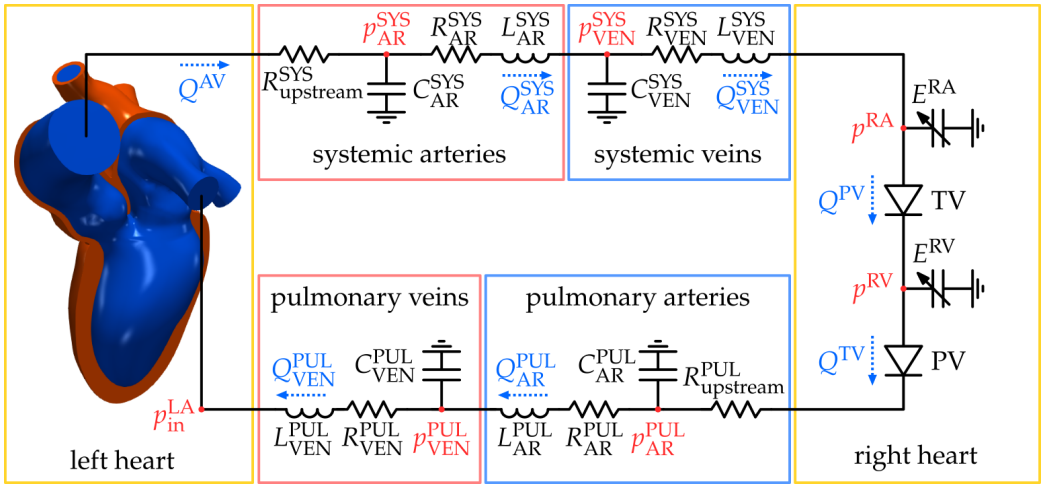

Figure 4.3: Representation through a circuital analogy of the 0D circulation model, coupled to a 3D model of the LH.

the transition between the Guccione constitutive and neo-Hooke models. Active contraction is modeled with the RDQ20-MF model. MV and AV are included by means of the RIIS model (Section 2.5.3). The fluid domain displacement is computed using the non-linear operator (2.13). While its computational cost is small but not negligible, I found that less expensive operators such as the harmonic or linear elastic one frequently lead to mesh element inversion and solver breakdown, whereas the chosen non-linear operator has proven to be significantly more robust with respect to deformations. Finally, Navier-Stokes equations are stabilized with the VMS-LES approach to stabilization and turbulence modeling.

At inlet and outlet sections, the fluid domain model is coupled with the circulatory system as shown in Figure 4.3: the equations for p^{LA}, p^{LV}, V^{LA}, V^{LV}, Q^{MV}, Q^{AV}, Q^{PUL}_{VEN} are removed from the circulation model, and

replaced with the following coupling conditions:

$$\begin{cases} \sigma_f(\mathbf{u},p)\mathbf{n} = -p^{\mathrm{LA}}(t)_{\mathrm{in}}\mathbf{n} & \text{on } \Gamma_{\text{pul. ven.}}\,, \\ \sigma_f(\mathbf{u},p)\mathbf{n} = -\left(p^{\mathrm{SYS}}_{\mathrm{AR}}(t) + R^{\mathrm{SYS}}_{\mathrm{upstream}}Q^{\mathrm{AV}}(t)\right)\mathbf{n} & \text{on } \Gamma_{\text{aorta}}\,, \\ Q^{\mathrm{PUL}}_{\mathrm{VEN}}(t) = -\displaystyle\int_{\Gamma_{\text{pul. ven.}}} (\mathbf{u}-\mathbf{u}_{\mathrm{ALE}})\cdot\mathbf{n}d\gamma\,, \\ Q_{\mathrm{AV}}(t) = \displaystyle\int_{\Gamma_{\text{aorta}}} (\mathbf{u}-\mathbf{u}_{\mathrm{ALE}})\cdot\mathbf{n}d\gamma\,. \end{cases} \tag{4.1}$$

I set the duration of a heartbeat to $T_{\mathrm{hb}} = 800\,\mathrm{ms}$, and I simulate three heartbeats setting $T = 3T_{\mathrm{hb}}$. In the analysis that follows, I focus on the third heartbeat (starting at $t_0 = 2T_{\mathrm{hb}}$) to reduce the influence of initial conditions. In what follows, $t_{\mathrm{hb}} = t - t_0$ denotes the time relative to the third heartbeat.

I rely on the staggered scheme for EMF presented in Section 3.1, solving the FSI subproblem with the GE-M scheme (Section 3.2.4). The time step is set to $\Delta t = 0.2\,\mathrm{ms}$, with $N_{\mathrm{EP}} = 2$ and $\Delta t_{\mathrm{EP}} = 0.1\,\mathrm{ms}$. Finally, the electrophysiology problem is discretized in space with piecewise quadratic finite elements (whereas all other models use piecewise linear finite elements).

The values of the parameters used for this simulation are reported in Appendix B.3.

4.2 Simulation results

The simulation was run using 192 parallel processes on the GALILEO100 cluster[1] at the CINECA high-performance computing center (Italy). For each heartbeat, the simulation takes approximately 21 h of wall time, of which approximately 92 % is spent assembling and solving the FSI problem with the GE-M scheme (Section 3.2.4), including 6 % assembling and solving the fluid domain displacement problem, and 2 % assembling and solving the electrophysiology problem. The solution of the RDQ20-MF force generation model takes only around 0.2 % of the total time.

[1]Refer to the website https://wiki.u-gov.it/confluence/display/SCAIUS/UG3.3%3A+GALILEO100+UserGuide for technical specifications (last accessed: 23 September 2022).

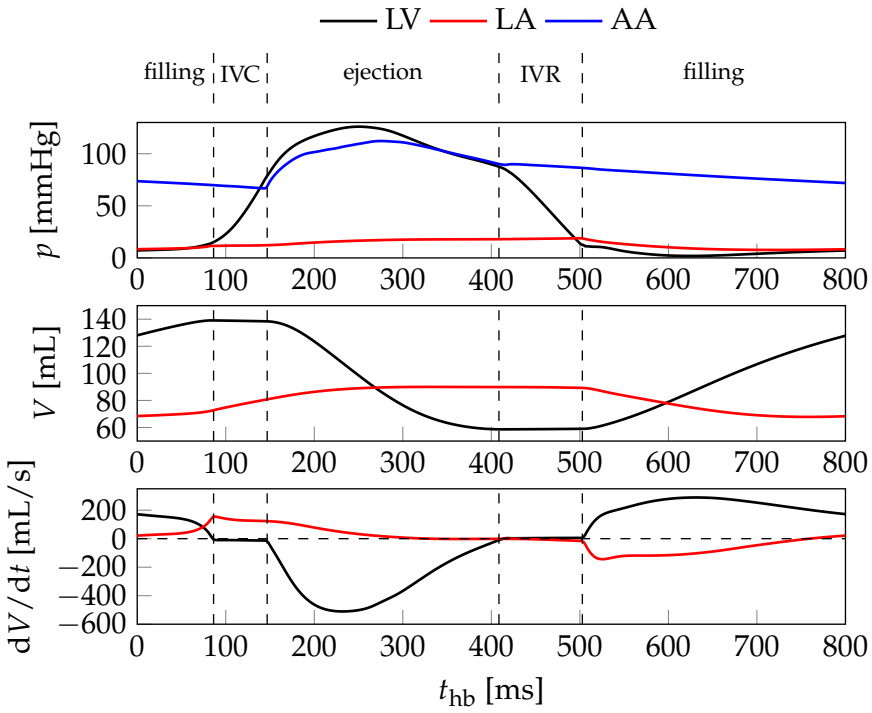

Figure 4.4: Realistic LH test case. Evolution, over the third simulated heartbeat, of the pressure p, volume V and volume derivative $\mathrm{d}V/\mathrm{d}t$ for the left heart compartments. Vertical dashed lines separate heartbeat phases, labelled on the top.

For post-processing, the average pressure of each fluid compartment (LA, LV, AA) is computed by averaging the pressure inside a spherical control volume within that compartment (see Figure 4.1b). Figure 4.4 reports the average pressure, volume and volume derivative over time of each the compartments, while Figure 4.5 shows the corresponding pressure-volume loops, and Figure 4.6 reports the evolution in time of the valve opening coefficients.

Table 4.2 collects some quantitative indicators for the heart function, comparing the values obtained by the simulation with data from the medical literature. The numerical results are consistent with the clinically measured ranges. In the clinical practice, most of the indicators reported in Table 4.2 are usually normalized with respect to the *body surface area* (BSA)

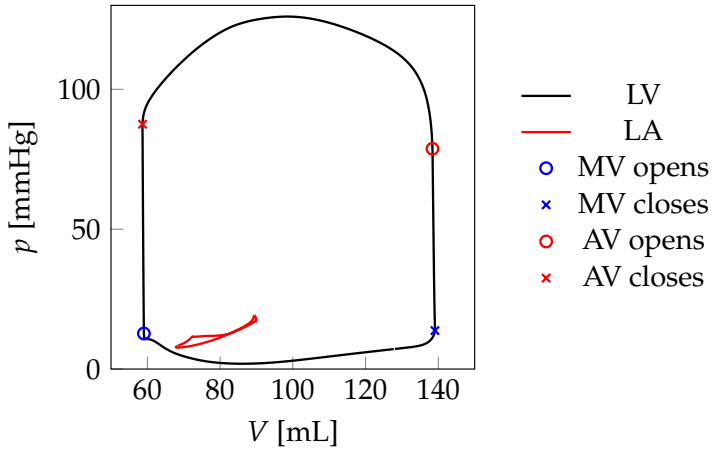

Figure 4.5: Realistic LH test case. Pressure-volume loops of left ventricle and atrium, with marks indicating valve opening and closing.

[340], to filter out the variability in size among individuals. However, as mentioned before, the heart model considered in this work is an average of several individuals, and no reference BSA is available. Therefore, absolute values (i.e. not normalized) are reported.

Figures 4.7, 4.9 to 4.13, 4.16 and 4.17 show several snapshots of the numerical solutions for all of the solution variables. In the following sections, I provide details on the simulation results for each of the heartbeat phases (identified by the plots in Figures 4.4 and 4.6).

4.2.1 Electrophysiology

Figure 4.7 reports snapshots of the electrophysiology solution over time, while Figure 4.8 reports the activation time, i.e. the time of maximum transmembrane potential upstroke:

$$t_{\text{act}} = \underset{t_{\text{hb}} \in (0, T_{\text{hb}})}{\arg\max} \frac{\partial v}{\partial t}(t_{\text{hb}}) \, . \tag{4.2}$$

The stimulus, initially applied at three points on the endocardium, propagates to the whole ventricle, which becomes completely activated within 90 ms. The rapid depolarization phase is followed by the long plateau

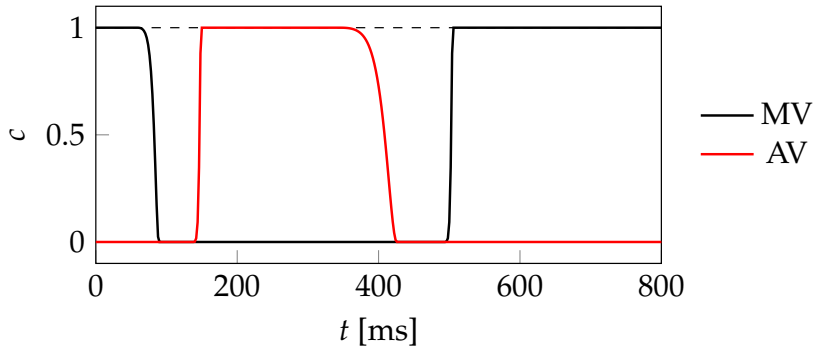

Figure 4.6: Realistic LH test case. Opening coefficients $c_k(t)$ over time for the MV and AV. The values 0 and 1 correspond to the closed and open configurations respectively.

Indicator		Sim.	Normal values		Description
EDV^{LV}	[mL]	139.1	126 to 208	[208]	LV end-diastolic volume
ESV^{LV}	[mL]	58.6	35 to 80	[208]	LV end-systolic volume
SV^{LV}	[mL]	80.4	81 to 137	[208]	LV stroke volume
EF^{LV}	[%]	57.8	57 to 74	[208]	LV ejection fraction
CO^{LV}	[L/min]	6.0	6.98 ± 1.50	[358]	LV cardiac output
p^{LV}_{max}	[mmHg]	126.0	119 ± 13	[312]	peak LV pressure
Q^{AV}_{max}	[mL/s]	510.0	427 ± 129	[146]	peak AV flow rate
T^{LV}_{IVC}	[ms]	64.2	51 to 90	[104]	IVC phase duration
T^{LV}_{ej}	[ms]	261.0	230 to 334	[104]	ejection phase duration
T^{LV}_{IVR}	[ms]	94.2	50 to 140	[32]	IVR phase duration
T^{LV}_{fil}	[ms]	379.0	280 to 472	[201]	filling phase duration
LFS	[%]	17.8	13 to 21	[102]	LV longitudinal shortening

Table 4.2: Realistic LH test case. Values of physiological indicators computed from simulation results ("Sim." column), and associated normal values from the medical literature. In the "Normal values" column, either normal ranges or mean $\pm$ standard deviation are reported.

phase, which spans most of the systole. The ventricle begins repolarizing around $t_{\text{hb}} = 250\,\text{ms}$, and by $t_{\text{hb}} = 400\,\text{ms}$ it has recovered its resting potential. This timing is consistent with medical observations [98].

Intracellular calcium concentration follows a similar evolution (Figure 4.9): the stimulus leads initially to an increase in calcium concentration, that causes the contraction, and is followed by a decrease of calcium concentration until the resting value is recovered.

4.2.2 Isovolumetric contraction

The simulated heartbeat starts from the end of the diastolic filling phase, with the MV open and the AV closed (Figure 4.4). The increase of intracellular calcium concentration (Figure 4.9) determines the generation of contractile force within the ventricular wall (Figure 4.10). Intraventricular pressure rises (Figure 4.13), triggering the closure of the MV. When the valve is closed ($t_{\text{hb}} = 89\,\text{ms}$), the ventricular volume is $\text{EDV}^{\text{LV}} = 139\,\text{mL}$.

At this point, the IVC phase starts: both valves are closed, and the ventricular pressure increases rapidly (Figures 4.4 and 4.13) while the volume is maintained approximately constant. The proposed model does not capture exactly the conservation of ventricular blood volume during this phase, due to the explicit discretization of the fluid domain displacement and to the use of the resistive model for valves, which allows for a little flow through the immersed surfaces. Nonetheless, during isovolumetric contraction the maximum volume variation equals 0.7 mL, corresponding to 0.5 % of EDV^{LV}. I deem this mismatch to be acceptable, in accordance with similar spurious variations observed in the cardiac modeling literature [348].

During the IVC, the ventricle undergoes a small deformation (at constant volume), with its shape becoming slightly more spherical (Figures 4.10 and 4.11), as described in [147, 180].

The IVC phase lasts for $T_{\text{IVC}} = 64.2\,\text{ms}$, consistently with physiological behavior [104, 110]. When the pressure in the ventricle becomes larger than the pressure in the aorta, the opening of the AV is triggered and the ejection phase starts.

The possibility of including isovolumetric phases in a three-dimensional hemodynamics model is distinctive of FSI [50], as those phases cannot

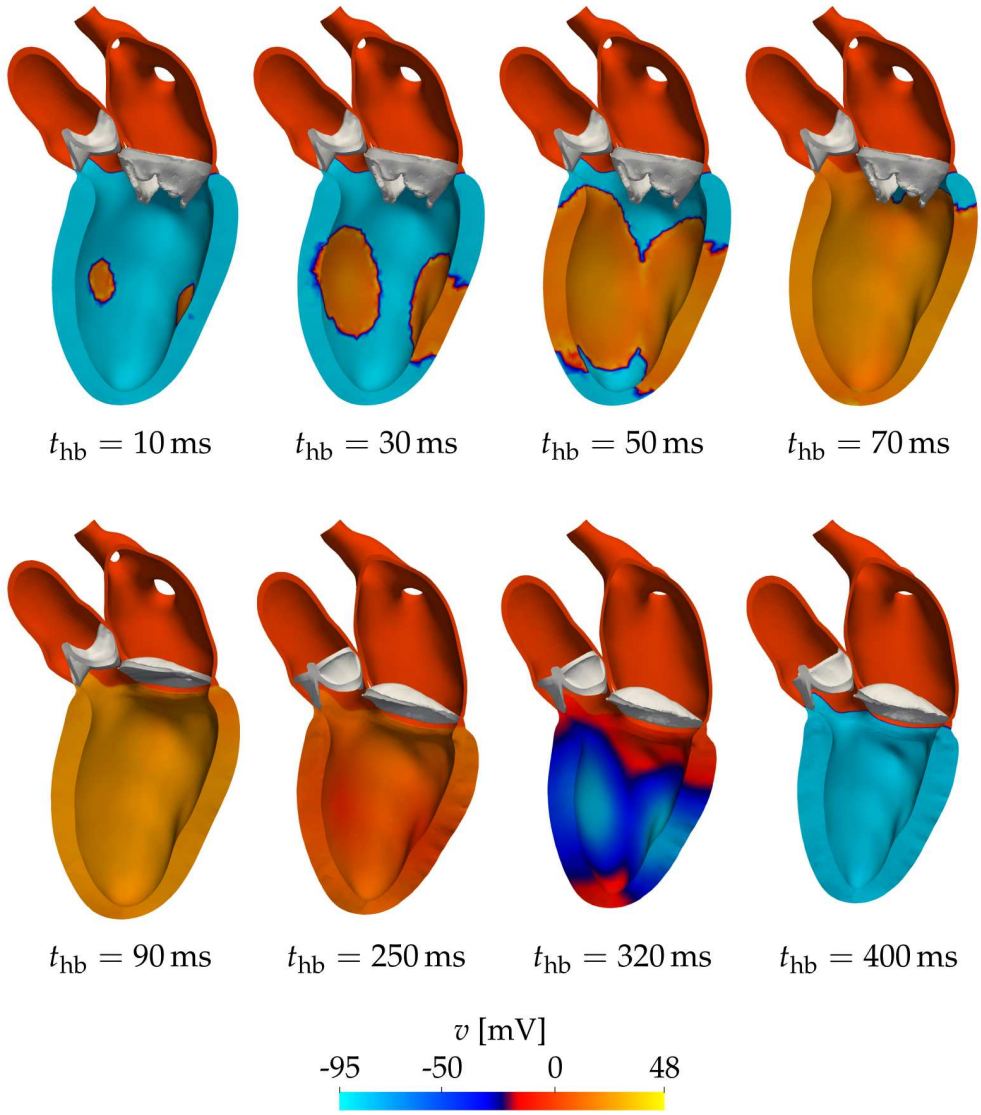

Figure 4.7: Realistic LH model. Time evolution of the transmembrane potential v as seen through a long-axis section. The domain is warped according to **d**.

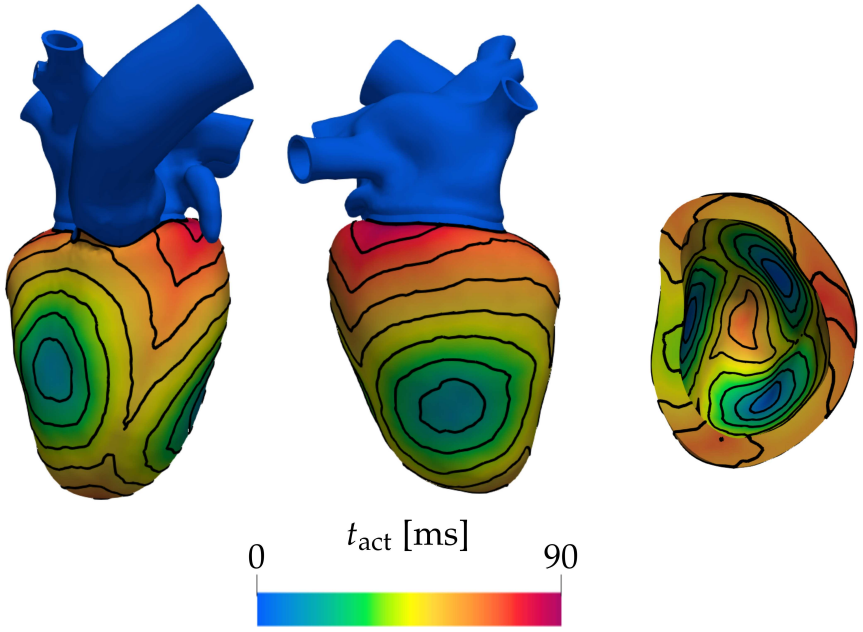

Figure 4.8: Realistic LH test case. Contour plot of the activation time t_{act} over the LV. The domain is shown in its reference configuration $\widehat{\Omega}_s$.

be represented by electromechanics-driven CFD models [364]. Indeed, in a standalone CFD model, this would require prescribing a Dirichlet datum on the whole boundary of the ventricular chamber. This might be incompatible with the assumption of blood incompressibility. Moreover, even if the compatibility is satisfied, the ventricular pressure is not uniquely defined [261]. The resistive approach is not a strict Dirichlet condition, so that the previous argument holds only in a qualitative sense. Nonetheless, very sharp unphysical oscillations are generally observed in the ventricular pressure when trying to simulate isovolumetric phases with CFD models [362]. While it is possible to introduce ad-hoc corrections to circumvent this issue [326, 362], these only have a limited effectiveness in preventing the oscillations. Conversely, with an FSI modeling approach the velocity on the fluid-solid interface is an unknown of the problem, and as such it is determined accounting for the incompressibility constraint. On top of that, FSI interface conditions include a condition on stress, so that the ventricular pressure is uniquely defined.

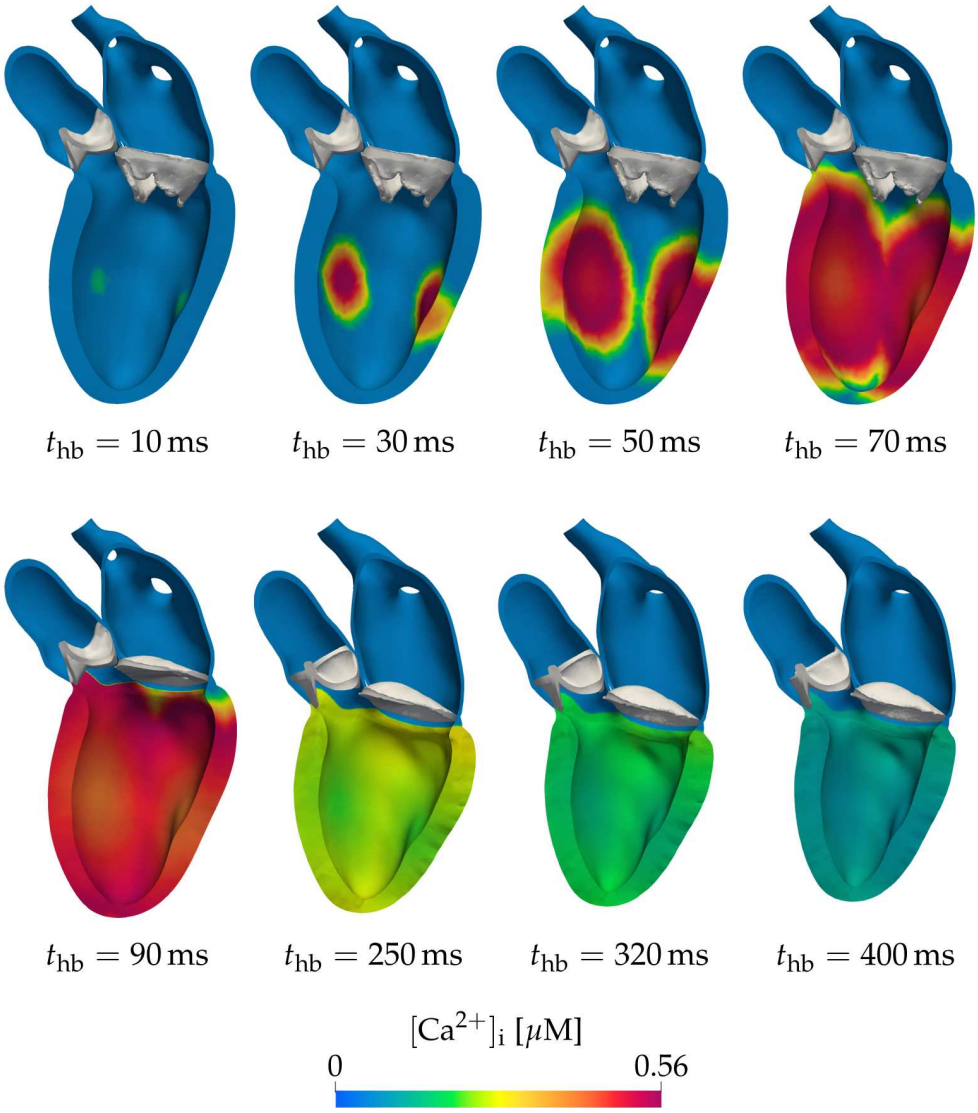

Figure 4.9: Realistic LH model. Time evolution of the intracellular calcium concentration $[Ca^{2+}]_i$ as seen through a long-axis section. The domain is warped according to **d**.

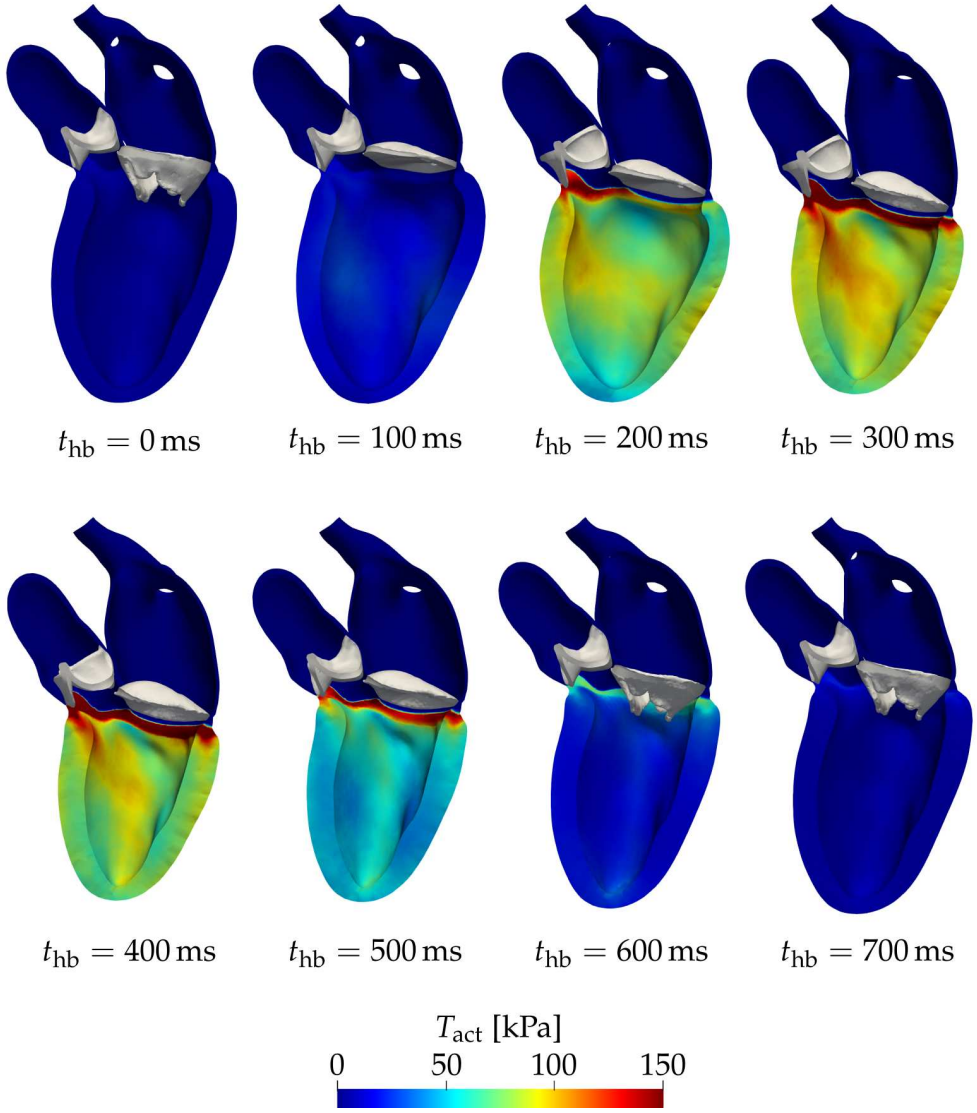

Figure 4.10: Realistic LH model. Time evolution of the active contraction T_{act} as seen through a long-axis section. The domain is warped according to **d**.

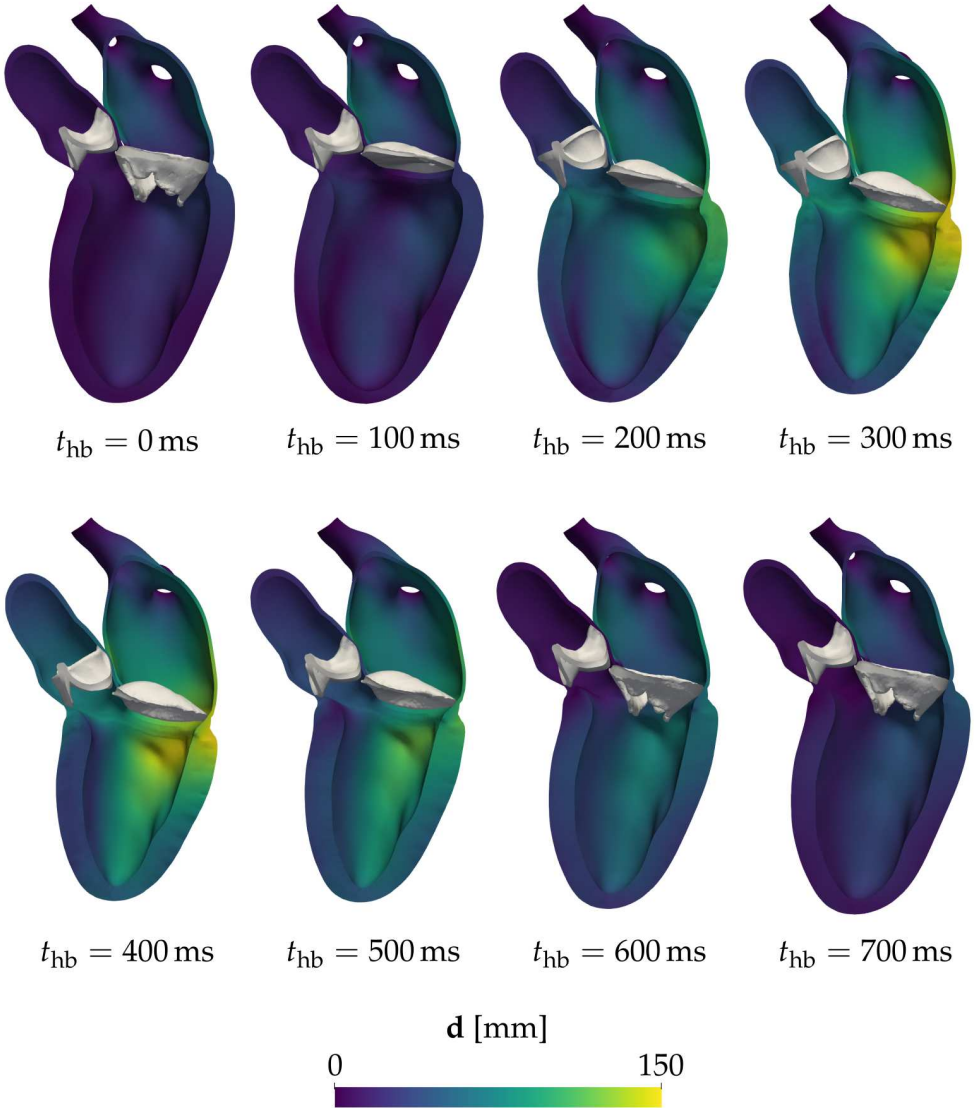

Figure 4.11: Realistic LH model. Time evolution of the solid displacement magnitude $|\mathbf{d}|$ seen through a long-axis section. The domain is warped according to $\mathbf{d}$.

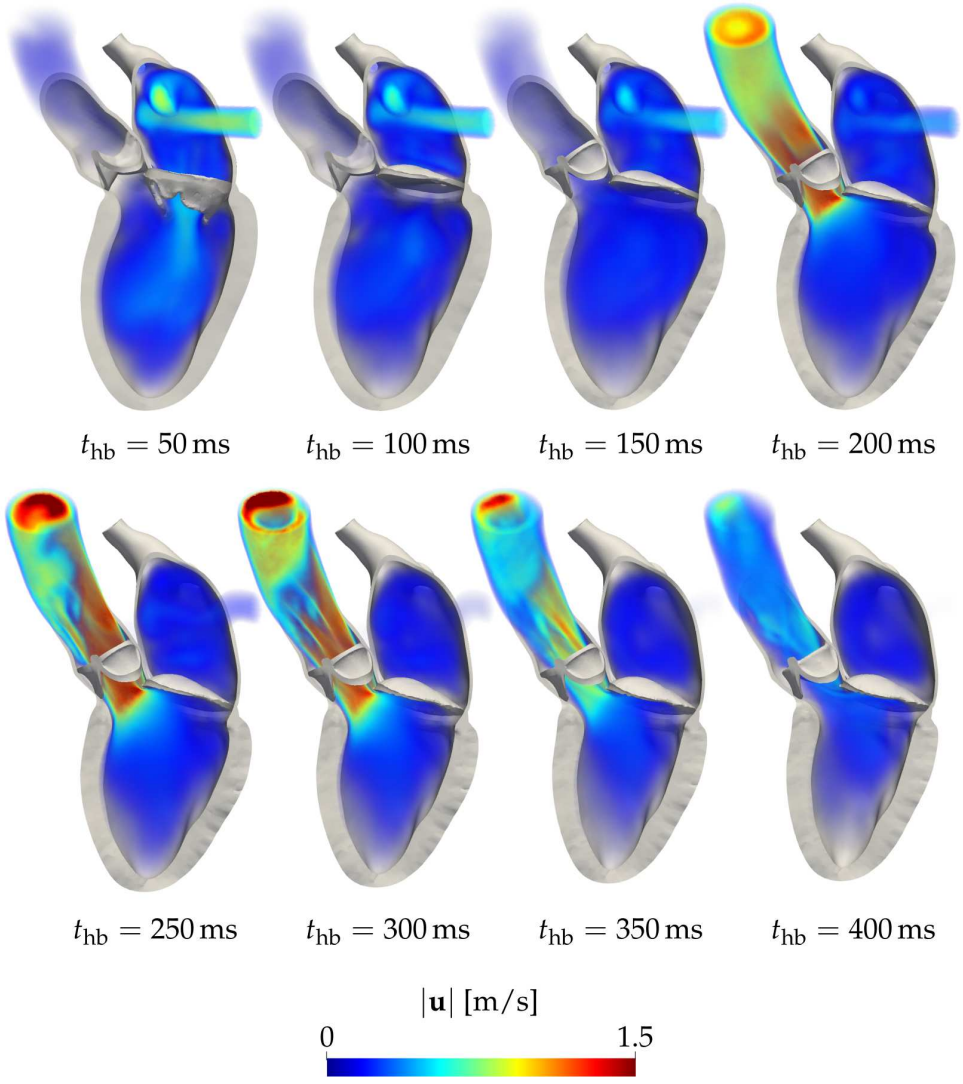

Figure 4.12: Realistic LH model. Volume rendering of the velocity magnitude $|\mathbf{u}|$, for the IVC and ejection phases. The domain is warped according to $\mathbf{d}$ and $\mathbf{d}_{\text{ALE}}$.

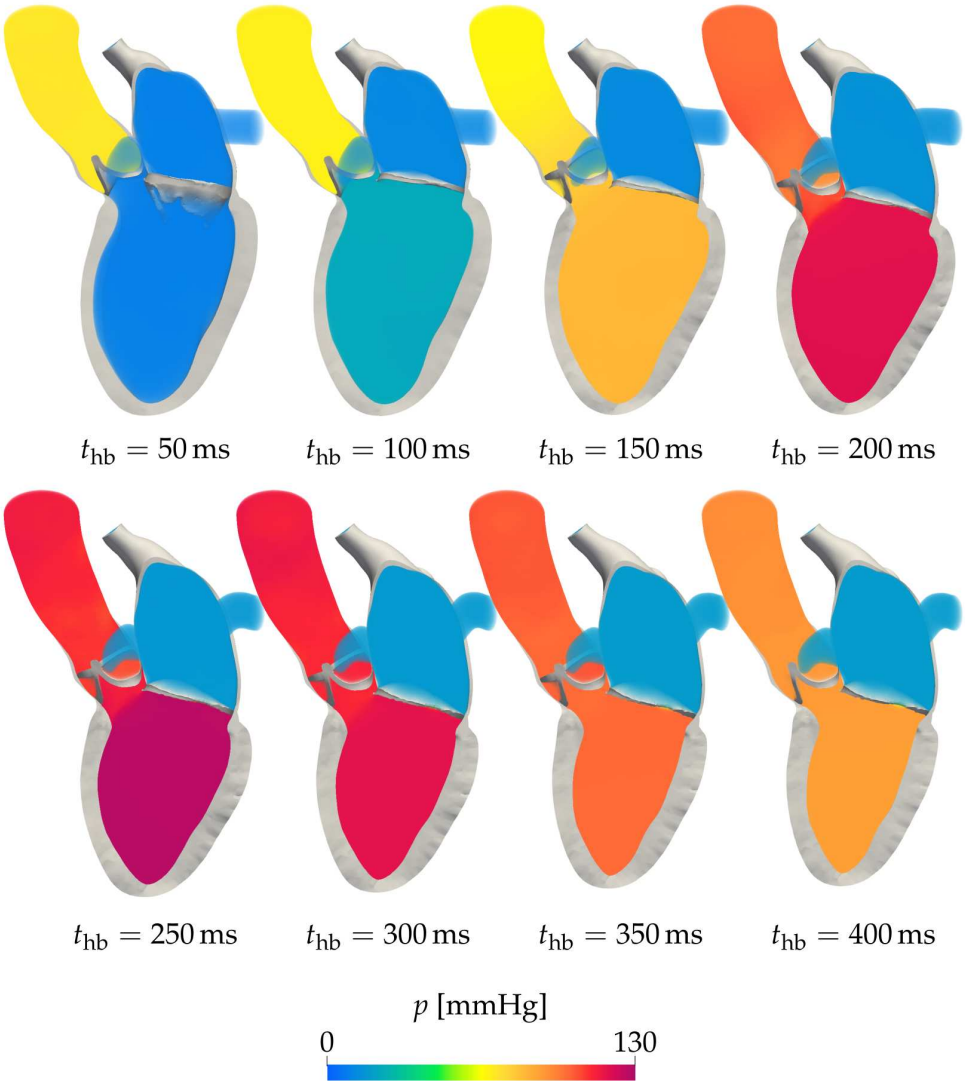

Figure 4.13: Realistic LH model. Volume rendering of the pressure p, for the IVC and ejection phases. The domain is warped according to $\mathbf{d}$ and $\mathbf{d}_{\text{ALE}}$.

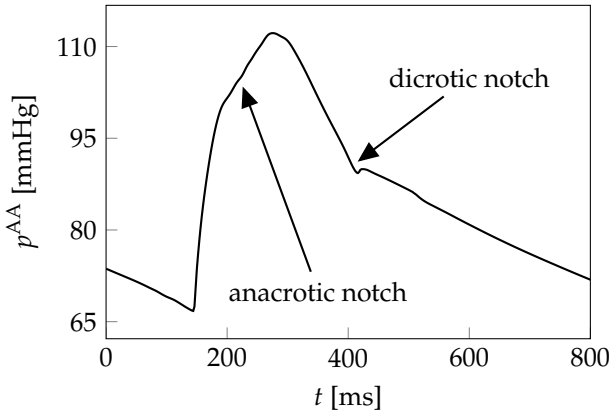

Figure 4.14: Average pressure in the AA over time. Notice the presence of the anacrotic notch during the systolic upstroke and of the dicrotic notch, or incisure, at the closing time of the AV.

4.2.3 Ejection

Blood is ejected from the ventricle into the aorta (Figure 4.12). The maximum flow rate through the AV orifice is attained at time $t_{\text{hb}} = 231\,\text{ms}$ and it equals $Q^{\text{AV}}_{\text{max}} = 510\,\text{mL/s}$, consistently with physiology [144, 146]. It corresponds to an average velocity magnitude $|\mathbf{u}|^{\text{AV}}_{\text{max}} = 1.46\,\text{m/s}$ on the AV section. The jet through the aortic valve is unsteady during all the ejection, consistently with the transitional nature of the flow (Figure 4.12). At the end of the ejection phase, the left ventricular volume equals $\text{ESV}^{\text{LV}} = 58.6\,\text{mL}$, so that $\text{SV} = 80.4\,\text{mL}$ and $\text{EF} = 57.8\,\%$, corresponding to a *cardiac output* (CO) of

$$\text{CO} = \frac{\text{SV}}{T_{\text{hb}}} = 100.5\,\text{mL/s} = 6\,\text{L/min}\,.$$

All these quantities are within normal physiological ranges (Table 4.2) [70, 110, 188, 208, 303].

During the ejection phase, the ventricular pressure increases until $t_{\text{hb}} = 250\,\text{ms}$, reaching a peak value of $p^{\text{LV}}_{\text{max}} = 126\,\text{mmHg}$ (Figure 4.4), within the physiological ranges [180, 312]. After that, pressure starts decreasing until it falls below the aortic pressure, at which point the AV starts closing.

A similar evolution characterizes the pressure in the ascending aorta, reported in Figure 4.14: starting from an end-diastolic value of 68 mmHg,

it reaches a peak at 112 mmHg and then declines until the next heartbeat. The pressure values are smaller than physiological ones [210], and there is a large pressure jump between the ventricle and the aorta, which is a common issue in the cardiovascular modeling literature when hemodynamics is considered [22, 348]. However, the time profile of the aortic pressure is remarkably similar to the ones obtained from in-vivo measurements [210, 224]. In particular, it features the *anacrotic notch*, resulting from the interaction of the forward and reflected pressure waves [224]. This effect is captured thanks to the FSI modeling framework, which, contrary to standalone CFD models, allows to obtain traveling pressure waves. The aortic pressure also features the *dicrotic notch* [180, 210, 303] corresponding to the AV closure. The dicroctic notch is an important landmark in the analysis of arterial pressure traces [210], and has been explained both as the effect of the AV closure or as the consequence of the interaction of traveling and reflected pressure waves [260].

As its volume reduces, the ventricle becomes shorter and the atrioventricular ring shifts towards the ventricular apex (Figure 4.15), as observed in healthy hearts [99, 180, 198]. This effect can be quantified by computing the *longitudinal fractional shortening* (LFS) [198, 259]: by denoting by $L_{\mathrm{ED}}^{\mathrm{LV}}$ and $L_{\mathrm{ES}}^{\mathrm{LV}}$ the apico-basal distances at the end of diastole and at the end of systole, respectively, the LFS is defined as

$$\mathrm{LFS}^{\mathrm{LV}} = \frac{L_{\mathrm{ED}}^{\mathrm{LV}} - L_{\mathrm{ES}}^{\mathrm{LV}}}{L_{\mathrm{ED}}^{\mathrm{LV}}} = 17.8\,\% \,,$$

which matches measurements on healthy hearts [102]. At the end of the systolic phase, the ventricular wall is approximately 14 % thicker than at the end of diastole [244].

Overall, the ejection phase lasts $T_{\mathrm{ej}} = 261$ ms, and the whole systolic phase lasts $T_{\mathrm{sys}} = 326$ ms, corresponding to 40.7 % of the heartbeat.

4.2.4 Isovolumetric relaxation

Once the AV is fully closed, the IVR phase starts. Ventricular pressure reduces as the ventricle relaxes at constant volume (Figures 4.5 and 4.17). This phase lasts for $T_{\mathrm{IVR}} = 94.2$ ms, consistently with physiology [32, 201],

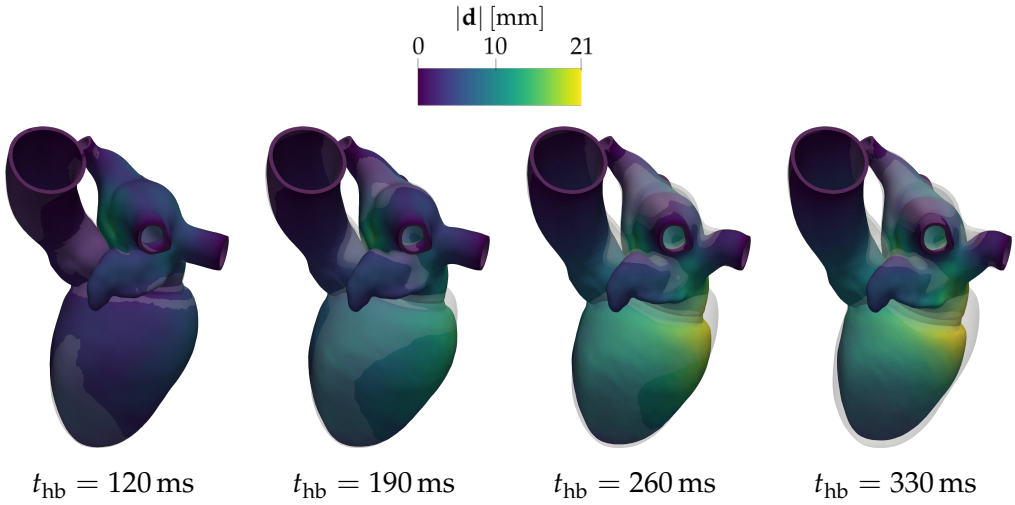

Figure 4.15: Realistic LH test case. Magnitude of the displacement $|\mathbf{d}|$ at four instants during the ejection phase. The initial configuration is overlaid in trasparency, and the domain is warped by $\mathbf{d}$. The ventricle becomes shorter during the ejection, mostly due to the shift of the atrioventricular plane towards the apex.

and the MV starts opening as soon as the ventricular pressure becomes smaller than the atrial pressure.

As observed for the IVC phase, the simulation results feature a small spurious variation in volume during isovolumetric phases. In the case of the IVR phase, the variation amounts to 0.4 mL, corresponding to 0.6 % of ESV^{LV}. Also in this case, I deem the spurious variation to be acceptable.

4.2.5 Filling

Once the MV is open, blood flows from the atrium into the ventricle (Figure 4.16). The flow is characterized by the formation of a jet through the MV, that is associated to a vortex ring (Figure 4.18). The vortex ultimately dissipates near to the ventricular free wall, while becoming larger near the septum, resulting in a single vortex that rotates clockwise if observed from a long-axis view with the septum on the left. This behavior is observed in medical images of healthy hearts [95, 249]. At the same time,

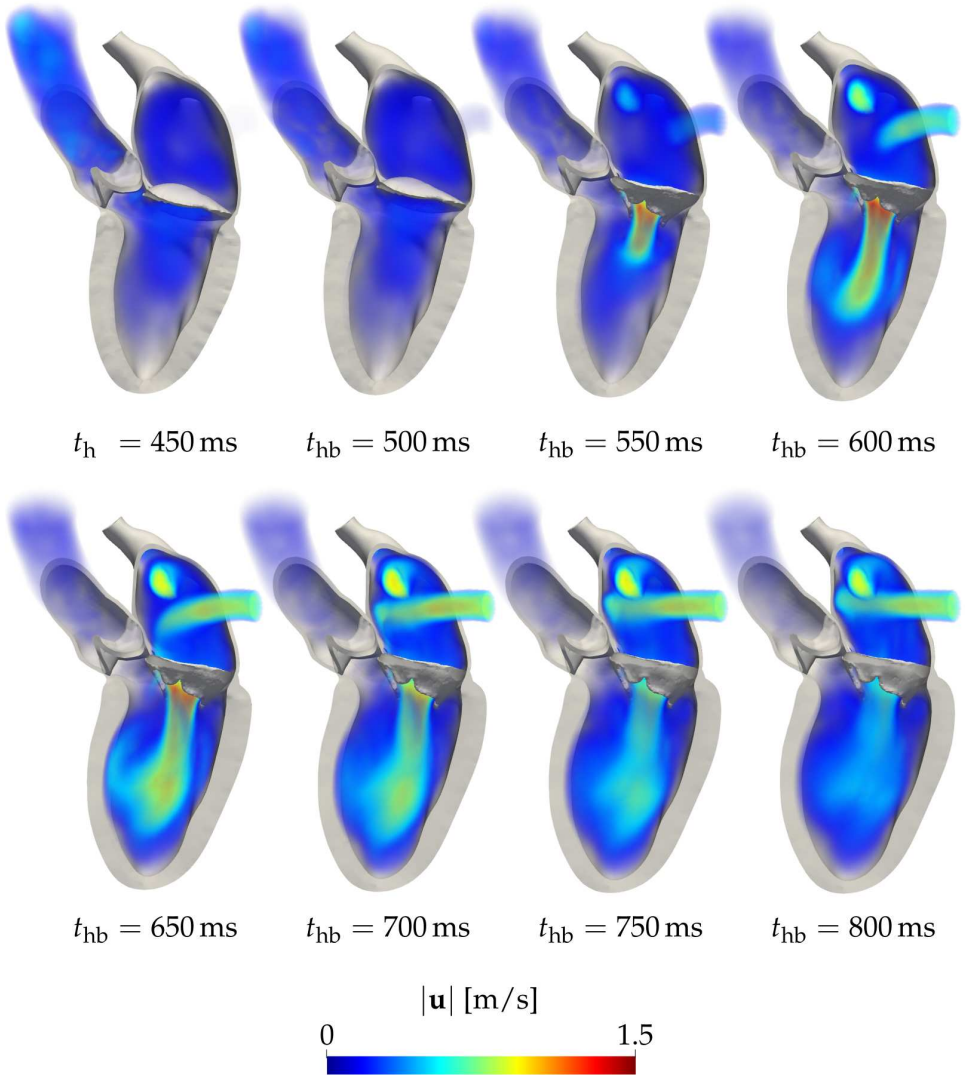

Figure 4.16: Realistic LH model. Volume rendering of the velocity magnitude $|\mathbf{u}|$, for the IVR and filling phases. The domain is warped according to $\mathbf{d}$ and $\mathbf{d}_{\mathrm{ALE}}$.

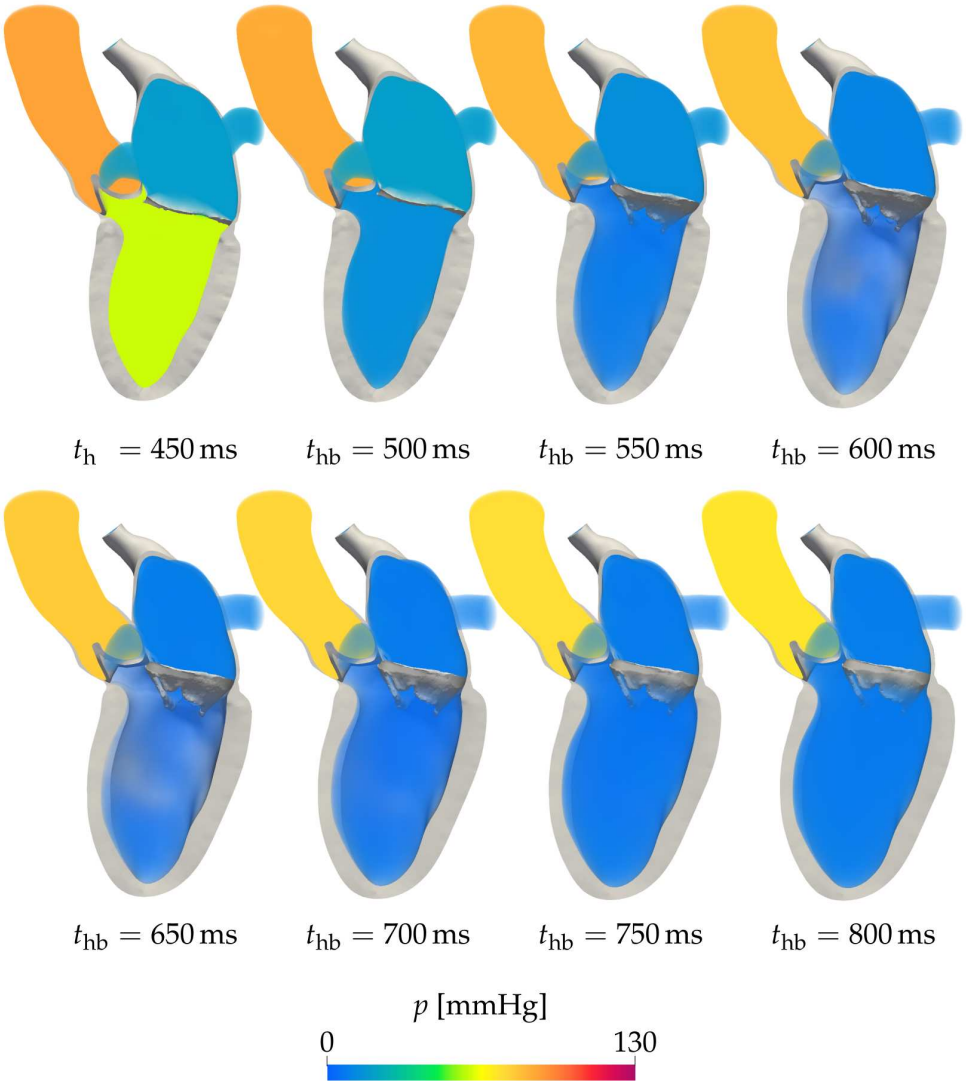

Figure 4.17: Realistic LH model. Volume rendering of the pressure p, for the IVR and filling phases. The domain is warped according to $\mathbf{d}$ and $\mathbf{d}_{\mathrm{ALE}}$.

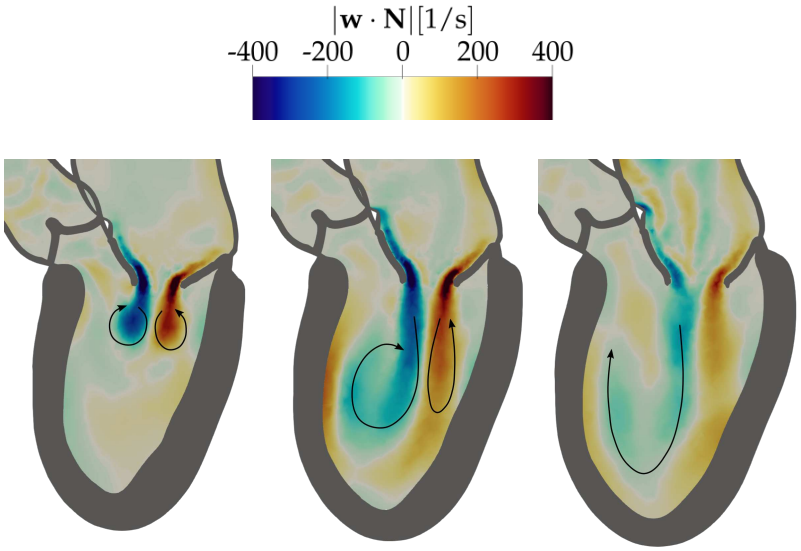

(a) $t_{\text{hb}} = 550\,\text{ms}$ (b) $t_{\text{hb}} = 650\,\text{ms}$ (c) $t_{\text{hb}} = 750\,\text{ms}$

Figure 4.18: Vorticity $\mathbf{w} \cdot \mathbf{N} = (\boldsymbol{\nabla} \times \mathbf{u}) \cdot \mathbf{N}$ of the velocity field, projected onto a slice of the domain (with normal $\mathbf{N}$ pointing outwards from the slice plane). The arrows indicate the direction of the rotating vortices.

the atrioventricular plane shifts towards the atrium, while the ventricular volume increases. Since in this test case atrial contraction is not included, the simulated diastolic phase lacks the atrial kick [180]. This also determines higher-than-normal pressure and volume in the left atrium (with a peak pressure of 19 mmHg, against a normal value of about 8 mmHg [110]). Filling continues until the ventricle starts contracting again, leading to the closure of the MV and the beginning of a new cardiac cycle. The filling phase lasts for $T_{\text{fil}} = 379\,\text{ms}$, and the whole diastolic phase lasts for $T_{\text{dia}} = 474\,\text{ms}$, corresponding to 59.3 % of the heartbeat.

4.2.6 Conservation of blood volume

The explicit treatment of the geometric FSI coupling condition and of the coupling between the Navier-Stokes equations and the circulation model might in principle lead to variations over time in the total blood volume. To assess whether this has an impact on simulation results, the total blood

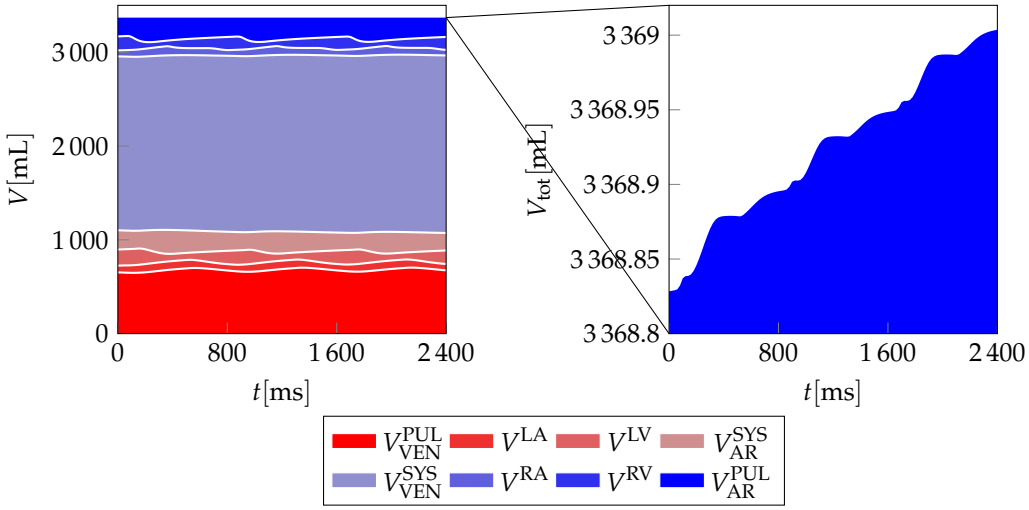

Figure 4.19: Blood volume over three heartbeats in each compartment of the heart and circulation. The zoom on the right shows how the total blood volume exhibits a very small variation in time: the mass gain over three heartbeats is only 0.0052 % of the total.

volume over time is computed as follows:

$$\begin{aligned} V_{\text{tot}}(t) = {} & V_{\text{VEN}}^{\text{PUL}}(t) + V^{\text{LA}}(t) + V^{\text{LV}}(t) + V_{\text{AR}}^{\text{SYS}}(t) \\ & + V_{\text{VEN}}^{\text{SYS}}(t) + V^{\text{RA}}(t) + V^{\text{RV}}(t) + V_{\text{AR}}^{\text{PUL}}(t) \,, \end{aligned}$$

where

$$\begin{aligned} V_{\text{AR}}^{\text{SYS}}(t) &= V_{\text{AR},0}^{\text{SYS}} + V^{\text{AA}}(t) + C_{\text{AR}}^{\text{SYS}}(p_{\text{AR}}^{\text{SYS}}(t) - p_{\text{ex}}(t)) \,, \\ V_{\text{VEN}}^{\text{SYS}}(t) &= V_{\text{VEN},0}^{\text{SYS}} + C_{\text{VEN}}^{\text{SYS}}(p_{\text{VEN}}^{\text{SYS}}(t) - p_{\text{ex}}(t)) \,, \\ V_{\text{AR}}^{\text{PUL}}(t) &= V_{\text{AR},0}^{\text{PUL}} + C_{\text{AR}}^{\text{PUL}}(p_{\text{AR}}^{\text{PUL}}(t) - p_{\text{ex}}(t)) \,, \\ V_{\text{VEN}}^{\text{PUL}}(t) &= V_{\text{VEN},0}^{\text{PUL}} + C_{\text{VEN}}^{\text{PUL}}(p_{\text{VEN}}^{\text{PUL}}(t) - p_{\text{ex}}(t)) \,, \end{aligned}$$

and $V^{\text{LA}}(t)$, $V^{\text{LV}}(t)$ and $V(t)$ are the volumes of $\Omega_{\text{f}}^{\text{LA}}$, $\Omega_{\text{f}}^{\text{LV}} \cup \Omega_{\text{f}}^{\text{ring}}$ and $\Omega_{\text{f}}^{\text{AA}}$, respectively. The zero-pressure volumes $V_{\text{j},0}^{\text{i}}$ are assumed to be zero for simplicity, since they are constant in time and do not influence the assessment of blood volume conservation.

The blood volume over time for the different compartments, as well as the total blood volume, are reported in Figure 4.19. The distribution of blood

between the different compartments varies over time, but the total volume remains approximately constant. Indeed, the range of variation of the total volume over the three simulated heartbeats equals

$$\frac{\max_{t\in(0,T)} V_{\text{tot}}(t) - \min_{t\in(0,T)} V_{\text{tot}}(t)}{\max_{t\in(0,T)} V_{\text{tot}}(t)} = 0.0052\,\% \,.$$

I deem this very small variation over three heartbeats negligible and the result to be highly accurate. Therefore, the approximation introduced by the explicit discretization of geometric FSI coupling and circulation coupling does not introduce significant errors in terms of mass conservation.

Chapter 5

An integrated model of the whole heart

In this chapter, I present a proof-of-concept simulation using the EMF model to reproduce the cardiac cycle of the whole heart with its four chambers (LH and RH). This extends the results presented in Chapter 4 by including the RH and accounting for atrial electromechanics. The results are in qualitative accordance with cardiac physiology, indicating that EMF model has the potential of reproducing the physiology of the whole heart. The evolution of some variables, although qualitatively correct, still shows a quantitative mismatch with experimental observations, requiring further calibration of the model parameters: this is the subject of ongoing work.

5.1 Setup of the test case

Let us consider the whole heart domain represented in Figure 5.1, generated from the Zygote model. As done in Chapter 4, both the fluid and the solid domain are partitioned into subdomains, corresponding to the four chambers, large arteries and valvular rings. With respect to the setup in Chapter 4, the LH portion of the domain contains a longer tract of the aorta, including the bifurcations of the brachioencephalic, common and subclavian arteries. The symbols used to identify the subdomains are listed in Table 5.1. The spatial discretization parameters are reported in Table 5.2.

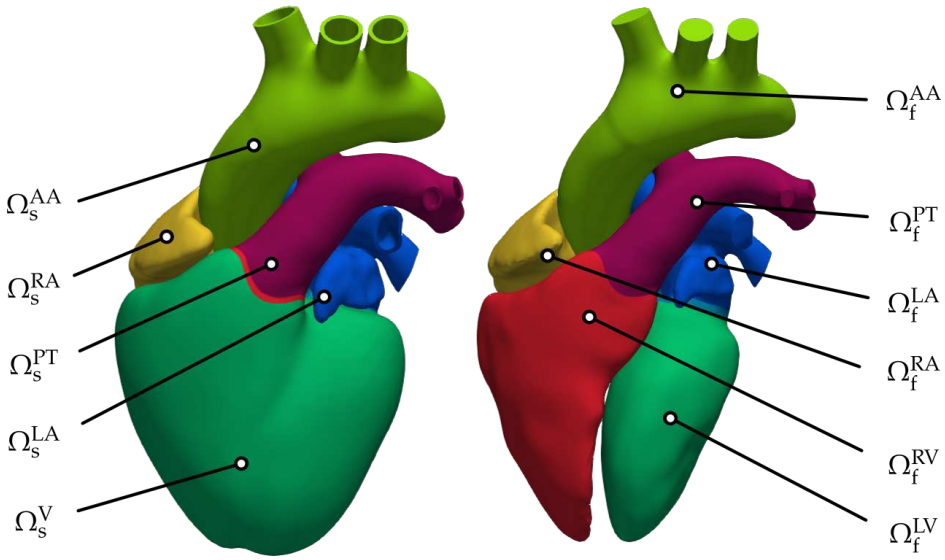

Figure 5.1: Solid (left) and fluid (right) computational domains for the whole heart simulation. Colors indicate the different subdomains.

Solid		**Fluid**	
Ω_s^{LA}	left atrium	Ω_f^{LA}	left atrium
Ω_s^{RA}	right atrium	Ω_f^{RA}	right atrium
Ω_s^{V}	ventricles	Ω_f^{LV}	left ventricle
		Ω_f^{RV}	right ventricle
Ω_s^{AA}	aortic arch	Ω_f^{AA}	aortic arch
Ω_s^{PT}	pulmonary trunk	Ω_f^{PT}	pulmonary trunk
Ω_s^{LR}	mitral valve ring and aortic root	Ω_f^{LR}	mitral valve and aortic root
Ω_s^{TV}	tricuspid valve ring	Ω_f^{TV}	tricuspid valve
Ω_s^{PV}	pulmonary valve ring	Ω_f^{PV}	pulmonary valve

Table 5.1: Subdomains that compose the whole heart model (see also Figure 5.1).

	h_{min}[mm]	h_{avg}[mm]	h_{max}[mm]	**# elem.**	**# nodes**
fluid	0.77	2.6	5.5	557 568	98 409
solid	0.83	2.6	4.8	246 671	59 518
torso	0.58	4.5	11.2	2 413 758	407 028

Table 5.2: Minimum, average and maximum mesh element diameter, number of elements and number of nodes used for the spatial discretization of the whole heart domain (Chapter 5) and of the torso (Section 5.2.3).

Fibers are generated using the whole heart method presented in [258], stemming from a combination of the method proposed in [97] for ventricular fibers (both left and right) and that of [258] for the atria. The resulting fiber field is shown in Figure 2.3a.

With respect to Chapter 4, not only ventricles but also atria are treated as both electrically and mechanically active, i.e. $\widehat{\Omega}_s^{\text{active}} = \widehat{\Omega}_s^{\text{V}} \cup \widehat{\Omega}_s^{\text{LA}} \cup \widehat{\Omega}_s^{\text{RA}}$. I choose the TTP06 ionic model in $\widehat{\Omega}_s^{\text{V}}$ and the CRN model in $\widehat{\Omega}_s^{\text{LA}}$ and $\widehat{\Omega}_s^{\text{RA}}$. A stimulus is applied at the junction between the RA and the superior vena cava, corresponding to the location of the SAN. The geometrical model includes interatrial connections (Bachmann's bundle and fossa ovalis [292]), so that the electical stimulus can propagate from the RA to the LA, and there is no need to stimulate directly the LA. On the contrary, atrioventricular rings are electrically passive and insulate ventricles from atria. Due to the lack of a model for the CCS, it is surrogated by applying stimuli at 5 points on the ventricular endocardium (2 on the LV endocardium, 2 on the RV endocardium and one on the interventricular septum), suitably delayed with respect to the SAN stimulus, to mimic the effect of the AVN and bundle branches [258].

For both atria and ventricles we use the Guccione constitutive law (2.7) and the RDQ20-MF model for force generation (Section 2.3). The RDQ20-MF model is calibrated differently in ventricles and atria (Appendix B.4). For valvular rings and arteries, instead, we rely on the neo-Hooke model (2.8). Figure 5.2 summarizes the boundary conditions for this test case: Robin conditions are set on the epicardium, and Dirichlet conditions are imposed on the terminal sections of veins and arteries. The fluid domain is also kept

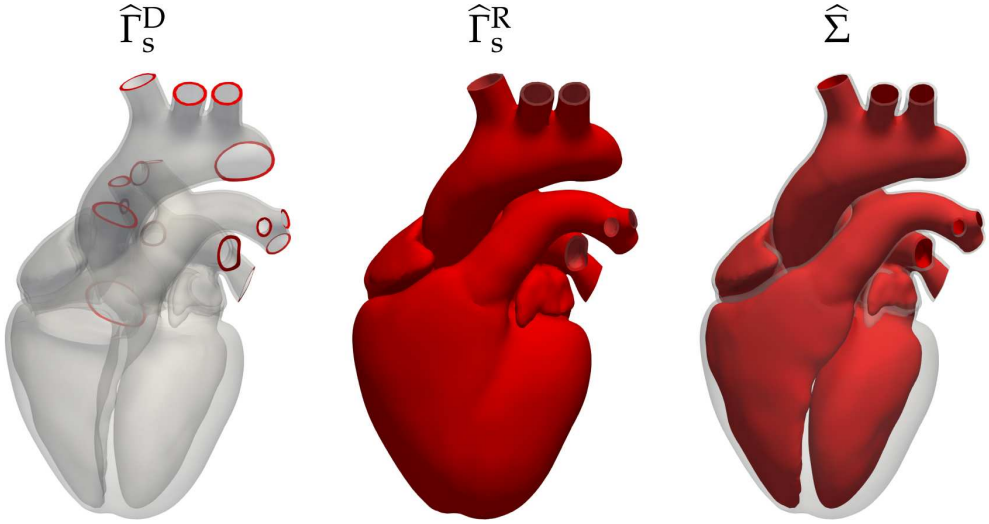

Figure 5.2: Dirichlet (left), Robin (middle) and fluid-solid interface (right) boundaries for the solid mechanics problem (2.6) for the whole heart model.

fixed at the terminal sections.

All four cardiac valves (MV, AV, TV and PV) are included by means of the RIIS model. The fluid domain displacement is obtained by solving (2.11) with the neo-Hooke constitutive relation for the fictitious material representing the fluid domain. The numerical approximation of the fluid problem is stabilized with the VMS-LES method.

The fluid model is coupled with the circulatory system at inlets and outlets. To this end, the equations for the pressure and volume of all four cardiac chambers are removed from the circulation model, as well as those for flow rates through valves, and they are replaced with the coupling conditions

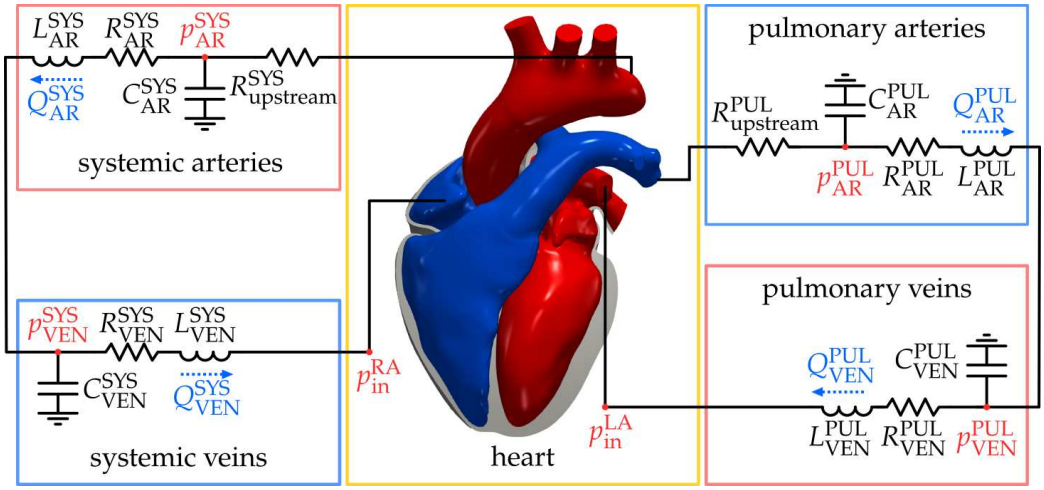

Figure 5.3: Representation through a circuital analogy of the 0D circulation model, coupled to a 3D model of the whole heart.

(4.1) for the LH, together with the following ones for the RH:

$$\begin{cases} \sigma_f(\mathbf{u},p)\mathbf{n} = -p^{RA}(t)_{in}\mathbf{n} & \text{on } \Gamma_{\text{ven. cav.}}\,, \\ \sigma_f(\mathbf{u},p)\mathbf{n} = -\left(p^{PUL}_{AR}(t) + R^{PUL}_{upstream}Q^{AV}(t)\right)\mathbf{n} & \text{on } \Gamma_{PT}\,, \\ Q^{SYS}_{VEN}(t) = -\displaystyle\int_{\Gamma_{\text{ven. cav.}}} (\mathbf{u}-\mathbf{u}_{ALE})\cdot\mathbf{n}d\gamma\,, \\ Q_{PV}(t) = \displaystyle\int_{\Gamma_{PT}} (\mathbf{u}-\mathbf{u}_{ALE})\cdot\mathbf{n}d\gamma\,, \end{cases}$$

where $\Gamma_{\text{ven. cav.}}$ and Γ_{PT} are the terminal sections of venae cavae and pulmonary arteries respectively. The resulting closed-loop system is schematically represented in Figure 5.3.

As before, the simulation lasts for three heartbeats, that is until $T = 3T_{hb}$, and the analysis considers the results of the third heartbeat, starting at $t_0 = 2T_{hb}$. In the following sections, $t_{hb} = t - t_0$ denotes the time relative to the third heartbeat.

The EMF problem is solved with the staggered scheme of Section 3.1 using the GE-M scheme for the FSI subproblem (Section 3.2.4). As done in the previous chapter, electrophysiology is discretized with piecewise quadratic finite elements, while linear elements are used for all other models.

The values of the parameters used for this simulation are reported in Appendix B.4.

5.2 Simulation results

The simulation was run using 288 cores on the GALILEO100 cluster at the CINECA high-performance computing center (Italy). Each simulated heartbeat takes approximately 20 h of wall time. 85 % of the wall time is spent solving the FSI subproblem, including 10 % to compute the fluid domain displacement, and 10 % is spent solving the electrophysiology subproblem.

5.2.1 Electrophysiology

Figure 5.4 displays some snapshots of the transmembrane potential, Figure 5.5 shows the corresponding intracellular calcium concentration, and Figure 5.6 depicts the activation time (defined as in Equation (4.2)).

The activation is initiated at the sinoatrial node, and propagates from there to the right atrium first and then to the left atrium through the interatrial connections. Both atria are fully activated within 120 ms from the SAN stimulus, with the latest activated region located on the superior pulmonary veins (Figure 5.6).

At a later stage, a stimulus is applied on the ventricles, leading to their activation. Both ventricles are activated within 270 ms from the SAN stimulus, and 110 ms from the first ventricular stimulus. The latest activated region is located on the left ventricular free wall. The activation sequence is consistent with experimental observations [98].

5.2.2 Pressure and volume of cardiac chambers

Figures 5.7 and 5.8 display the blood velocity and pressure at some time instants during the simulation. Figure 5.9 reports average pressure, volume and volume derivative (corresponding to the net flow rate incoming or outgoing from each chamber) over time for the four chambers, while Figures 5.10 and 5.11 display the corresponding pressure-volume loops. The LV pressure-volume loop is qualitatively similar to the one discussed

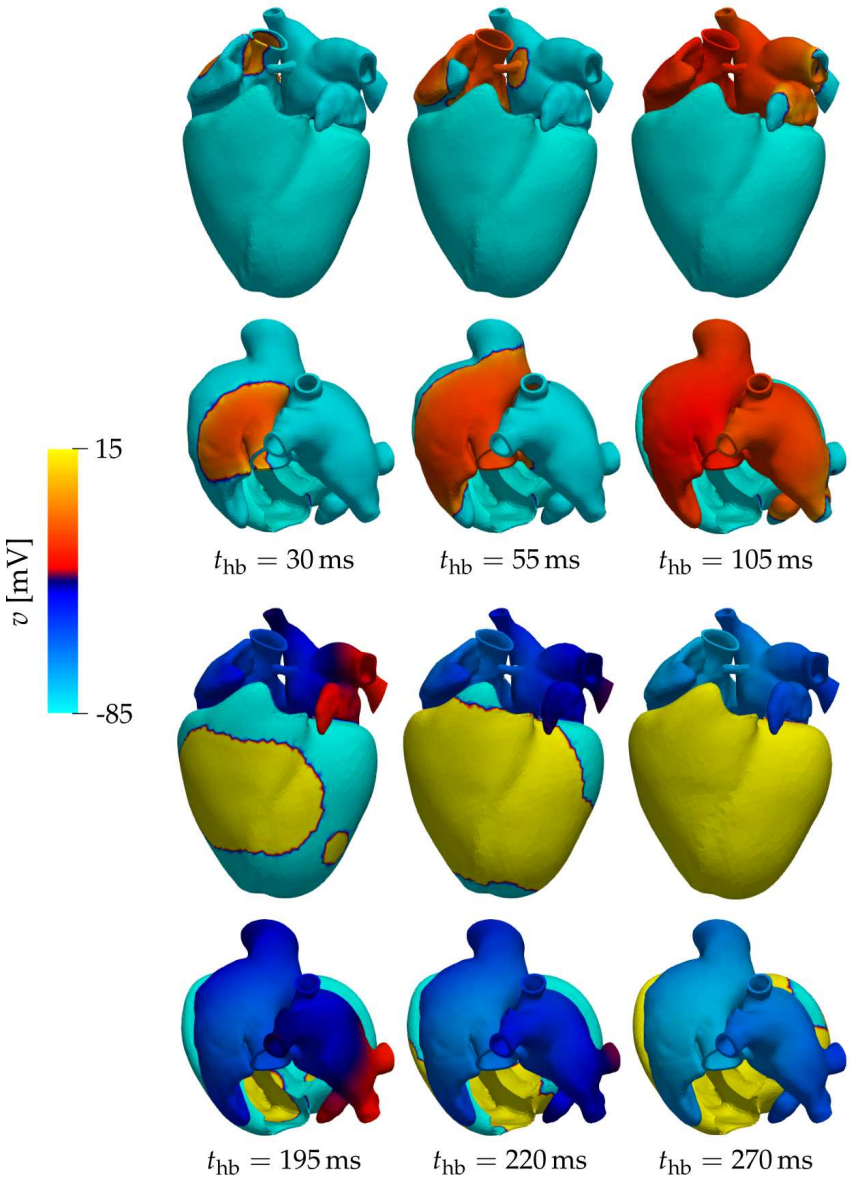

Figure 5.4: Whole heart test case. Transmembrane potential at different time instants. Arteries are clipped for visualization, and the domain is warped by **d**.

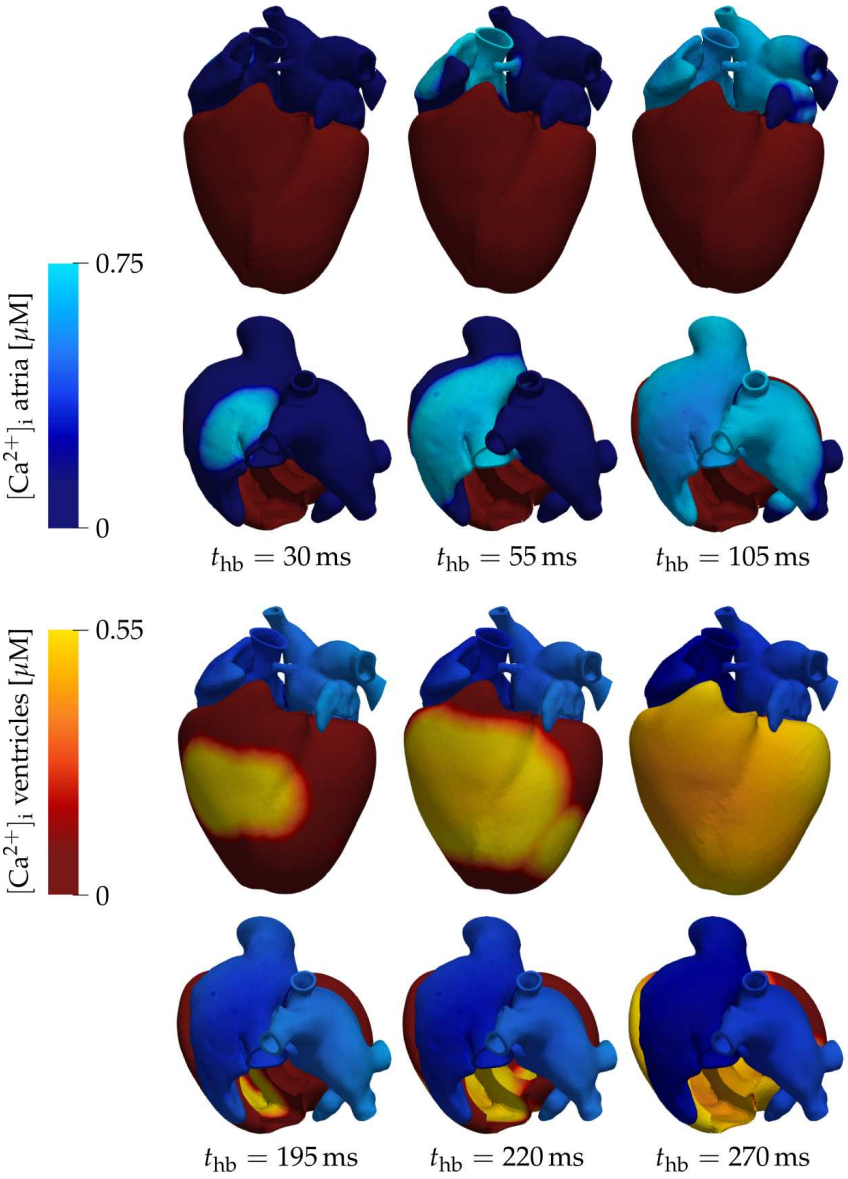

Figure 5.5: Whole heart test case. Intracellular calcium concentration in atria and ventricles at different time instants. Arteries are clipped for visualization, and the domain is warped by **d**. Two different scales are used to account for the different calcium ranges of the TTP06 and CRN models.

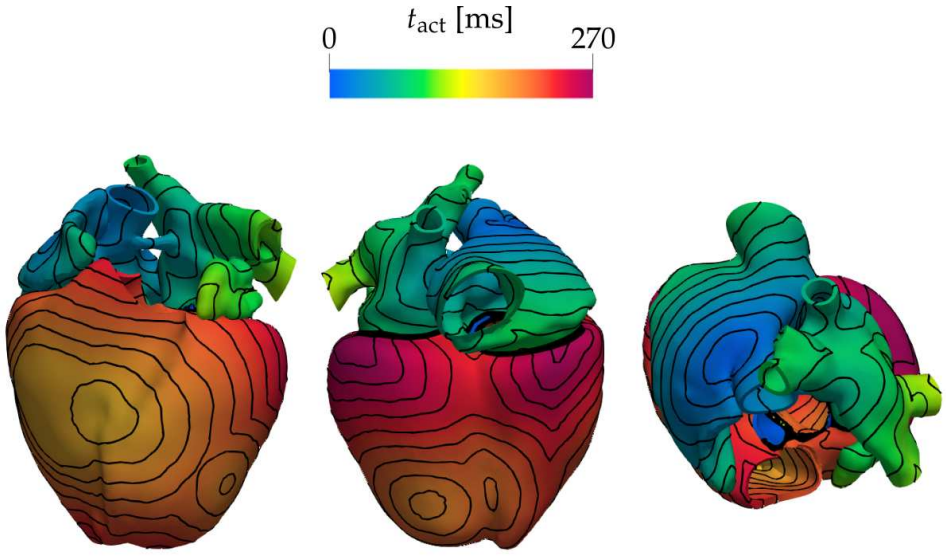

Figure 5.6: Whole heart test case. Contour plot of the activation time t_{act}. The domain is shown in its reference configuration $\widehat{\Omega}_s$, and the passive subdomain $\widehat{\Omega}_s^{passive}$ has been clipped for visualization.

in Chapter 4. The major difference is that, at the end of the diastolic phase (bottom right part of the loop) pressure increases slightly as a consequence of the atrial contraction. The RV pressure-volume loop is characterized by a more rounded shape, if compared to the rectangular one of the LV, in agreement with experimental observations [37, 213, 226, 268, 279]. Moreover, the RV peak systolic pressure is significantly smaller than that of the LV, consistently with physiology, due to the pressure in the pulmonary arteries being lower than that in the systemic ones.

The peak systolic pressure of the LV equals $p_{max}^{LV} = 113.3\,\text{mmHg}$, within the physiological range $(119 \pm 13)\,\text{mmHg}$ [312]. For the RV, the peak systolic pressure equals 36.1 mmHg, also within the physiological range $(36 \pm 11)\,\text{mmHg}$ [37].

Indicators for ventricular volumes are reported in Table 5.3. While the indicators for the LV are in substantial agreement with physiological values, those for the RV are not (especially the SV and EF). In particular, the SVs of left and right ventricles are significantly different, whereas they should be

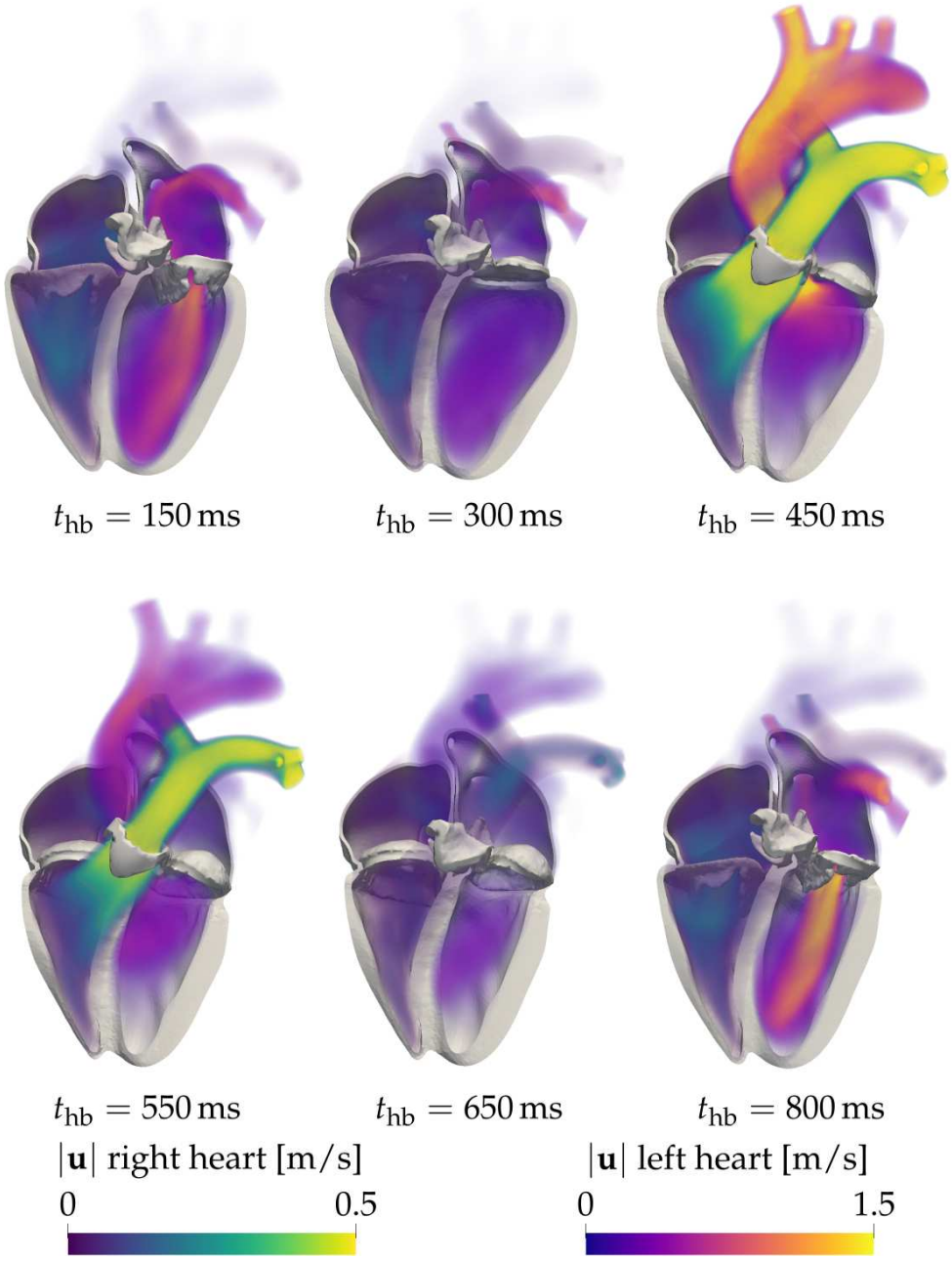

Figure 5.7: Volume rendering of the velocity magnitude $|\mathbf{u}|$ in the whole heart simulation. The domain is warped by $\mathbf{d}$ and $\mathbf{d}_{\text{ALE}}$. Notice that the LH and RH have different color scales.

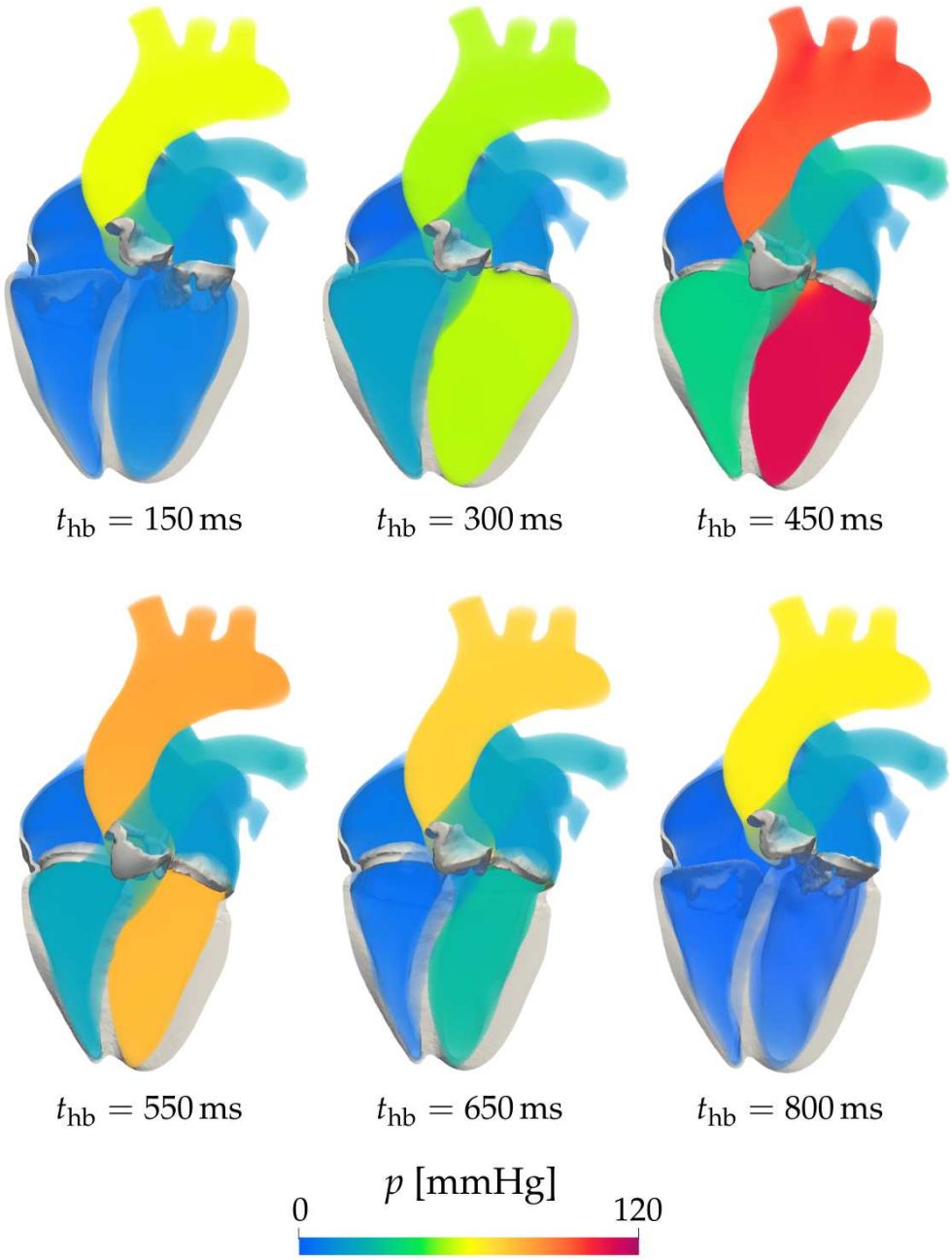

Figure 5.8: Volume rendering of the pressure p in the whole heart simulation. The domain is warped by $\mathbf{d}$ and $\mathbf{d}_{\mathrm{ALE}}$.

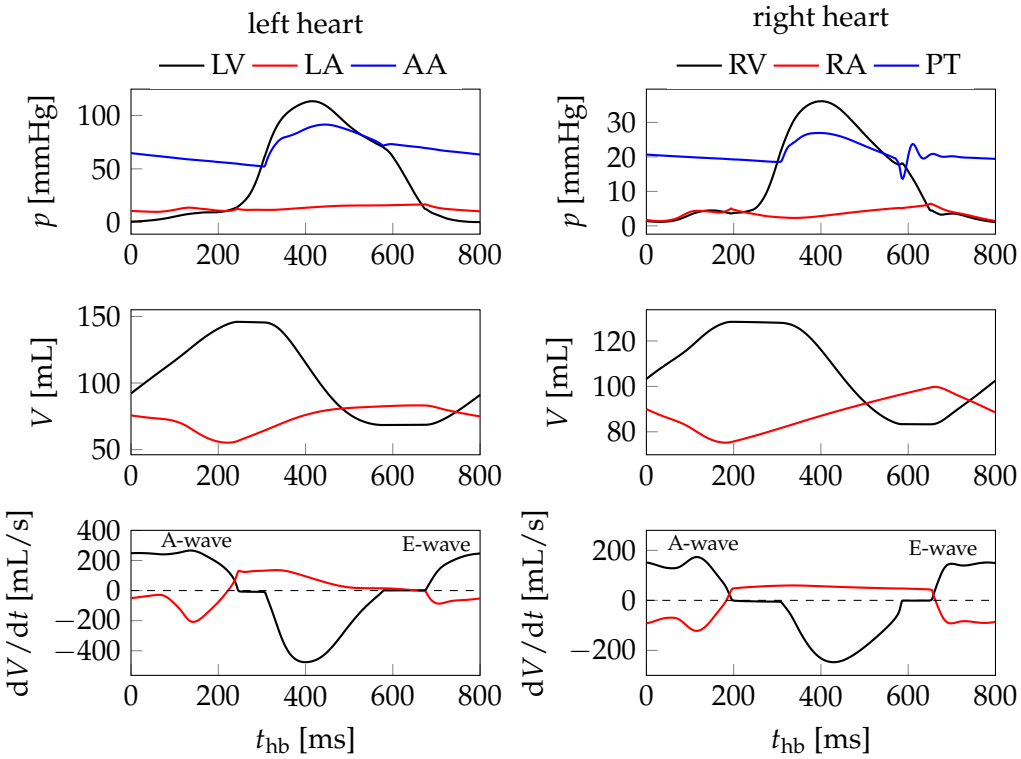

Figure 5.9: Pressure, volume and volume derivative over time for the cardiac chambers and arteries in the whole heart simulation. The LH and the RH are on the left and right sides, respectively. Notice that the vertical axes of the LH and RH plots have different scales.

equal, since the LV and RV act as pumps connected in series through the circulation. Similarly, the peak flow rate through the AV ($Q^{\mathrm{AV}}_{\mathrm{max}} = 475.8\,\mathrm{mL/s}$) is significantly higher than that through the PV ($Q^{\mathrm{PV}}_{\mathrm{max}} = 247.3\,\mathrm{mL/s}$). This indicates that the simulation has not reached a limit cycle yet, and the final time T should be increased to cover more heartbeats. The calibration of the model to reproduce the physiology of the right heart in a more quantitatively accurate way is the subject of ongoing work.

The pressure and volume of the atria are qualitatively consistent with experimental measurements [41, 243]. The pressure-volume loops have the characteristic figure-of-eight shape [41, 243], resulting from the interplay

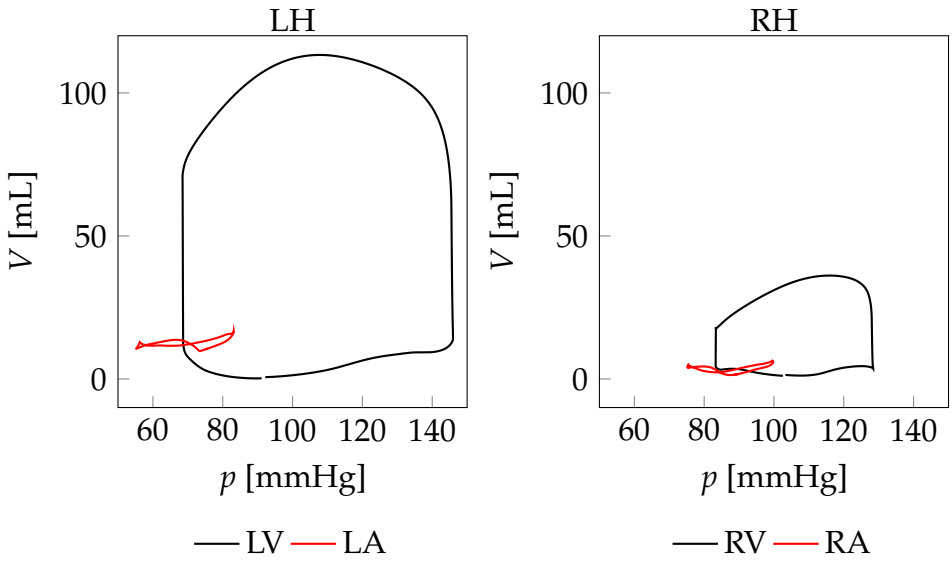

Figure 5.10: Pressure-volume loops for the four cardiac chambers in the whole heart simulation.

Indicator		Sim.	Normal values		Description
EDV^{LV}	[mL]	145.9	126 to 208	[208]	LV end-diastolic volume
ESV^{LV}	[mL]	68.5	35 to 80	[208]	LV end-systolic volume
SV^{LV}	[mL]	77.5	81 to 137	[208]	LV stroke volume
EF^{LV}	[%]	53.1	57 to 74	[208]	LV ejection fraction
EDV^{RV}	[mL]	128.4	144 ± 23	[209]	RV end-diastolic volume
ESV^{RV}	[mL]	83.3	69 ± 22	[163]	RV end-systolic volume
SV^{RV}	[mL]	45.1	94 ± 15	[209]	RV stroke volume
EF^{RV}	[%]	35.1	53 ± 6	[56]	RV ejection fraction

Table 5.3: Ventricular volumetric indicators for the whole heart simulation.

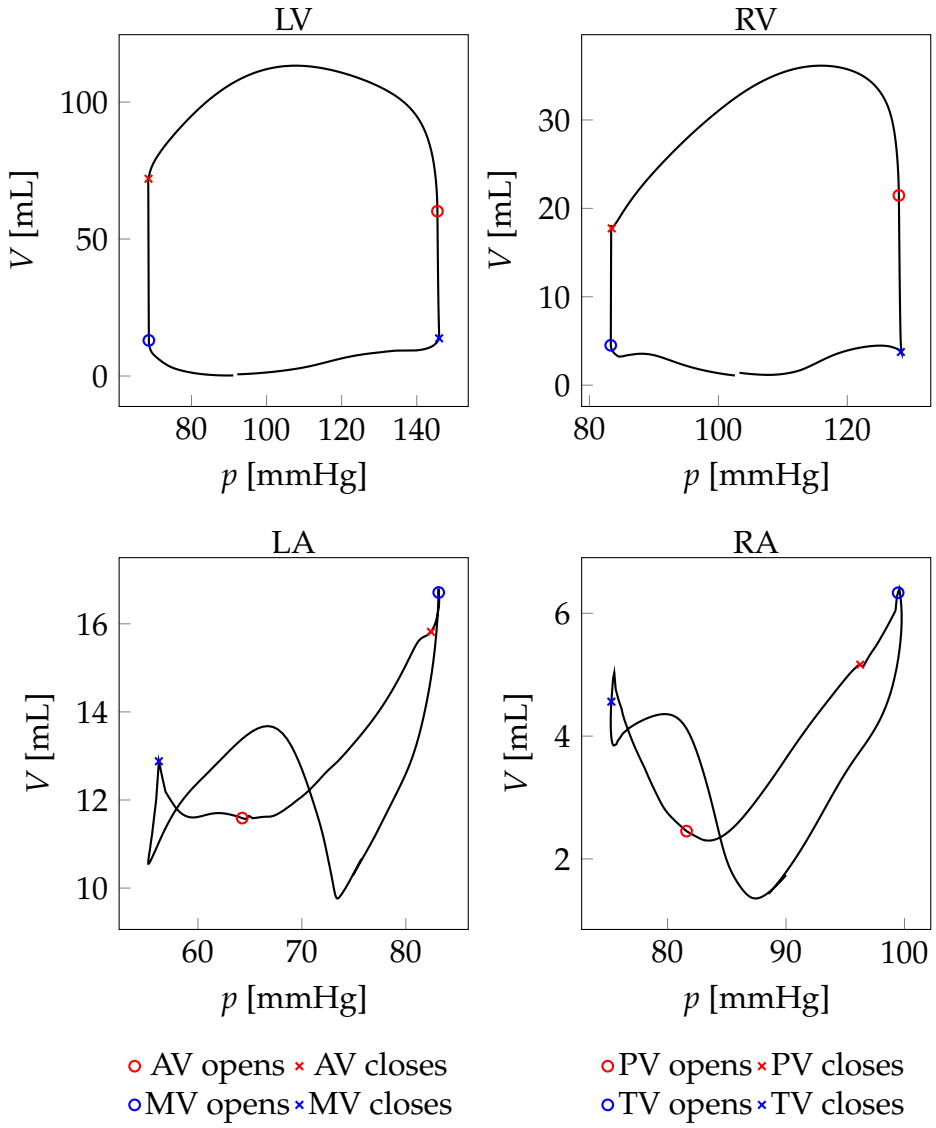

Figure 5.11: Pressure-volume loops for the four cardiac chambers in the whole heart simulation. Markers indicate the opening and closing of valves. Notice that all plots have different scales on both axes.

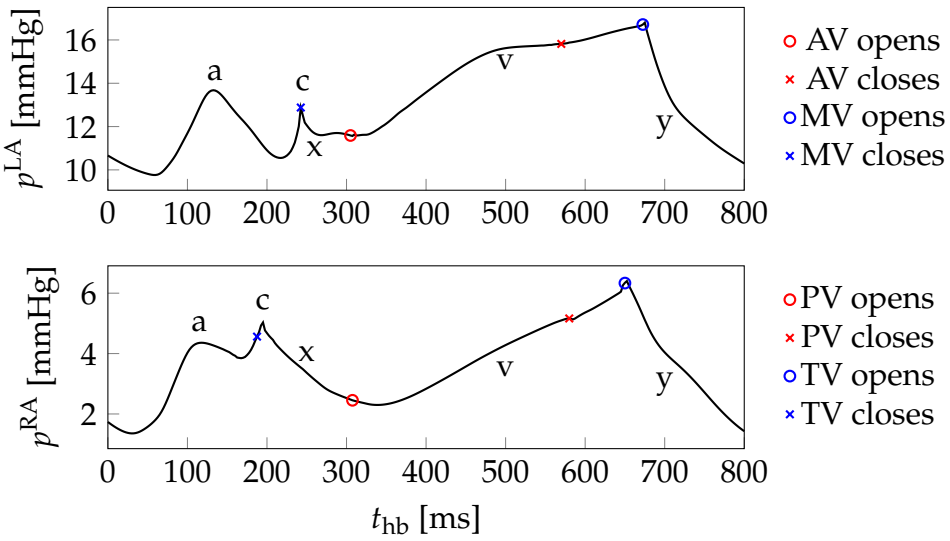

Figure 5.12: Pressure of the LA (top) and RA (bottom). Letters indicate the landmarks of the pressure trace: a-wave, c-wave, x-descent, v-wave and y-descent.

between the atrial passive and active mechanics with the ventricular contraction and relaxation. As shown in Figure 5.12, the evolution of the atrial pressure is characterized by different landmarks [243]:

- the *a-wave*, an increase in pressure associated to atrial contraction;
- the *c-wave*, a pressure upstroke corresponding to the closure of atrioventricular valves and the ventricular isovolumetric contraction;
- the *x-descent*, caused by the downward displacement of the atrioventricular plane that leads to the atrial filling;
- the *v-wave*, associated to the venous return and the atrial filling;
- the *y-descent*, corresponding to the ventricular passive filling phase, during which the atrial volume reduces together with the pressure.

All these features are reproduced by the simulation (Figure 5.12). The c-wave is also visible as an upstroke in the leftmost part of the pressure-volume loop (Figure 5.11), causing the formation of an extra intersection in the loop. This is an unphysical effect, which is most likely related to the

simplified modeling of valves through RIIS, and it will be the subject of further investigation (see Section 6.1).

The atria are filled at an almost constant rate during ventricular systole (Figure 5.9), while atrioventricular valves are closed, then their volume decreases during ventricular diastole. The latter is characterized by two local peaks in the flow rate, the early and the after wave (*E-wave* and *A-wave*, on the bottom of Figure 5.9), caused by passive ventricular filling and atrial contraction, respectively. The E-wave should provide most of the filling of the ventricles, and be characterized by a higher flow rate than the A-wave. This can be quantified by computing the *EA ratio*, defined as the ratio between the peak atrioventricular flow rate during passive filling and the peak flow rate during atrial contraction. Normally, the EA ratio should be 1.30 ± 0.57 [328]. However, the simulation yields an EA ratio of 0.94 for the LH and 0.84 for the right heart: for both sides, the A-wave has a slightly higher flow rate than the E-wave. A similar result was observed in [108]. A possible explanation of this mismatch is an excessively slow ventricular relaxation, which can be improved by resorting to more detailed, yet more computationally expensive, ionic models [332].

While the simulation reproduces qualitatively the cardiac physiology, in quantitative terms there still is some mismatch, and the calibration of the model is the subject of ongoing work. Nonetheless, the results indicate that the computational framework proposed in this thesis has the capability of replicating the cardiac function for a four-chamber heart model.

5.2.3 Simulation of electrocardiograms

Electrocardiograms (ECGs) are commonly used in the clinical practice to evaluate the electrical function of the heart [180, 184, 303]. They are obtained by measuring the elecrical potential at some points on the body surface. The depolarization and repolarization of the heart chambers induce measurable variations in the body surface potential, that can be used to infer the way the heart is activating for diagnostic purposes.

Being able to replicate ECGs is an important step towards patient-specific personalization of cardiac models, allowing to calibrate the parameters of the electrophysiology models using commonly available and non-invasive measurements.

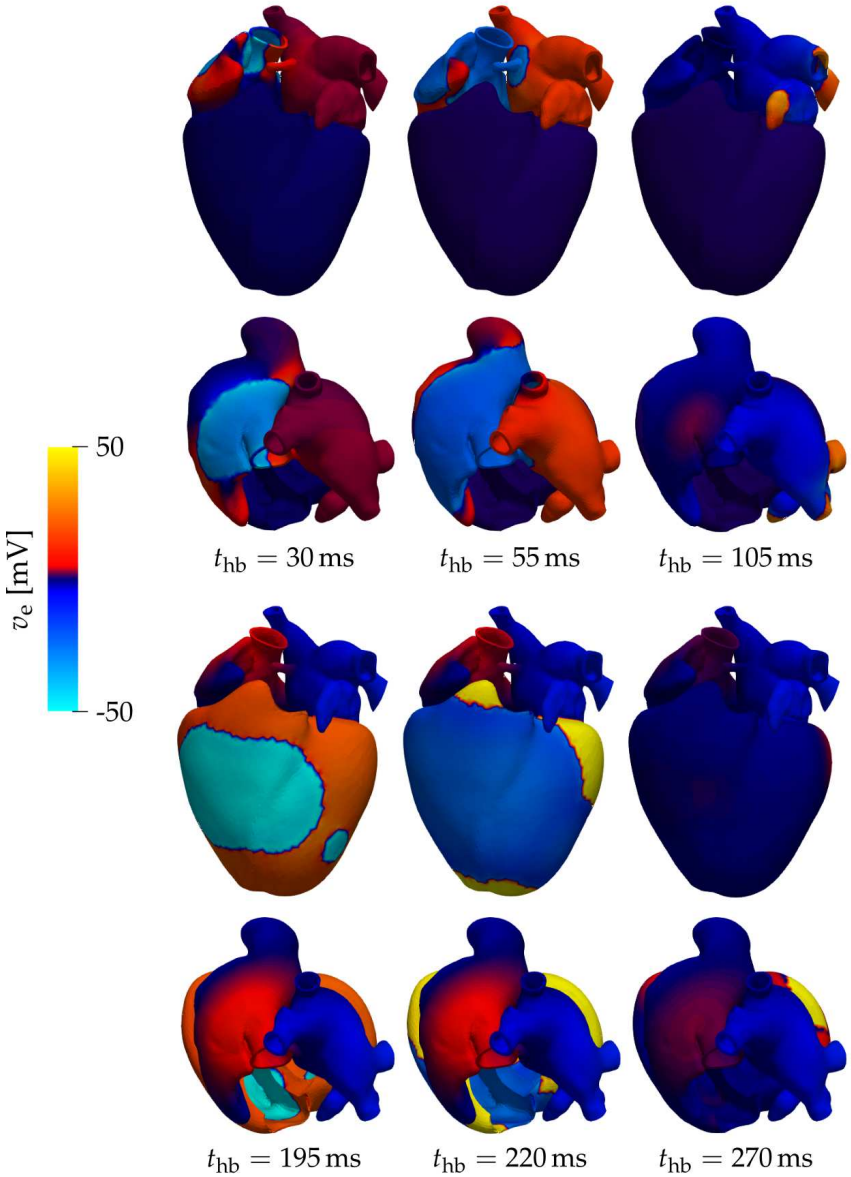

Figure 5.13: Whole heart test case. Extracellular potential. Arteries are clipped for visualization, and the domain is warped by **d**.

As a proof of concept, I include a model for the simulation of ECGs starting from the results of our EMF simulation. The results presented in this section are part of a collaboration with Elena Zappon, MOX, Dipartimento di Matematica, Politecnico di Milano. At every time t, the *extracellular potential* $v_e : \widehat{\Omega}_s^{\text{active}} \times (0,T) \to \mathbb{R}$ within the heart is computed by solving [44, 74]

$$\begin{cases} -\boldsymbol{\nabla} \cdot \left(JF^{-1}(D_i + D_e)F^{-T}\boldsymbol{\nabla} v_e \right) = \boldsymbol{\nabla} \cdot \left(JF^{-1}D_i F^{-T}\boldsymbol{\nabla} v \right) & \text{in } \widehat{\Omega}_s^{\text{active}}, \\ JF^{-1}(D_i + D_e)F^{-T}\boldsymbol{\nabla} v_e \cdot \mathbf{n} = JF^{-1}D_i F^{-T}\boldsymbol{\nabla} v & \text{on } \partial\widehat{\Omega}_s^{\text{active}}, \end{cases} \tag{5.1}$$

where D_i and D_e are intra- and extracellular conductivity tensors that, in analogy to (2.2), are defined as

$$D_{i,e} = \sigma_{i,e}^{l} \frac{F\mathbf{f}_0 \otimes F\mathbf{f}_0}{\|F\mathbf{f}_0\|^2} + \sigma_{i,e}^{t} \frac{F\mathbf{s}_0 \otimes F\mathbf{s}_0}{\|F\mathbf{s}_0\|^2} + \sigma_{i,e}^{n} \frac{F\mathbf{n}_0 \otimes F\mathbf{n}_0}{\|F\mathbf{n}_0\|^2},$$

with $\sigma_{i,e}^{l}$, $\sigma_{i,e}^{t}$ and $\sigma_{i,e}^{n}$ intra- and extracellular conductivities in the direction of fibers, fiber sheets and normal to fiber sheets, respectively, satisfying the condition

$$\sigma_m^j = \frac{\sigma_i^j \sigma_e^j}{\sigma_i^j + \sigma_e^j}.$$

The solution to (5.1) is defined up to an additive constant (since only the gradient of v_e appears in the system). To obtain a unique solution, v_e is constrained to have zero mean, i.e.

$$\int_{\widehat{\Omega}_s^{\text{active}}} v_e \, d\mathbf{x} = 0.$$

Figure 5.13 reports some snapshots of the extracellular potential v_e.

Let us introduce a domain $\widehat{\Omega}_T$ representing the torso, such that the epicardial surface is a subset of its boundary, i.e. $\widehat{\Gamma}_s^R \subset \partial\widehat{\Omega}_T$ (see Figure 5.14a). The electrical potential within the torso, $v_T : \widehat{\Omega}_T \times (0,T) \to \mathbb{R}$ is obtained by solving the generalized Laplace equation [44, 133, 200]

$$\begin{cases} -\boldsymbol{\nabla} \cdot (D_T \boldsymbol{\nabla} v_T) = 0 & \text{in } \widehat{\Omega}_T, \\ v_T = v_e & \text{on } \widehat{\Gamma}_s^R, \\ D_T \boldsymbol{\nabla} v_T \cdot \mathbf{n} = 0 & \text{on } \partial\widehat{\Omega}_T \backslash \widehat{\Gamma}_s^R, \end{cases}$$

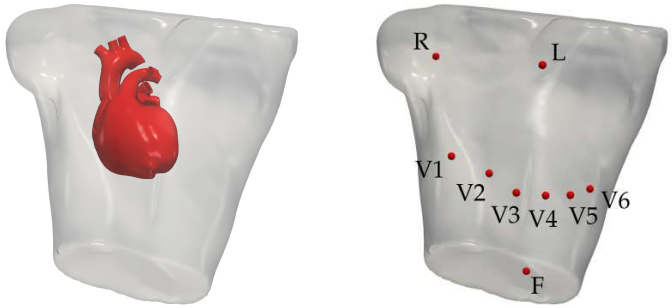

(a) (b)

Figure 5.14: (a) Location of the heart inside the torso model. (b) Location of the electrodes on the surface of the torso.

with D_T a suitable conductivity tensor, here assumed constant and isotropic (i.e $D_T = d_T I$, with $d_T > 0$). Some snapshots of the body surface potential v_T are reported in Figure 5.15.

Finally, v_T is evaluated on the external surface of the torso domain at specific points corresponding to the ECG electrodes (Figure 5.14b). Then, the following differences of potential (*leads*) are computed:

$$
\begin{aligned}
\mathrm{I} &= v_T(\mathbf{x}_L) - v_T(\mathbf{x}_R) \,, \\
\mathrm{II} &= v_T(\mathbf{x}_R) - v_T(\mathbf{x}_F) \,, \\
\mathrm{III} &= v_T(\mathbf{x}_L) - v_T(\mathbf{x}_F) \,, \\
\mathrm{aVL} &= v_T(\mathbf{x}_L) - \frac{1}{2}(v_T(\mathbf{x}_R) + v_T(\mathbf{x}_F)) \,, \\
\mathrm{aVR} &= v_T(\mathbf{x}_R) - \frac{1}{2}(v_T(\mathbf{x}_L) - v_T(\mathbf{x}_F)) \,, \\
\mathrm{aVF} &= v_T(\mathbf{x}_F) - \frac{1}{2}(v_T(\mathbf{x}_L) + v_T(\mathbf{x}_R)) \,, \\
\mathrm{V1} &= v_T(\mathbf{x}_{V1}) - \overline{v_T} \,, \\
\mathrm{V2} &= v_T(\mathbf{x}_{V2}) - \overline{v_T} \,, \\
\mathrm{V3} &= v_T(\mathbf{x}_{V3}) - \overline{v_T} \,, \\
\mathrm{V4} &= v_T(\mathbf{x}_{V4}) - \overline{v_T} \,, \\
\mathrm{V5} &= v_T(\mathbf{x}_{V5}) - \overline{v_T} \,, \\
\mathrm{V6} &= v_T(\mathbf{x}_{V6}) - \overline{v_T} \,.
\end{aligned}
$$

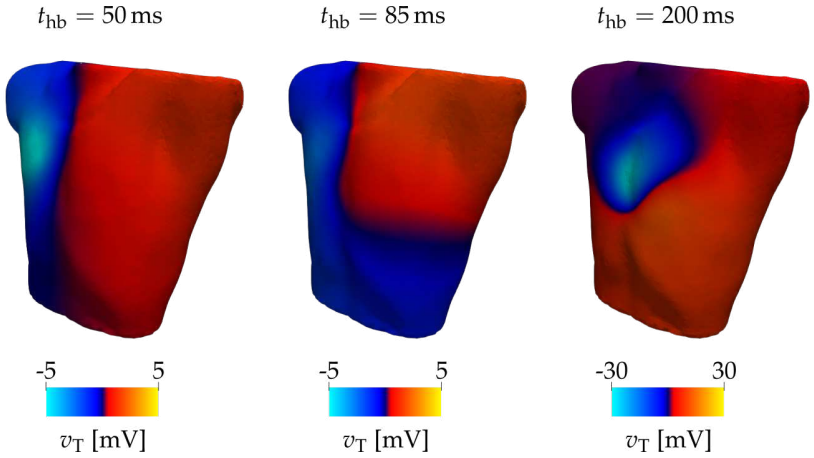

Figure 5.15: Potential within the torso at three representative times, corresponding to atrial depolarization (left and middle) and ventricular depolarization (right). Notice that the contour plot uses different scales for atrial and ventricular depolarization.

where $\overline{v_T} = \frac{1}{3}(v_T(\mathbf{x}_L) + v_T(\mathbf{x}_R) + v_T(\mathbf{x}_F))$, and $\mathbf{x}_i$ are the coordinates of the electrode locations as shown in Figure 5.14b. I, II, III, aVL, -aVR and aVF are known as *limb leads*, and V1, V2, V3, V4, V5, V6 as *precordial leads*. The evolution in time of the leads is what is observed by clinicians in 12-lead ECGs. The simulated signal of the leads is filtered with a band-pass filter, to replicate the signal filters used by ECG recording machines.

A limitation of this approach is that it neglects the dependence of D_T on space, i.e. it does not account for the presence of organs, and ignores the displacement of the heart and torso over time, due to breathing and to the heartbeat itself. Both these limitations can be removed by adding detail to the torso model, including material heterogeneity [143, 181] and solid mechanics.

The simulated 12-lead ECG is reported in Figure 5.16. The P wave (corresponding to atrial depolarization) and the QRS complex (corresponding to ventricular depolarization) are properly captured [180]. The T wave, that corresponds to ventricular repolarization, is correctly timed but has an incorrect sign if compared with ECGs of healthy individuals. This is most likely due to the model's lack of heterogeneity in the action potential,

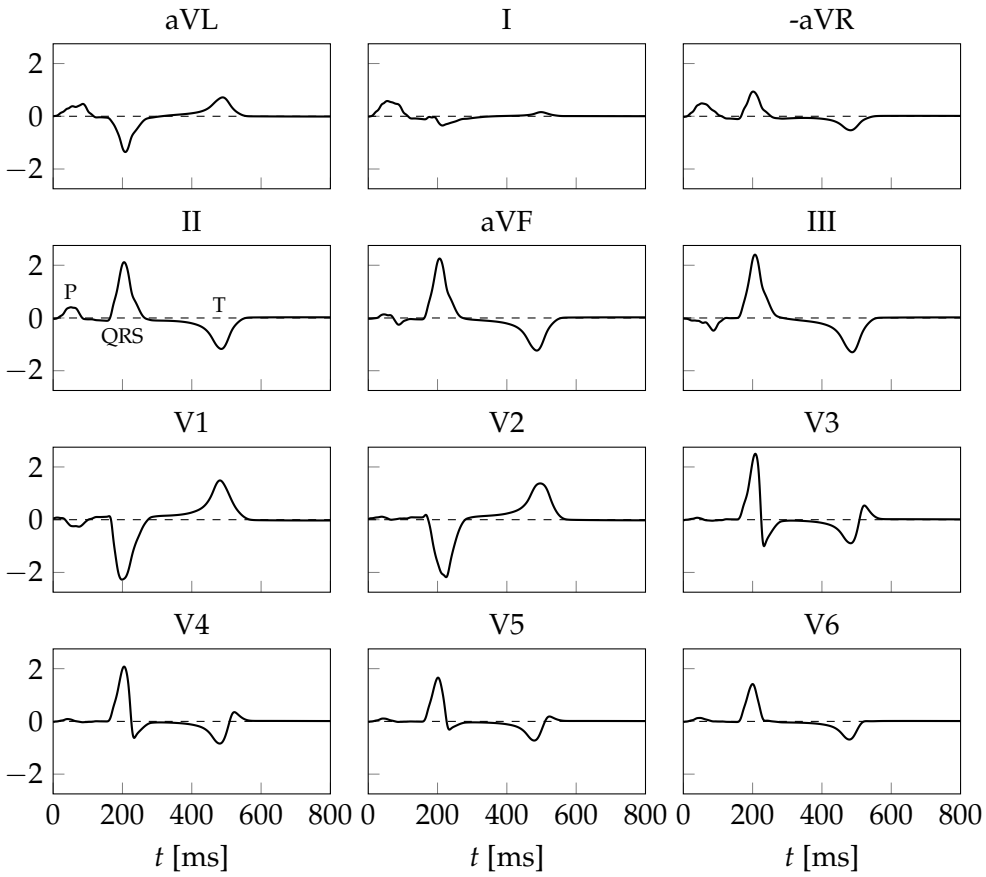

Figure 5.16: Simulated 12-lead ECG for the whole heart simulation. The plot for lead II also indicates the P wave, the QRS complex and the T wave.

in both the transmural and apico-basal directions. Overall, the simulated ECG is qualitatively acceptable, although minor mismatches with physiology can be observed. Nonetheless, the results show how the computation of ECGs can be incorporated in the simulation pipeline of the integrated EMF model. The electrophysiology model, and thus the simulated ECG, may benefit from a more sophisticated model for the CCS (see also Section 6.1).

Chapter 6

Conclusions and future perspectives

In this thesis, I presented an integrated model for the numerical simulation of the heart function, built from the combination of several state-of-the-art core models for the individual components of heart physiology: electrophysiology, contractile force generation, active and passive muscular mechanics, fluid dynamics of the blood, and interaction with the circulatory system, including a reduced model for valve dynamics based on the RIIS method. All the core models are coupled together, to provide a physically accurate representation of their interaction, and therefore allowing to capture the complex interplay of different processes that characterizes the heart function. The result is a comprehensive and integrated computational framework for cardiac simulations, coupling 7 different physical systems, with more than 60 scalar unknowns, acting across very different spatial and temporal scales. The proposed model represents one of the very first examples of a fully integrated, fully coupled and mathematically rigorous model of the heart.

I introduced a novel segregated-staggered time advancing scheme for the numerical solution of the coupled EMF problem. The scheme is designed to be efficient, given the large scale and complexity of the problem, by using an explicit treatment of coupling conditions whenever possible. This includes electro-mechanical and mechano-electrical coupling, as well as the feedback between muscle displacement and force generation and the

coupling with the circulation.

The fluid-solid coupling is more delicate from both the numerical stability and computational efficiency viewpoints. I discussed several different schemes for the solution of the FSI problem in the cardiac regime, providing a comparison among them by means of ventricular benchmark problems. I first compared monolithic and partitioned schemes within the family of strongly coupled FSI methods, finding that the monolithic approach is computationally more efficient than the partitioned one in the cardiac setting. Then, I considered a fully explicit scheme, resulting in a significant reduction in computational time with respect to the monolithic scheme. However, the method provides less accurate results due to the introduction of a splitting error. The main result of this analysis is that a geometrically explicit, strongly coupled, monolithic method provides the best trade-off among the accuracy of the solution, the robustness and reliability of the solver, and the computational cost. The monolithic scheme was therefore used for all subsequent simulations.

Then, I carried out a simulation on a realistic human left heart in physiological conditions. The simulation is carried out in the software framework of the `life`^{x} HPC library in a parallel computing environment. The model was calibrated to reproduce the behavior of a healthy left heart in terms of ventricular pressure and volume over time, pressure-volume loop and flow rates through the aortic valve, obtaining a substantial agreement with normal ranges for several biomarkers. The simulation reproduced accurately all four phases of the heartbeat, by recovering their physiological duration as well as their distinctive features in terms of ventricular displacement and blood flow patterns. This is true in particular for the isovolumetric phases of the heart cycle, that are faithfully simulated thanks to the use of appropriate numerical methods for the FSI subproblem.

The left heart model neglects atrial contraction and the interplay between the right and left sides of the heart. I presented a proof-of-concept four chamber heart simulation that overcomes these issues. Although this test case still requires fine tuning of its parameters, the simulation is in qualitative agreement with heart physiology, showcasing the huge potential of the proposed computational framework. I also show how the EMF model can be coupled to a model for the electrical potential in the torso, allowing to obtain numerical ECGs that, in future developments, can be used as a

starting point for model personalization.

Overall, both the left heart and whole heart simulations indicate that the proposed EMF model, together with the related numerical methods, can allow to faithfully capture the physics underlying the heart function. Therefore, the model can serve as an important step towards the construction of digital twins of the human heart, and it can become a fundamental tool in cardiac computational medicine by providing extremely useful and accurate insight for personalized treatment, supporting the design of medical devices and therapies, and allowing to perform in silico clinical trials based on virtual patients.

6.1 Discussion, limitations and future developments

One major limitation of the current model is the simplified model used for valves. Indeed, while neglected by the RIIS method, the dynamic interplay between valves and blood flow has important physiological and clinical implications [7, 81, 161, 197, 206, 218, 359]. While the RIIS method allows to capture the main effects of the valves on the flow, it still requires prescribing the valve kinematics, which in turn requires fine and a priori tuning of the duration of valves' opening and closing phases. Moreover, it does not account for the way the valve is attached to the cardiac wall. Finally, the valves move coherently with the motion of the fluid domain: this allows them to follow the motion of the atrioventricular plane during ventricular shortening, but the resulting displacement is not physically derived. All these issues can be overcome by including a suitable FSI model of valves, featuring contact between leaflets. Although few studies model valve FSI by means of the ALE approach [7, 301], immersed approaches are more effective in handling the large leaflet displacements and, most notably, the topological changes induced by contact. Therefore, a combination of ALE for ventricular and arterial walls and an immersed method for valves appears to be the most suited approach [42, 116, 175, 240, 317].

Moreover, the cardiac conduction system is surrogated by applying localized stimuli, timed to replicate the typical activation sequence of the heart. While effective, this approach is an approximation with respect to the com-

plex network of specialized cells that conduct the electrical signal through the heart. These can be included in the model by introducing geometrically multiscale electrophysiology models [78, 89, 191, 285, 341], including explicit representation of the SAN, AVN, Purkinje network, and electrically conducting bundles that form the CCS. The inclusion of such features can significantly improve the physiological accuracy of the electrophysiology solution. This can become more relevant if pathological conditions such as bundle branch blocks are considered [233, 341, 347].

In terms of numerical methods, the proposed approach can be made more efficient by introducing suitable time adaptivity schemes [34, 105, 214, 348]. Indeed, the alternating systolic and diastolic phases are characterized by very different flow regimes. The current approach uses the time step required by the fast systolic dynamics for the whole heartbeat, in practice resulting in an excessively fine time discretization during the diastolic phase. Dynamic adaptation of the time step during the simulation may lead to significant savings in terms of computational time.

Finally, the model may benefit from the introduction of automated parameter estimation procedures, facilitating the personalization for new patients and the assimilation of clinical data. The problem of model calibration can typically be expressed in terms of an optimization problem: methods for its solution would require a large amount of simulations. Given the complexity and computational cost of each, this is, in practice, unfeasible. The simulations of this thesis were calibrated manually by trial and error. This issue can be overcome by introducing suitable surrogate models, i.e. by training models of reduced complexity to reproduce the input-output relation between the parameters of the EMF model and the quantities of interest [150, 264]. This can be achieved e.g. by means of artificial neural networks [273, 276], Gaussian processes [178], or ad-hoc surrogate models [274]. Once the reduced model is built, it can be used in place of the full model for a variety of tasks, including sensitivity analysis, uncertainty quantification and parameter identification.

Appendix A

Relaxation and convergence acceleration

We provide the definition of convergence relaxation and acceleration operators used in the FSI partitioned schemes of Sections 3.2.2 and 3.2.3. We consider a generic sequence of vectors $\mathbf{x}_{(k)}, k \in \{0, 1, 2, \dots\}$, with $\mathbf{x}_{(k)} \in \mathbb{R}^n$. We denote by $\widetilde{\mathbf{x}}_{(k+1)}$ the proposed $k+1$-th element of the sequence.

A.1 Static relaxation (SR)

The new element of the sequence is given by [18, 63, 189]

$$\mathbf{x}_{(k+1)} = \lambda \widetilde{\mathbf{x}}_{(k+1)} + (1-\lambda)\mathbf{x}_{(k)} \ ,$$

where $\lambda \in (0, 1]$ is a suitable parameter whose choice is critical to the convergence of the sequence. Large values of λ typically lead to faster convergence (when convergence occurs), but large values of λ may cause the scheme to diverge [63].

A.2 Aitken acceleration (AitA)

Given $\lambda_0 > 0$, we set [18, 189, 222]

$$\mathbf{x}_{(k+1)} = \lambda_{(k)} \widetilde{\mathbf{x}}_{(k+1)} + (1-\lambda_{(k)})\mathbf{x}_{(k)} \ ,$$

$$\lambda_{(k+1)} = \lambda_{(k)} \frac{\widetilde{\mathbf{x}}_{(k)} \cdot \left(\widetilde{\mathbf{x}}_{(k+1)} - \mathbf{x}_{(k)} - \widetilde{\mathbf{x}}_{(k)} + \mathbf{x}_{(k-1)} \right)}{\left| \widetilde{\mathbf{x}}_{(k+1)} - \mathbf{x}_{(k)} - \widetilde{\mathbf{x}}_{(k)} + \mathbf{x}_{(k-1)} \right|} .$$

This scheme typically improves the convergence with respect to static relaxation [189]. However, the choice of the initial relaxation parameter λ_0 is problem dependent and requires manual tuning [189].

A.3 Anderson acceleration (AndA)

Anderson acceleration [11, 106, 353], also known as Anderson mixing, can be interpreted as a multi-secant method [106] or as a non-linear generalization of GMRES [353]. It is based on computing the new iterate making use of the previous m ones, with m a suitable, user-defined integer parameter. While generally used for self-consistent field iterations in the computation of electronic structures [106], it has been also applied to domain decomposition [353] and multiphysics problems [43] and can be used to accelerate the convergence of FSI partitioned schemes [216].

The procedure behind Anderson acceleration can be detailed as follows [353]. Given an initial guess $\mathbf{x}_{(0)} \in \mathbb{R}^n$, consider the fixed-point iteration

$$\mathbf{x}_{(k+1)} = \mathbf{g}(\mathbf{x}_{(k)}) \qquad k = 0, 1, 2, \ldots$$

for solving $\mathbf{x} = \mathbf{g}(\mathbf{x})$. Then, given $m \in \mathbb{N}$ and an initial guess $\mathbf{x}_0$, the Anderson acceleration of the sequence $\mathbf{x}_{(k)}$ can be obtained as follows:

1. set $m_{(k)} = \min\{m, k\}$;
2. set $F_{(k)} = \left[\mathbf{f}_{k-m_{(k)}}, \mathbf{f}_{k-m_{(k)}+1}, \ldots, \mathbf{f}_{(k)} \right]$, where $\mathbf{f}_i = \mathbf{g}(\mathbf{x}_i) - \mathbf{x}_i$;
3. find $\boldsymbol{\alpha}_{(k)} = \left[\alpha_{(k),0}, \alpha_{(k),1}, \ldots, \alpha_{(k),m_{(k)}} \right]^T = \arg\min_{\boldsymbol{\alpha} \in A} \left\| F_{(k)} \boldsymbol{\alpha} \right\|$, with
$$A = \left\{ \boldsymbol{\alpha} = \left[\alpha_0, \alpha_1, \ldots, \alpha_{m_{(k)}} \right]^T \text{ such that } \sum_{i=0}^{m_{(k)}} \alpha_i = 1 \right\} ;$$
4. set $\mathbf{x}_{(k+1)} = \sum_{i=0}^{m_{(k)}} \alpha_{(k),i} \mathbf{g}(\mathbf{x}_{(k-m_{(k)}+i)})$.

Appendix B

Model parameters

We report tables with the numerical values of the parameters used in the numerical experiments.

B.1 Benchmark for strong FSI comparison

We report in Table B.1 the values of physical parameters for the simulations of Section 3.4. Table B.2 reports the parameters used for partitioned schemes, including those of convergence relaxation and acceleration methods.

B.2 Benchmark for strong and loose FSI comparison

We report in Table B.3 the parameters used in the idealized benchmark of Section 3.5 for the comparison between strong and loose FSI coupling. For the sake of brevity, we only report parameters whose values are different from the corresponding ones in Table B.1. In Table B.4, we report the parameters for the simulation of Section 3.5.5 whose values are different from those in Tables B.1 and B.3.

	Parameter	Value	
Guccione	c	8.8×10^2	Pa
	a_{ff}	8	
	a_{ss}	6	
	a_{nn}	3	
	a_{fs}	12	
	a_{fn}	3	
	a_{sn}	3	
	κ	5×10^4	Pa
Active stress	$T_{\mathrm{act}}^{\mathrm{max}}$	60×10^3	Pa
	t_{act}^{0}	0	ms
	$t_{\mathrm{act}}^{\mathrm{peak}}$	100	ms
	p_{act}	1	
Mechanics	ρ_{s}	1000	$\mathrm{kg/m^3}$
	$K_{\perp}^{\mathrm{epi}}$	2×10^5	$\mathrm{Pa/m}$
	$K_{\parallel}^{\mathrm{epi}}$	2×10^4	$\mathrm{Pa/m}$
	$C_{\perp}^{\mathrm{epi}}$	2×10^4	$\mathrm{Pa \cdot s/m}$
	$C_{\parallel}^{\mathrm{epi}}$	2×10^3	$\mathrm{Pa \cdot s/m}$
Fluid dynamics	ρ_{f}	1060	$\mathrm{kg/m^3}$
	μ_{f}	3.5×10^{-3}	$\mathrm{Pa \cdot s}$
	p_{AV}	6000	Pa
	R_{AV}	10^7	$\mathrm{kg/(s \cdot m^4)}$
	p_{MV}	1333	Pa

Table B.1: Parameters for the idealized ventricular simulation used in the comparison among strongly coupled FSI schemes.

B.3 Left heart model

We report in this section the parameter values used for the simulation described in Chapter 4.

Table B.5 reports parameters for the electrophysiology model. The conductivities of the monodomain equation were tuned so as to obtain conduction velocities 0.6 m/s, 0.4 m/s and 0.2 m/s along fibers, sheets and normal-to-fiber directions, respectively. The parameters of the TTP06 ionic model are

	Parameter	Value	
Dirichlet-Neumann	λ (SR)	0.005	
	λ_0 (AitA)	0.005	
	m (AndA)	10	
Robin-Neumann	α	5000	$\mathrm{kg}/(\mathrm{m}^2 \cdot \mathrm{s})$
	λ (SR)	1.0	
	λ_0 (AitA)	1.0	
	m (AndA)	10	

Table B.2: Parameters of the partitioned schemes used in the comparison among strongly coupled FSI schemes.

those of the original paper [321].

We report in Table B.7 the parameters used for the RDQ20-MF force generation model. For the sake of brevity, we only report those parameters that are different from the original setting described in [272].

Table B.6 reports parameters for the solid mechanics model. The parameters for the Guccione constitutive law and for boundary conditions were taken from [275].

We list in Table B.8 the parameters used in the fluid dynamics model. Valve half-thicknesses $\varepsilon_{\mathrm{MV}}$ and $\varepsilon_{\mathrm{AV}}$ were chosen to match literature data [100, 291]. Resistances R_{MV}, R_{AV} were chosen to be sufficiently high to guarantee minimal spurious flow through valves without hindering the conditioning of the FSI system. Finally, Tables B.9 and B.10 display the parameters of the circulation model.

B.4 Whole heart model

We report the parameter values used for the whole-heart simulation described in Chapter 5. We only report parameters whose values are different from the corresponding ones in the LH simulation, as listed in Appendix B.3.

Table B.11 reports monodomain conductivities in the ventricular and atrial subdomains, as well as the intra- and extracellular conductivities used in

	Parameter	Value	Unit
Electrophysiology	σ_m^f	1.68	m^2/s
	σ_m^s	0.769	m^2/s
	σ_m^n	0.248	m^2/s
Force generation	a_{XB}	500	kPa
Mechanics	$K_\perp^{epi}$		Pa/m
	$K_\parallel^{epi}$	2	Pa/m
	$C_\perp^{epi}$	2	$Pa \cdot s/m$
	$C_\parallel^{epi}$	2	$Pa \cdot s/m$
Fluid	p_{MV}	1333	Pa
	R_{AV}	1.3	$kg/(s \cdot m^4)$

Table B.3: Parameters for the idealized ventricular simulation used in the comparison between strong and loose FSI coupling.

	Parameter	Value	Unit
Electrophysiology	σ_m^f	2	m^2/s
	σ_m^s	1.05	m^2/s
	σ_m^n	0.55	m^2/s
Mechanics	$K_\perp^{epi}$	200	kPa/m
	$K_\parallel^{epi}$	20	kPa/m
	$C_\perp^{epi}$	20	$kPa \cdot s/m$
	$C_\parallel^{epi}$	2	$kPa \cdot s/m$
Neo-Hooke	μ_{NH}	5000	kPa
	κ_{NH}	5000	kPa
Fluid	R_{AV}		$kg/(s \cdot m^4)$

Table B.4: Parameters for the realistic ventriular simulation used in the comparison between strong and loose FSI coupling.

	Parameter	Value	
Monodomain	χ	1400	$1/\mathrm{cm}$
	C_m	1	$\mu\mathrm{F}/\mathrm{cm}^2$
Conductivities	$\sigma_m^l/(\chi C_m)$	2.00×10^{-4}	m^2/s
	$\sigma_m^t/(\chi C_m)$	1.05×10^{-4}	m^2/s
	$\sigma_m^n/(\chi C_m)$	0.55×10^{-4}	m^2/s
Stimulus	A_{app}/C_m	25.71	V/s
	σ_{app}	2.5×10^{-3}	m
	T_{app}	3	ms

Table B.5: LH model. Parameters used for electrophysiology.

computing the extracellular potential in (5.1). All other parameters are the same as in the LH model (see Appendix B.3). The parameters for the TTP06 and CRN ionic models are the same as in the original papers [79, 321]. Table B.12 reports the parameters for the force generation model in the LA and RA, and Table B.13 reports those used for the mechanics model. Finally, Table B.14 reports the parameters for the circulation model.

	Parameter	Value	
	ρ_s	1000	kg/m^2
Guccione (atrium and ventricle)	c	8.8×10^2	Pa
	a_{ff}	8	
	a_{ss}	6	
	a_{nn}	3	
	a_{fs}	12	
	a_{fn}	3	
	a_{sn}	3	
	κ	5×10^4	Pa
Atrioventricular ring	μ	5×10^6	Pa
	κ	10^6	Pa
Ascending aorta	μ	5.25×10^5	Pa
	κ	10^6	Pa
Boundary conditions	$K_{\perp}^{epi}$	2×10^5	Pa/m
	$K_{\parallel}^{epi}$	2×10^4	Pa/m
	$C_{\perp}^{epi}$	2×10^4	$Pa \cdot s/m$
	$C_{\parallel}^{epi}$	2×10^3	$Pa \cdot s/m$
Initial conditions	p_0^{LA}	9.75	mmHg
	p_0^{ring}	11.25	mmHg
	p_0^{LV}	11.25	mmHg
	p_0^{AA}	80	mmHg
Interface regularization	ψ_{th}^{LV}	0.2	
	ψ_{th}^{LA}	0.1	

Table B.6: LH model. Parameters used for solid mechanics.

Parameter	Value	
γ	30	
k_d	0.36	
α_{k_d}	-0.2083	
K_{off}	8	$1/\text{s}$
K_{basic}	4	$1/\text{s}$
μ_{fp}^0	32.255	$1/\text{s}$
μ_{fp}^1	0.768	$1/\text{s}$
a_{XB}	8.9491×10^8	Pa
SL_0	2.1	µm

Table B.7: LH model. Parameters used in the RDQ20-MF force generation model.

	Parameter	Value	
Navier-Stokes	ρ_{f}	1060	kg/m^3
	μ_{f}	3.5×10^{-3}	$\text{Pa} \cdot \text{s}$
Valve modeling	R_{MV}, R_{AV}	10^5	$\text{kg}/(\text{m} \cdot \text{s})$
	ε_{MV}, ε_{AV}	0.75×10^{-3}	m
	$\Delta t_{\text{MV}}^{\text{open}}$	10	ms
	$\Delta t_{\text{AV}}^{\text{open}}$	10	ms
	$\Delta t_{\text{MV}}^{\text{close}}$	30	ms
	$\Delta t_{\text{AV}}^{\text{close}}$	80	ms
	χ_{MV}, χ_{AV}	-3	

Table B.8: LH model. Parameters used in the fluid dynamics model.

	Parameter	Value	
Systemic arteries	$R_{\mathrm{AR}}^{\mathrm{SYS}}$	0.45	$\mathrm{mmHg \cdot s/mL}$
	$C_{\mathrm{AR}}^{\mathrm{SYS}}$	2.19	$\mathrm{mL/mmHg}$
	$L_{\mathrm{AR}}^{\mathrm{SYS}}$	2.7×10^{-3}	$\mathrm{mmHg \cdot s^2/mL}$
	$R_{\mathrm{upstream}}^{\mathrm{SYS}}$	0.07	$\mathrm{mmHg \cdot s/mL}$
	$p_{\mathrm{AR}}^{\mathrm{SYS}}(0)$	80	mmHg
	$Q_{\mathrm{AR}}^{\mathrm{SYS}}(0)$	66.5775	mL/s
Systemic veins	$R_{\mathrm{VEN}}^{\mathrm{SYS}}$	0.26	$\mathrm{mmHg \cdot s/mL}$
	$C_{\mathrm{VEN}}^{\mathrm{SYS}}$	60	$\mathrm{mL/mmHg}$
	$L_{\mathrm{VEN}}^{\mathrm{SYS}}$	5×10^{-4}	$\mathrm{mmHg \cdot s^2/mL}$
	$p_{\mathrm{VEN}}^{\mathrm{SYS}}(0)$	30.9029	mmHg
	$Q_{\mathrm{VEN}}^{\mathrm{SYS}}(0)$	89.6295	mL/s
Pulmonary arteries	$R_{\mathrm{AR}}^{\mathrm{PUL}}$	0.05	$\mathrm{mmHg \cdot s/mL}$
	$C_{\mathrm{AR}}^{\mathrm{PUL}}$	10	$\mathrm{mL/mmHg}$
	$L_{\mathrm{AR}}^{\mathrm{PUL}}$	5×10^{-4}	$\mathrm{mmHg \cdot s^2/mL}$
	$p_{\mathrm{AR}}^{\mathrm{PUL}}(0)$	20.0	mmHg
	$Q_{\mathrm{AR}}^{\mathrm{PUL}}(0)$	69.3166	mL/s
Pulmonary veins	$R_{\mathrm{VEN}}^{\mathrm{PUL}}$	0.025	$\mathrm{mmHg \cdot s/mL}$
	$C_{\mathrm{VEN}}^{\mathrm{PUL}}$	38.4	$\mathrm{mL/mmHg}$
	$L_{\mathrm{VEN}}^{\mathrm{PUL}}$	2.083×10^{-4}	$\mathrm{mmHg \cdot s^2/mL}$
	$p_{\mathrm{VEN}}^{\mathrm{PUL}}(0)$	17.0	mmHg
	$Q_{\mathrm{VEN}}^{\mathrm{PUL}}(0)$	105.523	mL/s

Table B.9: LH model. Parameters used in the circulation model: systemic and pulmonary circulation.

	Parameter	Value	
Valves	R_{min}	7.5×10^{-3}	$\text{mmHg} \cdot \text{s/mL}$
	R_{max}	7.5×10^{4}	$\text{mmHg} \cdot \text{s/mL}$
Right atrium	E_{A}	0.06	mmHg/mL
	E_{B}	0.07	mmHg/mL
	t_{C}	0.8	
	T_{C}	0.17	
	T_{R}	0.17	
	$V_{0,\text{RA}}$	4	mL
	$V_{\text{RA}}(0)$	64.1702	mL
Right ventricle	E_{A}	0.55	mmHg/mL
	E_{B}	0.05	mmHg/mL
	t_{C}	0.0	
	T_{C}	0.34	
	T_{R}	0.15	
	$V_{0,\text{RV}}$	16	mL
	$V_{\text{RV}}(0)$	148.9384	mL

Table B.10: LH model. Parameters used in the circulation model: right heart.

	Parameter	Value	
Ventricular conductivities	$\sigma_m^l/(\chi C_m)$	2.00×10^{-4}	m^2/s
	$\sigma_m^t/(\chi C_m)$	1.05×10^{-4}	m^2/s
	$\sigma_m^n/(\chi C_m)$	0.55×10^{-4}	m^2/s
	$\sigma_i^l/(\chi C_m)$	8.67×10^{-4}	m^2/s
	$\sigma_i^t/(\chi C_m)$	3.89×10^{-4}	m^2/s
	$\sigma_i^n/(\chi C_m)$	0.86×10^{-4}	m^2/s
	$\sigma_e^l/(\chi C_m)$	2.60×10^{-4}	m^2/s
	$\sigma_e^t/(\chi C_m)$	1.53×10^{-4}	m^2/s
	$\sigma_e^n/(\chi C_m)$	1.53×10^{-4}	m^2/s
Atrial conductivities	$\sigma_m^l/(\chi C_m)$	7.00×10^{-4}	m^2/s
	$\sigma_m^t/(\chi C_m)$	1.41×10^{-4}	m^2/s
	$\sigma_m^n/(\chi C_m)$	1.41×10^{-4}	m^2/s
	$\sigma_i^l/(\chi C_m)$	3×10^{-3}	m^2/s
	$\sigma_i^t/(\chi C_m)$	2×10^{-4}	m^2/s
	$\sigma_i^n/(\chi C_m)$	2×10^{-4}	m^2/s
	$\sigma_e^l/(\chi C_m)$	9.1×10^{-4}	m^2/s
	$\sigma_e^t/(\chi C_m)$	5.37×10^{-4}	m^2/s
	$\sigma_e^n/(\chi C_m)$	5.37×10^{-4}	m^2/s

Table B.11: Whole heart model. Parameters used for electrophysiology.

Parameter	Value	
γ	20	
k_d	0.865	
α_{k_d}	-1.25	
K_{off}	180	1/s
K_{basic}	20	1/s
μ^0_{fp}	32.235	1/s
μ^1_{fp}	0.768	1/s
a_{XB}	30×10^7	Pa
SL_0	2.2	µm

Table B.12: Whole heart model. Parameters used in the RDQ20-MF force generation model for the atria. Ventricular parameters are the same as in the LH model (see Table B.7). The table lists only parameters whose values are different from those in the original paper [272].

	Parameter	Value	
Guccione (LA)	c	1.76×10^3	Pa
Guccione (RA)	c	1.47×10^3	Pa
Valve rings	μ	5.25×10^5	Pa
	κ	10^6	Pa
Ascending aorta	μ	5.25×10^5	Pa
	κ	10^6	Pa
Pulmonary trunk	μ	5.25×10^5	Pa
	κ	10^6	Pa
Initial conditions	p_0^{LA}	8.25	mmHg
	p_0^{RA}	8.25	mmHg
	p_0^{LV}	6	mmHg
	p_0^{RV}	6	mmHg
	p_0^{AA}	80	mmHg
	p_0^{PT}	30	mmHg

Table B.13: Whole heart model. Parameters used for solid mechanics. Only parameters that are different from those listed in Table B.6 are reported.

	Parameter	Value	
Systemic arteries	$R_{\text{AR}}^{\text{SYS}}$	0.45	$\text{mmHg} \cdot \text{s/mL}$
	$C_{\text{AR}}^{\text{SYS}}$	2.19	mL/mmHg
	$L_{\text{AR}}^{\text{SYS}}$	2.7×10^{-3}	$\text{mmHg} \cdot \text{s}^2\text{/mL}$
	$R_{\text{upstream}}^{\text{SYS}}$	0.07	$\text{mmHg} \cdot \text{s/mL}$
	$p_{\text{AR}}^{\text{SYS}}(0)$	80	mmHg
	$Q_{\text{AR}}^{\text{SYS}}(0)$	0.0	mL/s
Systemic veins	$R_{\text{VEN}}^{\text{SYS}}$	0.26	$\text{mmHg} \cdot \text{s/mL}$
	$C_{\text{VEN}}^{\text{SYS}}$	60	mL/mmHg
	$L_{\text{VEN}}^{\text{SYS}}$	5×10^{-4}	$\text{mmHg} \cdot \text{s}^2\text{/mL}$
	$p_{\text{VEN}}^{\text{SYS}}(0)$	17.0	mmHg
	$Q_{\text{VEN}}^{\text{SYS}}(0)$	0.0	mL/s
Pulmonary arteries	$R_{\text{AR}}^{\text{PUL}}$	0.05	$\text{mmHg} \cdot \text{s/mL}$
	$C_{\text{AR}}^{\text{PUL}}$	10	mL/mmHg
	$L_{\text{AR}}^{\text{PUL}}$	5×10^{-4}	$\text{mmHg} \cdot \text{s}^2\text{/mL}$
	$R_{\text{upstream}}^{\text{PUL}}$	0.0032	$\text{mmHg} \cdot \text{s/mL}$
	$p_{\text{AR}}^{\text{PUL}}(0)$	30.0	mmHg
	$Q_{\text{AR}}^{\text{PUL}}(0)$	0	mL/s
Pulmonary veins	$R_{\text{VEN}}^{\text{PUL}}$	0.02	$\text{mmHg} \cdot \text{s/mL}$
	$C_{\text{VEN}}^{\text{PUL}}$	38.4	mL/mmHg
	$L_{\text{VEN}}^{\text{PUL}}$	2.083×10^{-4}	$\text{mmHg} \cdot \text{s}^2\text{/mL}$
	$p_{\text{VEN}}^{\text{PUL}}(0)$	13.58	mmHg
	$Q_{\text{VEN}}^{\text{PUL}}(0)$	0.0	mL/s

Table B.14: Whole heart model. Parameters used in the circulation model for the systemic and pulmonary circulation.

Appendix C

List of acronyms

AA	*ascending aorta*
ALE	*Arbitrary Lagrangian Eulerian*
AMG	*algebraic multigrid*
AV	*aortic valve*
AVN	*atrioventricular node*
BSA	*body surface area*
CCS	*cardiac conduction system*
CFD	*computational fluid dynamics*
CG	*conjugate gradient*
CO	*cardiac output*
DN	*Dirichlet-Neumann*
DoF	*degree of freedom*
DTI	*diffusion-tensor imaging*
ECG	*electrocardiogram*
EDV	*end-diastolic volume*
EF	*ejection fraction*
EMF	*electro-mechanics-fluid dynamics*
ESV	*end-systolic volume*
FEM	*finite element method*
FSI	*fluid-structure interaction*
HPC	*high-performance computing*
ICI	*ionic current interpolation*

ILI	*isovolumetric loss index*
IMEX	*implicit-explicit*
IVC	*isovolumetric contraction*
IVR	*isovolumetric relaxation*
LA	*left atrium*
LDRBM	*Laplace-Dirichlet rule-based method*
LFS	*longitudinal fractional shortening*
LH	*left heart*
LV	*left ventricle*
MEF	*mechano-electric feedback*
MV	*mitral valve*
ODE	*ordinary differential equation*
PDE	*partial differential equation*
PT	*pulmonary trunk*
PV	*pulmonary valve*
RA	*right atrium*
RH	*right heart*
RIIS	*Resistive Immersed Implicit Surface*
RN	*Robin-Neumann*
RR	*Robin-Robin*
RV	*right ventricle*
SAN	*sinoatrial node*
SV	*stroke volume*
TV	*tricuspid valve*

Bibliography

[1] P. C. Africa. lifex: a flexible, high performance library for the numerical solution of complex finite element problems. *arXiv preprint arXiv:2207.14668*, 2022.

[2] P. C. Africa, R. Piersanti, M. Fedele, L. Dede', and A. Quarteroni. lifex–heart module: a high-performance simulator for the cardiac function package 1: Fiber generation. *arXiv preprint arXiv:2201.03303*, 2022.

[3] P. C. Africa, M. Salvador, P. Gervasio, L. Dede, and A. Quarteroni. A matrix-free high-order solver for the numerical solution of cardiac electrophysiology. *arXiv preprint arXiv:2205.05136*, 2022.

[4] F. Ahmad, S. Soe, N. White, R. Johnston, I. Khan, J. Liao, M. Jones, R. Prabhu, I. Maconochie, and P. Theobald. Region-specific microstructure in the neonatal ventricles of a porcine model. *Annals of Biomedical Engineering*, 46(12):2162–2176, 2018.

[5] M. G. Al-Azawy, A. Turan, and A. Revell. Investigating the impact of non-Newtonian blood models within a heart pump. *International Journal for Numerical Methods in Biomedical Engineering*, 33(1):e02780, 2017.

[6] A. L. Alexander, K. M. Hasan, M. Lazar, J. S. Tsuruda, and D. L. Parker. Analysis of partial volume effects in diffusion-tensor mri. *Magnetic Resonance in Medicine: An Official Journal of the International Society for Magnetic Resonance in Medicine*, 45(5):770–780, 2001.

[7] Y. Alharbi, A. Al Abed, A. A. Bakir, N. H. Lovell, D. W. Muller, J. Otton, and S. Dokos. Fluid structure computational model of sim-

ulating mitral valve motion in a contracting left ventricle. *Computers in Biology and Medicine*, 148:105834, 2022.

[8] R. R. Aliev and A. V. Panfilov. A simple two-variable model of cardiac excitation. *Chaos, Solitons & Fractals*, 7(3):293–301, 1996.

[9] D. G. Allen and J. C. Kentish. The cellular basis of the length-tension relation in cardiac muscle. *Journal of Molecular and Cellular Cardiology*, 17(9):821–840, 1985.

[10] D. Ambrosi and S. Pezzuto. Active stress vs. active strain in mechanobiology: constitutive issues. *Journal of Elasticity*, 107(2):199–212, 2012.

[11] D. G. Anderson. Iterative procedures for nonlinear integral equations. *Journal of the ACM*, 1965.

[12] R. H. Anderson, M. Smerup, D. Sanchez-Quintana, M. Loukas, and P. P. Lunkenheimer. The three-dimensional arrangement of the myocytes in the ventricular walls. *Clinical Anatomy: The Official Journal of the American Association of Clinical Anatomists and the British Association of Clinical Anatomists*, 22(1):64–76, 2009.

[13] H. J. Arevalo, F. Vadakkumpadan, E. Guallar, A. Jebb, P. Malamas, K. C. Wu, and N. A. Trayanova. Arrhythmia risk stratification of patients after myocardial infarction using personalized heart models. *Nature Communications*, 7(1):1–8, 2016.

[14] D. Arndt, W. Bangerth, B. Blais, T. C. Clevenger, M. Fehling, A. V. Grayver, T. Heister, L. Heltai, M. Kronbichler, M. Maier, P. Munch, J. Pelteret, R. Rastak, I. Thomas, B. Turcksin, Z. Wang, and D. Wells. The `deal.II` library, version 9.2. *Journal of Numerical Mathematics*, 28(3):131–146, 2020.

[15] D. Arndt, W. Bangerth, D. Davydov, T. Heister, L. Heltai, M. Kronbichler, M. Maier, J. Pelteret, B. Turcksin, and D. Wells. The `deal.II` finite element library: design, features, and insights. *Computers & Mathematics with Applications*, 81:407–422, 2021.

[16] M. Astorino, J.-F. Gerbeau, O. Pantz, and K.-F. Traoré. Fluid–structure interaction and multi-body contact: application to aor-

tic valves. *Computer Methods in Applied Mechanics and Engineering*, 198(45-46):3603–3612, 2009.

[17] C. M. Augustin, A. Crozier, A. Neic, A. J. Prassl, E. Karabelas, T. Ferreira da Silva, J. F. Fernandes, F. Campos, T. Kuehne, and G. Plank. Patient-specific modeling of left ventricular electromechanics as a driver for haemodynamic analysis. *EP Europace*, 18:iv121–iv129, 2016.

[18] S. Badia, F. Nobile, and C. Vergara. Fluid-structure partitioned procedures based on Robin transmission conditions. *Journal of Computational Physics*, 227:7021–7051, 2008.

[19] S. Badia, F. Nobile, and C. Vergara. Robin-Robin preconditioned Krylov methods for fluid-structure interaction problems. *Computer Methods in Applied Mechanics and Engineering*, 198:2768–2784, 2009.

[20] S. Badia, A. Quaini, and A. Quarteroni. Modular vs. non-modular preconditioners for fluid–structure systems with large added-mass effect. *Computer Methods in Applied Mechanics and Engineering*, 197(49-50):4216–4232, 2008.

[21] B. Baillargeon, N. Rebelo, D. D. Fox, R. L. Taylor, and E. Kuhl. The living heart project: a robust and integrative simulator for human heart function. *European Journal of Mechanics-A/Solids*, 48:38–47, 2014.

[22] A. A. Bakir, A. Al Abed, M. C. Stevens, N. H. Lovell, and S. Dokos. A multiphysics biventricular cardiac model: Simulations with a left-ventricular assist device. *Frontiers in Physiology*, 9:1259, 2018.

[23] J. M. Ball. Convexity conditions and existence theorems in nonlinear elasticity. *Archive for Rational Mechanics and Analysis*, 63(4):337–403, 1976.

[24] J. W. Banks, W. D. Henshaw, and D. W. Schwendeman. An analysis of a new stable partitioned algorithm for FSI problems. Part I: Incompressible flow and elastic solids. *Journal of Computational Physics*, 269:108–137, 2014.

[25] N. A. Barnafi, L. F. Pavarino, and S. Scacchi. Parallel inexact newton-krylov and quasi-newton solvers for nonlinear elasticity. *arXiv preprint arXiv:2203.05610*, 2022.

[26] C. Bartolucci, E. Passini, J. Hyttinen, M. Paci, and S. Severi. Simulation of the effects of extracellular calcium changes leads to a novel computational model of human ventricular action potential with a revised calcium handling. *Frontiers in Physiology*, 11:314, 2020.

[27] A. M. Bavo, G. Rocatello, F. Iannaccone, J. Degroote, J. Vierendeels, and P. Segers. Fluid-structure interaction simulation of prosthetic aortic valves: comparison between immersed boundary and arbitrary Lagrangian-Eulerian techniques for the mesh representation. *PloS One*, 11(4):e0154517, 2016.

[28] J. D. Bayer, R. C. Blake, G. Plank, and N. A. Trayanova. A novel rule-based algorithm for assigning myocardial fiber orientation to computational heart models. *Annals of Biomedical Engineering*, 40(10):2243–2254, 2012.

[29] Y. Bazilevs, V. M. Calo, J. A. Cottrell, T. J. R. Hughes, A. Reali, and Scovazzi. Variational multiscale residual-based turbulence modeling for large eddy simulation of incompressible flows. *Computer Methods in Applied Mechanics and Engineering*, 197(1-4):173–201, 2007.

[30] Y. Bazilevs, V. M. Calo, T. J. R. Hughes, and Y. Zhang. Isogeometric fluid-structure interaction: theory, algorithms, and computations. *Computational Mechanics*, 43(1):3–37, 2008.

[31] Y. Bazilevs, K. Takizawa, and T. E. Tezduyar. *Computational fluid-structure interaction: methods and applications*. John Wiley & Sons, 2013.

[32] A. Benchimol and J. G. Ellis. A study of the period of isovolumic relaxation in normal subjects and in patients with heart disease. *The American Journal of Cardiology*, 19(2):196–206, 1967.

[33] E. J. Benjamin, M. J. Blaha, S. E. Chiuve, M. Cushman, S. R. Das, R. Deo, S. D. De Ferranti, J. Floyd, M. Fornage, C. Gillespie, et al. Heart disease and stroke statistics – 2017 update: a report from the american heart association. *Circulation*, 135(10):e146–e603, 2017.

[34] S. Berrone and M. Marro. Space–time adaptive simulations for unsteady navier–stokes problems. *Computers & Fluids*, 38(6):1132–1144, 2009.

[35] D. Bers. *Excitation-contraction coupling and cardiac contractile force*, volume 237. Springer Science & Business Media, 2001.

[36] C. Bertoglio and A. Caiazzo. A tangential regularization method for backflow stabilization in hemodynamics. *Journal of Computational Physics*, 261:162–171, 2014.

[37] A. Bishop, P. White, P. Oldershaw, R. Chaturvedi, C. Brookes, and A. Redington. Clinical application of the conductance catheter technique in the adult human right ventricle. *International Journal of Cardiology*, 58(3):211–221, 1997.

[38] P. J. Blanco, M. Discacciati, and A. Quarteroni. Modeling dimensionally-heterogeneous problems: analysis, approximation and applications. *Numerische Mathematik*, 119(2):299–335, 2011.

[39] P. J. Blanco and R. A. Feijóo. A 3D-1D-0D computational model for the entire cardiovascular system. *Mecánica Computacional*, 29(59):5887–5911, 2010.

[40] D. Bluestein and S. Einav. Transition to turbulence in pulsatile flow through heart valves – a modified stability approach. *Journal of Biomechanical Engineering*, 116(4):477–487, 1994.

[41] G. G. Blume, C. J. Mcleod, M. E. Barnes, J. B. Seward, P. A. Pellikka, P. M. Bastiansen, and T. S. Tsang. Left atrial function: physiology, assessment, and clinical implications. *European Journal of Echocardiography*, 12(6):421–430, 2011.

[42] D. Boffi, N. Cavallini, and L. Gastaldi. The finite element immersed boundary method with distributed lagrange multiplier. *SIAM Journal on Numerical Analysis*, 53(6):2584–2604, 2015.

[43] J. W. Both, N. A. Barnafi, F. A. Radu, P. Zunino, and A. Quarteroni. Iterative splitting schemes for a soft material poromechanics model. *Computer Methods in Applied Mechanics and Engineering*, 388:114183, 2022.

[44] M. Boulakia, S. Cazeau, M. A. Fernández, J.-F. Gerbeau, and N. Zemzemi. Mathematical modeling of electrocardiograms: a numerical study. *Annals of Biomedical Engineering*, 38(3):1071–1097, 2010.

[45] Y. Bourgault, Y. Coudiere, and C. Pierre. Existence and uniqueness of the solution for the bidomain model used in cardiac electrophysiology. *Nonlinear Analysis: Real WOrld Applications*, 10(1):458–482, 2009.

[46] P. M. Boyle, T. Zghaib, S. Zahid, R. L. Ali, D. Deng, W. H. Franceschi, J. B. Hakim, M. J. Murphy, A. Prakosa, S. L. Zimmerman, et al. Computationally guided personalized targeted ablation of persistent atrial fibrillation. *Nature Biomedical Engineering*, 3(11):870–879, 2019.

[47] J. Brenneisen, A. Daub, T. Gerach, E. Kovacheva, L. Huetter, B. Frohnapfel, O. Dössel, and A. Loewe. Sequential coupling shows minor effects of fluid dynamics on myocardial deformation in a realistic whole-heart model. *Frontiers in Cardiovascular Medicine*, 8(December):1–13, 2021.

[48] J. A. Brown, J. H. Lee, M. A. Smith, D. R. Wells, A. Barrett, C. Puelz, J. P. Vavalle, and B. E. Griffith. Patient-specific immersed finite element-difference model of transcatheter aortic valve replacement. *Annals of Biomedical Engineering*, 2022.

[49] P. N. Brown and Y. Saad. Hybrid krylov methods for nonlinear systems of equations. *SIAM Journal on Scientific and Statistical Computing*, 11(3):450–481, 1990.

[50] M. Bucelli, L. Dede', A. Quarteroni, and C. Vergara. Partitioned and monolithic FSI schemes for the numerical simulation of the heart. *Communications in Computational Physics (accepted)*, 2022.

[51] M. Bucelli, M. G. Gabriel, G. Gigante, A. Quarteroni, and C. Vergara. A stable loosely-coupled scheme for cardiac electro-fluid-structure interaction. *arXiv preprint arXiv:2210.00917*, 2022.

[52] M. Bucelli, M. Salvador, L. Dede', and A. Quarteroni. Multipatch isogeometric analysis for electrophysiology: simulation in a human heart. *Computer Methods in Applied Mechanics and Engineering*, 376:113666, 2021.

[53] M. Bucelli, A. Zingaro, P. C. Africa, I. Fumagalli, L. Dede', and A. Quarteroni. A mathematical model that integrates cardiac electrophysiology, mechanics and fluid dynamics: application to a human left heart. *arXiv preprint arXiv:2208.05551*, 2022.

[54] A. Bueno-Orovio, E. M. Cherry, and F. H. Fenton. Minimal model for human ventricular action potentials in tissue. *Journal of Theoretical Biology*, 253(3):544–560, 2008.

[55] M. Bukač, S. Čanić, R. Glowinski, J. Tambača, and A. Quaini. Fluid–structure interaction in blood flow capturing non-zero longitudinal structure displacement. *Journal of Computational Physics*, 235:515–541, 2013.

[56] B. E. U. Burkhardt, C. J. Kellenberger, F. D. Franzoso, J. Geiger, A. Oxenius, and E. R. Valsangiacomo Buechel. Right and left ventricular strain patterns after the atrial switch operation for d-transposition of the great arteries—a magnetic resonance feature tracking study. *Frontiers in Cardiovascular Medicine*, 6:39, 2019.

[57] E. Burman, R. Durst, M. A. Fernández, and J. Guzmán. Fully discrete loosely coupled Robin-Robin scheme for incompressible fluid-structure interaction: stability and error analysis. *Numerische Mathematik*, 151:807–840, 2022.

[58] E. Burman and M. A. Fernández. Explicit strategies for incompressible fluid-structure interaction problems: Nitsche type mortaring versus Robin–Robin coupling. *International Journal for Numerical Methods in Engineering*, 97(10):739–758, 2014.

[59] A. Caballero, W. Mao, R. McKay, C. Primiano, S. Hashim, and W. Sun. New insights into mitral heart valve prolapse after chordae rupture through fluid–structure interaction computational modeling. *Scientific Reports*, 8(1):1–14, 2018.

[60] F. Caforio, C. M. Augustin, J. Alastruey, M. A. Gsell, and G. Plank. A coupling strategy for a first 3D-1D model of the cardiovascular system to study the effects of pulse wave propagation on cardiac function. *Computational Mechanics*, pages 1–20, 2022.

[61] F. O. Campos, M. Orini, R. Arnold, J. Whitaker, M. O'Neill, R. Razavi, G. Plank, B. Hanson, B. Porter, C. A. Rinaldi, et al. Assessing the ability of substrate mapping techniques to guide ventricular tachycardia ablation using computational modelling. *Computers in Biology and Medicine*, 130:104214, 2021.

[62] M. Caruel and L. Truskinovsky. Physics of muscle contraction. *Reports on Progress in Physics*, 81(3):036602, 2018.

[63] P. Causin, J.-F. Gerbeau, and F. Nobile. Added-mass effect in the design of partitioned algorithms for fluid–structure problems. *Computer Methods in Applied Mechanics and Engineering*, 194(42-44):4506–4527, 2005.

[64] L. A. Charawi. Isogeometric overlapping schwarz preconditioners for the bidomain reaction–diffusion system. *Computer Methods in Applied Mechanics and Engineering*, 319:472–490, 2017.

[65] P. H. Charlton, J. Mariscal Harana, S. Vennin, Y. Li, P. Chowienczyk, and J. Alastruey. Modeling arterial pulse waves in healthy aging: a database for in silico evaluation of hemodynamics and pulse wave indexes. *American Journal of Physiology-Heart and Circulatory Physiology*, 317(5):H1062–H1085, 2019.

[66] Y. Cheng, H. Oertel, and T. Schenkel. Fluid-structure coupled CFD simulation of the left ventricular flow during filling phase. *Annals of Biomedical Engineering*, 33(5):567–576, 2005.

[67] C. Chnafa, S. Mendez, and F. Nicoud. Image-based large-eddy simulation in a realistic left heart. *Computers & Fluids*, 94:173–187, 2014.

[68] C. Chnafa, S. Mendez, and F. Nicoud. Image-based simulations show important flow fluctuations in a normal left ventricle: what could be the implications? *Annals of Biomedical Engineering*, 44(11):3346–3358, 2016.

[69] Y. J. Choi, J. Constantino, V. Vedula, N. Trayanova, and R. Mittal. A new mri-based model of heart function with coupled hemodynamics and application to normal and diseased canine left ventricles. *Frontiers in Bioengineering and Biotechnology*, 3:140, 2015.

[70] S. Clay, K. Alfakih, A. Radjenovic, T. Jones, and J. P. Ridgway. Normal range of human left ventricular volumes and mass using steady state free precession MRI in the radial long axis orientation. *Magnetic Resonance Materials in Physics, Biology and Medicine*, 19(1):41–45, 2006.

[71] R. Codina, S. Badia, J. Baiges, and J. Principe. Variational multiscale methods in computational fluid dynamics. *Encyclopedia of Computational Mechanics*, pages 1–28, 2018.

[72] A. Collet. *Numerical modeling of the cardiac mechano-electric feedback within a thermo-electro-mechanical framework. Study of its consequences on arrhythmogenesis.* PhD thesis, Université de Liège, Liège, Belgique, 2015.

[73] P. Colli Franzone, L. Pavarino, and B. Taccardi. Simulating patterns of excitation, repolarization and action potential duration with cardiac bidomain and monodomain models. *Mathematical Biosciences*, 197(1):35–66, 2005.

[74] P. Colli Franzone, L. F. Pavarino, and S. Scacchi. *Mathematical cardiac electrophysiology*, volume 13. Springer, 2014.

[75] P. Colli Franzone, L. F. Pavarino, and S. Scacchi. A numerical study of scalable cardiac electro-mechanical solvers on hpc architectures. *Frontiers in physiology*, 9:268, 2018.

[76] D. Collia, L. Zovatto, and G. Pedrizzetti. Analysis of mitral valve regurgitation by computational fluid dynamics. *APL Bioengineering*, 3(3):036105, 2019.

[77] M. Corti, A. Zingaro, L. Dede, and A. M. Quarteroni. Impact of atrial fibrillation on left atrium haemodynamics: A computational fluid dynamics study. *arXiv preprint arXiv:2202.10893*, 2022.

[78] F. S. Costabal, D. E. Hurtado, and E. Kuhl. Generating Purkinje networks in the human heart. *Journal of Biomechanics*, 49(12):2455–2465, 2016.

[79] M. Courtemanche, R. J. Ramirez, and S. Nattel. Ionic mechanisms underlying human atrial action potential properties: insights from a mathematical model. *American Journal of Physiology-Heart and Circulatory Physiology*, 275(1):H301–H321, 1998.

[80] P. Crosetto, S. Deparis, G. Fourestey, and A. Quarteroni. Parallel algorithms for fluid-structure interaction problems in haemodynamics. *SIAM Journal on Scientific Computing*, 33(4):1598–1622, 2011.

[81] Y. Dabiri, J. Yao, K. L. Sack, G. S. Kassab, and J. M. Guccione. Tricuspid valve regurgitation decreases after mitraclip implantation: Fluid structure interaction simulation. *Mechanics Research Communications*, 97:96–100, 2019.

[82] A. Daub, J. Kriegseis, and B. Frohnapfel. Replication of left ventricular haemodynamics with a simple planar mitral valve model. *Biomedical Engineering/Biomedizinische Technik*, 65(5):595–603, 2020.

[83] A. De Boer, M. S. Van der Schoot, and H. Bijl. Mesh deformation based on radial basis function interpolation. *Computers & structures*, 85(11-14):784–795, 2007.

[84] A. De Vecchi, D. Nordsletten, R. Razavi, G. Greil, and N. P. Smith. Patient specific fluid-structure ventricular modelling for integrated cardiac care. *Medical and Biological Engineering*, 51(11):1261–1270, 2013.

[85] F. De Vita, M. De Tullio, and R. Verzicco. Numerical simulation of the non-newtonian blood flow through a mechanical aortic valve. *Theoretical and Computational Fluid Dynamics*, 30(1):129–138, 2016.

[86] Official `deal.ii` website. https://www.dealii.org/ (last accessed: 23 september 2022).

[87] L. Dede', A. Gerbi, and A. Quarteroni. Segregated algorithms for the numerical simulation of cardiac electromechanics in the left human ventricle. In D. Ambrosi and P. Ciarletta, editors, *The Mathematics of Mechanobiology*, pages 81–116. Springer, 2020.

[88] L. Dede', F. Menghini, and A. Quarteroni. Computational fluid dynamics of blood flow in an idealized left human heart. *International Journal for Numerical Methods in Biomedical Engineering*, 37(11):e3287, 2021.

[89] G. Del Corso, R. Verzicco, and F. Viola. A fast computational model for the electrophysiology of the whole human heart. *Journal of Computational Physics*, 457:111084, 2022.

[90] S. Deparis, M. Discacciati, G. Fourestey, and A. Quarteroni. Fluid–structure algorithms based on steklov–poincaré operators. *Computer*

Methods in Applied Mechanics and Engineering, 195(41-43):5797–5812, 2006.

[91] S. Deparis, D. Forti, P. Gervasio, and A. Quarteroni. INTERNODES: an accurate interpolation-based method for coupling the galerkin solutions of PDEs on subdomains featuring non-conforming interfaces. *Computers & Fluids*, 141:22–41, 2016.

[92] S. Deparis, D. Forti, G. Grandperrin, and A. Quarteroni. FaCSI: A block parallel preconditioner for fluid-structure interaction in hemodynamics. *Journal of Computational Physics*, 327:700–718, 2016.

[93] S. Deparis, G. Grandperrin, and A. Quarteroni. Parallel preconditioners for the unsteady Navier–Stokes equations and applications to hemodynamics simulations. *Computers & Fluids*, 92:253–273, 2014.

[94] W. Dettmer and D. Perić. A computational framework for fluid–structure interaction: finite element formulation and applications. *Computer Methods in Applied Mechanics and Engineering*, 195(41-43):5754–5779, 2006.

[95] G. Di Labbio and L. Kadem. Jet collisions and vortex reversal in the human left ventricle. *Journal of Biomechanics*, 78:155–160, 2018.

[96] J. Donea, S. Giuliani, and J.-P. Halleux. An arbitrary Lagrangian-Eulerian finite element method for transient dynamic fluid-structure interactions. *Computer Methods in Applied Mechanics and Engineering*, 33(1-3):689–723, 1982.

[97] R. Doste, D. Soto-Iglesias, G. Bernardino, A. Alcaine, R. Sebastian, S. Giffard-Roisin, M. Sermesant, A. Berruezo, D. Sanchez-Quintana, and O. Camara. A rule-based method to model myocardial fiber orientation in cardiac biventricular geometries with outflow tracts. *International Journal for Numerical Methods in Biomedical Engineering*, 35(4):e3185, 2019.

[98] D. Durrer, R. T. Van Dam, G. Freud, M. Janse, F. Meijler, and R. Arzbaecher. Total excitation of the isolated human heart. *Circulation*, 41(6):899–912, 1970.

[99] M. N. Dusch, S. R. Thadani, G. S. Dhillon, and M. D. Hope. Diastolic function assessed by cardiac MRI using longitudinal left ventricular fractional shortening. *Clinical Imaging*, 38(5):666–668, 2014.

[100] D. R. Einstein, F. Del Pin, X. Jiao, A. P. Kuprat, J. P. Carson, K. S. Kunzelman, R. P. Cochran, J. M. Guccione, and M. B. Ratcliffe. Fluid–structure interactions of the mitral valve and left heart: comprehensive strategies, past, present and future. *International Journal for Numerical Methods in Biomedical Engineering*, 26(3-4):348–380, 2010.

[101] S. C. Eisenstat and H. F. Walker. Choosing the forcing terms in an inexact newton method. *SIAM Journal on Scientific Computing*, 17(1):16–32, 1996.

[102] K. Emilsson, R. Egerlid, B.-M. Nygren, and B. Wandt. Mitral annulus motion versus long-axis fractional shortening. *Experimental & Clinical Cardiology*, 11(4):302, 2006.

[103] T. S. Eriksson, A. J. Prassl, G. Plank, and G. A. Holzapfel. Influence of myocardial fiber/sheet orientations on left ventricular mechanical contraction. *Mathematics and Mechanics of Solids*, 18(6):592–606, 2013.

[104] J. Fabian, E. Epstein, and N. Coulshed. Duration of phases of left ventricular systole using indirect methods. i. normal subjects. *British Heart Journal*, 34(9):874, 1972.

[105] L. Failer and T. Wick. Adaptive time-step control for nonlinear fluid–structure interaction. *Journal of Computational Physics*, 366:448–477, 2018.

[106] H. R. Fang and Y. Saad. Two classes of multisecant methods for nonlinear acceleration. *Numerical Linear Algebra with Applications*, 16:197–221, 2009.

[107] M. Fedele, E. Faggiano, L. Dede', and A. Quarteroni. A patient-specific aortic valve model based on moving resistive immersed implicit surfaces. *Biomechanics and Modeling in Mechanobiology*, 16(5):1779–1803, 2017.

[108] M. Fedele, R. Piersanti, F. Regazzoni, M. Salvador, P. C. Africa, M. Bucelli, A. Zingaro, L. Dede', and A. Quarteroni. A comprehensive and

biophysically detailed computational model of the whole human heart electromechanics. *arXiv preprint arXiv:2207.12460*, 2022.

[109] M. Fedele and A. Quarteroni. Polygonal surface processing and mesh generation tools for the numerical simulation of the cardiac function. *International Journal for Numerical Methods in Biomedical Engineering*, 37(4):e3435, 2021.

[110] J. J. Feher. *Quantitative human physiology: an introduction*. Academic Press, 2017.

[111] L. Feng, H. Gao, B. Griffith, S. Niederer, and X. Luo. Analysis of a coupled fluid-structure interaction model of the left atrium and mitral valve. *International Journal for Numerical Methods in Biomedical Engineering*, 35(11):e3254, 2019.

[112] M. A. Fernández and M. Moubachir. A Newton method using exact jacobians for solving fluid-structure coupling. *Computers & Structures*, 83(2-3):127–142, 2005.

[113] M. A. Fernández, J. Mullaert, and M. Vidrascu. Explicit Robin–Neumann schemes for the coupling of incompressible fluids with thin-walled structures. *Computer Methods in Applied Mechanics and Engineering*, 267:566–593, 2013.

[114] M. A. Fernández, J. Mullaert, and M. Vidrascu. Generalized Robin–Neumann explicit coupling schemes for incompressible fluid-structure interaction: Stability analysis and numerics. *International Journal for Numerical Methods in Engineering*, 101(3):199–229, 2015.

[115] A. Frontera, S. Pagani, L. R. Limite, A. Peirone, F. Fioravanti, B. Enache, J. Cuellar Silva, K. Vlachos, C. Meyer, G. Montesano, et al. Slow conduction corridors and pivot sites characterize the electrical remodeling in atrial fibrillation. *Clinical Electrophysiology*, 8(5):561–577, 2022.

[116] I. Fumagalli. A reduced 3D-0D FSI model of the aortic valve including leaflets curvature. *arXiv preprint arXiv:2106.00571*, 2021.

[117] I. Fumagalli, M. Fedele, C. Vergara, L. Dede', S. Ippolito, F. Nicolò, C. Antona, R. Scrofani, and A. Quarteroni. An image-based compu-

tational hemodynamics study of the systolic anterior motion of the mitral valve. *Computers in Biology and Medicine*, 123:103922, 2020.

[118] I. Fumagalli, P. Vitullo, C. Vergara, M. Fedele, A. F. Corno, S. Ippolito, R. Scrofani, and A. Quarteroni. Image-based computational hemodynamics analysis of systolic obstruction in hypertrophic cardiomyopathy. *Frontiers in Physiology*, page 2437, 2022.

[119] L. Gander, R. Krause, M. Multerer, and S. Pezzuto. Space–time shape uncertainties in the forward and inverse problem of electrocardiography. *International Journal for Numerical Methods in Biomedical Engineering*, 37(10):e3522, 2021.

[120] H. Gao, L. Feng, N. Qi, C. Berry, B. E. Griffith, and X. Luo. A coupled mitral valve–left ventricle model with fluid–structure interaction. *Medical Engineering & Physics*, 47:128–136, 2017.

[121] M. Gao, C. Chen, S. Zhang, Z. Qian, M. Vannan, S. Rinehart, D. Metaxas, and L. Axel. Morphological analysis of the papillary muscles and the trabeculae. In *2014 IEEE 11th International Symposium on Biomedical Imaging (ISBI)*, pages 373–376. IEEE, 2014.

[122] M. Gee, C. Siefert, J. Hu, R. Tuminaro, and M. Sala. ML 5.0 smoothed aggregation user's guide. Technical Report SAND2006-2649, Sandia National Laboratories, 2006.

[123] T. Gerach, S. Schuler, J. Fröhlich, L. Lindner, E. Kovacheva, R. Moss, E. M. Wülfers, G. Seemann, C. Wieners, and A. Loewe. Electromechanical whole-heart digital twins: a fully coupled multi-physics approach. *Mathematics*, 9(11):1247, 2021.

[124] T. Gerach, S. Schuler, E. Kovacheva, O. Dössel, and A. Loewe. Consequences of using an orthotropic stress tensor for left ventricular systole. In *2020 Computing in Cardiology*, pages 1–4. IEEE, 2020.

[125] L. Gerardo-Giorda, L. Mirabella, F. Nobile, M. Perego, and A. Veneziani. A model-based block-triangular preconditioner for the bidomain system in electrocardiology. *Journal of Computational Physics*, 228(10):3625–3639, 2009.

[126] L. Gerardo-Giorda, F. Nobile, and C. Vergara. Analysis and optimization of Robin-Robin partitioned procedures in fluid-structure

interaction problems. *SIAM Journal on Numerical Analysis*, 48(6):2091–2116, 2010.

[127] A. Gerbi. *Numerical approximation of cardiac electro-fluid-mechanical models*. PhD thesis, EPFL, 2018.

[128] A. Gerbi, L. Dede', and A. Quarteroni. A monolithic algorithm for the simulation of cardiac electromechanics in the human left ventricle. *Mathematics in Engineering*, 1(1):1–37, 2018.

[129] A. Gharaviri, S. Pezzuto, M. Potse, S. Verheule, G. Conte, R. Krause, U. Schotten, and A. Auricchio. Left atrial appendage electrical isolation reduces atrial fibrillation recurrences: a simulation study. *Circulation: Arrhythmia and Electrophysiology*, 14(1):e009230, 2021.

[130] G. Gigante and C. Vergara. On the choice of interface parameters in Robin–Robin loosely coupled schemes for fluid–structure interaction. *Fluids*, 6(6):213, 2021.

[131] G. Gigante and C. Vergara. On the stability of a loosely-coupled scheme based on a Robin interface condition for fluid-structure interaction. *Computers & Mathematics with Applications*, 96:109–119, 2021.

[132] D. Gil, R. Aris, A. Borras, E. Ramírez, R. Sebastian, and M. Vazquez. Influence of fiber connectivity in simulations of cardiac biomechanics. *International Journal of Computer Assisted Radiology and Surgery*, 14(1):63–72, 2019.

[133] K. Gillette, M. A. Gsell, A. J. Prassl, E. Karabelas, U. Reiter, G. Reiter, T. Grandits, C. Payer, D. Štern, M. Urschler, J. D. Bayer, C. M. Augustin, A. Neic, T. Pock, E. J. Vigmond, and G. Plank. A framework for the generation of digital twins of cardiac electrophysiology from clinical 12-leads ECGs. *Medical Image Analysis*, 71:102080, 2021.

[134] S. Göktepe and E. Kuhl. Electromechanics of the heart: a unified approach to the strongly coupled excitation–contraction problem. *Computational Mechanics*, 45(2):227–243, 2010.

[135] R. Gordan, J. K. Gwathmey, and L.-H. Xie. Autonomic and endocrine control of cardiovascular function. *World Journal of Cardiology*, 7(4):204, 2015.

[136] L. Goubergrits, K. Vellguth, L. Obermeier, A. Schlief, L. Tautz, J. Bruening, H. Lamecker, A. Szengel, O. Nemchyna, C. Knosalla, et al. Ct-based analysis of left ventricular hemodynamics using statistical shape modeling and computational fluid dynamics. *Frontiers in Cardiovascular Medicine*, 9, 2022.

[137] R. A. Gray and P. Pathmanathan. Patient-specific cardiovascular computational modeling: diversity of personalization and challenges. *Journal of Cardiovascular Translational Research*, 11(2):80–88, 2018.

[138] B. E. Griffith, X. Luo, D. M. McQueen, and C. S. Peskin. Simulating the fluid dynamics of natural and prosthetic heart valves using the immersed boundary method. *International Journal of Applied Mechanics*, 1(01):137–177, 2009.

[139] D. Guan, J. Yao, X. Luo, and H. Gao. Effect of myofibre architecture on ventricular pump function by using a neonatal porcine heart model: from DT-MRI to rule-based methods. *Royal Society Open Science*, 7(4):191655, 2020.

[140] D. Guan, X. Zhuan, W. Holmes, X. Luo, and H. Gao. Modelling of fibre dispersion and its effects on cardiac mechanics from diastole to systole. *Journal of Engineering Mathematics*, 128(1):1–24, 2021.

[141] J. M. Guccione and A. D. McCulloch. Finite element modeling of ventricular mechanics. In L. Glass, P. Hunter, and A. McCulloch, editors, *Theory of Heart*, pages 121–144. Springer, 1991.

[142] G. Guidoboni, R. Glowinski, N. Cavallini, and S. Canic. Stable loosely-coupled-type algorithm for fluid–structure interaction in blood flow. *Journal of Computational Physics*, 228(18):6916–6937, 2009.

[143] R. M. Gulrajani and G. E. Mailloux. A simulation study of the effects of torso inhomogeneities on electrocardiographic potentials, using realistic heart and torso models. *Circulation Research*, 52(1):45–56, 1983.

[144] G. Gulsin, A. Singh, and G. P. McCann. Cardiovascular magnetic resonance in the evaluation of heart valve disease. *BMC Medical Imaging*, 17(1):1–14, 2017.

[145] V. Gurev, T. Lee, J. Constantino, H. Arevalo, and N. A. Trayanova. Models of cardiac electromechanics based on individual hearts imaging data: Image-based electromechanical models of the heart. *Biomechanics and Modeling in Mechanobiology*, 10(3):295–306, 2011.

[146] K. Hammermeister, R. Brooks, and J. Warbasse. The rate of change of left ventricular volume in man: I. validation and peak systolic ejection rate in health and disease. *Circulation*, 49(4):729–738, 1974.

[147] E. W. Hawthorne. Dynamic geometry of the left ventricle. *The American Journal of Cardiology*, 18(4):566–573, 1966.

[148] J. Heijman, H. Sutanto, H. J. Crijns, S. Nattel, and N. A. Trayanova. Computational models of atrial fibrillation: Achievements, challenges, and perspectives for improving clinical care. *Cardiovascular Research*, 117(7):1682–1699, 2021.

[149] M. Heil. An efficient solver for the fully coupled solution of large-displacement fluid–structure interaction problems. *Computer Methods in Applied Mechanics and Engineering*, 193(1-2):1–23, 2004.

[150] J. S. Hesthaven, G. Rozza, B. Stamm, et al. *Certified reduced basis methods for parametrized partial differential equations*, volume 590. Springer, 2016.

[151] A. V. Hill. The heat of shortening and the dynamic constants of muscle. *Proceedings of the Royal Society of London. Series B-Biological Sciences*, 126(843):136–195, 1938.

[152] M. Hirschhorn, V. Tchantchaleishvili, R. Stevens, J. Rossano, and A. Throckmorton. Fluid–structure interaction modeling in cardiovascular medicine–a systematic review 2017–2019. *Medical Engineering & Physics*, 78:1–13, 2020.

[153] M. Hirschvogel, M. Bassilious, L. Jagschies, S. M. Wildhirt, and M. W. Gee. A monolithic 3D-0D coupled closed-loop model of the heart and the vascular system: experiment-based parameter estimation for patient-specific cardiac mechanics. *International Journal for Numerical Methods in Biomedical Engineering*, 33(8):e2842, 2017.

[154] S. Y. Ho, R. H. Anderson, and D. Sánchez-Quintana. Atrial structure and fibres: morphologic bases of atrial conduction. *Cardiovascular Research*, 54(2):325–336, 2002.

[155] A. L. Hodgkin and A. F. Huxley. A quantitative description of membrane current and its application to conduction and excitation in nerve. *The Journal of Physiology*, 117(4):500, 1952.

[156] J. Hoffman, J. Jansson, and M. Stöckli. Unified continuum modeling of fluid-structure interaction. *Mathematical Models and Methods in Applied Sciences*, 21(03):491–513, 2011.

[157] G. A. Holzapfel. *Nonlinear solid mechanics: a continuum approach for engineering science*. John Wiley & Sons, 2000.

[158] A. Hosoi, T. Washio, J.-i. Okada, Y. Kadooka, K. Nakajima, and T. Hisada. A multi-scale heart simulation on massively parallel computers. In *SC'10: Proceedings of the 2010 ACM/IEEE International Conference for High Performance Computing, Networking, Storage and Analysis*, pages 1–11. IEEE, 2010.

[159] J. Hron and S. Turek. A monolithic fem/multigrid solver for an ale formulation of fluid-structure interaction with applications in biomechanics. In H. J. Bungartz and M. Schäfer, editors, *Fluid-Structure Interaction*, pages 146–170. Springer, 2006.

[160] E. W. Hsu, A. Muzikant, S. Matulevicius, R. Penland, and C. Henriquez. Magnetic resonance myocardial fiber-orientation mapping with direct histological correlation. *American Journal of Physiology-Heart and Circulatory Physiology*, 274(5):H1627–H1634, 1998.

[161] M.-C. Hsu, D. Kamensky, Y. Bazilevs, M. S. Sacks, and T. J. R. Hughes. Fluid–structure interaction analysis of bioprosthetic heart valves: significance of arterial wall deformation. *Computational Mechanics*, 54(4):1055–1071, 2014.

[162] Q. Huang, Z. Liu, L. Wang, S. Ravi, J. Young, J. C. Lai, and F.-B. Tian. Streamline penetration, velocity error, and consequences of the feedback immersed boundary method. *Physics of Fluids*, 34(9):097101, 2022.

[163] L. E. Hudsmith, S. E. Petersen, J. M. Francis, M. D. Robson, and S. Neubauer. Normal human left and right ventricular and left atrial dimensions using steady state free precession magnetic resonance imaging. *Journal of Cardiovascular Magnetic Resonance*, 7(5):775–782, 2005.

[164] T. J. Hughes, G. Scovazzi, and L. P. Franca. Multiscale and stabilized methods. *Encyclopedia of Computational Mechanics*, pages 1–64, 2018.

[165] T. J. R. Hughes. *The finite element method: linear static and dynamic finite element analysis*. Courier Corporation, 2012.

[166] T. J. R. Hughes, W. K. Liu, and T. K. Zimmermann. Lagrangian-Eulerian finite element formulation for incompressible viscous flows. *Computer Methods in Applied Mechanics and Engineering*, 29(3):329–349, 1981.

[167] P. Hunter, A. D. McCulloch, and H. Ter Keurs. Modelling the mechanical properties of cardiac muscle. *Progress in Biophysics and Molecular Biology*, 69(2-3):289–331, 1998.

[168] J. W. Hurst, R. A. Walsh, V. Fuster, and J. C. Fang. *Hurst's the heart manual of cardiology*. McGraw-Hill, 2013.

[169] R. Jacob, B. Dierberger, and G. Kissling. Functional significance of the frank-starling mechanism under physiological and pathophysiological conditions. *European Heart Journal*, 13(suppl_E):7–14, 1992.

[170] J. Janela, A. Moura, and A. Sequeira. Absorbing boundary conditions for a 3D non-Newtonian fluid–structure interaction model for blood flow in arteries. *International Journal of Engineering Science*, 48(11):1332–1349, 2010.

[171] H. Jasak and Z. Tukovic. Automatic mesh motion for the unstructured finite volume method. *Transactions of FAMENA*, 30(2):1–20, 2006.

[172] M. Jaworska-Wilczynska, P. Trzaskoma, A. A. Szczepankiewicz, and T. Hryniewiecki. Pericardium: structure and function in health and disease. *Folia Histochemica et Cytobiologica*, 54(3):121–125, 2016.

[173] D. Jodlbauer, U. Langer, and T. Wick. Parallel block-preconditioned monolithic solvers for fluid-structure interaction problems. *Inter-*

national Journal for Numerical Methods in Engineering, 117(6):623–643, 2019.

[174] V. John and S. Kaya. A finite element variational multiscale method for the navier–stokes equations. *SIAM Journal on Scientific Computing*, 26(5):1485–1503, 2005.

[175] D. Kamensky, M.-C. Hsu, D. Schillinger, J. A. Evans, A. Aggarwal, Y. Bazilevs, M. S. Sacks, and T. J. R. Hughes. An immersogeometric variational framework for fluid–structure interaction: Application to bioprosthetic heart valves. *Computer Methods in Applied Mechanics and Engineering*, 284:1005–1053, 2015.

[176] A. Kanai and G. Salama. Optical mapping reveals that repolarization spreads anisotropically and is guided by fiber orientation in guinea pig hearts. *Circulation Research*, 77(4):784–802, 1995.

[177] E. Karabelas, M. A. Gsell, C. M. Augustin, L. Marx, A. Neic, A. J. Prassl, L. Goubergrits, T. Kuehne, and G. Plank. Towards a computational framework for modeling the impact of aortic coarctations upon left ventricular load. *Frontiers in Physiology*, 9:538, 2018.

[178] E. Karabelas, S. Longobardi, J. Fuchsberger, O. Razeghi, C. Rodero, M. Strocchi, R. Rajani, G. Haase, G. Plank, and S. Niederer. Global sensitivity analysis of four chamber heart hemodynamics using surrogate models. *IEEE Transactions on Biomedical Engineering*, 2022.

[179] T. Kariya, T. Washio, J.-i. Okada, M. Nakagawa, M. Watanabe, Y. Kadooka, S. Sano, R. Nagai, S. Sugiura, and T. Hisada. Personalized perioperative multi-scale, multi-physics heart simulation of double outlet right ventricle. *Annals of Biomedical Engineering*, 48(6):1740–1750, 2020.

[180] A. M. Katz. *Physiology of the Heart*. Lippincott Williams & Wilkins, 2010.

[181] D. U. Keller, F. M. Weber, G. Seemann, and O. Dössel. Ranking the influence of tissue conductivities on forward-calculated ecgs. *IEEE Transactions on Biomedical Engineering*, 57(7):1568–1576, 2010.

[182] R. C. Kerckhoffs, M. L. Neal, Q. Gu, J. B. Bassingthwaighte, J. H. Omens, and A. D. McCulloch. Coupling of a 3D finite element model

of cardiac ventricular mechanics to lumped systems models of the systemic and pulmonic circulation. *Annals of Biomedical Engineering*, 35(1):1–18, 2007.

[183] S. Khodaei, A. Henstock, R. Sadeghi, S. Sellers, P. Blanke, J. Leipsic, A. Emadi, and Z. Keshavarz-Motamed. Personalized intervention cardiology with transcatheter aortic valve replacement made possible with a non-invasive monitoring and diagnostic framework. *Scientific Reports*, 11(1):1–28, 2021.

[184] R. Klabunde. *Cardiovascular physiology concepts*. Lippincott Williams & Wilkins, 2011.

[185] P. M. Knupp. Hexahedral and tetrahedral mesh untangling. *Engineering with Computers*, 17(3):261–268, 2001.

[186] S. Krishnamoorthi, M. Sarkar, and W. S. Klug. Numerical quadrature and operator splitting in finite element methods for cardiac electrophysiology. *International Journal for Numerical Methods in Biomedical Engineering*, 29(11):1243–1266, 2013.

[187] J. Kronborg, F. Svelander, S. Eriksson-Lidbrink, L. Lindström, C. Homs-Pons, D. Lucor, and J. Hoffman. Computational analysis of flow structures in turbulent ventricular blood flow associated with mitral valve intervention. *Frontiers in Physiology*, page 752, 2022.

[188] V. Kumar, A. K. Abbas, N. Fausto, and J. C. Aster. *Robbins and Cotran pathologic basis of disease, professional edition e-book*. Elsevier Health Sciences, 2014.

[189] U. Küttler and W. A. Wall. Fixed-point fluid-structure interaction solvers with dynamic relaxation. *Computational Mechanics*, 43(1):61–72, 2008.

[190] S. Land, S.-J. Park-Holohan, N. P. Smith, C. G. Dos Remedios, J. C. Kentish, and S. A. Niederer. A model of cardiac contraction based on novel measurements of tension development in human cardiomyocytes. *Journal of Molecular and Cellular Cardiology*, 106:68–83, 2017.

[191] M. Landajuela, C. Vergara, A. Gerbi, L. Dedè, L. Formaggia, and A. Quarteroni. Numerical approximation of the electromechanical coupling in the left ventricle with inclusion of the Purkinje network.

International Journal for Numerical Methods in Biomedical Engineering, 34(7):e2984, 2018.

[192] M. Landajuela, M. Vidrascu, D. Chapelle, and M. A. Fernández. Coupling schemes for the FSI forward prediction challenge: Comparative study and validation. *International Journal for Numerical Methods in Biomedical Engineering*, 33(4):2813, 2017.

[193] U. Langer and H. Yang. Robust and efficient monolithic fluid-structure-interaction solvers. *International Journal for Numerical Methods in Engineering*, 108(4):303–325, 2016.

[194] J. Lantz, S. Bäck, C.-J. Carlhäll, A. Bolger, A. Persson, M. Karlsson, and T. Ebbers. Impact of prosthetic mitral valve orientation on the ventricular flow field: Comparison using patient-specific computational fluid dynamics. *Journal of Biomechanics*, 116:110209, 2021.

[195] J. Lantz, L. Henriksson, A. Persson, M. Karlsson, and T. Ebbers. Patient-specific simulation of cardiac blood flow from high-resolution computed tomography. *Journal of Biomechanical Engineering*, 138(12), 2016.

[196] A. W. Lee, U. C. Nguyen, O. Razeghi, J. Gould, B. S. Sidhu, B. Sieniewicz, J. Behar, M. Mafi-Rad, G. Plank, F. W. Prinzen, C. A. Rinaldi, K. Vernooy, and S. Niederer. A rule-based method for predicting the electrical activation of the heart with cardiac resynchronization therapy from non-invasive clinical data. *Medical Image Analysis*, 57:197–213, 2019.

[197] J. H. Lee, A. D. Rygg, E. M. Kolahdouz, S. Rossi, S. M. Retta, N. Duraiswamy, L. N. Scotten, B. A. Craven, and B. E. Griffith. Fluid–structure interaction models of bioprosthetic heart valve dynamics in an experimental pulse duplicator. *Annals of Biomedical Engineering*, 48(5):1475–1490, 2020.

[198] F. Levrero-Florencio, F. Margara, E. Zacur, A. Bueno-Orovio, Z. Wang, A. Santiago, J. Aguado-Sierra, G. Houzeaux, V. Grau, D. Kay, M. Vázquez, R. Ruiz-Baier, and B. Rodriguez. Sensitivity analysis of a strongly-coupled human-based electromechanical cardiac model: Effect of mechanical parameters on physiologically relevant

biomarkers. *Computer Methods in Applied Mechanics and Engineering*, 361:112762, 2020.

[199] Official `life`^{x} website. https://lifex.gitlab.io/ (last accessed: 23 september 2022).

[200] G. Lines, M. Buist, P. Grottum, A. Pullan, J. Sundnes, and A. Tveito. Mathematical models and numerical methods for the forward problem in cardiac electrophysiology. *Computing and Visualization in Science*, 5(4):215–239, 2003.

[201] W. C. Little and T. R. Downes. Clinical evaluation of left ventricular diastolic performance. *Progress in Cardiovascular Diseases*, 32(4):273–290, 1990.

[202] J. Liu and A. L. Marsden. A unified continuum and variational multiscale formulation for fluids, solids, and fluid–structure interaction. *Computer Methods in Applied Mechanics and Engineering*, 337:549–597, 2018.

[203] A. Loppini, A. Gizzi, R. Ruiz-Baier, C. Cherubini, F. H. Fenton, and S. Filippi. Competing mechanisms of stress-assisted diffusivity and stretch-activated currents in cardiac electromechanics. *Frontiers in Physiology*, 9:1714, 2018.

[204] R. Loubère, P.-H. Maire, M. Shashkov, J. Breil, and S. Galera. ReALE: A reconnection-based arbitrary-Lagrangian–Eulerian method. *Journal of Computational Physics*, 229(12):4724–4761, 2010.

[205] C. Luo and Y. Rudy. A model of the ventricular cardiac action potential. depolarization, repolarization, and their interaction. *Circulation Research*, 68(6):1501–1526, 1991.

[206] G. Luraghi, W. Wu, F. De Gaetano, J. F. R. Matas, G. D. Moggridge, M. Serrani, J. Stasiak, M. L. Costantino, and F. Migliavacca. Evaluation of an aortic valve prosthesis: Fluid-structure interaction or structural simulation? *Journal of Biomechanics*, 58:45–51, 2017.

[207] X. Ma, H. Gao, B. E. Griffith, C. Berry, and X. Luo. Image-based fluid–structure interaction model of the human mitral valve. *Computers & Fluids*, 71:417–425, 2013.

[208] A. M. Maceira, S. K. Prasad, M. Khan, and D. J. Pennell. Normalized left ventricular systolic and diastolic function by steady state free precession cardiovascular magnetic resonance. *Journal of Cardiovascular Magnetic Resonance*, 8(3):417–426, 2006.

[209] A. M. Maceira, S. K. Prasad, M. Khan, and D. J. Pennell. Reference right ventricular systolic and diastolic function normalized to age, gender and body surface area from steady-state free precession cardiovascular magnetic resonance. *European Heart Journal*, 27(23):2879–2888, 2006.

[210] J. B. Mark. *Atlas of cardiovascular monitoring*. Churchill Livingstone, 1998.

[211] A. L. Marsden, V. M. Reddy, S. C. Shadden, F. P. Chan, C. A. Taylor, and J. A. Feinstein. A new multiparameter approach to computational simulation for fontan assessment and redesign. *Congenital Heart Disease*, 5(2):104–117, 2010.

[212] A. Masci, M. Alessandrini, D. Forti, F. Menghini, L. Dede', C. Tomasi, A. Quarteroni, and C. Corsi. A proof of concept for computational fluid dynamic analysis of the left atrium in atrial fibrillation on a patient-specific basis. *Journal of Biomechanical Engineering*, 142(1), 2020.

[213] W. L. Maughan, A. A. Shoukas, K. Sagawa, and M. L. Weisfeldt. Instantaneous pressure-volume relationship of the canine right ventricle. *Circulation Research*, 44(3):309–315, 1979.

[214] M. Mayr, W. Wall, and M. Gee. Adaptive time stepping for fluid-structure interaction solvers. *Finite Elements in Analysis and Design*, 141:55–69, 2018.

[215] K. S. McDowell, F. Vadakkumpadan, R. Blake, J. Blauer, G. Plank, R. S. MacLeod, and N. A. Trayanova. Mechanistic inquiry into the role of tissue remodeling in fibrotic lesions in human atrial fibrillation. *Biophysical Journal*, 104(12):2764–2773, 2013.

[216] M. Mehl, B. Uekermann, H. Bijl, D. Blom, B. Gatzhammer, and A. Van Zuijlen. Parallel coupling numerics for partitioned fluid–structure interaction simulations. *Computers & Mathematics with Applications*, 71(4):869–891, 2016.

[217] V. Meschini, M. D. de Tullio, and R. Verzicco. Effects of mitral chordae tendineae on the flow in the left heart ventricle. *The European Physical Journal E*, 41(2):1–9, 2018.

[218] V. Meschini, R. Mittal, and R. Verzicco. Systolic anterior motion in hypertrophic cardiomyopathy: a fluid–structure interaction computational model. *Theoretical and Computational Fluid Dynamics*, 35(3):381–396, 2021.

[219] J. H. Mitchell, D. N. Gupta, and R. M. PAYNE. Influence of atrial systole on effective ventricular stroke volume. *Circulation Research*, 17(1):11–18, 1965.

[220] J. R. Mitchell and J.-J. Wang. Expanding application of the wiggers diagram to teach cardiovascular physiology. *Advances in Physiology Education*, 38(2):170–175, 2014.

[221] M. E. Moghadam, Y. Bazilevs, T.-Y. Hsia, I. E. Vignon-Clementel, and A. L. Marsden. A comparison of outlet boundary treatments for prevention of backflow divergence with relevance to blood flow simulations. *Computational Mechanics*, 48(3):277–291, 2011.

[222] D. P. Mok, W. A. Wall, and E. Ramm. Accelerated iterative substructuring schemes for instationary fluid-structure interaction. *Computational Fluid and Solid Mechanics*, 2:1325–1328, 2001.

[223] F. Muldoon and S. Acharya. Mass conservation in the immersed boundary method. In *Fluids Engineering Division Summer Meeting*, volume 41987, pages 411–419, 2005.

[224] J. P. Murgo, N. Westerhof, J. P. Giolma, and S. A. Altobelli. Aortic input impedance in normal man: relationship to pressure wave forms. *Circulation*, 62(1):105–116, 1980.

[225] A. Nagler, C. Bertoglio, M. Gee, and W. Wall. Personalization of cardiac fiber orientations from image data using the unscented kalman filter. In *International Conference on Functional Imaging and Modeling of the Heart*, pages 132–140. Springer, 2013.

[226] T. Nakaya, I. Tsujino, J. Nakamura, Y. Chiba, and H. Iwano. Right ventricular pressure–volume loop produced with simultaneous application of three-dimensional echocardiography and high-fidelity

micromanometry in a patient with pulmonary arterial hypertension. *Echocardiography*, 38(5):805–807, 2021.

[227] V. Namana, S. S. Gupta, N. Sabharwal, and G. Hollander. Clinical significance of atrial kick. *QJM: An International Journal of Medicine*, 2018.

[228] M. P. Nash and A. V. Panfilov. Electromechanical model of excitable tissue to study reentrant cardiac arrhythmias. *Progress in Biophysics and Molecular Biology*, 85(2-3):501–522, 2004.

[229] F. Nicoud, C. Chnafa, J. Siguenza, V. Zmijanovic, and S. Mendez. Large-eddy simulation of turbulence in cardiovascular flows. In P. Wriggers and T. Lenarz, editors, *Biomedical Technology*, pages 147–167. Springer, 2018.

[230] S. A. Niederer, J. Lumens, and N. A. Trayanova. Computational models in cardiology. *Nature Reviews Cardiology*, 16(2):100–111, 2019.

[231] F. Nobile and L. Formaggia. A stability analysis for the arbitrary Lagrangian Eulerian formulation with finite elements. *East-West Journal of Numerical Mathematics*, 7(2):105–132, 1999.

[232] F. Nobile, M. Pozzoli, and C. Vergara. Time accurate partitioned algorithms for the solution of fluid–structure interaction problems in haemodynamics. *Computers & Fluids*, 86:470–482, 2013.

[233] A. Nogami. Purkinje-related arrhythmias part i: monomorphic ventricular tachycardias. *Pacing and Clinical Electrophysiology*, 34(5):624–650, 2011.

[234] D. Nordsletten, M. McCormick, P. Kilner, P. Hunter, D. Kay, and N. Smith. Fluid–solid coupling for the investigation of diastolic and systolic human left ventricular function. *International Journal for Numerical Methods in Biomedical Engineering*, 27(7):1017–1039, 2011.

[235] D. Nordsletten, S. Niederer, M. Nash, P. Hunter, and N. Smith. Coupling multi-physics models to cardiac mechanics. *Progress in Biophysics and Molecular Biology*, 104(1-3):77–88, 2011.

[236] L. Obermeier, K. Vellguth, A. Schlief, L. Tautz, J. Bruening, C. Knosalla, T. Kuehne, N. Solowjowa, and L. Goubergrits. Ct-based simulation of left ventricular hemodynamics: A pilot study in mitral

regurgitation and left ventricle aneurysm patients. *Frontiers in Cardiovascular Medicine*, 9:828556, 2022.

[237] R. Ogden. *Non-Linear Elastic Deformations*. Courier Corporation, 2013.

[238] T. O'Hara, L. Virág, A. Varró, and Y. Rudy. Simulation of the undiseased human cardiac ventricular action potential: model formulation and experimental validation. *PLoS Computational Biology*, 7(5):e1002061, 2011.

[239] J.-i. Okada, T. Washio, S. Sugiura, and T. Hisada. Clinical and pharmacological application of multiscale multiphysics heart simulator, UT-Heart. *The Korean Journal of Physiology & Pharmacology*, 23(5):295–303, 2019.

[240] D. Oks, C. Samaniego, C. Houzeaux, G.and Butakoff, and M. Vázquez. Fluid-structure interaction analysis of eccentricity and leaflet rigidity on thrombosis biomarkers in bioprosthetic heart valve replacements. *International Journal for Numerical Methods in Biomedical Engineering*, 2022.

[241] L. H. Opie. *Heart physiology: from cell to circulation*. Lippincott Williams & Wilkins, 2004.

[242] S. Pagani, L. Dede, A. Frontera, M. Salvador, L. Limite, A. Manzoni, F. Lipartiti, G. Tsitsinakis, A. Hadjis, P. Della Bella, et al. A computational study of the electrophysiological substrate in patients suffering from atrial fibrillation. *Frontiers in Physiology*, page 927, 2021.

[243] P. S. Pagel, F. Kehl, M. Gare, D. A. Hettrick, J. R. Kersten, and D. C. Warltier. Mechanical function of the left atrium: new insights based on analysis of pressure–volume relations and doppler echocardiography. *The Journal of the American Society of Anesthesiologists*, 98(4):975–994, 2003.

[244] N. G. Pandian, D. J. Skorton, S. M. Collins, H. L. Falsetti, E. R. Burke, and R. E. Kerber. Heterogeneity of left ventricular segmental wall thickening and excursion in 2-dimensional echocardiograms of normal human subjects. *The American Journal of Cardiology*, 51(10):1667–1673, 1983.

[245] F. Pashakhanloo, D. A. Herzka, H. Ashikaga, S. Mori, N. Gai, D. A. Bluemke, N. A. Trayanova, and E. R. McVeigh. Myofiber architecture of the human atria as revealed by submillimeter diffusion tensor imaging. *Circulation: Arrhythmia and Electrophysiology*, 9(4):e004133, 2016.

[246] P. Pathmanathan, S. Chapman, D. Gavaghan, and J. Whiteley. Cardiac electromechanics: the effect of contraction model on the mathematical problem and accuracy of the numerical scheme. *The Quarterly Journal of Mechanics & Applied Mathematics*, 63(3):375–399, 2010.

[247] P. Pathmanathan, G. R. Mirams, J. Southern, and J. P. Whiteley. The significant effect of the choice of ionic current integration method in cardiac electro-physiological simulations. *International Journal for Numerical Methods in Biomedical Engineering*, 27(11):1751–1770, 2011.

[248] G. Pedrizzetti, G. Faganello, E. Croatto, and A. Di Lenarda. The hemodynamic power of the heart differentiates normal from diseased right ventricles. *Journal of Biomechanics*, 119:110312, 2021.

[249] G. Pedrizzetti, G. La Canna, O. Alfieri, and G. Tonti. The vortex – an early predictor of cardiovascular outcome? *Nature Reviews Cardiology*, 11(9):545–553, 2014.

[250] M. Peirlinck, F. S. Costabal, J. Yao, J. Guccione, S. Tripathy, Y. Wang, D. Ozturk, P. Segars, T. Morrison, S. Levine, et al. Precision medicine in human heart modeling. *Biomechanics and Modeling in Mechanobiology*, 20(3):803–831, 2021.

[251] J. Peiró and A. Veneziani. Reduced models of the cardiovascular system. In L. Formaggia, A. Quarteroni, and A. Veneziani, editors, *Cardiovascular Mathematics*, pages 347–394. Springer, 2009.

[252] C. S. Peskin. Numerical analysis of blood flow in the heart. *Journal of Computational Physics*, 25(3):220–252, 1977.

[253] S. Pezzuto, P. Perdikaris, and F. S. Costabal. Learning cardiac activation maps from 12-lead ecg with multi-fidelity bayesian optimization on manifolds. *arXiv preprint arXiv:2203.06222*, 2022.

[254] S. Pezzuto, F. W. Prinzen, M. Potse, F. Maffessanti, F. Regoli, M. L. Caputo, G. Conte, R. Krause, and A. Auricchio. Reconstruction of

three-dimensional biventricular activation based on the 12-lead electrocardiogram via patient-specific modelling. *EP Europace*, 23(4):640–647, 2021.

[255] M. R. Pfaller, J. M. Hörmann, M. Weigl, A. Nagler, R. Chabiniok, C. Bertoglio, and W. A. Wall. The importance of the pericardium for cardiac biomechanics: from physiology to computational modeling. *Biomechanics and Modeling in Mechanobiology*, 18(2):503–529, 2019.

[256] C. Pierre and Y. Bourgault. A comparison of the bidomain and the adapted monodomain models in electro-cardiology. *HAL-00545888,(1)*, 103, 2010.

[257] R. Piersanti. *Mathematical and numerical modeling of cardiac fiber generation and electromechanical function: towards a realistic simulation of the whole heart*. PhD thesis, Politecnico di Milano, 2022.

[258] R. Piersanti, P. C. Africa, M. Fedele, C. Vergara, L. Dede', A. F. Corno, and A. Quarteroni. Modeling cardiac muscle fibers in ventricular and atrial electrophysiology simulations. *Computer Methods in Applied Mechanics and Engineering*, 373:113468, 2021.

[259] R. Piersanti, F. Regazzoni, M. Salvador, A. F. Corno, C. Vergara, A. Quarteroni, et al. 3D–0D closed-loop model for the simulation of cardiac biventricular electromechanics. *Computer Methods in Applied Mechanics and Engineering*, 391:114607, 2022.

[260] M. T. Politi, A. Ghigo, J. M. Fernández, I. Khelifa, J. Gaudric, J. M. Fullana, and P.-Y. Lagrée. The dicrotic notch analyzed by a numerical model. *Computers in Biology and Medicine*, 72:54–64, 2016.

[261] A. Quarteroni. *Numerical Models for Differential Problems*, volume 16. Springer, 2017.

[262] A. Quarteroni, L. Dede', A. Manzoni, and C. Vergara. *Mathematical modelling of the human cardiovascular system: data, numerical approximation, clinical applications*, volume 33. Cambridge University Press, 2019.

[263] A. Quarteroni, T. Lassila, S. Rossi, and R. Ruiz-Baier. Integrated heart – coupling multiscale and multiphysics models for the simulation

of the cardiac function. *Computer Methods in Applied Mechanics and Engineering*, 314:345–407, 2017.

[264] A. Quarteroni, A. Manzoni, and F. Negri. *Reduced Basis Methods for Partial Differential Equations: an Introduction*, volume 92. Springer, 2015.

[265] A. Quarteroni and A. Valli. *Domain decomposition methods for partial differential equations*. Oxford University Press, 1999.

[266] A. Quarteroni, A. Veneziani, and C. Vergara. Geometric multiscale modeling of the cardiovascular system, between theory and practice. *Computer Methods in Applied Mechanics and Engineering*, 302:193–252, 2016.

[267] T. C. Rebollo and R. Lewandowski. *Mathematical and numerical foundations of turbulence models and applications*. Springer, 2014.

[268] A. N. Redington, H. H. Gray, M. E. Hodson, M. Rigby, and P. Oldershaw. Characterisation of the normal right ventricular pressure-volume relation by biplane angiography and simultaneous micromanometer pressure measurements. *Heart*, 59(1):23–30, 1988.

[269] F. Regazzoni. *Mathematical modeling and Machine Learning for the numerical simulation of cardiac electromechanics*. PhD thesis, Politecnico di Milano, 2020.

[270] F. Regazzoni, L. Dedè, and A. Quarteroni. Active contraction of cardiac cells: a reduced model for sarcomere dynamics with cooperative interactions. *Biomechanics and Modeling in Mechanobiology*, 17(6):1663–1686, 2018.

[271] F. Regazzoni, L. Dede, and A. Quarteroni. Machine learning for fast and reliable solution of time-dependent differential equations. *Journal of Computational Physics*, 397:108852, 2019.

[272] F. Regazzoni, L. Dede', and A. Quarteroni. Biophysically detailed mathematical models of multiscale cardiac active mechanics. *PLoS Computational Biology*, 16(10):e1008294, 2020.

[273] F. Regazzoni, L. Dedè, and A. Quarteroni. Machine learning of multiscale active force generation models for the efficient simulation

of cardiac electromechanics. *Computer Methods in Applied Mechanics and Engineering*, 370:113268, 2020.

[274] F. Regazzoni and A. Quarteroni. Accelerating the convergence to a limit cycle in 3D cardiac electromechanical simulations through a data-driven 0D emulator. *Computers in Biology and Medicine*, 135:104641, 2021.

[275] F. Regazzoni, M. Salvador, P. C. Africa, M. Fedele, L. Dede', and A. Quarteroni. A cardiac electromechanical model coupled with a lumped-parameter model for closed-loop blood circulation. *Journal of Computational Physics*, 457:111083, 2022.

[276] F. Regazzoni, M. Salvador, L. Dede', and A. Quarteroni. A machine learning method for real-time numerical simulations of cardiac electromechanics. *Computer Methods in Applied Mechanics and Engineering*, 393:114825, 2022.

[277] J. J. Rice, F. Wang, D. M. Bers, and P. P. De Tombe. Approximate model of cooperative activation and crossbridge cycling in cardiac muscle using ordinary differential equations. *Biophysical Journal*, 95(5):2368–2390, 2008.

[278] S. I. H. Richardson, H. Gao, J. Cox, R. Janiczek, B. E. Griffith, C. Berry, and X. Luo. A poroelastic immersed finite element framework for modelling cardiac perfusion and fluid–structure interaction. *International Journal for Numerical Methods in Biomedical Engineering*, 37(5):e3446, 2021.

[279] M. J. Richter, S. Hsu, A. Yogeswaran, F. Husain-Syed, I. Vadász, H. A. Ghofrani, R. Naeije, S. Harth, F. Grimminger, W. Seeger, et al. Right ventricular pressure-volume loop shape and systolic pressure change in pulmonary hypertension. *American Journal of Physiology-Lung Cellular and Molecular Physiology*, 320(5):L715–L725, 2021.

[280] T. Richter. A monolithic geometric multigrid solver for fluid-structure interactions in ale formulation. *International Journal for Numerical Methods in Engineering*, 104(5):372–390, 2015.

[281] T. Richter. *Fluid-structure interactions: models, analysis and finite elements*. Springer, 2017.

[282] G. Rigatelli, C. Chiastra, G. Pennati, G. Dubini, F. Migliavacca, and M. Zuin. Applications of computational fluid dynamics to congenital heart diseases: a practical review for cardiovascular professionals. *Expert Review of Cardiovascular Therapy*, 19(10):907–916, 2021.

[283] D. E. Roberts, L. T. Hersh, and A. M. Scher. Influence of cardiac fiber orientation on wavefront voltage, conduction velocity, and tissue resistivity in the dog. *Circulation Research*, 44(5):701–712, 1979.

[284] J. M. Rogers and A. D. McCulloch. A collocation-galerkin finite element model of cardiac action potential propagation. *IEEE Transactions on Biomedical Engineering*, 41(8):743–757, 1994.

[285] D. Romero, R. Sebastian, B. H. Bijnens, V. Zimmerman, P. M. Boyle, E. J. Vigmond, and A. F. Frangi. Effects of the Purkinje system and cardiac geometry on biventricular pacing: a model study. *Annals of Biomedical Engineering*, 38(4):1388–1398, 2010.

[286] C. H. Roney, M. L. Beach, A. M. Mehta, I. Sim, C. Corrado, R. Bendikas, J. A. Solis-Lemus, O. Razeghi, J. Whitaker, L. O'Neill, et al. In silico comparison of left atrial ablation techniques that target the anatomical, structural, and electrical substrates of atrial fibrillation. *Frontiers in Physiology*, 11:1145, 2020.

[287] C. H. Roney, R. Bendikas, F. Pashakhanloo, C. Corrado, E. J. Vigmond, E. R. McVeigh, N. A. Trayanova, and S. A. Niederer. Constructing a human atrial fibre atlas. *Annals of Biomedical Engineering*, 49(1):233–250, 2021.

[288] S. Rossi, T. Lassila, R. Ruiz-Baier, A. Sequeira, and A. Quarteroni. Thermodynamically consistent orthotropic activation model capturing ventricular systolic wall thickening in cardiac electromechanics. *European Journal of Mechanics-A/Solids*, 48:129–142, 2014.

[289] Y. Saad. *Iterative methods for sparse linear systems*. SIAM, 2003.

[290] F. Sacco, B. Paun, O. Lehmkuhl, T. L. Iles, P. A. Iaizzo, G. Houzeaux, M. Vázquez, C. Butakoff, and J. Aguado-Sierra. Left ventricular trabeculations decrease the wall shear stress and increase the intraventricular pressure drop in CFD simulations. *Frontiers in Physiology*, 9:458, 2018.

[291] Y. Sahasakul, W. D. Edwards, J. M. Naessens, and A. J. Tajik. Age-related changes in aortic and mitral valve thickness: implications for two-dimensional echocardiography based on an autopsy study of 200 normal human hearts. *The American Journal of Cardiology*, 62(7):424–430, 1988.

[292] S.-I. Sakamoto, T. Nitta, Y. Ishii, Y. Miyagi, H. Ohmori, and K. Shimizu. Interatrial electrical connections: the precise location and preferential conduction. *Journal of Cardiovascular Electrophysiology*, 16(10):1077–1086, 2005.

[293] M. Salvador, L. Dede', and A. Quarteroni. An intergrid transfer operator using radial basis functions with application to cardiac electromechanics. *Computational Mechanics*, 66:491–511, 2020.

[294] M. Salvador, M. Fedele, P. C. Africa, E. Sung, L. Dede', A. Prakosa, J. Chrispin, N. A. Trayanova, and A. Quarteroni. Electromechanical modeling of human ventricles with ischemic cardiomyopathy: numerical simulations in sinus rhythm and under arrhythmia. *Computers in Biology and Medicine*, 136:104674, 2021.

[295] M. Salvador, F. Regazzoni, S. Pagani, N. A. Trayanova, A. Quarteroni, et al. The role of mechano-electric feedbacks and hemodynamic coupling in scar-related ventricular tachycardia. *Computers in Biology and Medicine*, 142:105203, 2022.

[296] L. F. Santana, E. P. Cheng, and W. J. Lederer. How does the shape of the cardiac action potential control calcium signaling and contraction in the heart? *Journal of Molecular and Cellular Cardiology*, 49(6):901, 2010.

[297] A. Santiago, J. Aguado-Sierra, M. Zavala-Aké, R. Doste-Beltran, S. Gómez, R. Arís, J. C. Cajas, E. Casoni, and M. Vázquez. Fully coupled fluid-electro-mechanical model of the human heart for supercomputers. *International Journal for Numerical Methods in Biomedical Engineering*, 34(12):e3140, 2018.

[298] R. Shabetai, L. Mangiardi, V. Bhargava, J. Ross Jr, and C. B. Higgins. The pericardium and cardiac function. *Progress in Cardiovascular Diseases*, 22(2):107–134, 1979.

[299] N. Smith, D. Nickerson, E. Crampin, and P. Hunter. Multiscale computational modelling of the heart. *Acta Numerica*, 13:371–431, 2004.

[300] J. H. Spühler and J. Hoffman. An interface-tracking unified continuum model for fluid-structure interaction with topology change and full-friction contact with application to aortic valves. *International Journal for Numerical Methods in Engineering*, 122(19):5258–5278, 2021.

[301] J. H. Spühler, J. Jansson, N. Jansson, and J. Hoffman. 3D fluid-structure interaction simulation of aortic valves using a unified continuum ALE FEM model. *Frontiers in Physiology*, 9:363, 2018.

[302] J. H. Spühler, J. Jansson, N. Jansson, and J. Hoffman. A high performance computing framework for finite element simulation of blood flow in the left ventricle of the human heart. In H. Van Brummelen, A. Corsini, S. Perotto, and G. Rozza, editors, *Numerical Methods for Flows*, pages 155–164. Springer, 2020.

[303] C. L. Stanfield. *Principles of human physiology*. Pearson, 2016.

[304] K. Stein, T. Tezduyar, and R. Benney. Mesh moving techniques for fluid-structure interactions with large displacements. *Journal of Applied Mechanics*, 70(1):58–63, 2003.

[305] P. D. Stein and H. N. Sabbah. Turbulent blood flow in the ascending aorta of humans with normal and diseased aortic valves. *Circulation Research*, 39(1):58–65, 1976.

[306] D. Stephenson and D. Williams. Effects of sarcomere length on the force—pca relation in fast-and slow-twitch skinned muscle fibres from the rat. *The Journal of Physiology*, 333(1):637–653, 1982.

[307] R. S. Stephenson, P. Agger, P. P. Lunkenheimer, J. Zhao, M. Smerup, P. Niederer, R. H. Anderson, and J. C. Jarvis. The functional architecture of skeletal compared to cardiac musculature: Myocyte orientation, lamellar unit morphology, and the helical ventricular myocardial band. *Clinical Anatomy*, 29(3):316–332, 2016.

[308] D. D. Streeter Jr, H. M. Spotnitz, D. P. Patel, J. Ross Jr, and E. H. Sonnenblick. Fiber orientation in the canine left ventricle during diastole and systole. *Circulation Research*, 24(3):339–347, 1969.

[309] M. Strocchi, C. M. Augustin, M. A. Gsell, E. Karabelas, A. Neic, K. Gillette, O. Razeghi, A. J. Prassl, E. J. Vigmond, J. M. Behar, et al. A publicly available virtual cohort of four-chamber heart meshes for cardiac electro-mechanics simulations. *PloS One*, 15(6):e0235145, 2020.

[310] M. Strocchi, M. A. Gsell, C. M. Augustin, O. Razeghi, C. H. Roney, A. J. Prassl, E. J. Vigmond, J. M. Behar, J. S. Gould, C. A. Rinaldi, M. J. Bishop, G. Plank, and S. A. Niederer. Simulating ventricular systolic motion in a four-chamber heart model with spatially varying Robin boundary conditions to model the effect of the pericardium. *Journal of Biomechanics*, 101:109645, 2020.

[311] M. Strocchi, A. W. Lee, A. Neic, J. Bouyssier, K. Gillette, G. Plank, M. K. Elliott, J. Gould, J. M. Behar, B. Sidhu, et al. His-bundle and left bundle pacing with optimized atrioventricular delay achieve superior electrical synchrony over endocardial and epicardial pacing in left bundle branch block patients. *Heart Rhythm*, 17(11):1922–1929, 2020.

[312] T. Sugimoto, R. Dulgheru, A. Bernard, F. Ilardi, L. Contu, K. Addetia, L. Caballero, N. Akhaladze, G. D. Athanassopoulos, D. Barone, et al. Echocardiographic reference ranges for normal left ventricular 2D strain: results from the EACVI NORRE study. *European Heart Journal-Cardiovascular Imaging*, 18(8):833–840, 2017.

[313] S. Sugiura, J.-I. Okada, T. Washio, and T. Hisada. UT-Heart: A finite element model designed for the multiscale and multiphysics integration of our knowledge on the human heart. In S. Cortassa and M. A. Aon, editors, *Computational Systems Biology in Medicine and Biotechnology*, pages 221–245. Springer, 2022.

[314] J. Sundnes, G. T. Lines, X. Cai, B. F. Nielsen, K.-A. Mardal, and A. Tveito. *Computing the electrical activity in the heart*, volume 1. Springer Science & Business Media, 2007.

[315] E. Sung, A. Prakosa, K. N. Aronis, S. Zhou, S. L. Zimmerman, H. Tandri, S. Nazarian, R. D. Berger, J. Chrispin, and N. A. Trayanova. Personalized digital-heart technology for ventricular tachycardia ablation targeting in hearts with infiltrating adiposity. *Circulation: Arrhythmia and Electrophysiology*, 13(12):e008912, 2020.

[316] A. Tagliabue, L. Dede', and A. Quarteroni. Complex blood flow patterns in an idealized left ventricle: A numerical study. *Chaos*, 27(9):093939, 2017.

[317] B. Tayllamin, S. Mendez, R. Moreno, M. Chau, and F. Nicoud. Comparison of body-fitted and immersed boundary methods for biomechanical applications. In *Proc. of the Fifth European Conf. on Computational Fluid Dynamics, ECCOMAS CFD*, pages 1–20, 2010.

[318] C. A. Taylor, T. A. Fonte, and J. K. Min. Computational fluid dynamics applied to cardiac computed tomography for noninvasive quantification of fractional flow reserve: scientific basis. *Journal of the American College of Cardiology*, 61(22):2233–2241, 2013.

[319] C. A. Taylor, T. J. R. Hughes, and C. K. Zarins. Finite element modeling of blood flow in arteries. *Computer Methods in Applied Mechanics and Engineering*, 158(1-2):155–196, 1998.

[320] R. Temam. *Navier-Stokes equations: theory and numerical analysis*, volume 343. American Mathematical Society, 2001.

[321] K. H. Ten Tusscher and A. V. Panfilov. Alternans and spiral breakup in a human ventricular tissue model. *American Journal of Physiology-Heart and Circulatory Physiology*, 291(3):H1088–H1100, 2006.

[322] T. Terahara, T. Kuraishi, K. Takizawa, and T. E. Tezduyar. Computational flow analysis with boundary layer and contact representation: II. heart valve flow with leaflet contact. *Journal of Mechanics*, 38:185–194, 2022.

[323] T. Terahara, K. Takizawa, T. E. Tezduyar, Y. Bazilevs, and M.-C. Hsu. Heart valve isogeometric sequentially-coupled FSI analysis with the space–time topology change method. *Computational Mechanics*, 65:1167–1187, 2020.

[324] T. Tezduyar, S. Aliabadi, M. Behr, A. Johnson, and S. Mittal. Parallel finite-element computation of 3d flows. *Computer*, 26(10):27–36, 1993.

[325] T. Tezduyar and S. Sathe. Stabilization parameters in supg and pspg formulations. *Journal of Computational and Applied Mechanics*, 4(1):71–88, 2003.

[326] A. This, L. Boilevin-Kayl, M. A. Fernández, and J.-F. Gerbeau. Augmented resistive immersed surfaces valve model for the simulation of cardiac hemodynamics with isovolumetric phases. *International Journal for Numerical Methods in Biomedical Engineering*, 36(3):e3223, 2020.

[327] A. This, H. G. Morales, O. Bonnefous, M. A. Fernández, and J.-F. Gerbeau. A pipeline for image based intracardiac CFD modeling and application to the evaluation of the PISA method. *Computer Methods in Applied Mechanics and Engineering*, 358:112627, 2020.

[328] L. Thomas, E. Foster, and N. B. Schiller. Peak mitral inflow velocity predicts mitral regurgitation severity. *Journal of the American College of Cardiology*, 31(1):174–179, 1998.

[329] V. Timmermann, L. A. Dejgaard, K. H. Haugaa, A. G. Edwards, J. Sundnes, A. D. McCulloch, and S. T. Wall. An integrative appraisal of mechano-electric feedback mechanisms in the heart. *Progress in Biophysics and Molecular Biology*, 130:404–417, 2017.

[330] A. Timmis, N. Townsend, C. P. Gale, A. Torbica, M. Lettino, S. E. Petersen, E. A. Mossialos, A. P. Maggioni, D. Kazakiewicz, H. T. May, et al. European society of cardiology: cardiovascular disease statistics 2019. *European Heart Journal*, 41(1):12–85, 2020.

[331] M. Toma, D. R. Einstein, C. H. Bloodworth IV, R. P. Cochran, A. P. Yoganathan, and K. S. Kunzelman. Fluid–structure interaction and structural analyses using a comprehensive mitral valve model with 3D chordal structure. *International Journal for Numerical Methods in Biomedical Engineering*, 33(4):e2815, 2017.

[332] J. Tomek, A. Bueno-Orovio, E. Passini, X. Zhou, A. Minchole, O. Britton, C. Bartolucci, S. Severi, A. Shrier, L. Virag, et al. Development, calibration, and validation of a novel human ventricular myocyte model in health, disease, and drug block. *Elife*, 8, 2019.

[333] N. A. Trayanova. Whole-heart modeling: applications to cardiac electrophysiology and electromechanics. *Circulation Research*, 108(1):113–128, 2011.

[334] N. A. Trayanova, F. Pashakhanloo, K. C. Wu, and H. R. Halperin. Imaging-based simulations for predicting sudden death and guiding

ventricular tachycardia ablation. *Circulation: Arrhythmia and Electrophysiology*, 10(7):e004743, 2017.

[335] The Trilinos Project Website. https://trilinos.github.io (last accessed: 23 september 2022).

[336] A. Updegrove, N. M. Wilson, J. Merkow, H. Lan, A. L. Marsden, and S. C. Shadden. Simvascular: an open source pipeline for cardiovascular simulation. *Annals of Biomedical Engineering*, 45(3):525–541, 2017.

[337] T. Usyk, R. Mazhari, and A. McCulloch. Effect of laminar orthotropic myofiber architecture on regional stress and strain in the canine left ventricle. *Journal of Elasticity and the Physical Science of Solids*, 61(1):143–164, 2000.

[338] T. P. Usyk, I. J. LeGrice, and A. D. McCulloch. Computational model of three-dimensional cardiac electromechanics. *Computing and Visualization in Science*, 4(4):249–257, 2002.

[339] V. Vedula, J.-H. Seo, A. C. Lardo, and R. Mittal. Effect of trabeculae and papillary muscles on the hemodynamics of the left ventricle. *Theoretical and Computational Fluid Dynamics*, 30(1):3–21, 2016.

[340] J. Verbraecken, P. Van de Heyning, W. De Backer, and L. Van Gaal. Body surface area in normal-weight, overweight, and obese adults. a comparison study. *Metabolism*, 55(4):515–524, 2006.

[341] C. Vergara, M. Lange, S. Palamara, T. Lassila, A. F. Frangi, and A. Quarteroni. A coupled 3D–1D numerical monodomain solver for cardiac electrical activation in the myocardium with detailed Purkinje network. *Journal of Computational Physics*, 308:218–238, 2016.

[342] C. Vergara, S. Stella, M. Maines, P. C. Africa, D. Catanzariti, C. Dematté, M. Centonze, F. Nobile, A. Quarteroni, and M. Del Greco. Computational electrophysiology of the coronary sinus branches based on electro-anatomical mapping for the prediction of the latest activated region. *Medical & Biological Engineering & Computing*, 60(8):2307–2319, 2022.

[343] A. Verkaik, A. Bogaerds, F. Storti, and F. Van De Vosse. A coupled overlapping domain method for the computation of transitional flow

through artificial heart valves. In *ASME 2012 Summer Bioengineering Conference (SBC 2012)*, pages 217–218. American Society of Mechanical Engineers, 2012.

[344] R. Verzicco. Electro-fluid-mechanics of the heart. *Journal of Fluid Mechanics*, 941, 2022.

[345] E. J. Vigmond, C. Clements, D. M. McQueen, and C. S. Peskin. Effect of bundle branch block on cardiac output: a whole heart simulation study. *Progress in Biophysics and Molecular Biology*, 97(2-3):520–542, 2008.

[346] I. E. Vignon-Clementel, C. Figueroa, K. Jansen, and C. Taylor. Outflow boundary conditions for 3D simulations of non-periodic blood flow and pressure fields in deformable arteries. *Computer Methods in Biomechanics and Biomedical Engineering*, 13(5):625–640, 2010.

[347] F. Viola, G. Del Corso, R. De Paulis, and R. Verzicco. GPU accelerated digital twins of the human heart open new routes for cardiovascular research. *Research Square Preprint*, 2022.

[348] F. Viola, V. Meschini, and R. Verzicco. Fluid–structure–electrophysiology interaction (FSEI) in the left-heart: a multi-way coupled computational model. *European Journal of Mechanics-B/Fluids*, 79:212–232, 2020.

[349] F. Viola, V. Meschini, and R. Verzicco. Effects of stenotic aortic valve on the left heart hemodynamics: A fluid-structure-electrophysiology approach. *arXiv preprint arXiv:2103.14680*, 2021.

[350] F. Viola, V. Spandan, V. Meschini, J. Romero, M. Fatica, M. D. de Tullio, and R. Verzicco. FSEI-GPU: GPU accelerated simulations of the fluid–structure–electrophysiology interaction in the left heart. *Computer Physics Communications*, 273:108248, 2022.

[351] S. S. Virani, A. Alonso, E. J. Benjamin, M. S. Bittencourt, C. W. Callaway, A. P. Carson, A. M. Chamberlain, A. R. Chang, S. Cheng, F. N. Delling, et al. Heart disease and stroke statistics—2020 update: a report from the american heart association. *Circulation*, 141(9):e139–e596, 2020.

[352] VMTK. Website: http://www.vmtk.org/; code repository: https://github.com/marco-fedele/vmtk (last accessed: 23 september 2022).

[353] H. F. Walker and P. Ni. Anderson acceleration for fixed-point iterations. *SIAM Journal on Numerical Analysis*, 49:1715–1735, 2011.

[354] T. Washio, J.-i. Okada, A. Takahashi, K. Yoneda, Y. Kadooka, S. Sugiura, and T. Hisada. Multiscale heart simulation with cooperative stochastic cross-bridge dynamics and cellular structures. *Multiscale Modeling & Simulation*, 11(4):965–999, 2013.

[355] H. Watanabe, T. Hisada, S. Sugiura, J.-i. Okada, and H. Fukunari. Computer simulation of blood flow, left ventricular wall motion and their interrelationship by fluid-structure interaction finite element method. *JSME International Journal Series C Mechanical Systems, Machine Elements and Manufacturing*, 45(4):1003–1012, 2002.

[356] N. Westerhof, J.-W. Lankhaar, and B. E. Westerhof. The arterial windkessel. *Medical & biological engineering & computing*, 47(2):131–141, 2009.

[357] T. Wick. Solving monolithic fluid-structure interaction problems in arbitrary Lagrangian Eulerian coordinates with the deal.ii library. *Archive of Numerical Software*, 1(1):1–19, 2013.

[358] L. R. Williams. Reference values for total blood volume and cardiac output in humans. Technical report, Oak Ridge National Lab., TN (United States), 1994.

[359] F. Xu, E. L. Johnson, C. Wang, A. Jafari, C.-H. Yang, M. S. Sacks, A. Krishnamurthy, and M.-C. Hsu. Computational investigation of left ventricular hemodynamics following bioprosthetic aortic and mitral valve replacement. *Mechanics Research Communications*, 112:103604, 2021.

[360] J. Xu and L. Zikatanov. Algebraic multigrid methods. *Acta Numerica*, 26:591–721, 2017.

[361] Q. Zhang and T. Hisada. Analysis of fluid–structure interaction problems with structural buckling and large domain changes by ALE finite element method. *Computer Methods in Applied Mechanics and Engineering*, 190(48):6341–6357, 2001.

[362] A. Zingaro, M. Bucelli, I. Fumagalli, L. Dede', and A. Quarteroni. Modeling isovolumetric phases in cardiac flows by an Augmented Resistive Immersed Implicit Surface method. *arXiv preprint arXiv:arXiv:2208.09435*, 2022.

[363] A. Zingaro, L. Dede', F. Menghini, and A. Quarteroni. Hemodynamics of the heart's left atrium based on a variational multiscale-LES numerical method. *European Journal of Mechanics-B/Fluids*, 89:380–400, 2021.

[364] A. Zingaro, I. Fumagalli, L. Dede', M. Fedele, P. C. Africa, A. F. Corno, and A. Quarteroni. A geometric multiscale model for the numerical simulation of blood flow in the human left heart. *Discrete & Continuous Dynamical Systems-S*, 15:2391–2427, 2022.

[365] Zygote Media Group Inc. Zygote solid 3D heart generation II developement report. Technical report. 2014.